COLLEGE DOCTORAL PAYS DE LA LOIRE
ED MATIERE, MOLECULES MATERIAUX ET GEOSCIENCES

IMT Atlantique
Bretagne-Pays de la Loire
École Mines-Télécom

# Thèse de doctorat de

L'École Nationale Supérieure Mines-Télécom Atlantique
Bretagne Pays de la Loire – IMT Atlantique

École Doctorale N° 596
Matière, Molécules, Matériaux et Géosciences
Spécialité : Physique subatomique (nucléaire et des particules)

Par


## Antoine Amy


# Impurities & Radioactive Background Control in a Cryogenic Liquid-Xenon $0\nu\beta\beta$ Rare-Event Detector


© 2026 Antoine Amy — CC BY 4.0, hors éléments de tiers.


Thèse présentée et soutenue à IMT Atlantique, Nantes, le 28 septembre 2026
Unité de recherche : Laboratoire SUBATECH, UMR 6457
Thèse N° : 2026IMTA0549


**Composition du jury :**

**Président :**

Damir Buskulic, Professeur, Université Savoie Mont Blanc, LAPP, Annecy

**Rapporteurs :**

Pia Loaiza, Chargée de Recherche - HDR, Université Paris-Saclay / CNRS, IJCLab
Francesc Monrabal, Professeur associé, DIPC, Donostia-San Sebastián, Espagne

**Examinateurs :**

Dominique Leduc, Professeur, Nantes Université, Nantes
Yajing Xing, Maîtresse de conférences, LPNHE, Paris

**Directeurs de thèse :**

Julien Masbou, Maître de conférences - HDR, Nantes Université
Andrea Pocar, Professeur, University of Massachusetts Amherst
Dominique Thers, Professeur, IMT Atlantique




University *of*
Massachusetts
Amherst

Cette thèse a été réalisée à l'IMT Atlantique, au sein du laboratoire SUBATECH, en collaboration avec l'université du Massachusetts à Amherst (UMass Amherst). La moitié de ce travail doctoral a bénéficié du soutien financier d'UMass Amherst, incluant un séjour de quinze mois en tant que chercheur invité au sein du groupe du professeur Andrea Pocar, au département de physique.

University of Massachusetts Amherst
Department of Physics
Research group of Prof. Andrea Pocar

# Acknowledgments

Cette thèse représente l'accomplissement de trois années de travail, mais aussi de nombreuses années d'études et de rencontres qui m'ont mené jusqu'ici. Il serait impossible de remercier toutes les personnes qui m'ont accompagné sans écrire une seconde thèse. Je voudrais néanmoins remercier celles et ceux avec qui j'ai eu la chance de travailler ces trois dernières années, à Subatech comme à UMass, où j'ai rencontré de nombreuses personnes bienveillantes, toujours prêtes à aider.

Julien et Andrea, mes encadrants, vous avez toujours été disponibles, encourageants et à l'écoute, même avec des emplois du temps de ministres ! Merci de m'avoir donné envie de continuer dans la recherche et de m'avoir donné la chance de faire cette thèse. Julien, tu m'avais dit qu'une thèse était d'abord une aventure humaine avant d'être une expérience de recherche, et tu avais raison ! Je remercie également mes collègues de la collaboration nEXO, en particulier Samuele, qui m'a beaucoup aidé sur la partie Monte-Carlo. Je remercie aussi Pia Loaiza et Francesc Monrabal d'avoir accepté d'être les rapporteurs de cette thèse, ainsi que les autres membres du jury pour le temps consacré à l'évaluation de ce travail.

Un très grand merci à tous les merveilleux amis que j'ai pu me faire durant cette thèse. Je n'aurais jamais imaginé recevoir autant de soutien et d'amour à Subatech, en particulier de la part de Pietro, Félix, Solène, Nadège, Quentin, Tobie, Jad, Sarah, Léonard, Laurine, Yohann, Jakub, Ugo, Baptiste et Johan, ainsi que de tous les nouveaux arrivants. Tous nos moments à La Flèche, à Prague, à Brest ou au Nouvel An me sont très chers. I would also like to thank all my friends on the other side of the Atlantic, especially Shannen, Abdul, Graeme, Seth, Sean, Albert, and Mark, as well as Emma, Marion, Thomas, Alyssa, Anaëlle, Kévin, and Charlotte and her family, for making my stay at UMass so enjoyable, even in a small town in the middle of nowhere like Amherst. I hope to see you all again one day! Je souhaite aussi remercier mes amis de longue date, que je considère aujourd'hui comme ma famille : Antonin et Alexandre, Till, Léo, ainsi que la famille Thoprieux-Ferraris.

Je terminerai ces remerciements par mes parents, que je voudrais remercier pour l'éducation et le soutien qu'ils m'ont donnés et qui m'ont permis d'arriver jusqu'ici. Merci de m'avoir toujours encouragé à faire de mon mieux et d'avoir été à mes côtés tout au long de ce parcours.

À toutes les personnes que j'ai pu oublier : désolé... Vous savez à quel point ma mémoire, surtout pour les prénoms, est loin d'être infaillible ! Mais ne doutez pas que vous avez aussi une place dans mon cœur.

# Contents

**Acknowledgments** ii

**Acronyms** vii

**Introduction** 1

**1 Neutrinoless Double Beta Decay as a Probe for New Physics** 3
- 1.1 Standard Model basics for rare-event searches . . . 4
  - 1.1.1 Fundamental particles and forces . . . 5
  - 1.1.2 Electroweak gauge structure . . . 6
  - 1.1.3 Chiral charged current weak interaction . . . 7
  - 1.1.4 Conservation laws and selection rules . . . 8
- 1.2 Neutrinos in contemporary physics . . . 8
  - 1.2.1 Beta decay Pauli hypothesis . . . 9
  - 1.2.2 Neutrinos in weak interactions . . . 10
  - 1.2.3 Neutrino mixing oscillations . . . 11
  - 1.2.4 Neutrino mass ordering . . . 12
  - 1.2.5 Dirac versus Majorana neutrinos . . . 14
- 1.3 Double beta decay . . . 17
  - 1.3.1 Double beta decay two neutrino mode . . . 18
  - 1.3.2 Neutrinoless double beta decay signature . . . 19
  - 1.3.3 Half-life decomposition . . . 20
  - 1.3.4 Implications of neutrinoless double beta decay . . . 21
  - 1.3.5 Current limits and experimental landscape . . . 22

**2 Dedicated Liquid Xenon Detector for $0\nu\beta\beta$ Searches** 24
- 2.1 $^{136}$Xe as a Detection Medium . . . 25
- 2.2 Liquid Xenon TPC Working Principle . . . 27
- 2.3 EXO-200 as a technology pathfinder . . . 28
- 2.4 Detector Design Overview . . . 29
  - 2.4.1 Light and charge collection . . . 30
  - 2.4.2 Cryostat . . . 35
  - 2.4.3 External shielding . . . 36
- 2.5 Signal & Background Model . . . 36
  - 2.5.1 Signal definition . . . 36

2.5.2 Background sources . . . 37
2.5.3 Selection criteria . . . 39
2.5.4 Sensitivity metrics . . . 41
2.5.5 Projected reach in $T^{0\nu}_{1/2}$ and $m_{\beta\beta}$ . . . 42
2.5.6 Running and next-generation $0\nu\beta\beta$ programs . . . 44

**3 Charge Transport and Liquid Xenon Purity 46**
3.1 Charge Transport in Liquid Xenon . . . 47
3.1.1 O2-equivalent Concentration and Electron Attachment in LXe 48
3.1.2 Electron Lifetime Requirement . . . 51
3.1.3 Allowed Impurity Source Rate . . . 52
3.1.4 Impurity Budgeting . . . 56
3.2 Detector Material Outgassing . . . 57
3.2.1 Gas Sources in Xenon-Contact Materials . . . 59
3.2.2 Total Outgassing Model . . . 64
3.3 Measurement Methods . . . 67
3.3.1 Vacuum Chambers . . . 68
3.3.2 Liquid Xenon Drift Chambers . . . 77
3.4 Mitigation Techniques . . . 78
3.4.1 Material Choice and Geometry . . . 78
3.4.2 Cleaning and Preparation Techniques . . . 79
3.4.3 Storage After Cleaning . . . 80

**4 Background Mitigation with Cryogenic Shields 81**
4.1 Background Model . . . 82
4.1.1 Internal Background Sources . . . 82
4.1.2 Background Calculation Method . . . 84
4.1.3 Reference Background Budget . . . 88
4.2 Cryogenic Fluorinated Liquid Shield (HFE) . . . 90
4.2.1 HFE Properties, Radiopurity, and Shielding Role . . . 90
4.2.2 Ultra-Radiopure Nickel Cryostat . . . 92
4.3 Internal Backgrounds vs. HFE Thickness . . . 95
4.3.1 HFE . . . 96
4.3.2 Cryostat Vessels . . . 100
4.3.3 Water Shield . . . 103
4.3.4 Other Components . . . 107
4.3.5 Updated Background Budget . . . 112
4.4 Possible Design Optimizations . . . 114
4.4.1 Reduced HFE Configuration . . . 114
4.4.2 Improved Water Shielding with a Smaller Outer Vessel . . . 121
4.4.3 Cylindrical Cryostat . . . 123

**5 Characterization of Cryogenic Hydrofluoroether Flow** **128**
5.1 Cooling Hydrofluoroether Fluids . . . 130
5.1.1 Thermophysical Properties of HFE . . . 130
5.1.2 Differential Scanning Calorimetry Measurements . . . 134
5.2 UMass HFE Recirculation System . . . 137
5.2.1 Piping and Instrumentation Diagram . . . 139
5.2.2 Cryogenic Recirculation Pump . . . 142
5.2.3 Sensor Suite . . . 144
5.2.4 Thermal Insulation . . . 146
5.2.5 Liquid-Nitrogen Heat Exchanger . . . 149
5.3 Support Infrastructure . . . 154
5.3.1 HFE Reservoir . . . 155
5.3.2 Fluid Manifold . . . 158
5.3.3 Gas Trap . . . 159
5.3.4 Feed and Return Lines . . . 160
5.4 Slow-Control System . . . 163
5.4.1 Electrical Architecture . . . 164
5.4.2 Control Logic . . . 168
5.4.3 Data Acquisition and Logging . . . 169
5.5 Commissioning and Performance Tests . . . 170
5.5.1 Room-Temperature Pump Commissioning . . . 170
5.5.2 Thermocouple Calibration . . . 174
5.5.3 Heat-Exchanger Performance . . . 178
5.5.4 Leak-Tightness Tests . . . 182
5.5.5 Initial System Fill . . . 185
5.6 Analysis of Cryogenic Runs . . . 187
5.6.1 System Performance . . . 188
5.6.2 Pump Performance . . . 194
5.6.3 Cryogenic HFE Behavior . . . 198
5.7 Future Developments . . . 202
5.7.1 Controls and Monitoring . . . 202
5.7.2 HFE Mixtures . . . 202

**Conclusion** **204**

**Résumé en français** **206**
1 Double désintégration bêta sans neutrinos . . . 207
2 Détecteur au xénon liquide pour la recherche de $0\nu\beta\beta$ . . . 208
3 Transport de charge et pureté du xénon liquide . . . 210
4 Réduction du bruit de fond par le cryostat et le blindage HFE . . . 212
5 Refroidissement et recirculation du HFE . . . 214

**Appendix A Additional Details on Background-Rate Propagation** **217**
A.1 Monte Carlo Uncertainty on Hit Efficiencies . . . 217
A.2 Standard-Normal Functions and Mills Ratio . . . 218
A.3 Moments of the One-Sided Truncated Gaussian . . . 218
A.4 Equivalent Form in Terms of exp and erf . . . 220

**Appendix B Mean HFE and Attenuation-Equivalent Thicknesses** **221**
B.1 Geometry and Definitions . . . 221
B.2 Minimum Thickness . . . 222
B.3 Angular Mean Thickness and Transmission . . . 223
B.4 Interpretation . . . 224

**Appendix C Hit-Efficiency and Water Radioassay Tables** **225**
C.1 Parent-normalized hit-efficiency tables . . . 225
C.1.1 HFE hit efficiencies . . . 225
C.1.2 Cryostat-vessel hit efficiencies . . . 226
C.1.3 Direct HFE-shielding comparison for the inner vessel . . . 226
C.2 Water-radioactivity assay values . . . 228

**Appendix D Pressure-Drop in the HFE Recirculation Loop** **229**

**Appendix E Preliminary Sizing of the LN2 Heat Exchanger** **232**

**Appendix F Purification Model Solution** **236**

**Appendix G Diffusion Model Details** **238**
G.1 Initial Bulk Concentration . . . 238
G.2 Finite-Slab Diffusion Solution . . . 239

**Bibliography** **241**

**Abstract** **250**

# Acronyms

**$0\nu\beta\beta$** neutrinoless double-beta decay
**$2\nu\beta\beta$** two-neutrino double-beta decay
**ABS** acrylonitrile butadiene styrene
**ASIC** application-specific integrated circuit
**CC** charged current
**CFC** carbon-fiber composite
**CP** charge–parity
**DNN** deep neural network
**DSC** differential scanning calorimetry
**ENC** equivalent noise charge
**EPDM** ethylene propylene diene monomer
**EXO-200** Enriched Xenon Observatory 200
**FEP** fluorinated ethylene propylene
**FWHM** full width at half maximum
**GXe** gaseous xenon
**HFE** hydrofluoroether
**HX** heat exchanger
**IO** inverted neutrino-mass ordering
**IV** inner vessel
**LAr** liquid argon
**$LN_2$** liquid nitrogen
**LXe** liquid xenon
**MC** Monte Carlo
**m.w.e.** meters water equivalent
**MLI** multilayer insulation
**NC** neutral current
**nEXO** next-generation Enriched Xenon Observatory
**NME** nuclear matrix element
**NO** normal neutrino-mass ordering
**NPT** National Pipe Taper thread
**OD** outer detector
**OV** outer vessel
**$O_2$-eq.** oxygen-equivalent
**PDE** photon detection efficiency
**P&ID** piping and instrumentation diagram
**PMNS** Pontecorvo–Maki–Nakagawa–Sakata
**PMT** photomultiplier tube
**PTE** photon transport efficiency
**PTFE** polytetrafluoroethylene
**RGA** residual gas analyzer
**ROI** region of interest
**SD** standoff distance
**SiPM** silicon photomultiplier
**SLPM** standard liters per minute
**SM** Standard Model
**SPAD** single-photon avalanche diode
**SS** single-site
**STP** standard temperature and pressure
**TG** truncated Gaussian
**TPC** time projection chamber
**VCR** metal-gasket face-seal fitting
**VFD** variable-frequency drive
**VUV** vacuum ultraviolet

# Introduction

Neutrino oscillations have established that neutrinos have nonzero masses, a fact not explained by the Standard Model. This discovery leaves several fundamental questions open:

- What is the absolute neutrino mass scale?
- Are neutrinos Dirac particles, distinct from their antiparticles, or Majorana particles, identical to them?
- Is lepton number an exact symmetry of nature?

These questions reach beyond neutrino physics alone, since Majorana neutrinos and lepton-number violation would point to physics beyond the Standard Model and may be connected to the origin of the matter–antimatter asymmetry of the Universe.

Neutrinoless double beta decay, denoted $0\nu\beta\beta$, addresses the Dirac-vs-Majorana and lepton-number questions directly. In this hypothetical nuclear decay, two electrons are emitted without the two antineutrinos present in the Standard-Model-allowed two-neutrino mode. Its observation would demonstrate lepton-number violation and establish that neutrinos have a Majorana mass component. The expected signal is a peak at the isotope $Q$ value: in the absence of emitted neutrinos, the two electrons carry nearly all of the available decay energy. The challenge is that the process, if it exists, is extremely rare: current searches probe half-lives at the $10^{26}$ yr scale, while future-generation experiments aim for sensitivities near $10^{28}$ yr.

The isotope $^{136}$Xe is one of the leading candidates for this search. Xenon can be enriched in $^{136}$Xe and operated as a liquid-xenon time projection chamber, so the source isotope is also the active detector medium. Liquid xenon provides a dense, homogeneous, self-shielding target in which scintillation light and ionization charge can be measured. These observables allow reconstruction of energy, position, and topology, providing strong discrimination between signal-like events and radioactive backgrounds.

The dissertation is organized as follows:

1. **Chapter 1** introduces neutrinoless double beta decay as a probe of physics beyond the Standard Model.
2. **Chapter 2** presents liquid-xenon TPCs for $^{136}$Xe $0\nu\beta\beta$ searches, with emphasis on nEXO.
3. **Chapter 3** discusses charge transport in liquid xenon and the purity requirements associated with long electron drift.

4. **Chapter 4** studies radioactive-background mitigation through cryostat and cryogenic-shield design choices.
5. **Chapter 5** presents the characterization of cryogenic HFE flow using the recirculation system developed at UMass Amherst.

The work reported here was carried out first at SUBATECH in Nantes, France, from October 2023 to April 2025, and then at the University of Massachusetts Amherst in the United States from April 2025 to August 2026. Within this broader physics context, the dissertation focuses on three detector conditions that affect the sensitivity of a large liquid-xenon $0\nu\beta\beta$ search.

| **Theme** | **Experimental focus** |
|---|---|
| LXe purity | Electronegative-impurity effects on charge collection |
| Radiogenic background | Radiopurity and shielding requirements |
| Cryogenic shield | HFE cooling and circulation near $-110\,^{\circ}\mathrm{C}$ |

Table 1: Experimental scope of this dissertation.

The purpose of this dissertation is therefore to examine how these experimental constraints enter the design and operation of a liquid-xenon rare-event detector. The following chapters move from the physics case for $0\nu\beta\beta$ to the detector requirements needed to search for it at the next sensitivity scale.

# Chapter 1

# Neutrinoless Double Beta Decay as a Probe for New Physics

## Contents


**1.1 Standard Model basics for rare-event searches . . . . . 4**
1.1.1 Fundamental particles and forces . . . . . 5
1.1.2 Electroweak gauge structure . . . . . 6
1.1.3 Chiral charged current weak interaction . . . . . 7
1.1.4 Conservation laws and selection rules . . . . . 8
**1.2 Neutrinos in contemporary physics . . . . . 8**
1.2.1 Beta decay Pauli hypothesis . . . . . 9
1.2.2 Neutrinos in weak interactions . . . . . 10
1.2.3 Neutrino mixing oscillations . . . . . 11
1.2.4 Neutrino mass ordering . . . . . 12
1.2.5 Dirac versus Majorana neutrinos . . . . . 14
**1.3 Double beta decay . . . . . 17**
1.3.1 Double beta decay two neutrino mode . . . . . 18
1.3.2 Neutrinoless double beta decay signature . . . . . 19
1.3.3 Half-life decomposition . . . . . 20
1.3.4 Implications of neutrinoless double beta decay . . . . . 21
1.3.5 Current limits and experimental landscape . . . . . 22

The Standard Model (SM) provides a very good description of the strong, electromagnetic, and weak interactions. However, neutrino flavor oscillations show that the minimal SM is incomplete: neutrinos have nonzero masses, and the lepton flavor states mix. Accommodating neutrino masses requires physics beyond the SM as usually formulated, but the origin of these masses remains unknown, including whether neutrinos are Dirac fermions distinct from their antiparticles or Majorana fermions identical to their antiparticles. Neutrinoless double beta decay ($0\nu\beta\beta$) is a direct experimental test of this question. Its observation would establish lepton-number violation by two units ($\Delta L = 2$).

## 1.1 Standard Model basics for rare-event searches

The Standard Model (SM) is the established framework for interpreting laboratory measurements of the strong, weak, and electromagnetic interactions [1]. It specifies the known particle content, summarized in Fig. 1.1.

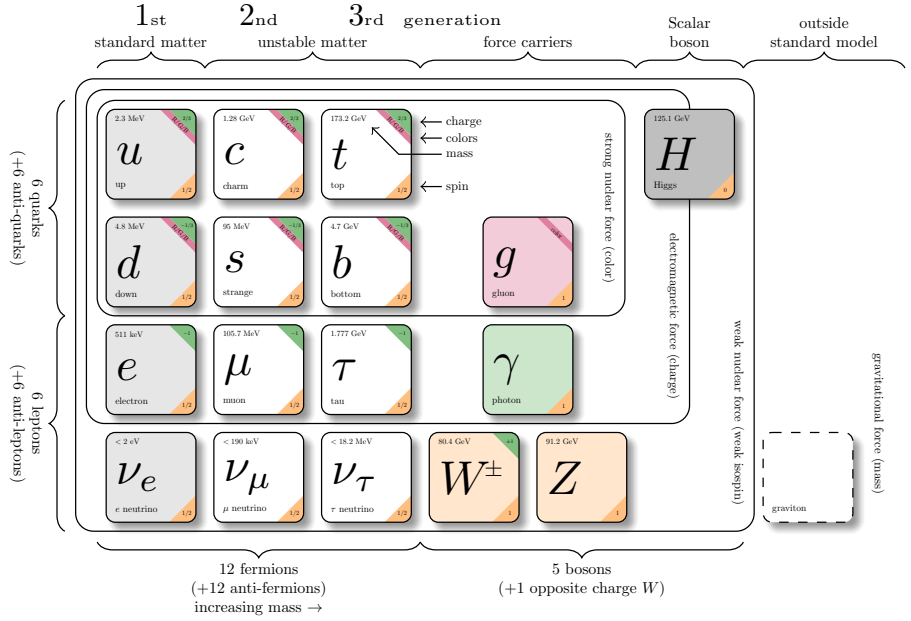


Figure 1.1: Particle content of the Standard Model: three generations of fermions and the bosons associated with the gauge interactions and electroweak symmetry breaking. Artwork by David Galbraith and Carsten Burgard.

Figure 1.1 groups the SM fields into fermions and bosons. The fermions appear in three generations with the same charge pattern but increasing mass: $(u, d)$ with $(\nu_e, e)$, then $(c, s)$ with $(\nu_\mu, \mu)$, then $(t, b)$ with $(\nu_\tau, \tau)$. Quarks carry color and participate in the strong interaction, while charged leptons do not. In the minimal SM, neutrinos are electrically neutral and interact only through the weak interaction. The heavier fermions are unstable and decay through weak interactions to lighter states. The bosons shown are the gluon $g$, photon $\gamma$, weak bosons $W^\pm$ and $Z$,

and the Higgs boson $H$. The nonzero Higgs vacuum expectation value sets the electroweak mass scale, giving masses to $W^{\pm}$ and $Z$, while charged-fermion masses arise from Yukawa couplings to the Higgs field [1, 2, 3].

A particle and its antiparticle have the same mass and spin but opposite additive quantum numbers. For example, $e^-$ and $e^+$ have charges $-1$ and $+1$, quarks $q$ and antiquarks $\bar{q}$ have opposite electric and color charges, and neutrinos and antineutrinos carry opposite lepton number. Neutral bosons such as $\gamma$ and $Z$ are their own antiparticles, while $W^+$ and $W^-$ are charge-conjugate partners [1].

### 1.1.1 Fundamental particles and forces

Table 1.1 summarizes the interactions in an experimental language, giving the mediator, the charge to which it couples, an indicative range, and representative processes. In the SM, electromagnetism and the weak interaction arise from a single electroweak gauge theory, discussed in more detail in Sec. 1.1.2. At the low energies relevant for nuclear physics, this unified interaction appears as electromagnetism, weak charged-current (CC) interactions mediated by $W^{\pm}$, and weak neutral-current (NC) interactions mediated by the $Z$ boson.

| Interaction | Carrier | Couples to | Range | Processes |
|---|---|---|---|---|
| Strong (QCD) | $g$ | color (quarks) | $\lesssim 1\,\mathrm{fm}$ | hadron structure, nuclear binding |
| Electro-magnetic | $\gamma$ | electric charge | long ($\infty$) | atomic binding, ionization/radiative |
| Weak (CC) | $W^{\pm}$ | left-chiral fermions | $\approx 10^{-3}\,\mathrm{fm}$ | nuclear $\beta^{\pm}$ decay, $\nu_\ell$ CC scattering |
| Weak (NC) | $Z$ | fermions (chiral couplings) | $\approx 10^{-3}\,\mathrm{fm}$ | $\nu_\ell$ NC scattering |
| Gravi-tational | — | mass–energy | long ($\infty$) | astro/geophysical, negl. at nuclear scales |

Table 1.1: Summary of the fundamental interactions and how they appear in nature (CC/NC = charged/neutral current).

The strong interaction acts on quarks through color charge and is mediated by gluons. At low energies it confines quarks into hadrons and sets the structure of nucleons. In nuclei, the residual strong interaction between nucleons provides the attractive force responsible for nuclear binding and fixes the characteristic nuclear length scale at the femtometer level.

Electromagnetism is mediated by the photon and couples to electric charge. Because the photon is massless, the interaction is long ranged and dominates atomic structure and the propagation of charged particles in matter. In detector media, electromagnetic interactions govern ionization, radiative losses, and multiple scattering,

and in many cases also produce scintillation. They therefore largely determine how electron-recoil energy depositions are measured.

The weak interaction is mediated by the massive $W^{\pm}$ and $Z$ bosons and is therefore short ranged compared with electromagnetism. Charged-current interactions mediated by $W^{\pm}$ change fermion flavor and electric charge and govern nuclear beta decay. Neutral-current interactions mediated by the $Z$ boson leave electric charge unchanged and provide additional flavor-preserving neutrino scattering channels.

Gravity couples universally to mass–energy and is long ranged, but its strength is negligible for microscopic processes. It plays no direct role in nuclear decays or in particle interactions in detector volumes and is therefore omitted from the detailed discussions in the remainder of this dissertation.

### 1.1.2 Electroweak gauge structure

The SM is formulated as a gauge theory. Rather than introducing arbitrary couplings, one imposes invariance under specified symmetry transformations acting on the fields. This implies the existence of the corresponding gauge fields and strongly constrains the allowed couplings between matter and force carriers, leaving a limited set of parameters to be fixed by experiment. The SM symmetry structure is

$$G_{\mathrm{SM}} = SU(3)_c \times SU(2)_L \times U(1)_Y, \tag{1.1}$$

where $SU(3)_c$ describes QCD and the electroweak interaction arises from the product $SU(2)_L \times U(1)_Y$. Gravity is not included in $G_{\mathrm{SM}}$ because the SM is a quantum field theory formulated on a fixed spacetime background and does not incorporate a quantum theory of gravity.

Electroweak symmetry breaking is implemented through the Higgs mechanism. The Higgs field is an $SU(2)_L$ doublet,

$$\Phi(x) = \begin{pmatrix} \phi^{+}(x) \\ \phi^{0}(x) \end{pmatrix}, \qquad Q\big(\phi^{+}\big) = +1, \;\; Q\big(\phi^{0}\big) = 0, \tag{1.2}$$

with charged and neutral components treated together by the weak interaction. The neutral component acquires a nonzero vacuum expectation value,

$$\langle \Phi \rangle = \frac{1}{\sqrt{2}} \begin{pmatrix} 0 \\ v \end{pmatrix}, \qquad v \simeq 246\,\mathrm{GeV}, \tag{1.3}$$

which breaks the electroweak symmetry according to

$$SU(2)_L \times U(1)_Y \;\rightarrow\; U(1)_{\mathrm{em}}. \tag{1.4}$$

As a result, the gauge fields reorganize into the observed electroweak bosons: the charged fields form the massive $W^{\pm}$, while the neutral electroweak fields mix into the photon $\gamma$ and the massive $Z$, with the mixing parametrized by the weak mixing angle $\theta_W$ [3].

For nuclear beta processes relevant to rare-event searches, the key low-energy consequence is the charged-current weak interaction mediated by $W^{\pm}$. A defining feature of this interaction is its chiral structure: it couples only to left-chiral fermion fields.

### 1.1.3 Chiral charged current weak interaction

A defining feature of the SM charged-current (CC) weak interaction is its chirality: it couples only to left-chiral fermion fields and, equivalently, to right-chiral antifermion fields. For a spin-$\frac{1}{2}$ field $\psi$, the left- and right-chiral components are defined through the Dirac matrix $\gamma^5$ and the projectors

$$P_{L,R} \equiv \frac{1 \mp \gamma^5}{2}, \qquad \psi_L \equiv P_L \psi, \qquad \psi_R \equiv P_R \psi. \tag{1.5}$$

Because parity exchanges left and right, the fact that the charged-current weak interaction couples only to the left-chiral component implies maximal parity violation in CC weak processes [4, 5].

In a Lorentz-invariant formulation, handedness selection is expressed in terms of chirality, which is a property of the field, while experiments often discuss helicity, which is a property of a one-particle state. For a particle with momentum $\vec{p}$ and spin $\vec{S}$, the helicity is

$$h \equiv \frac{\vec{S} \cdot \vec{p}}{|\vec{p}|}, \tag{1.6}$$

so that $h = +\frac{1}{2}$ $(-\frac{1}{2})$ corresponds to spin aligned (anti-aligned) with the momentum. In the ultrarelativistic limit ($E \gg m$), helicity approximately matches chirality, while for massive particles helicity can be reversed by a boost even though the chirality of the field is unchanged [6].

In the SM, the charged weak current has the vector-minus-axial-vector $(V-A)$ structure

$$\overline{\psi}\gamma^\mu(1-\gamma^5)\chi \;=\; \underbrace{\overline{\psi}\gamma^\mu\chi}_{V^\mu} \;-\; \underbrace{\overline{\psi}\gamma^\mu\gamma^5\chi}_{A^\mu} \;=\; 2\,\overline{\psi}\gamma^\mu P_L\chi, \tag{1.7}$$

where $V^\mu$ and $A^\mu$ denote the vector and axial-vector currents. Writing the current as $2\,\overline{\psi}\gamma^\mu P_L\chi$ makes explicit that only left-chiral fermion fields enter the CC weak interaction [4].

Grouping generations into flavor vectors[1] $\ell \equiv (e, \mu, \tau)^T$, $\nu \equiv (\nu_e, \nu_\mu, \nu_\tau)^T$, $u \equiv (u, c, t)^T$, and $d \equiv (d, s, b)^T$, the SM charged-current interaction Lagrangian can be written as [7, 8]

$$\mathcal{L}_{\mathrm{CC}} = -\frac{g}{\sqrt{2}} \left(\overline{\nu}\,\gamma^\mu P_L\,\ell + \overline{u}\,\gamma^\mu P_L\,V_{\mathrm{CKM}}\,d\right) W_\mu^+ + \mathrm{h.c.}, \tag{1.8}$$

where $g$ is the $SU(2)_L$ gauge coupling, $W_\mu^\pm$ are the charged weak gauge fields, and the unitary $3 \times 3$ matrix $V_{\mathrm{CKM}}$ encodes quark flavor mixing.

At nuclear energies, the CC interaction governs beta decay. For example, $\beta^-$ decay proceeds as

$$n \;\to\; p \;+\; e^- \;+\; \bar{\nu}_e. \tag{1.9}$$

This interaction will be used repeatedly below in discussing beta decay and double beta decay.

[1] The superscript $T$ denotes transpose; e.g. $(e, \mu, \tau)^T$ is a column vector of flavor fields.

### 1.1.4 Conservation laws and selection rules

Conservation laws in the SM follow from symmetries of the underlying relativistic quantum field theory. Continuous symmetries imply conserved currents and associated conserved charges. For example, electromagnetism is described by a $U(1)_{\mathrm{em}}$ symmetry, and the corresponding conserved quantity is the total electric charge $Q$ [9]. Baryon number $B$ and total lepton number $L$ are also conserved in the SM processes considered in this dissertation [1]. A selection rule states that if a quantum number $X$ is conserved, any allowed process must satisfy $\Delta X = 0$ between initial and final states. Table 1.2 summarizes the quantum numbers used throughout this dissertation, focusing on electric charge $Q$, baryon number $B$, and lepton number $L$.

| Particle | Electric charge $Q$ | Baryon number $B$ | Lepton number $L$ |
|---|---|---|---|
| $e^- \,/\, e^+$ | $-1 \,/\, +1$ | $0$ | $+1 \,/\, -1$ |
| $\nu \,/\, \bar{\nu}$ | $0$ | $0$ | $+1 \,/\, -1$ |
| $q \,/\, \bar{q}$ | $+\frac{2}{3}, -\frac{1}{3} \,/\, -\frac{2}{3}, +\frac{1}{3}$ | $+\frac{1}{3} \,/\, -\frac{1}{3}$ | $0$ |

Table 1.2: Global quantum numbers used throughout this dissertation. Electric charge $Q$ is given in units of $e$; for quarks, the two charge values correspond to up-type and down-type flavors.

Other conserved or approximately conserved quantities are also used in particle and nuclear physics, such as individual lepton-flavor numbers ($L_e$, $L_\mu$, $L_\tau$), quark-flavor numbers, approximate strong-interaction symmetries such as isospin, and discrete symmetries such as parity $P$, charge conjugation $C$, and time reversal $T$, but they are not required for the discussions of this dissertation [1].

Electric charge is conserved in all SM processes. Baryon number counts the net number of quarks minus antiquarks, in units of one third. Lepton number describes lepton production in weak processes: in the SM charged-current vertex, a charged lepton is produced or absorbed together with the corresponding neutrino or antineutrino in such a way that the net lepton number is unchanged. A standard example is nuclear $\beta^-$ decay, Eq. (1.9), where the emitted electron carries $L = +1$ and the emitted electron antineutrino carries $L = -1$, giving $\Delta L = 0$ overall.

Any observed transition with $\Delta Q \neq 0$ would contradict gauge invariance as implemented in the SM, while evidence for $\Delta B \neq 0$ or $\Delta L \neq 0$ would show that the SM symmetries are incomplete and that additional interactions must exist. In particular, neutrinoless double beta decay would correspond to $\Delta L = 2$ and is therefore a direct probe of lepton-number violation beyond the SM [10].

## 1.2 Neutrinos in contemporary physics

Neutrinos are the only SM fermions whose masses are not accounted for by the SM Lagrangian. Oscillation measurements establish that neutrino flavor states mix

and that at least two neutrino mass eigenstates have nonzero masses, while leaving open the absolute mass scale, the mass ordering, and whether neutrinos are Dirac or Majorana fermions.

### 1.2.1 Beta decay Pauli hypothesis

Precision measurements of nuclear $\beta$ decay in the 1910s–1920s revealed a key puzzle. The emitted electron has a continuous kinetic-energy spectrum that extends up to a well-defined endpoint. In a two-body decay,

$$ {}^{A}_{Z}X \;\rightarrow\; {}^{A}_{Z+1}Y \;+\; e^{-}, \tag{1.10} $$

energy–momentum conservation would instead fix the electron energy to a discrete value, up to small recoil corrections. The observed continuum therefore implies that an additional particle carries away a variable fraction of the decay energy.

Pauli proposed in 1930 that $\beta$ decay emits a new, light, electrically neutral particle to preserve energy, momentum, and angular-momentum conservation event-by-event [11]. $\beta^{-}$ decay can be written as

$$ {}^{A}_{Z}X \;\rightarrow\; {}^{A}_{Z+1}Y \;+\; e^{-} \;+\; \bar{\nu}_{e}, \tag{1.11} $$

and the electron spectrum is continuous because the available energy is shared among three final-state particles. Figure 1.2 illustrates the characteristic spectral shape, emphasizing the endpoint at the decay $Q$ value.

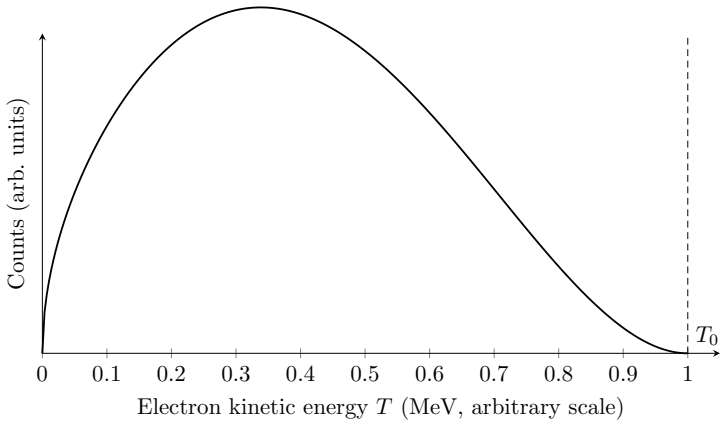


Figure 1.2: Schematic electron kinetic-energy spectrum in allowed nuclear $\beta^{-}$ decay (arbitrary units), drawn from the leading leptonic phase-space dependence $dN/dT \propto pE\,(T_0 - T)^2$ [12]. The spectrum is continuous and terminates at the endpoint energy $T_0 \simeq Q_\beta$ (dashed line).

Fermi developed Pauli's hypothesis into a quantitative theory of $\beta$ decay in 1933–1934, introducing a point-like four-fermion interaction that reproduces the observed rates and spectral shapes at nuclear energies [13]. The three-body interpretation of the $\beta$ spectrum is summarized in Fig. 1.3.

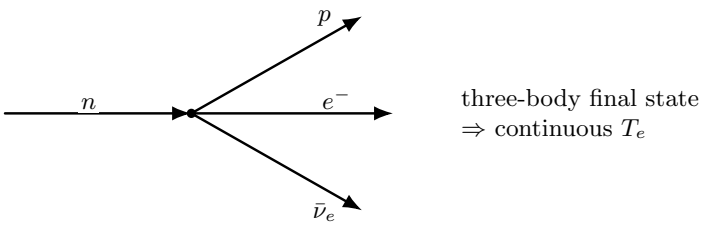


Figure 1.3: Schematic of $\beta^-$ decay including the neutral particle proposed by Pauli. The three-body final state allows the electron to carry a variable kinetic energy $T_e$, producing a continuous spectrum up to the endpoint.

The weakness of neutrino interactions was emphasized soon after; Bethe and Peierls estimated extremely small interaction probabilities, implying that direct detection would be difficult [14]. Experimental confirmation followed in 1956 when Cowan and Reines observed reactor $\bar{\nu}_e$ via inverse beta decay,

$$\bar{\nu}_e + p \;\rightarrow\; e^+ + n, \tag{1.12}$$

using a delayed-coincidence signature to identify events [15].

### 1.2.2 Neutrinos in weak interactions

In the SM, neutrinos appear in three flavor fields, $\nu_e$, $\nu_\mu$, and $\nu_\tau$, grouped as $\nu \equiv (\nu_e, \nu_\mu, \nu_\tau)^T$ and paired with the charged-lepton flavor fields $\ell \equiv (e, \mu, \tau)^T$ in $SU(2)_L$ doublets. At laboratory energies, neutrinos interact via the weak interaction through charged-current (CC) exchange of $W^\pm$ bosons or neutral-current (NC) exchange of the $Z$ boson [1].

The leptonic charged-current interaction is the leptonic part of Eq. (1.8). Experimentally, CC interactions tag flavor because they produce the charged lepton associated with the neutrino flavor. Representative CC processes are

$$\nu_\ell + n \rightarrow \ell^- + p, \qquad \bar{\nu}_\ell + p \rightarrow \ell^+ + n, \tag{1.13}$$

with $\ell \in \{e, \mu, \tau\}$ and $n, p$ denoting nucleons or, more generally, hadronic targets.

Neutral-current interactions leave electric charge unchanged and do not produce a charged lepton. In the SM, neutrinos couple to the $Z$ only through their left-chiral fields, so the neutrino NC interaction can be written as

$$\mathcal{L}_{\mathrm{NC}} \supset -\frac{g}{2\cos\theta_W}\,\overline{\nu}\gamma^\mu P_L \nu\, Z_\mu, \tag{1.14}$$

where $\theta_W$ is the weak mixing angle and $Z_\mu$ is the neutral weak gauge field [1]. Typical NC processes include

$$\nu_\ell + N \;\rightarrow\; \nu_\ell + N, \qquad \nu_\ell + e^- \rightarrow \nu_\ell + e^-, \tag{1.15}$$

where $N$ denotes a nucleon or nucleus. In these reactions, the initial and final particles are of the same type, but the outgoing neutrino and target carry different momenta from the incoming particles, so the interaction is observed through

the recoil of the target rather than through the appearance of a charged lepton. Neutral-current interactions were established experimentally by observing neutrino-induced hadronic events in a neutrino beam with no associated charged-lepton track ("neutral" events) [16].

| Channel | Mediator | What changes | Typical experimental signature |
|---|---|---|---|
| CC | $W^{\pm}$ | charge and flavor | charged lepton $\ell^{\pm}$ in final state |
| NC | $Z$ | neither charge nor flavor | recoil only (no charged lepton) |

Table 1.3: Comparison of charged-current (CC) and neutral-current (NC) neutrino interactions at laboratory energies. CC processes tag flavor through the associated charged lepton, while NC processes are flavor preserving and identified via recoils.

As discussed in Sec. 1.1, weak interactions violate parity. This was established in the Wu experiment, which measured the angular distribution of electrons emitted in the $\beta$ decay of polarized $^{60}$Co nuclei and found a clear asymmetry with respect to the nuclear-spin direction [17]. In the SM, this follows from the left-chiral structure of the charged current, Eq. (1.8). Accordingly, neutrinos produced in charged-current processes are predominantly of negative helicity, and antineutrinos of positive helicity, up to corrections of order $\mathcal{O}(m_\nu/E_\nu)$. This was verified directly by Goldhaber *et al.*, who inferred the neutrino helicity from the circular polarization of the de-excitation photon emitted following electron capture [18].

In the minimal SM, neutrinos are massless. A Dirac mass term would require an additional right-chiral neutrino field $\nu_R$, which is absent, and a Majorana mass term cannot be formed from the SM neutrino fields alone while preserving the electroweak gauge symmetry [19]. The observed nonzero neutrino masses therefore show that the minimal SM is incomplete in the neutrino sector. The resulting phenomenology is introduced in the next subsection through neutrino mixing and oscillations, while the Dirac-versus-Majorana question is discussed later in Sec. 1.2.5.

### 1.2.3 Neutrino mixing oscillations

Neutrino oscillations demonstrate that at least two neutrino mass eigenstates have nonzero masses and that the flavor states produced and detected in weak interactions are coherent superpositions of mass eigenstates. In the three-flavor framework, the relation between flavor states $\nu_\alpha$ ($\alpha = e, \mu, \tau$) and mass eigenstates $\nu_i$ ($i = 1, 2, 3$) is written

$$\begin{pmatrix} \nu_e \\ \nu_\mu \\ \nu_\tau \end{pmatrix} = U_{\mathrm{PMNS}} \begin{pmatrix} \nu_1 \\ \nu_2 \\ \nu_3 \end{pmatrix}, \qquad \nu_\alpha = \sum_{i=1}^{3} U_{\alpha i}\, \nu_i, \tag{1.16}$$

where $U_{\mathrm{PMNS}}$ is the unitary Pontecorvo–Maki–Nakagawa–Sakata (PMNS) lepton mixing matrix [20]. A convenient parameterization uses three mixing angles, one Dirac CP-violating phase, and, if neutrinos are Majorana particles, two additional

phases [21].

$$U_{\mathrm{PMNS}} = R_{23}(\theta_{23})\, R_{13}(\theta_{13}, \delta_{\mathrm{CP}})\, R_{12}(\theta_{12}) \times \mathrm{diag}\left(1, e^{i\alpha_1/2}, e^{i\alpha_2/2}\right), \tag{1.17}$$

These "Majorana phases" cancel in oscillation probabilities, which depend on products of PMNS elements and their complex conjugates, $U_{\beta i}U^*_{\alpha i}$. Oscillations therefore depend on $\theta_{12}$, $\theta_{13}$, $\theta_{23}$, and the Dirac phase $\delta_{\mathrm{CP}}$, but cannot determine whether neutrinos are Dirac or Majorana.

The origin of oscillations is the relative phase accumulated by different mass components during propagation. In the ultrarelativistic limit, $E \gg m_i$, appropriate for neutrino-oscillation experiments, the probability to detect flavor $\beta$ after an initial flavor state $|\nu_\alpha\rangle$ has traveled a distance $L$ in vacuum can be written as [21]

$$P_{\alpha\to\beta}(L, E) = \left|\sum_{i=1}^{3} U_{\beta i}\, U^*_{\alpha i}\, \exp\left(-i\,\frac{m_i^2 L}{2E}\right)\right|^2 . \tag{1.18}$$

This expression makes explicit that oscillations are controlled by mass-squared differences $\Delta m^2_{ij} \equiv m_i^2 - m_j^2$ and depend on the ratio $L/E$. For intuition and for many experimental configurations, the survival probability can be written

$$P_{\alpha\to\alpha} \simeq 1 - \sin^2 2\theta\, \sin^2\left(\frac{\Delta m^2\, L}{4E}\right), \tag{1.19}$$

which is often written in practical units as

$$P_{\alpha\to\alpha} \simeq 1 - \sin^2 2\theta\, \sin^2\left(1.27\,\frac{\Delta m^2(\mathrm{eV}^2)\, L(\mathrm{km})}{E(\mathrm{GeV})}\right). \tag{1.20}$$

Here $\theta$ and $\Delta m^2$ denote the mixing angle and mass-squared splitting for the channel under study [21].

Oscillations have been observed with atmospheric, solar, reactor, and accelerator neutrinos. Atmospheric $\nu_\mu$ disappearance provided an early definitive measurement of oscillations [22], while solar data established flavor transformation and, together with reactor measurements, determined the "solar" splitting $\Delta m^2_{21}$ and mixing angle $\theta_{12}$ [23, 24]. Reactor experiments subsequently measured a nonzero $\theta_{13}$ [25], enabling precision three-flavor tests including sensitivity to $\delta_{\mathrm{CP}}$ in accelerator measurements.

Oscillations constrain the mixing angles and the mass-squared splittings $\Delta m^2_{ij}$, but leave the absolute mass scale undetermined and cannot establish whether neutrinos are Dirac or Majorana [21]. These open questions motivate complementary probes such as kinematic endpoint measurements, cosmological constraints, and neutrinoless double beta decay.

### 1.2.4 Neutrino mass ordering

By convention the solar splitting is defined as $\Delta m^2_{21} \equiv m_2^2 - m_1^2 > 0$. For the larger atmospheric-scale splitting, oscillation data determine its magnitude but not yet unambiguously its sign, because that sign depends on whether $\nu_3$ lies above or

| Scale | Definition | Value |
|---|---|---|
| Solar ($\Delta m^2_{\text{sol}}$) | $\Delta m^2_{21}$ | $(7.49 \pm 0.19) \times 10^{-5}$ eV$^2$ |
| Atmospheric ($\lvert\Delta m^2_{\text{atm}}\rvert$) | $\lvert\Delta m^2_{31}\rvert$ (NO)<br>$\lvert\Delta m^2_{32}\rvert$ (IO) | $(2.513^{+0.021}_{-0.019}) \times 10^{-3}$ eV$^2$<br>$(2.484 \pm 0.020) \times 10^{-3}$ eV$^2$ |

Table 1.4: Solar and atmospheric neutrino mass-squared splittings from a global oscillation fit [26].

below the $(\nu_1, \nu_2)$ pair. The neutrino mass ordering therefore specifies whether $\nu_3$ is the heaviest state (normal ordering, NO) or the lightest state (inverted ordering, IO) [26].

A compact visualization of the two allowed spectra is shown in Fig. 1.4, which summarizes how the solar and atmospheric splittings arrange the three mass eigenstates in the normal- and inverted-ordering hypotheses while leaving the overall mass offset set by $m_{\text{lightest}}$ unconstrained.

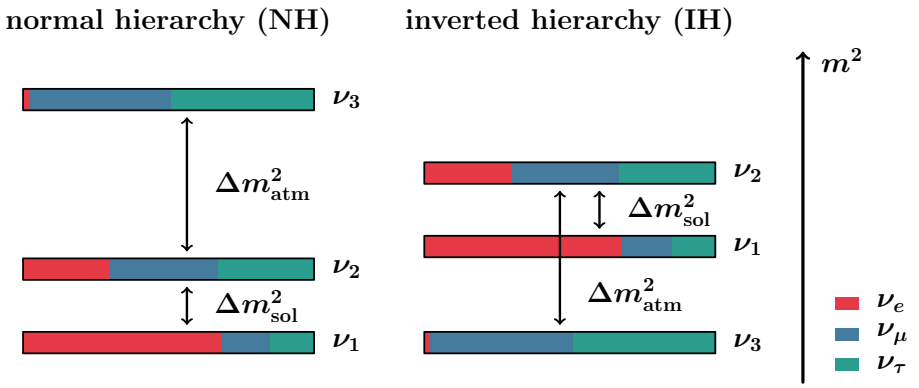


Figure 1.4: Schematic spectra for normal ordering (NO) and inverted ordering (IO). The colored fractions indicate the flavor content of each mass eigenstate [26].

Figure 1.4 also illustrates the flavor composition of each mass eigenstate. The colored fractions of the bars indicate the relative weights $|U_{ei}|^2$, $|U_{\mu i}|^2$, and $|U_{\tau i}|^2$ of the electron-, muon-, and tau-flavor components in the mass state $\nu_i$, as set by the PMNS mixing matrix.

It is often useful to express the three masses in terms of the lightest mass $m_{\text{lightest}}$ and the measured splittings. For normal ordering (NO), $m_{\text{lightest}} = m_1$ and

$$m_2 = \sqrt{m_1^2 + \Delta m^2_{21}}, \qquad m_3 = \sqrt{m_1^2 + |\Delta m^2_{31}|}, \tag{1.21}$$

while for inverted ordering (IO), $m_{\text{lightest}} = m_3$ and

$$m_2 = \sqrt{m_3^2 + |\Delta m^2_{32}|}, \qquad m_1 = \sqrt{m_3^2 + |\Delta m^2_{32}| - \Delta m^2_{21}}. \tag{1.22}$$

In both cases, oscillations fix the splittings that set the relative spacing of the spectrum, and $m_{\text{lightest}}$ sets the overall mass scale [26].

Experimentally, the ordering is probed by comparing oscillation patterns that change depending on whether $m_3$ lies above or below the $(m_1, m_2)$ pair. In long-baseline accelerator experiments and in atmospheric measurements, neutrinos crossing matter experience an additional potential (MSW effect) that modifies the energy dependence of oscillation probabilities in an ordering-dependent way [27]. In medium-baseline reactor experiments such as JUNO, the ordering affects the fine interference pattern between the solar and atmospheric oscillation frequencies in the detected $\bar{\nu}_e$ spectrum [28]. Global fits still provide only limited discrimination between NO and IO; the small difference between the NO and IO best-fit atmospheric-scale splittings in Table 1.4 arises because the global analysis is performed separately under each ordering hypothesis [26].

The ordering is one ingredient in the broader determination of neutrino masses. Complementary probes constrain different combinations of the mass eigenvalues: beta-decay endpoint measurements are sensitive to the kinematic mass $m_\beta$, which controls how a nonzero neutrino mass slightly modifies the electron spectrum within the last few eV below the endpoint,

$$m_\beta^2 \equiv \sum_{i=1}^{3} |U_{ei}|^2 \, m_i^2, \tag{1.23}$$

where $U_{ei}$ is the $(e, i)$ element of the PMNS matrix. Cosmology constrains the neutrino mass sum

$$\sum m_\nu \equiv \sum_{i=1}^{3} m_i. \tag{1.24}$$

This follows because massive neutrinos contribute to the energy density of the Universe and modify the growth of structure. Their large thermal velocities suppress clustering on small scales, leaving measurable imprints in observables such as the cosmic microwave background and the large-scale distribution of matter. Comparing cosmological data with these predictions therefore constrains $\sum m_\nu$ [29].

Neutrinoless double beta decay is sensitive to the effective Majorana mass $m_{\beta\beta}$, which combines the neutrino masses with the electron-flavor mixing factors and their relative phases, so that different contributions can add or partially cancel,

$$m_{\beta\beta} \equiv \left| \sum_{i=1}^{3} U_{ei}^2 \, m_i \right|. \tag{1.25}$$

Together, these observables connect oscillation results to the absolute mass scale through $m_\beta$ and $\sum m_\nu$ [30, 29], and, through $m_{\beta\beta}$, to the Dirac/Majorana question that motivates $0\nu\beta\beta$ searches [21].

### 1.2.5 Dirac versus Majorana neutrinos

Oscillations establish that neutrinos are massive, but they do not determine whether the neutrino mass is of Dirac or Majorana type, that is, whether neutrinos are distinct from antineutrinos or identical to them. Because neutrinos are electrically neutral, both possibilities are consistent with the known gauge interactions. The

physical distinction is tied to whether total lepton number $L$ is an exact symmetry. As introduced in Sec. 1.1.4, $L$ is assigned as $+1$ for leptons and $-1$ for antileptons, so ordinary weak decays conserve $\Delta L = 0$. A Dirac mass term preserves this assignment and keeps neutrinos and antineutrinos as distinct states, whereas a Majorana mass term couples a neutrino field to its charge-conjugate field and therefore changes lepton number by two units ($\Delta L = 2$), enabling lepton-number-violating processes such as $0\nu\beta\beta$ [21].

At the level of mass terms, a Dirac neutrino requires two independent chiral fields, $\nu_L$ (where $\overline{\nu} \equiv \nu^\dagger\gamma^0$ is the Dirac adjoint) and $\nu_R$, and can be written as

$$\mathcal{L}_m^{\mathrm{D}} = -m_D\,\overline{\nu_L}\,\nu_R + \mathrm{h.c.}, \tag{1.26}$$

which conserves lepton number because $\nu_L$ and $\nu_R$ are both neutrino fields with $L = +1$, so the bilinear $\overline{\nu_L}\nu_R$ carries $\Delta L = 0$. In the SM, only $\nu_L$ participates in the weak interaction. A Dirac mass term therefore requires introducing an additional right-chiral neutrino field $\nu_R$ to pair with $\nu_L$. Because $\nu_R$ carries no SM weak charge, it does not couple to the $W$ or $Z$ bosons and is often referred to as a sterile neutrino.

A Majorana neutrino instead satisfies $\nu = \nu^c$, so the neutrino and antineutrino are not independent states; this is possible only for a neutral fermion [31]. A Majorana mass can then be written using a single chirality, for example

$$\mathcal{L}_m^{\mathrm{M}} = -\frac{1}{2}\,m_M\,\overline{\nu_L^c}\,\nu_L + \mathrm{h.c.}, \tag{1.27}$$

violating total lepton number by two units ($\Delta L = 2$). Unlike the Dirac case, no additional right-chiral neutrino field is required.

| Property | Dirac neutrino | Majorana neutrino |
|---|---|---|
| Particle vs antiparticle | distinct | identical ($\nu = \nu^c$) |
| Lepton number $L$ | conserved | violated ($\Delta L = 2$ possible) |
| Mass term | $\overline{\nu_L}\nu_R$ | $\overline{\nu_L^c}\nu_L$ |

Table 1.5: Key distinctions between Dirac and Majorana neutrinos and their experimental implications.

In Eqs. (1.26) and (1.27), $m_D$ and $m_M$ denote single mass parameters for one neutrino field. With three flavors, the Dirac mass term is written in matrix form as

$$\mathcal{L}_m^{\mathrm{D}} = -\,\overline{\nu_L}\,M_D\,\nu_R + \mathrm{h.c.}, \tag{1.28}$$

where $\nu_{L,R} \equiv (\nu_e, \nu_\mu, \nu_\tau)^T_{L,R}$. In general, $M_D$ is not diagonal, so the flavor fields produced in weak interactions are not mass eigenfields. The physical masses $m_i$ are obtained by rotating to a basis in which the mass matrix is diagonal, i.e.

$$U_L^\dagger M_D U_R = \mathrm{diag}(m_1, m_2, m_3) \equiv D_m, \tag{1.29}$$

with unitary matrices $U_L$ and $U_R$. The corresponding mass-eigenstate fields are then defined by

$$\nu_L^{\mathrm{mass}} = U_L^\dagger \nu_L, \qquad \nu_R^{\mathrm{mass}} = U_R^\dagger \nu_R, \tag{1.30}$$

so that the mass term becomes

$$\mathcal{L}_m^{\mathrm{D}} = -\overline{\nu_L^{\mathrm{mass}}}\, D_m\, \nu_R^{\mathrm{mass}} + \mathrm{h.c.}, \tag{1.31}$$

i.e. a sum of independent masses $m_i$ for the propagating neutrino states [21]. Because the SM weak interaction couples only to left-chiral neutrino fields, only the rotation of $\nu_L$ is visible experimentally; this left-handed rotation is what appears in the PMNS mixing matrix $U_{\mathrm{PMNS}}$.

Extending Eq. (1.27) to three flavors, the Majorana mass term can be written in matrix form as

$$\mathcal{L}_m^{\mathrm{M}} = -\frac{1}{2}\, \nu_L^T C^{-1} M_L \nu_L + \mathrm{h.c.}, \tag{1.32}$$

where $M_L$ is a complex symmetric matrix ($M_L^T = M_L$) and $C$ is the charge-conjugation matrix. The physical masses are obtained by rotating to a basis in which the mass matrix is diagonal,

$$U^T M_L U = \mathrm{diag}(m_1, m_2, m_3) \equiv D_m, \tag{1.33}$$

so that the propagating neutrino states have definite masses $m_i$ [21].

In this case the mixing matrix in the charged current is $U_{\mathrm{PMNS}} = U_\ell^\dagger U$ and contains two additional phases beyond the Dirac CP phase. These phases do not affect oscillation probabilities, but they appear in $\Delta L = 2$ observables, in particular in the coherent sum defining $m_{\beta\beta}$ in Eq. (1.25), where different mass-eigenstate contributions can add or partially cancel [21].

A widely studied explanation for the smallness of neutrino masses is the type-I see-saw mechanism. One extends the field content by adding heavy right-chiral neutrino fields $N_R$, allowing both a Dirac coupling to the SM left-chiral neutrinos and a Majorana mass term for $N_R$,

$$\mathcal{L}_m \supset -\overline{\nu_L}\, m_D\, N_R - \frac{1}{2}\, N_R^T C^{-1} M_R N_R + \mathrm{h.c.}, \tag{1.34}$$

where $m_D$ and $M_R$ are mass matrices in flavor space. In block form,

$$\mathcal{L}_m = -\frac{1}{2} \begin{pmatrix} \nu_L \\ N_R^c \end{pmatrix}^T C^{-1} \begin{pmatrix} 0 & m_D \\ m_D^T & M_R \end{pmatrix} \begin{pmatrix} \nu_L \\ N_R^c \end{pmatrix} + \mathrm{h.c.}, \tag{1.35}$$

which makes explicit the mixing between the light SM neutrinos and heavy states. In the limit $M_R \gg m_D$, the light-neutrino mass matrix is approximately

$$m_\nu \simeq -\, m_D\, M_R^{-1}\, m_D^T, \tag{1.36}$$

while the heavy states have masses of order $M_R$. The minus sign is conventional and has no physical consequence for the mass eigenvalues. For electroweak-scale Dirac masses and sub-eV light neutrino masses, Eq. (1.36) suggests a characteristic heavy scale near $10^{14}\,\mathrm{GeV}$, which is why the mechanism is often discussed in a GUT-motivated context [32].

## 1.3 Double beta decay

Double beta decay is a weak process involving two charged-current weak transitions, in which an even–even nucleus changes its charge by two units, $(A, Z) \to (A, Z+2)$, with the emission of two electrons. It becomes relevant for nuclei where ordinary single $\beta$ decay is energetically forbidden, or strongly suppressed, while the double-charge-change transition is allowed. The basic energetic situation is illustrated by the isobaric mass parabola in Fig. 1.5.

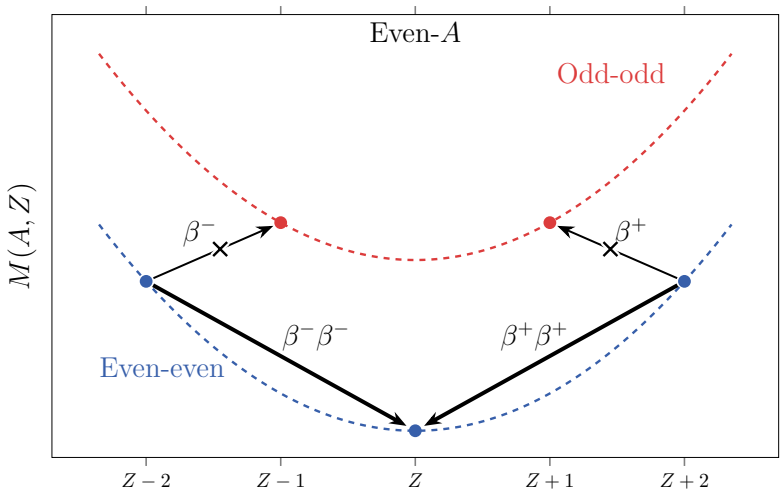


Figure 1.5: Schematic mass parabolas for an even-$A$ isobaric chain, where $M$ denotes the atomic mass, showing how an odd–odd nucleus can be heavier than both neighboring even–even nuclei. Crossed arrows indicate energetically forbidden single-$\beta$ transitions.

For a fixed even mass number $A$, the odd–odd nucleus at $Z \pm 1$ can lie above both neighboring even–even nuclei, blocking single-$\beta$ decay of the parent while permitting a net $|\Delta Z| = 2$ transition to a lighter even–even daughter [33].

In the SM, the allowed mode is two-neutrino double beta decay ($2\nu\beta\beta$), in which two antineutrinos accompany the electrons and total lepton number is conserved. A neutrinoless mode ($0\nu\beta\beta$) would instead require physics beyond the SM. In the standard light-neutrino-exchange picture, the neutrino is exchanged internally between the two weak vertices and a neutrino mass term is required to connect the left-chiral weak interactions [34]. Figure 1.6 summarizes the two processes at the quark level.

Experimentally, the two modes are distinguished primarily by the summed electron energy. In $2\nu\beta\beta$, the neutrinos carry away a variable fraction of the decay energy, producing a continuous spectrum up to $Q_{\beta\beta}$. In $0\nu\beta\beta$, no neutrinos are emitted and, neglecting nuclear recoil, the two electrons carry essentially the full transition energy, giving a monoenergetic line broadened only by detector resolution.

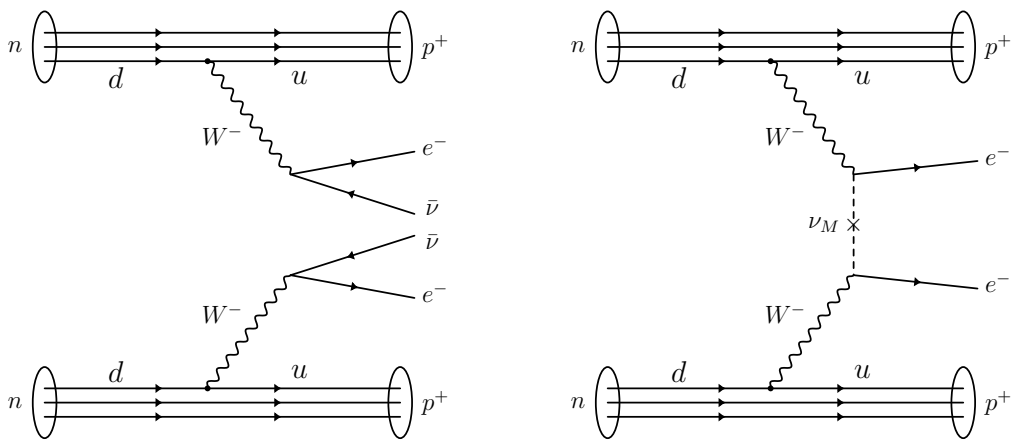


Figure 1.6: Schematic quark-level diagrams for double beta decay. Left: $2\nu\beta\beta$, allowed in the SM. Right: $0\nu\beta\beta$ via light-neutrino exchange, enabling $\Delta L = 2$.

### 1.3.1 Double beta decay two neutrino mode

In the dominant case relevant for $0\nu\beta\beta$ searches, $2\nu\beta\beta$ connects $0^+ \to 0^+$ ground states,

$$ {}^{A}_{Z}X \;\to\; {}^{A}_{Z+2}Y \;+\; 2e^- \;+\; 2\bar{\nu}_e, \tag{1.37}$$

and conserves total lepton number. As in regular $\beta$ decay discussed in Sec. 1.2.1, the emitted antineutrinos carry away variable energy and momentum, so the summed electron energy forms a continuous spectrum extending up to $Q_{\beta\beta}$.

Figure 1.7 summarizes the $\beta\beta$ decay scheme of $^{136}$Xe to $^{136}$Ba, including the branch to the first excited $0^+_1$ state. That excited-state transition is followed by a prompt two-$\gamma$ cascade and therefore has a distinct experimental signature [35].

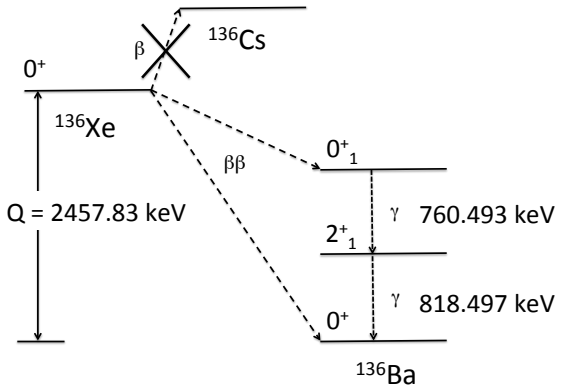


Figure 1.7: Level scheme for $\beta\beta$ decay of $^{136}$Xe. Decay to the first excited $0^+_1$ state of $^{136}$Ba is followed by a two-$\gamma$ cascade. From J. B. Albert et al. [35].

For $0^+ \to 0^+$ transitions, the $2\nu\beta\beta$ decay rate is commonly written as a phase-space factor times nuclear matrix elements,

$$ \left(T^{2\nu}_{1/2}\right)^{-1} = G^{2\nu}(Q_{\beta\beta}, Z) \left| M^{2\nu}_{GT} - \frac{g_V^2}{g_A^2} M^{2\nu}_{F} \right|^2 , \tag{1.38}$$

where $G^{2\nu}$ is the phase-space factor, $M^{2\nu}_{GT}$ and $M^{2\nu}_{F}$ are the Gamow–Teller and Fermi matrix elements, and $g_A$ and $g_V$ are the axial-vector and vector weak couplings [35]. Equation (1.38) mainly serves to identify the nuclear matrix elements that enter the decay rate and to motivate the use of measured $T^{2\nu}_{1/2}$ values as benchmarks for nuclear-structure calculations.

For reference, Table 1.6 lists evaluated $2\nu\beta\beta$ half-lives for several isotopes widely used in current and next-generation searches.

| Isotope | $T^{2\nu}_{1/2}$ (yr) |
|---|---|
| $^{76}$Ge | $(1.745 \pm 0.089) \times 10^{21}$ |
| $^{82}$Se | $(9.16 \pm 0.45) \times 10^{19}$ |
| $^{100}$Mo | $(7.08 \pm 0.14) \times 10^{18}$ |
| $^{130}$Te | $(8.69 \pm 0.18) \times 10^{20}$ |
| $^{136}$Xe | $(2.240 \pm 0.061) \times 10^{21}$ |

Table 1.6: $2\nu\beta\beta$ half-lives (evaluated values) for selected isotopes used in $0\nu\beta\beta$ searches [36].

$2\nu\beta\beta$ half-lives span more than two orders of magnitude among common candidate isotopes, reflecting both phase-space and nuclear-structure effects. For the $^{136}$Xe isotope, the half-life is of order $10^{21}$ yr, similar to $^{76}$Ge and longer than $^{130}$Te, while $^{100}$Mo is much faster at the $10^{18}$ yr scale. In $0\nu\beta\beta$ searches, a shorter $T^{2\nu}_{1/2}$ implies a higher intrinsic $2\nu\beta\beta$ rate and therefore stricter requirements on energy resolution to suppress leakage into the region of interest around $Q_{\beta\beta}$.

### 1.3.2 Neutrinoless double beta decay signature

As discussed above, neutrinoless double beta decay corresponds to the mode

$$ {}^{A}_{Z}X \;\rightarrow\; {}^{A}_{Z+2}Y \;+\; 2e^{-}. \tag{1.39} $$

Its defining experimental signature follows from energy conservation. In $0\nu\beta\beta$, no neutrinos carry away energy, so the summed electron energy is fixed by $Q_{\beta\beta}$ up to a negligible nuclear recoil. In contrast, in $2\nu\beta\beta$ the antineutrinos carry away a variable energy, producing a continuous summed-energy spectrum up to the same endpoint. Figure 1.8 illustrates this idealized distinction at the level of true kinematics.

In a real detector, finite energy resolution broadens the $0\nu\beta\beta$ line into a peak and allows events from the high-energy tail of continuous spectra to leak into a region of interest around $Q_{\beta\beta}$. Experiments therefore combine energy reconstruction with additional information, such as event topology and position, to suppress backgrounds near $Q_{\beta\beta}$. This is described for nEXO in Sec. 2.5.1.

An observed excess or a null result near $Q_{\beta\beta}$ can then be translated into a corresponding $0\nu\beta\beta$ half-life and, under a chosen mechanism, into neutrino-physics parameters.

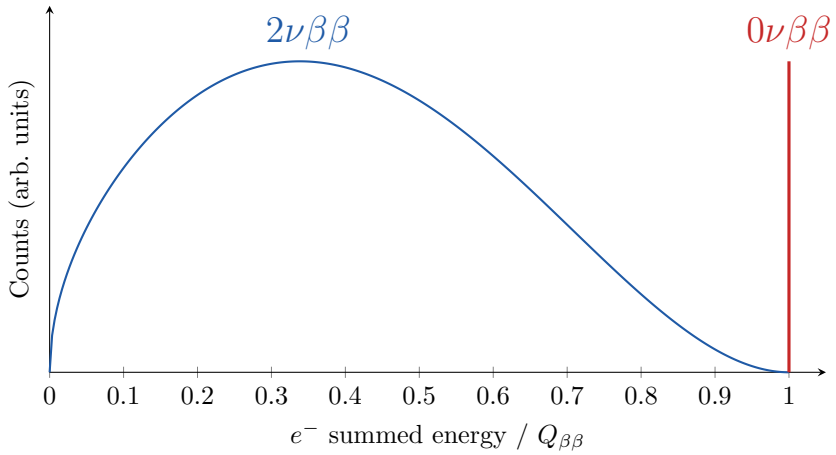


Figure 1.8: Ideal (true-kinematics) summed electron energy distributions for $2\nu\beta\beta$ and $0\nu\beta\beta$. The $2\nu\beta\beta$ mode produces a broad continuum, while $0\nu\beta\beta$ would appear as a line at $Q_{\beta\beta}$.

### 1.3.3 Half-life decomposition

The decay rate of a rare nuclear transition is commonly expressed in terms of its half-life $T_{1/2}$ via the decay constant $\lambda$,

$$\lambda \equiv \frac{\ln 2}{T_{1/2}}, \tag{1.40}$$

so that the expected number of decays scales linearly with exposure and inversely with $T_{1/2}$. For $0\nu\beta\beta$, the experimentally accessible quantity is therefore a limit or measurement of $T^{0\nu}_{1/2}$.

A standard baseline interpretation takes light-neutrino exchange to be the dominant mechanism. In this scenario, the $0\nu\beta\beta$ half-life factorizes as [37]

$$\left(T^{0\nu}_{1/2}\right)^{-1} = G^{0\nu}(Q_{\beta\beta}, Z)\, g_A^4 \left|M^{0\nu}\right|^2 \left|\frac{m_{\beta\beta}}{m_e}\right|^2, \tag{1.41}$$

where each factor is defined in Table 1.7.

The phase-space factor $G^{0\nu}$ is fixed by kinematics and electron wavefunctions in the nuclear Coulomb field, with a strong dependence on $Q_{\beta\beta}$ and a $Z$ dependence from Coulomb distortion [38]. The nuclear matrix element $M^{0\nu}$ encodes the nuclear-structure dependence of the transition; differences between many-body methods produce a spread in $M^{0\nu}$ for a given isotope, which dominates the theory uncertainty when converting between a half-life and $m_{\beta\beta}$ [39].

Equation (1.41) can be inverted to express a half-life limit as a constraint on $m_{\beta\beta}$,

$$m_{\beta\beta} \leq m_e \left[G^{0\nu}\, g_A^4\, |M^{0\nu}|^2\, T^{0\nu}_{1/2}\right]^{-1/2}. \tag{1.42}$$

In practice, the spread in $M^{0\nu}$ translates directly into a corresponding band in the inferred $m_{\beta\beta}$ reach.

| Factor | Meaning | Main dependencies & source |
|---|---|---|
| $G^{0\nu}(Q_{\beta\beta}, Z)$ | phase-space factor | kinematics and Coulomb effects; tabulated by isotope [38] |
| $M^{0\nu}$ | nuclear matrix element | nuclear-structure model; method-dependent spread [39] |
| $g_A$ | axial-vector weak coupling | free-nucleon value $g_A \simeq 1.27$; model-dependent value [1, 39] |
| $m_{\beta\beta}$ | effective Majorana mass | $\nu$ masses, mixing, phases (Eq. (1.25)) |

Table 1.7: Ingredients entering the standard $0\nu\beta\beta$ half-life factorization for light-neutrino exchange.

### 1.3.4 Implications of neutrinoless double beta decay

A $0\nu\beta\beta$ signal would establish a $\Delta L = 2$ process and therefore physics beyond the minimal SM. In the baseline interpretation, the decay is mediated by light-neutrino exchange and the rate depends on the effective Majorana mass $m_{\beta\beta}$ through Eq. (1.41). More generally, the Schechter–Valle argument shows that any mechanism capable of generating $0\nu\beta\beta$ induces a Majorana mass component for neutrinos, even if the dominant dynamics is not light-neutrino exchange [10]. Figure 1.9 illustrates this logic schematically.

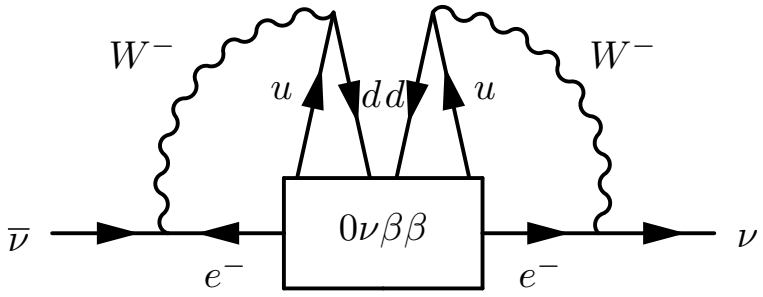


Figure 1.9: Feynman-diagram illustration of the Schechter–Valle black-box theorem, showing that any $\Delta L = 2$ mechanism generating $0\nu\beta\beta$ induces a Majorana mass term for neutrinos [10]. Figure from [40].

Light-neutrino exchange is used as the reference mechanism for interpreting experimental sensitivities, but $0\nu\beta\beta$ could in principle be mediated by other $\Delta L = 2$ interactions, such as heavy-particle exchange or right-handed weak currents [10]. At the nuclear scale, alternative mechanisms correspond to different effective interactions, so a given half-life would translate to different underlying parameters. Throughout this dissertation, sensitivities are expressed in terms of $m_{\beta\beta}$ assuming light-neutrino exchange.

A null result is commonly reported as a lower limit on $T^{0\nu}_{1/2}$ and, using Eq. (1.41), as a corresponding range in $m_{\beta\beta}$, since the spread in available $M^{0\nu}$ calculations maps directly into the $T^{0\nu}_{1/2} \to m_{\beta\beta}$ conversion. The neutrino-sector interpretation also

depends on the absolute mass scale, the mass ordering, and the unknown phases entering Eq. (1.25). Figure 1.10 summarizes the allowed ranges of $m_{\beta\beta}$ as a function of either the lightest neutrino mass $m_{\mathrm{min}}$ or the neutrino mass sum $\sum m_\nu$.

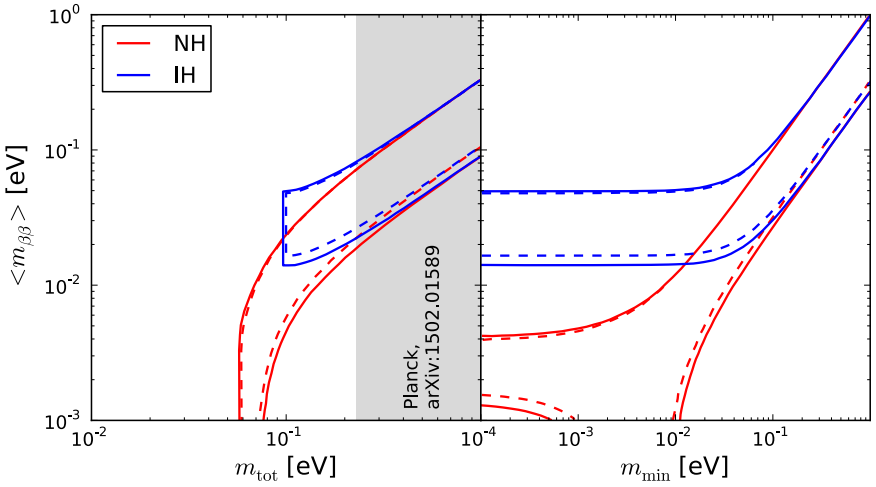


Figure 1.10: Allowed ranges of the effective Majorana mass $m_{\beta\beta}$ as a function of (left) the neutrino mass sum $\sum m_\nu$ and (right) the lightest neutrino mass $m_{\mathrm{min}}$. Normal ordering (red) and inverted ordering (blue) are shown. Dashed curves vary only the unknown Majorana phases, while solid curves also include uncertainties on oscillation parameters. Figure from [40].

The large spread in $m_{\beta\beta}$ at fixed mass scale is dominated by the unknown Majorana phases in Eq. (1.25), with a smaller contribution from uncertainties on the measured oscillation parameters [21]. For very small $m_{\mathrm{min}}$, the inverted-ordering band lies at higher $m_{\beta\beta}$ than the normal-ordering band, while at larger $m_{\mathrm{min}}$ the bands overlap. The vertical shaded exclusion corresponds to current cosmological limits on large neutrino mass sums [29].

Neutrinoless double beta decay is complementary to kinematic and cosmological probes: endpoint measurements constrain the kinematic mass $m_\beta$, cosmology constrains the mass sum $\sum m_\nu$ through observables set by the evolution of the early Universe and the growth of structure at late times, and $0\nu\beta\beta$ probes $m_{\beta\beta}$ and therefore $\Delta L = 2$ lepton-number violation.

### 1.3.5 Current limits and experimental landscape

Current $0\nu\beta\beta$ searches report lower limits on the half-life $T^{0\nu}_{1/2}$ at 90% confidence level. Table 1.8 summarizes selected published limits by isotope, indicating the experiments and detector media that set them.

The most stringent published constraints have reached the few-$10^{26}$ yr scale in both $^{76}$Ge and $^{136}$Xe (Table 1.8). In $^{136}$Xe, the strongest published limit is currently obtained by KamLAND-Zen using xenon-loaded liquid scintillator [42], while liquid-xenon TPCs provide a complementary approach with event reconstruction and topology information [44]. In $^{76}$Ge, the latest published result comes from

| Isotope | $T^{0\nu}_{1/2}$ limit (90% C.L.) | Experiment | Medium |
|---|---|---|---|
| $^{76}$Ge | $> 1.9 \times 10^{26}$ yr | LEGEND-200 [41] | HPGe+LAr |
| $^{136}$Xe | $> 3.8 \times 10^{26}$ yr | KamLAND-Zen [42] | Xe-LS |
| $^{130}$Te | $> 3.5 \times 10^{25}$ yr | CUORE [43] | $TeO_2$ bolometers |
| $^{136}$Xe | $> 3.5 \times 10^{25}$ yr | EXO-200 [44] | LXe TPC |
| $^{100}$Mo | $> 3.0 \times 10^{24}$ yr | AMoRE-I [45] | scint. bolometers |

Table 1.8: Representative best published $0\nu\beta\beta$ half-life limits by isotope (90% confidence level).

LEGEND-200 [41]. Bolometric searches in $^{130}$Te continue to provide competitive sensitivity at large exposure [43], and molybdate-based scintillating bolometers have recently improved the published $^{100}$Mo limit [45].

Next-generation ton-scale experiments aim to extend present sensitivities by one to two orders of magnitude, into the $\mathcal{O}(10^{28}\,\text{yr})$ regime. A compact comparison of running upgrades and planned experiments is given in Sec. 2.5.6, while Chapter 2 discusses how energy reconstruction, topology, and background control determine practical sensitivity.

# Chapter 2

# Dedicated Liquid Xenon Detector for $0\nu\beta\beta$ Searches

## Contents


**2.1 $^{136}$Xe as a Detection Medium . . . . . 25**

**2.2 Liquid Xenon TPC Working Principle . . . . . 27**

**2.3 EXO-200 as a technology pathfinder . . . . . 28**

**2.4 Detector Design Overview . . . . . 29**

2.4.1 Light and charge collection . . . . . 30

2.4.2 Cryostat . . . . . 35

2.4.3 External shielding . . . . . 36

**2.5 Signal & Background Model . . . . . 36**

2.5.1 Signal definition . . . . . 36

2.5.2 Background sources . . . . . 37

2.5.3 Selection criteria . . . . . 39

2.5.4 Sensitivity metrics . . . . . 41

2.5.5 Projected reach in $T^{0\nu}_{1/2}$ and $m_{\beta\beta}$ . . . . . 42

2.5.6 Running and next-generation $0\nu\beta\beta$ programs . . . . . 44

This chapter describes the proposed detector design of the neutrinoless double beta decay search in the nEXO project, a large single-phase liquid xenon time projection chamber in which $^{136}$Xe is both the source and the detection medium. nEXO is a proposed experiment and has not yet been built; the detector descriptions below refer to its baseline design.

## 2.1 $^{136}$Xe as a Detection Medium

Only a limited set of even–even nuclei are energetically allowed to undergo double beta decay and are therefore suitable for a $0\nu\beta\beta$ search. Among the commonly considered isotopes ($^{76}$Ge, $^{82}$Se, $^{100}$Mo, $^{130}$Te, $^{136}$Xe, ...), $^{136}$Xe offers a good combination of physics reach and experimental scalability. Next-generation sensitivity requires deploying several tonnes of candidate isotope while maintaining ultra-low backgrounds. Xenon is one of the few candidates for which enrichment to the multi-ton scale is realistic with established centrifugation methods. As a noble element, xenon can be enriched, transported, stored, and purified without the chemical constraints associated with solid or molecular source materials, and the purification methods developed for large noble-liquid detectors can be applied directly to achieve the required purity [46].

The $Q$–value of $^{136}$Xe, $Q_{\beta\beta} = (2458.10 \pm 0.31)\,\mathrm{keV}$ [47], lies above many of the strongest natural $\gamma$ lines from environmental radioactivity, reducing the density of intense photopeaks near the region of interest (ROI). Although $Q_{\beta\beta}$ is below the 2615 keV $^{208}$Tl line, the latter contributes to the ROI primarily through Compton scattering and spatially extended interactions, which can be mitigated by event-topology reconstruction and fiducialization in a large active volume. Xenon also has no long-lived radioactive isotopes relevant near $Q_{\beta\beta}$ other than $^{136}$Xe itself, allowing the source to be deployed directly in an active medium free of additional long-lived intrinsic radioactivity in this energy region [46].

Figure 2.1 illustrates how $^{136}$Xe compares to other commonly used $0\nu\beta\beta$ isotopes. Isotopes such as $^{82}$Se and $^{100}$Mo benefit from slightly higher $Q_{\beta\beta}$ values, and $^{130}$Te has a particularly large natural abundance, but these candidates are generally implemented in solid-state or crystalline detectors. In contrast, $^{136}$Xe combines a competitive $Q_{\beta\beta}$ and reasonable natural abundance with the possibility of deployment in large liquid-xenon detectors.

Operating xenon in the liquid phase provides a dense, homogeneous target in which the $0\nu\beta\beta$ source and active detector volume coincide. At typical operating conditions of about 165 K and 1 bar, liquid xenon has a density of $\sim 3\,\mathrm{g/cm^3}$, providing substantial self-shielding against external $\gamma$ rays. Meter-scale monolithic volumes are therefore feasible, with the outer tens of centimeters acting as an internal shield and the analysis restricted to an inner fiducial volume. In addition, liquid xenon can be continuously recirculated and purified during operation, allowing detector-scale control of electronegative and radioactive impurities in a way that is generally not available in solid source media.

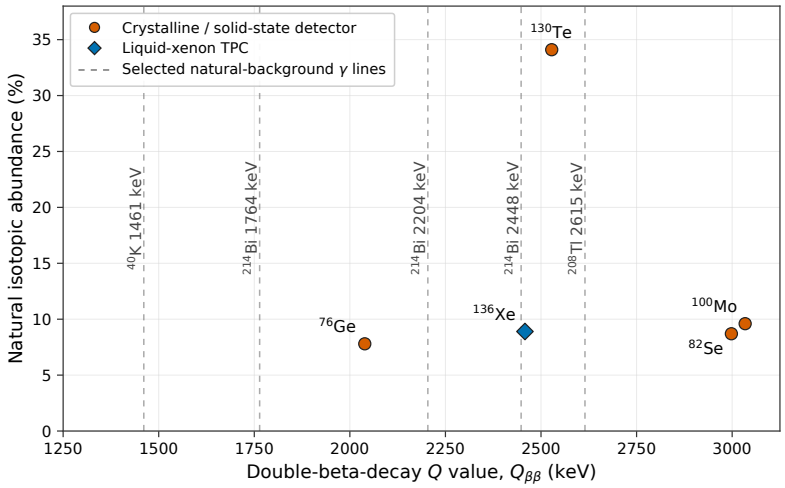


Figure 2.1: Comparison of the $Q_{\beta\beta}$ values and natural abundances of several commonly used $0\nu\beta\beta$ isotopes. Vertical dashed lines mark the energies of strong natural $\gamma$ lines from the $^{238}$U and $^{232}$Th decay chains and from $^{40}$K, including the 2615 keV $^{208}$Tl line.

Liquid xenon is also an excellent detection medium. As shown schematically in Fig. 2.2, energy depositions produce both prompt scintillation light and ionization charge. Excitation leads to the formation of $Xe_2^*$ states that de-excite and emit VUV photons at $\lambda \simeq 175$ nm, while ionization produces electron–ion pairs; in the presence of an electric field, some electrons escape recombination and drift to a segmented anode, while the remainder recombine and contribute additional scintillation light.

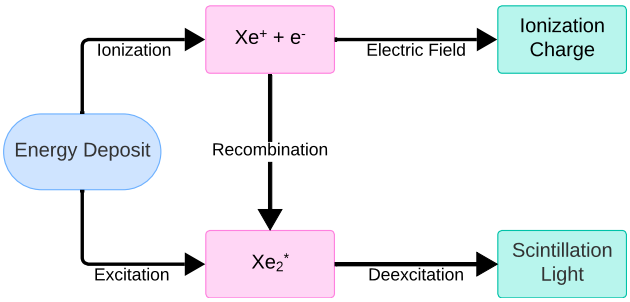


Figure 2.2: Schematic illustration of signal production in liquid xenon: an energy deposition creates excitations and ionization; excitations and recombination populate the $Xe_2^*$ state that de-excites emitting VUV scintillation light, while electrons that escape recombination are drifted by the electric field and collected as ionization charge.

Microscopically, a deposited energy $E$ first partitions into excitations and ion pairs,

$$n = N_{\mathrm{ex}} + N_{\mathrm{i}}, \tag{2.1}$$

where $N_{\mathrm{ex}}$ and $N_{\mathrm{i}}$ are the numbers of excitations and ion pairs, respectively. Recombination then redistributes the ion pairs between the two observable channels,

the scintillation-photon yield $n_p$ and the ionization-electron yield $n_q$,

$$n_p = N_{\mathrm{ex}} + r\, N_{\mathrm{i}}, \tag{2.2}$$

$$n_q = (1 - r)\, N_{\mathrm{i}}, \tag{2.3}$$

with $r$ the recombination fraction. The total number of quanta is approximately fixed by the work function $W$,

$$n \simeq \frac{E}{W}, \tag{2.4}$$

while the partition between scintillation and ionization depends on the local energy loss per unit length, $dE/dx$, and on the electric field. Recombination fluctuations redistribute quanta between light and charge, making the two signals anti-correlated while their sum remains nearly constant [48]. Combining them therefore improves the energy resolution, it forms the energy estimator defined in Eq. (2.7).

## 2.2 Liquid Xenon TPC Working Principle

A liquid xenon time projection chamber (LXe TPC) combines calorimetry and tracking in a single volume of LXe. A uniform electric field causes the ionization electrons produced in an interaction to drift toward the anode, while the prompt scintillation signal defines the event time. The delayed arrival of the charge then determines the coordinate along the drift direction, and segmentation of the anode provides the two transverse coordinates [48].

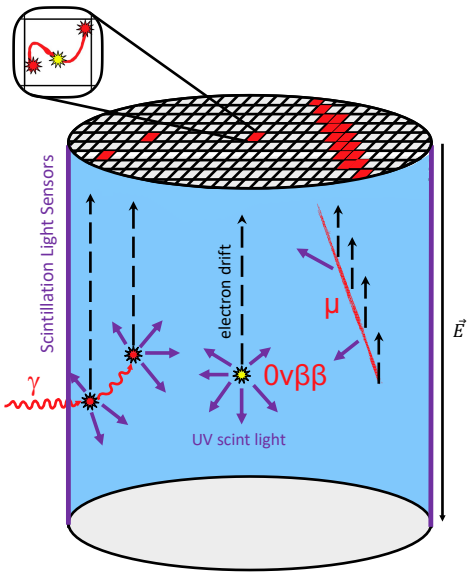


Figure 2.3: Schematic view of a single-phase LXe TPC. An energy deposition in the liquid produces prompt scintillation light detected by photosensors surrounding the active volume and ionization electrons that drift under the influence of a uniform electric field from the cathode to the segmented anode.

For a given drift field, the electron drift velocity $v_{\mathrm{d}}$ is approximately constant, so the drift coordinate can be written as

$$z \simeq v_{\mathrm{d}}\, t_{\mathrm{drift}}. \tag{2.5}$$

For typical drift fields of a few hundred V/cm in LXe, $v_{\mathrm{d}}$ is of order mm/µs, so drift times are of order 100 µs for decimeter-scale drift distances and extend to the sub-millisecond range for meter-scale TPCs. Attachment of drifting electrons to residual impurities attenuates the collected charge and imposes a requirement that the electron lifetime be significantly longer than the maximum drift time. The control and monitoring of these impurities are discussed in detail in Chapter 3.

**Single vs dual-phase TPC** Liquid xenon TPCs can also be operated in a dual-phase configuration, where the LXe volume is topped by a thin gas layer. Ionization electrons are drifted through the liquid and extracted across the liquid–gas interface into the gas, where a stronger electric field induces proportional scintillation. The primary scintillation in the liquid (S1) and the secondary signal in the gas (S2) are detected optically, providing amplification of the charge signal and excellent position resolution, particularly in the transverse plane. This approach is widely used in dark-matter detectors, where keV-scale recoils require a low detection threshold. Electrons extracted into the gas produce an amplified light signal, allowing very small ionization signals to be detected [49]. For the MeV-scale signals from neutrinoless double beta decay, this amplification is not required, and a single-phase LXe TPC avoids the need to control a stable liquid–gas interface, electron-extraction fields, and high-voltage structures in the gas phase.

## 2.3 EXO-200 as a technology pathfinder

The EXO-200 experiment served as a full-scale demonstration that a liquid-xenon TPC can simultaneously provide MeV calorimetry, 3D position reconstruction, and topology-based background rejection for a $^{136}$Xe $0\nu\beta\beta$ search. EXO-200 operated underground at the Waste Isolation Pilot Plant (WIPP) and demonstrated the main experimental handles used in xenon TPC searches for $0\nu\beta\beta$, including a combined light–and–charge energy estimator, as well as discrimination between single-site (SS) and multi-site $\gamma$ backgrounds using reconstructed charge topology [44].

Key detector-scale parameters that are most relevant for a next-generation $0\nu\beta\beta$ detector include the use of enriched LXe (80.6% $^{136}$Xe, compared with approximately 8.9% in natural xenon), a central cathode defining two symmetric drift regions, and an active drift region of radius 18.3 cm and length 38.4 cm, corresponding to an active xenon mass of about 110 kg in the TPC field cage [50].

In addition to validating the concept, EXO-200 delivered important physics results. It measured the $^{136}$Xe $2\nu\beta\beta$ half-life, $T^{2\nu}_{1/2} = (2.165 \pm 0.016_{\mathrm{stat}} \pm 0.059_{\mathrm{syst}}) \times 10^{21}$ yr [51], and performed progressively more sensitive searches for $0\nu\beta\beta$. Using the full dataset, EXO-200 set a lower limit of $T^{0\nu}_{1/2} > 3.5 \times 10^{25}$ yr at 90% C.L. [44].

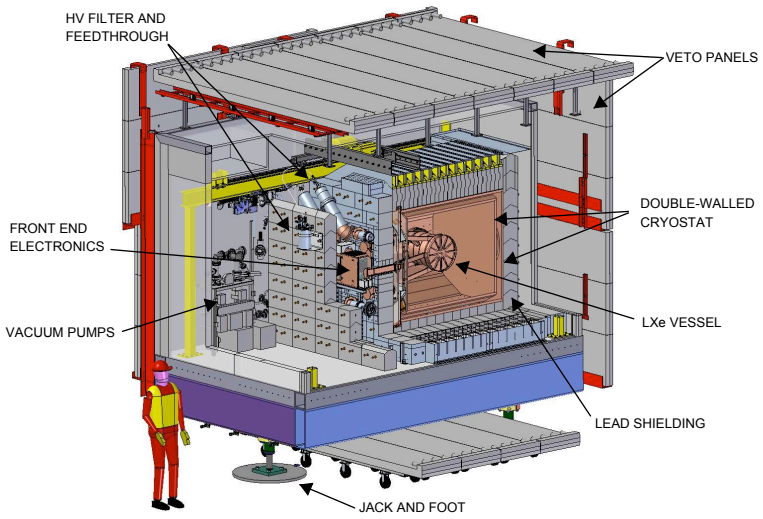


Figure 2.4: Schematic view of the EXO-200 detector © IOP Publishing all rights reserved, reproduced with permission [50].

## 2.4 Detector Design Overview

The detector is proposed for installation in the SNOLAB Cryopit within a nested shielding configuration comprising the xenon-filled TPC vessel, a cryostat with an intermediate liquid shield, and a surrounding water tank instrumented as an active outer detector. This geometry combines local self-shielding with the 6000 m w e overburden at SNOLAB, strongly reducing cosmogenic backgrounds [52].

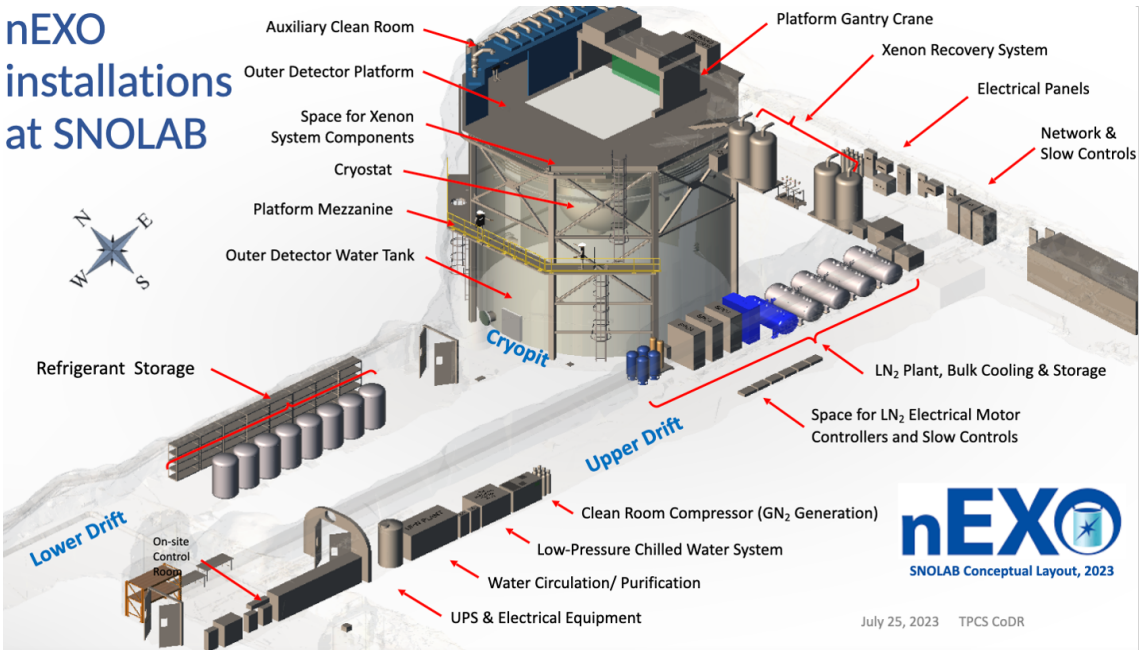


Figure 2.5: Conceptual layout of the detector in the SNOLAB Cryopit [46].

As shown in Fig. 2.5, the water tank and Cryopit define the outermost shielding and constrain the allowed cryostat dimensions, while service platforms and equip-

ment galleries provide access for installation, maintenance, and cryogenic and xenon systems.

Table 2.1 summarizes the main geometric parameters of the baseline nEXO configuration used throughout this dissertation [46, 47].

| Parameter | Symbol | Baseline value |
|---|---|---|
| **Site and outer detector** | | |
| Underground overburden | | $\sim 6000\,\mathrm{m\,w\,e}$ [52] |
| Water tank mass | $m_{\mathrm{H_2O}}$ | $\approx 1.75\,\mathrm{kt}$ |
| Water tank (height, diameter) | $(h, \varnothing)$ | $(\sim 13\,\mathrm{m}, \sim 13\,\mathrm{m})$ |
| **TPC active LXe volume** | | |
| Enriched xenon mass | $m_{\mathrm{Xe}}$ | $\approx 5\,\mathrm{t}$ |
| Enrichment in $^{136}$Xe | $f_{136}$ | 90% |
| Active drift height | $H$ | $118.3\,\mathrm{cm}$ |
| Active drift diameter | $d$ | $113.3\,\mathrm{cm}$ |
| Nominal drift field | $E_{\mathrm{drift}}$ | $400\,\mathrm{V/cm}$ |
| **TPC vessel and readout layout** | | |
| TPC vessel height and diameter | $(h_{\mathrm{TPC}}, \varnothing_{\mathrm{TPC}})$ | $(127.7\,\mathrm{cm}, 127.7\,\mathrm{cm})$ |
| Field-shaping ring pitch | | $1\,\mathrm{cm}$ |
| Charge tile footprint (one module) | | $10\,\mathrm{cm}\times 10\,\mathrm{cm}$ [53, 54] |
| Strips per tile | | 30 X strips + 30 Y strips |
| Number of SiPM staves | | 24 |
| Total SiPM area (barrel) | $A_{\mathrm{SiPM}}$ | $\approx 4.5\,\mathrm{m^2}$ |
| **Cryostat and inner shielding** | | |
| Inner vessel radius (IV) | $R_{\mathrm{IV}}$ | $\sim 1.7\,\mathrm{m}$ |
| Outer vessel radius (OV) | $R_{\mathrm{OV}}$ | $\sim 2.2\,\mathrm{m}$ |
| HFE mass | $m_{\mathrm{HFE}}$ | $\approx 32\,\mathrm{t}$ |
| HFE volume | $V_{\mathrm{HFE}}$ | $\approx 18.5\,\mathrm{m^3}$ |
| Minimum TPC to HFE thickness | $d_{\mathrm{min}}$ | $\approx 76\,\mathrm{cm}$ |

Table 2.1: Summary of key geometric parameters for the baseline nEXO detector configuration [46, 47].

The following subsections summarize the internal detector design, focusing on the light and charge collection system, the cryostat, and the shielding strategy.

### 2.4.1 Light and charge collection

The baseline design features a cylindrical LXe TPC with drift height $H = 118.3\,\mathrm{cm}$ and drift diameter $d = 113.3\,\mathrm{cm}$, enclosed in a TPC vessel of height and diameter 127.7 cm. A thin copper cathode at the bottom of the active volume establishes a drift field of about $400\,\mathrm{V/cm}$, causing electrons to drift toward the anode. Copper

field-shaping rings with 1 cm pitch define the inner TPC boundary and maintain field uniformity. The anode hosts the charge-readout tiles, while VUV-sensitive SiPM staves mounted around the barrel detect scintillation light [46].

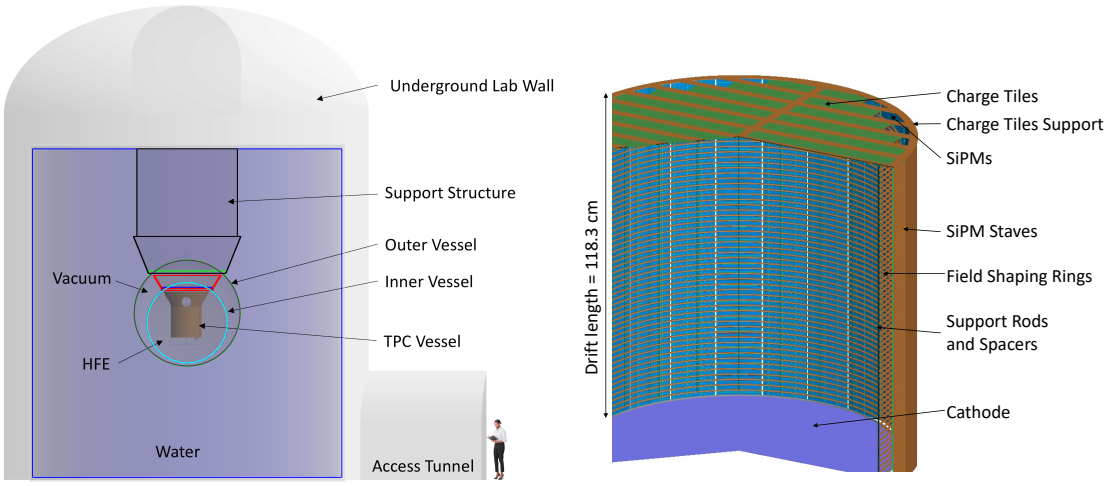


(a) Full detector cross-section

(b) Zoom on TPC internals

Figure 2.6: Cross-section views of the detector geometry used in Monte Carlo simulations © IOP Publishing all rights reserved, reproduced with permission [47]. Panel (a) shows the full detector. Panel (b) shows the TPC internals.

Figure 2.6 shows how the light and charge collection system is integrated into the nested detector geometry. The zoomed view in Fig. 2.6b highlights the components that define the detector response: the modular charge tiles forming the anode, the cylindrical array of SiPM staves, and the cathode and field-shaping rings that define the drift field. Prototype hardware for these subsystems is shown in Fig. 2.7.

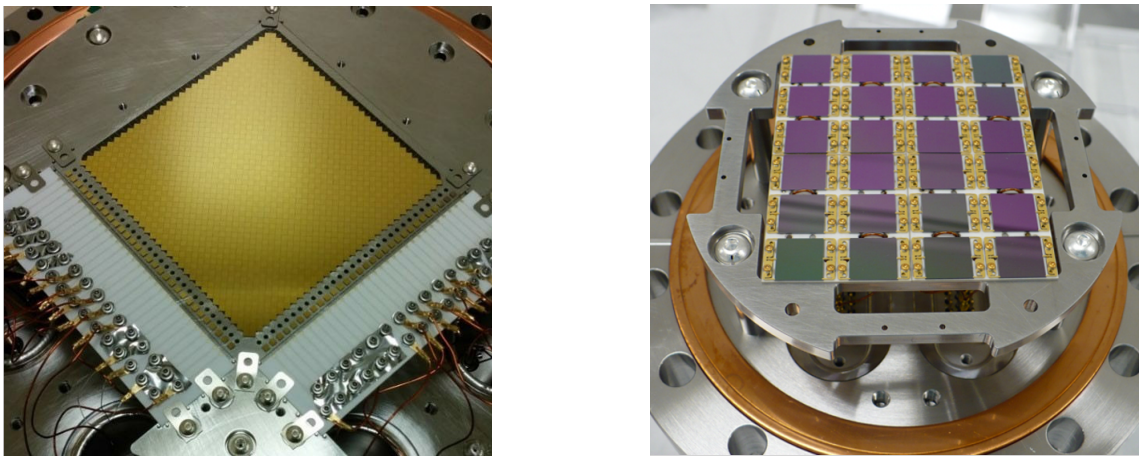

(a) Charge-collection tile prototype

(b) SiPM light-collection module

Figure 2.7: Prototype charge and light readout modules [46]. Panel (a) shows a crossed-strip charge tile. Panel (b) shows a VUV-sensitive SiPM module representative of the barrel staves.

### Charge collection with tiles

**Geometry** Charge is collected on modular fused-silica tiles that form the anode plane. Each tile consists of a thin fused-silica substrate of 10 cm×10 cm area, with metallic charge-collecting X and Y strips patterned on the same collecting face [53, 54]. Thirty X strips run parallel to one edge, while thirty orthogonal Y strips run parallel to the other edge. Each strip is implemented as a chain of square pads connected at their corners, with a pitch of a few millimeters. At each X–Y crossing, the traces are separated by a thin $SiO_2$ dielectric layer, so the two strip layers are capacitively coupled but electrically isolated. This crossed-strip geometry provides two-dimensional segmentation in the anode plane with only $N_x + N_y$ electronic channels for $N_x \times N_y$ effective pixels. For a $30 \times 30$ pattern, 60 channels replace the 900 channels of a fully pixelated anode. This geometry is illustrated schematically in Fig. 2.8.

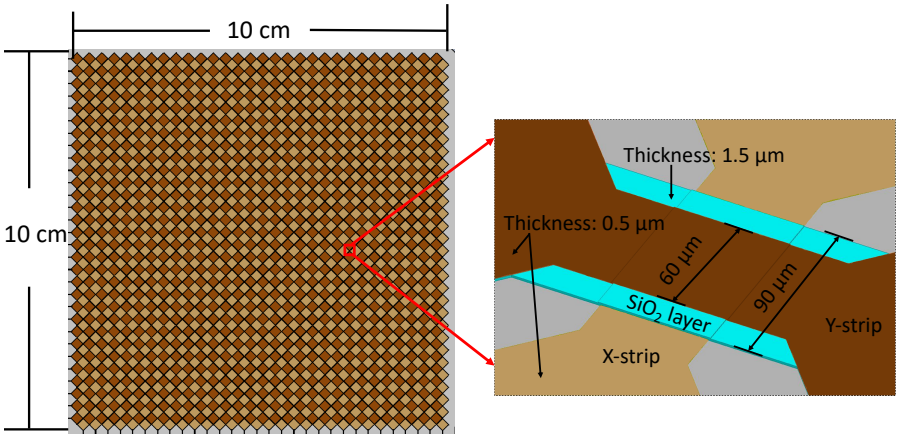


Figure 2.8: Schematic of a 10 cm×10 cm charge-collection tile with interleaved X and Y strips, each implemented as a chain of square pads on the same collecting face of a fused-silica substrate. The X/Y traces cross at narrow bridges separated by a thin dielectric layer, providing orthogonal readout with minimal inactive area. From Ref. [54].

**Working principle** When an ionizing event occurs in the LXe, the liberated electrons drift toward the anode under the influence of the uniform electric field. As the electron cloud approaches the tile, it induces charge on several neighboring pads and strips. The induced current on each strip is integrated by a charge-sensitive front-end amplifier, and the final pulse height is proportional to the fraction of electrons collected on its pads. Because the pads are small compared with the cloud size, a typical MeV-scale cluster shares charge among a handful of adjacent channels. The resulting signal pattern is then used to reconstruct the interaction position in the anode plane and to define the associated charge cluster.

**Performance** Earlier single-phase LXe TPCs such as EXO-200 used crossed wire planes to obtain two-dimensional charge information. In that approach, each readout element spans the detector width, which limits transverse granularity and imposes tight mechanical tolerances on long tensioned wires [50, 44]. The tiled crossed-strip anode replaces long wires with short traces on rigid fused-silica substrates, achieving fine segmentation with far fewer channels than a fully pixelated anode while reducing passive material near the active volume [53, 54]. A prototype tile operated in LXe has demonstrated an ionization-only energy resolution of $\sigma/E \simeq 5.5\%$ at 570 keV for a drift field of 936 V/cm [53]. This performance, together with cold-electronics equivalent noise charge (ENC) below the design requirement of ENC $\lesssim 200\,e^-$ per strip, is consistent with the baseline assumption that the tiled anode does not limit the combined light–and–charge energy resolution [46, 47, 54].

### Light collection with SiPM staves

**Geometry** Scintillation light is detected by VUV-sensitive silicon photomultipliers (SiPMs) covering the barrel of the TPC vessel. Approximately 4.5 $m^2$ of SiPMs would be mounted behind the field-shaping rings on staves that form a 24-sided polygon around the drift volume, providing nearly uniform coverage along the drift direction [46]. Each stave is built from photon-detection modules; a module groups several 1 $cm^2$ SiPM dies into a small number of readout channels to balance radiopurity, electronic noise, and cable count while keeping the inactive area small. The overall arrangement of tiles, staves, and TPC dimensions is illustrated in Fig. 2.9.

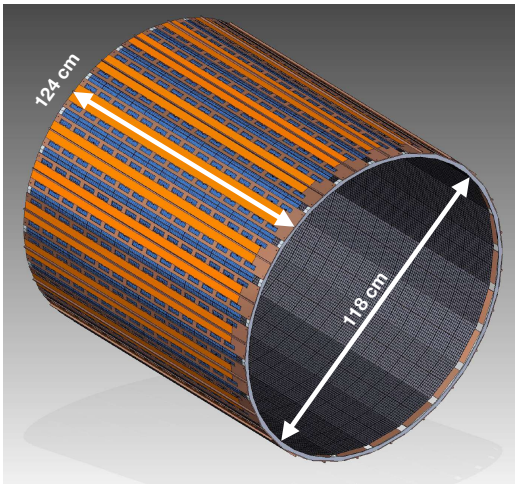


Figure 2.9: Arrangement of SiPM tiles and staves instrumenting the TPC barrel. The SiPMs are grouped into tiles mounted on staves that line the full lateral surface of the drift volume. From Ref. [55] © 2018 IEEE.

**Working principle** A SiPM is a matrix of microscopic photodetector cells, called single-photon avalanche diodes (SPADs), operated above breakdown so that each cell acts as an independent single-photon sensor. As sketched in Fig. 2.10, each microcell contains a small reverse-biased $p$–$n$ junction with a high-electric-field region located

a few micrometers below the surface. VUV photons at 175 nm enter through the top surface and are absorbed in this shallow active region, where they create an electron–hole pair. If this occurs in the high-field region, it can trigger a charge avalanche, producing a standard electrical pulse from that microcell. The avalanche is then quenched by an integrated resistor, after which the cell recharges and becomes sensitive again.

Many such microcells, typically with lateral dimensions of 10 µm to 100 µm, are connected in parallel on a common output. The total signal is therefore proportional to the number of cells that fire and thus to the number of detected photons, provided saturation remains limited. In the detector, the analog SiPM signals are first amplified by cryogenic application-specific integrated circuits (ASICs) mounted on each stave and are then digitized by analog-to-digital converter (ADC) ASICs located at the top of the stave. Design studies assume an integration window of order 1 µs for the light channel in the combined light–and–charge energy estimator [56, 47].

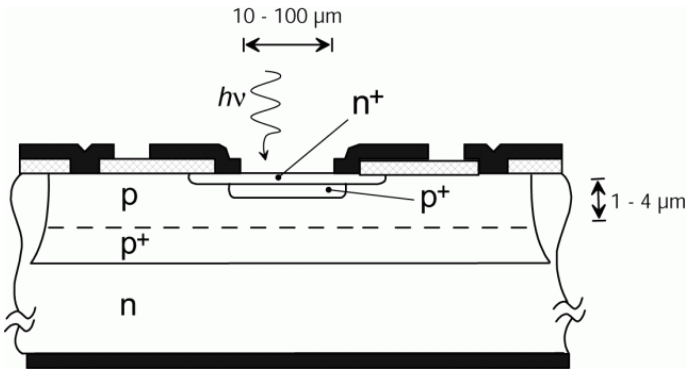


Figure 2.10: Cross-section of a single-photon avalanche diode (SPAD) microcell, showing the shallow high-field $p$–$n$ junction in which an absorbed photon ($h\nu$) can trigger a Geiger-mode avalanche. Typical microcell lateral dimensions are 10 µm to 100 µm, with a depletion depth of 1 µm to 4 µm.

**Performance and advantages** Compared with the large-area avalanche photodiodes (LAAPDs) used in EXO-200, SiPMs offer several advantages for a low-background LXe TPC. Their high gain, at the level of $\mathcal{O}(10^6)$, and single-photon sensitivity improve the scintillation-channel contribution to the energy resolution, while the required bias voltages are modest compared with those of LAAPDs. Their solid-state construction also allows compact tiling of the TPC barrel with a small amount of passive material per device. Radiopurity assays of candidate devices show U/Th/K activities consistent with the photon-system background budget [57]. Dedicated R&D with VUV-optimized devices from FBK and Hamamatsu has demonstrated that both vendors can deliver SiPMs meeting or exceeding the nEXO requirements on photon detection efficiency, dark count rate, and correlated avalanche probability at LXe temperature [55, 56]. These performances are consistent with the light-collection assumptions used to achieve a projected combined energy resolution of $\sigma/E \simeq 0.8\%$ at $Q_{\beta\beta}$ [47].

### 2.4.2 Cryostat

The LXe TPC would be housed in a cryostat that provides thermal control and additional passive shielding. Because the cryostat vessels are among the most massive structures close to the active xenon, any residual radioactivity in these materials can emit $\gamma$ rays that penetrate into the detection volume and generate unwanted energy depositions. The baseline design therefore uses two nested, vacuum-insulated spherical vessels: an inner vessel (IV) with radius $\sim 1.7\,\mathrm{m}$ and an outer vessel (OV) with radius $\sim 2.2\,\mathrm{m}$. The copper TPC vessel would be suspended inside the IV, while the annulus between IV and OV provides thermal insulation and routing for services and structural supports [47].

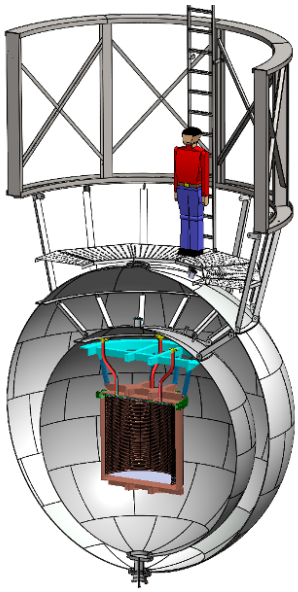

Figure 2.11: Three-dimensional rendering of the cryostat and support structure. The nested nickel inner and outer vessels surround the copper TPC vessel and are suspended from a top support frame that interfaces to the surrounding platforms.

Early designs considered carbon-fiber composite (CFC) shells, but sensitivity studies showed that residual U/Th contamination in these large structures could produce non-negligible backgrounds in the active xenon. This motivated a search for alternative ultra-radiopure structural materials, and the current conceptual design therefore uses welded low-activity nickel shells for both the IV and OV [47]. The implications of this material choice, and the associated optimization of the cryogenic shield, are discussed in Chapter 4.

The volume between the copper TPC vessel and the IV would be filled with a dense, radiopure organic heat-transfer fluid (HFE), which remains liquid from room temperature down to the operating temperature of about 165 K. It provides a large thermal bath around the TPC, provides $\gamma$-ray shielding, and helps maintain pressure balance across the thin copper vessel. In the baseline geometry, the HFE bath has a volume of about $18.5\,\mathrm{m}^3$, a mass of 32 t, and a minimum thickness of 76 cm [47]. Its large thermal inertia slows temperature drifts and provides additional time to

respond to interruptions of active cooling. During cooldown, the HFE would be recirculated through an external liquid-nitrogen-cooled heat exchanger; the same loop can also host purification or radon-mitigation stages. A cryogenic magnetically coupled gear pump would drive the flow through insulated piping between the cryostat and the heat exchanger [46]. A room-temperature and cryogenic HFE recirculation setup is presented in detail in Chapter 5.

### 2.4.3 External shielding

**Underground laboratory** The outermost shield is the underground location itself. The detector is proposed for installation at SNOLAB, beneath an overburden of about 6000 m w e , which suppresses the cosmic-muon flux by several orders of magnitude relative to surface operation [52]. At the SNOLAB Cryopit, the residual muon flux is about 0.3 $\mu\,\mathrm{m}^{-2}\,\mathrm{day}^{-1}$, strongly limiting cosmogenic backgrounds [46].

**Water tank and muon veto** Inside the underground laboratory, the detector would be surrounded by a large water tank that provides both passive shielding and an active outer detector. The water moderates neutrons and attenuates external $\gamma$ rays from the cavern rock and concrete, while photomultipliers instrumenting the tank detect Cherenkov light from through-going muons. The water tank is approximately 13 m in diameter and height. The water-Cherenkov veto is expected to tag more than 95% of relevant muons using 125 8-inch PMTs [46].

**Local self-shielding** Inside these external shields, the HFE bath and the xenon itself provide additional attenuation of nearby radiogenic backgrounds. The outer LXe absorbs a substantial fraction of the remaining incoming radiation, and the analysis is restricted to an inner fiducial volume where these backgrounds are minimized. The detailed impact of nearby materials and shielding geometry on the background model is discussed in Chapter 4.

## 2.5 Signal & Background Model

The $0\nu\beta\beta$ signal in LXe is defined by a set of reconstructed observables that distinguish it from background events depositing energy in the active volume. For the sensitivity analysis, backgrounds are grouped by source and quantified within a common detector model. The resulting physics reach depends on both the expected background level and the reconstruction of the scintillation and ionization signals.

### 2.5.1 Signal definition

A $0\nu\beta\beta$ decay in LXe is a monoenergetic two-electron event at the $^{136}$Xe $Q$-value, $Q_{\beta\beta} = (2458.10 \pm 0.31)\,\mathrm{keV}$. For the ground-state transition relevant here, no de-excitation $\gamma$ rays accompany the decay. With an average work function $W \simeq 11.5\,\mathrm{eV}$

in LXe [58], an event at $Q_{\beta\beta}$ produces

$$n(Q_{\beta\beta}) \simeq \frac{Q_{\beta\beta}}{W} \sim 2 \times 10^5 \text{ quanta.} \tag{2.6}$$

At the nominal drift field, the measured work function and scintillation yield imply approximately $9.1 \times 10^4$ scintillation photons and $1.23 \times 10^5$ ionization electrons [58]. The overall light collection efficiency of about 6% corresponds to approximately $5.5 \times 10^3$ detected photons. A full simulation of the light and charge response, including photon-counting fluctuations and charge-readout noise, gives a projected energy resolution of $\sigma/E \simeq 0.8\%$ [47].

The deposited energy is reconstructed from the corrected estimates of the numbers of scintillation photons and ionization electrons, $\widetilde{N}_P$ and $\widetilde{N}_Q$, using the combined observable

$$E = \left(\widetilde{N}_P + \widetilde{N}_Q\right) W_q, \tag{2.7}$$

where $W_q$ is the mean energy required to produce one quantum in LXe. The quantities $\widetilde{N}_P$ and $\widetilde{N}_Q$ are inferred from the measured light and charge signals after applying the corresponding detector-response corrections [47].

Table 2.2 lists representative baseline quantities evaluated at $Q_{\beta\beta}$ and at the nominal drift field.

This table also summarizes representative light and charge response parameters. The photon transport efficiency (PTE) is the probability that a 175 nm scintillation photon reaches the photosensors after transport through the detector geometry, while the photon detection efficiency (PDE) is the probability that an incident photon on the SiPM active area produces a registered photoelectron. Their product, $\epsilon_o = \text{PTE} \cdot \text{PDE}$, is the mean fraction of produced photons recorded.

For the ionization channel, the main physical loss comes from attachment of drifting electrons to residual impurities. The collected charge is therefore attenuated approximately as $\exp(-t_{\text{drift}}/\tau_e)$, so stable energy reconstruction over meter-scale drifts requires an electron lifetime much longer than the characteristic drift time. In the baseline model, $\tau_e = 10$ ms satisfies this condition. The corresponding purity requirements and charge corrections are discussed in Chapter 3.

The left panel of Fig. 2.12 shows how the anti-correlated light and charge responses are combined into a single energy observable. The narrow spread of monoenergetic events along the rotated axis reflects the improved energy resolution obtained when the two channels are combined, while the dashed diagonal boundaries indicate an auxiliary rejection of events with anomalous light-to-charge response. The resulting signal and background energy spectra are shown in the right panel.

### 2.5.2 Background sources

A $0\nu\beta\beta$ search in a tonne-scale LXe TPC is limited by backgrounds that can produce SS-like energy depositions near $Q_{\beta\beta}$. In the current background model, the main contributions are grouped into four broad categories:

| Parameter (at $Q_{\beta\beta}$ & $E_{\text{drift}}$) | Symbol | Value / relation |
|---|---|---|
| **General / signal & clustering** | | |
| Double-beta $Q$-value | $Q_{\beta\beta}$ | $2458.10 \pm 0.31$ keV [47] |
| Mean work function | $W$ | 11.5 eV [58] |
| Total quanta | $n$ | $2.137 \times 10^5$ $(= Q_{\beta\beta}/W)$ |
| Light yield | $\gamma_p$ | 0.037 ph/eV [58] |
| Produced photons | $n_p$ | $9.095 \times 10^4$ $(= \gamma_p\, Q_{\beta\beta})$ |
| Produced electrons | $n_q$ | $1.228 \times 10^5$ $(= n - n_p)$ |
| Charge/light ratio | $n_q/n_p$ | 1.35 |
| Clustering radius | $r_{\text{cl}}$ | 3 mm [46] |
| Cluster energy threshold | $E_{\text{cl}}$ | 75 keV [46] |
| **Charge signal** | | |
| Drift electric field | $E_{\text{drift}}$ | 400 V/cm [46] |
| Average drift length | $d_{\text{drift}}$ | 59.2 cm $(= H/2)$ |
| Drift velocity | $v_d$ | 1.71 mm µs$^{-1}$ [47] |
| Electron lifetime | $\tau_e$ | 10 ms [46] |
| **Light signal** | | |
| Photon transport efficiency | PTE | 33.3% [46] |
| Photon detection efficiency | PDE | 18.4% [59] |
| Light collection efficiency | $\epsilon_o$ | 6.1% $(= \text{PTE} \cdot \text{PDE})$ |

Table 2.2: Parameters used to define the $0\nu\beta\beta$ signal.

- $^{214}$Bi **from** $^{222}$Rn**:** radon emanation, transport, and plate-out produce distributed $^{214}$Bi activity in the detector, with important contributions from the cathode, field rings, heat-transfer fluid, and xenon volumes.
- **Intrinsic radioactivity of detector materials:** residual contamination from the $^{238}$U and $^{232}$Th chains, together with other long-lived isotopes where relevant, generates $\gamma$-ray backgrounds from detector components close to the active xenon.
- **Invariant backgrounds:** irreducible contributions such as solar-neutrino scatters and $^{137}$Xe are retained as a distinct category.
- **Exposure-based backgrounds:** activation and dust-related contributions accumulated through detector fabrication, handling, and operation are treated separately from intrinsic material radioactivity.

Figure 2.13 summarizes the corresponding SS-like total background budget as estimated from the Monte Carlo simulations used in the nEXO sensitivity study [47].

The largest share comes from $^{214}$Bi associated with $^{222}$Rn, followed by intrinsic radioactivity, while invariant and exposure-based backgrounds remain smaller.

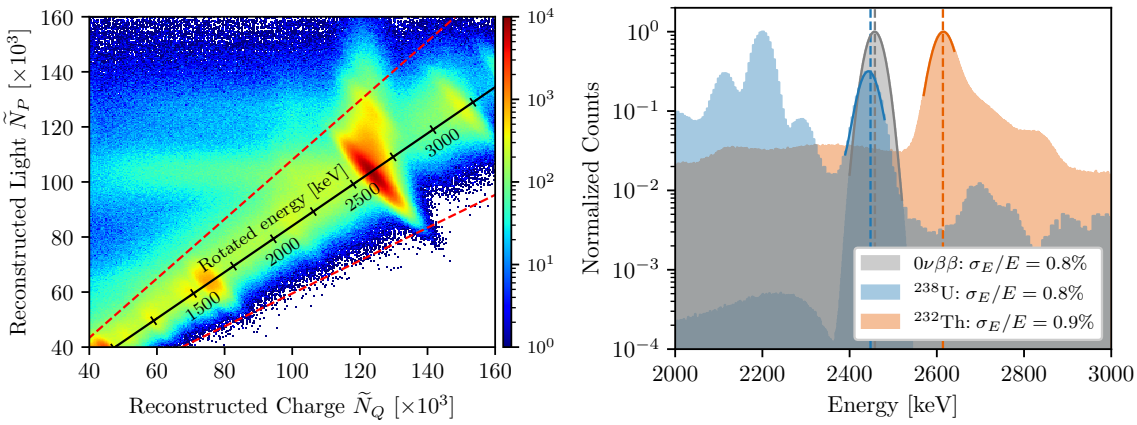


Figure 2.12: Left: light–charge plane and rotated axis used to construct the combined energy estimator. The dashed diagonal boundaries illustrate a selection against events with anomalous light-to-charge response. Right: reconstructed-energy spectra for $0\nu\beta\beta$ signal and $^{232}$Th- and $^{238}$U-chain backgrounds, normalized to the same maximum value [47].

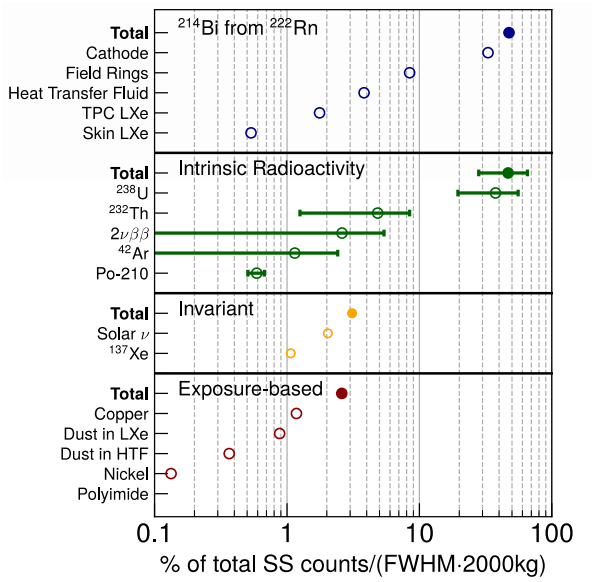


Figure 2.13: Total background budget, shown as fractional SS-like counts in the inner 2000 kg and within one FWHM around $Q_{\beta\beta}$. Updated from [47].

Intrinsic radioactivity is the category most directly tied to material choice, local geometry, and shielding configuration.

### 2.5.3 Selection criteria

The sensitivity of a $0\nu\beta\beta$ search is driven by how efficiently the analysis retains compact two-electron signal candidates while suppressing backgrounds that fall outside the ROI, exhibit spatially extended charge topologies, or cluster near detector boundaries. The baseline selection strategy is built around three reconstructed han-

dles: energy, topology, and standoff distance [46].

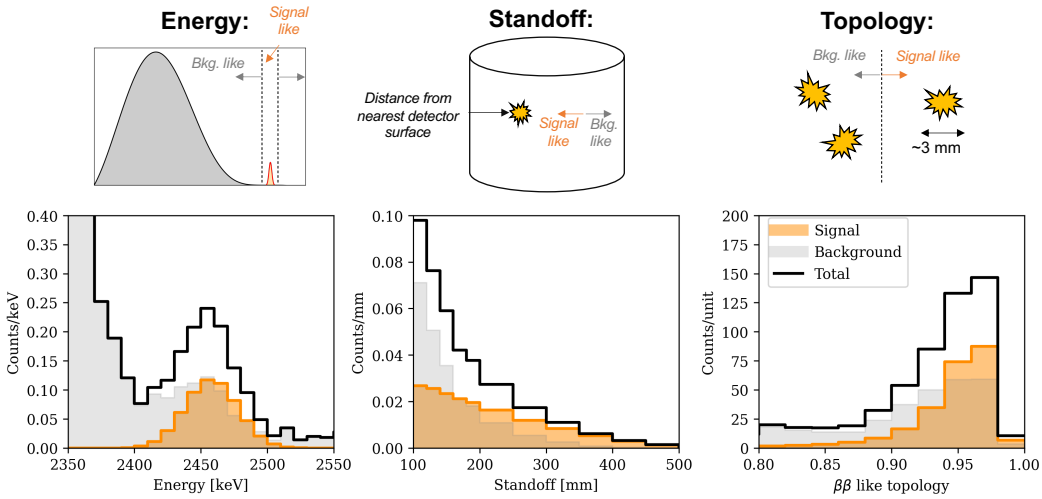


Figure 2.14: Illustration of the three primary analysis handles used to discriminate $0\nu\beta\beta$-like events from backgrounds: energy, topology, and standoff distance.

**Energy requirement (around $Q_{\beta\beta}$).** The analysis targets candidate events reconstructed in the vicinity of $Q_{\beta\beta}$, where a $0\nu\beta\beta$ decay would appear as a narrow spectral feature on top of a smoothly varying background.

**Topology discriminator (DNN score).** Beyond providing event localization, the reconstructed charge pattern carries information on the spatial distribution of the deposited energy. In the nEXO sensitivity framework, this information is encoded in a continuous deep-neural-network (DNN) discriminator trained to separate $0\nu\beta\beta$-like two-electron events from $\gamma$-induced backgrounds. Its output score is defined on $[0, 1]$, where values closer to 1 indicate a more $0\nu\beta\beta$-like topology. Near $Q_{\beta\beta}$, approximately 80% signal efficiency is achievable with 5% acceptance of TPC-vessel $^{238}$U-chain $\gamma$ backgrounds. For visualization, and for defining an SS-like working sample in some projections, a representative threshold of DNN $> 0.88$ is used, while the sensitivity calculation retains the full discriminator distribution in the likelihood [47].

**Standoff distance (SD) and fiducial definition.** A complementary position observable is the standoff distance (SD), defined as the minimum distance between the reconstructed energy-deposit location and the nearest detector surface. Events are required to lie in a bulk fiducial region, for example with SD $> 2\,$cm, and the SD distribution is then used together with energy and topology to separate bulk-like signal candidates from backgrounds originating near detector boundaries [47].

In addition, standard data-quality criteria would be applied to ensure that the reconstructed observables entering the fit are reliable, including a well-reconstructed scintillation $t_0$, stable operating conditions, and acceptable charge- and light-channel

response. Cosmogenic activity would be further suppressed using the external veto and timing-based rejection of events correlated with through-going muons.

### 2.5.4 Sensitivity metrics

The sensitivity of a $0\nu\beta\beta$ search is determined by the available $^{136}$Xe exposure and by how small a $0\nu\beta\beta$ signal can still be distinguished from the expected background by the analysis. In schematic form,

$$T_{1/2}^{0\nu} = \frac{\ln 2\, N_{136}\, \varepsilon\, t}{S_{90}(B)}, \tag{2.8}$$

where $N_{136}$ is the number of $^{136}$Xe nuclei in the fiducial volume, $\varepsilon$ is the total signal efficiency, and $S_{90}(B)$ is the median 90% C.L. upper limit on the number of $0\nu\beta\beta$ signal events for a background level $B$. In a simple counting experiment, $S_{90}$ can be written directly as a function of the expected background. In nEXO, however, the quoted sensitivity is obtained from a multi-parameter likelihood analysis, so this dependence should be understood as schematic rather than as a unique function of the total background rate alone [47].

For the baseline detector model, the projected 10-year median sensitivity is

$$T_{1/2}^{0\nu} \simeq 1.35 \times 10^{28}\ \text{yr} \tag{2.9}$$

at 90% C.L. [47]. The same study also defines an effective counting-experiment background index,

$$b = 7 \times 10^{-5}\ \text{cts}/(\text{FWHM} \cdot \text{kg} \cdot \text{yr}), \tag{2.10}$$

chosen such that a one-bin counting analysis reproduces the same half-life sensitivity as the full likelihood fit [47]. For comparison with the component-by-component background budgets used in this dissertation (like Fig. 2.13), it is more convenient to express the background scale in the inner 2000 kg xenon mass and within one FWHM around $Q_{\beta\beta}$. The baseline $1.35 \times 10^{28}$ yr sensitivity corresponds to an inner-2-ton ROI background of about

$$B \simeq 0.55\ \text{SS cts}/(\text{FWHM} \cdot 2\,\text{t} \cdot \text{yr}). \tag{2.11}$$

A power-law fit to the median 90% C.L. half-life sensitivities obtained in a multiparametric study gives the approximate relation [60]

$$T_{1/2}^{0\nu} \propto B^{-0.28}. \tag{2.12}$$

The sensitivities were calculated using a likelihood analysis of at least 5000 toy Monte Carlo experiments per configuration. The study varied energy resolution and topological discrimination, while simultaneously scaling all modeled background normalizations by factors between 1 and 2, except those of $2\nu\beta\beta$ and solar-$^8$B neutrinos, which remained fixed because their normalizations are set by the $2\nu\beta\beta$ half-life and solar-neutrino flux, respectively.

Here, $B$ is the total SS background rate in the energy window and fiducial region defined above, using the DNN discrimination described in Section 2.5.3. The simulated configurations span approximately $B = (0.5\text{–}3)\,\mathrm{SS\ cts/(FWHM \cdot 2000\,kg \cdot yr)}$. Within this range, the empirical relation provides an approximate way to translate changes in the background budget into changes in physics reach. Residual dependence on energy resolution and topological discrimination can remain as $B$ alone does not fully characterize the likelihood analysis.

### 2.5.5 Projected reach in $T^{0\nu}_{1/2}$ and $m_{\beta\beta}$

The exposure dependence of the physics reach for an nEXO-like single-phase LXe TPC is illustrated in Fig. 2.15.

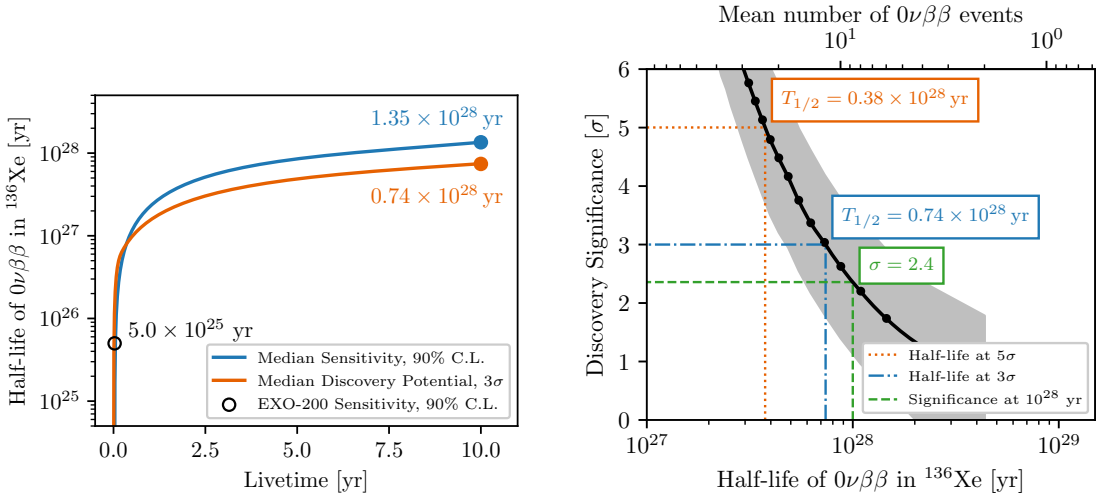


Figure 2.15: Projected sensitivity and discovery reach for the nEXO experiment © IOP Publishing all rights reserved, reproduced with permission [47]. Panel (a) shows the evolution with livetime; panel (b) shows the median discovery significance as a function of the true half-life.

Panel (a) shows the median 90% C.L. sensitivity and the median discovery reach as functions of livetime. Here, the sensitivity is the half-life for which the experiment would set a median 90% C.L. exclusion in the no-signal hypothesis, while the discovery reach is the half-life for which a discovery test at the stated significance would succeed with 50% probability. Panel (b) gives the complementary discovery view for a fixed exposure: the horizontal axis is the assumed true half-life, and the vertical axis is the median discovery significance [47].

For the baseline 10-year exposure, Fig. 2.15 shows the corresponding median exclusion sensitivity and discovery reach [47]. Relative to the final EXO-200 result, the projected half-life reach improves by roughly two to three orders of magnitude.

In the nEXO projection, the median discovery significance at $T^{0\nu}_{1/2} = 10^{28}\,\mathrm{yr}$ is about $2.4\sigma$; the median half-life for a $3\sigma$ discovery is $T^{0\nu}_{1/2} \simeq 0.74 \times 10^{28}\,\mathrm{yr}$, while a

$5\sigma$ discovery requires $T^{0\nu}_{1/2} \lesssim 0.38 \times 10^{28}$ yr.

The curves in Fig. 2.15 assume full deployment at the start of data taking. A staged deployment is also considered, in which the detector begins either with reduced $^{136}$Xe enrichment or with a 1 t, 90%-enriched configuration, and transitions to the baseline configuration as procurement progresses. For a 5 t single-phase LXe TPC and a 10-year exposure, the projected median 90% C.L. sensitivity is $\sim 1.3 \times 10^{27}$ yr with natural xenon ($f_{136} \simeq 8.9\%$), rising to $\sim 6.0 \times 10^{27}$ yr at 40% enrichment and $\sim 1.3 \times 10^{28}$ yr at 90% enrichment. A phased strategy reduces early reach but lowers initial cost and schedule risk while still accumulating sensitivity in the $\mathcal{O}(10^{27}\,\text{yr})$ range before the full enriched inventory is deployed.

A broader cross-isotope view of prospective $0\nu\beta\beta$ reach is shown in Fig. 2.16.

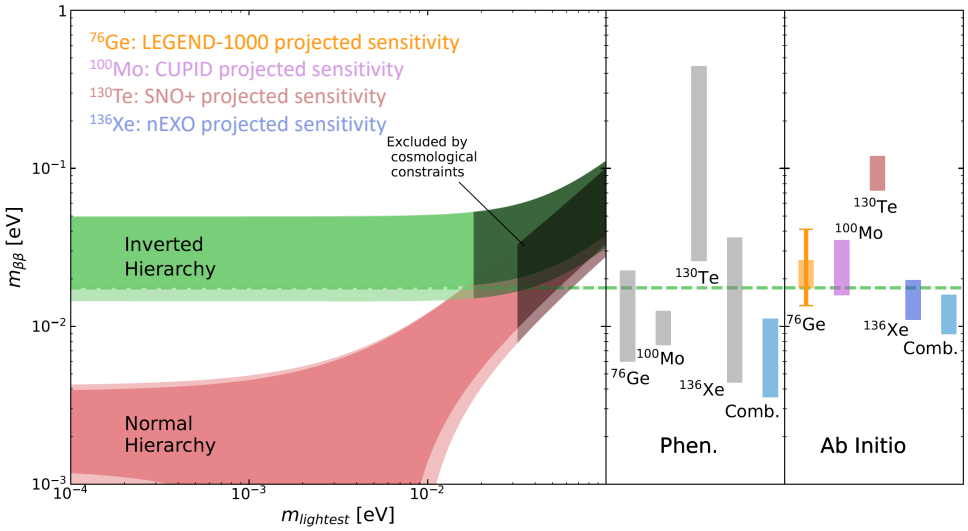


Figure 2.16: Projected effective Majorana mass sensitivities of selected proposed $0\nu\beta\beta$ programs, assuming light-Majorana-neutrino exchange and unquenched $g_A = 1.27$. The ranges reflect the nuclear-matrix-element calculations discussed below. Plot by T. Shickele and J. Holt.

The left part of Fig. 2.16 shows the allowed ranges of the effective Majorana mass $m_{\beta\beta}$ as a function of the lightest neutrino mass $m_{\text{lightest}}$ for normal and inverted mass orderings, while the right part shows the projected $m_{\beta\beta}$ sensitivities of the different programs. The labels "Phen." and "Ab initio" distinguish NME estimates based on phenomenological nuclear models from VS-IMSRG calculations starting from microscopic interactions between nucleons [61, 62]. Both sets use experimental half-life projections from the corresponding design reports and sensitivity studies [63, 64, 65, 47]. Next-generation tonne-scale programs target $\mathcal{O}(10^{28}\,\text{yr})$ half-life sensitivity, corresponding, for representative nuclear matrix elements, to $m_{\beta\beta}$ reach in the $\mathcal{O}(10\,\text{meV})$ range.

Figure 2.17 summarizes how the nEXO sensitivity is interpreted in terms of the effective Majorana mass $m_{\beta\beta}$. As discussed in Sec. 1.3.3 through Eq. (1.41), the half-life sensitivity is translated to $m_{\beta\beta}$ through the phase-space factor $G_{0\nu}$, the nuclear matrix element $M_{0\nu}$, and the axial coupling $g_A$.

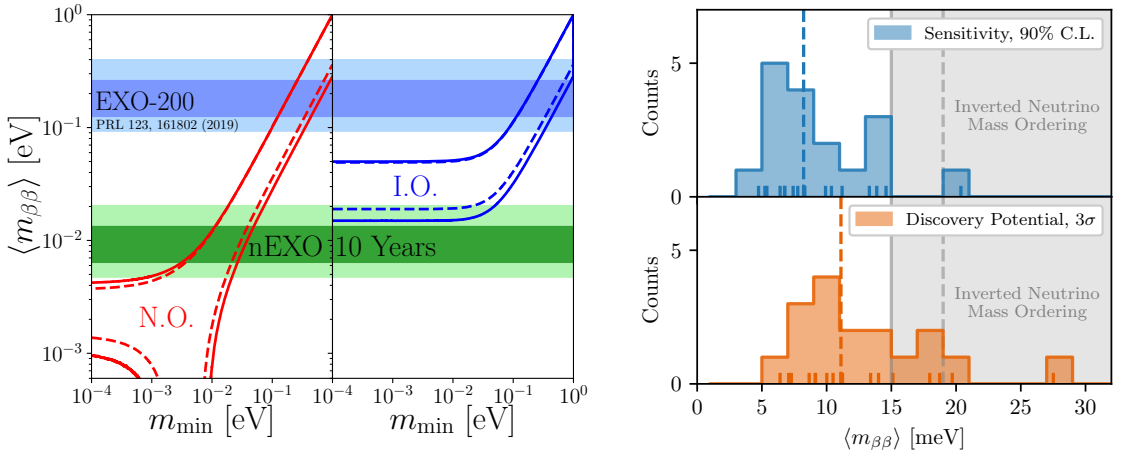


Figure 2.17: Effective Majorana-mass interpretation of the nEXO sensitivity © IOP Publishing all rights reserved, reproduced with permission [47]: $m_{\beta\beta}$ reach versus $m_{\text{lightest}}$ (left) and the dependence of nEXO sensitivity and discovery reach on nuclear-matrix-element choice (right), with the inverted-ordering band indicated for reference.

In Fig. 2.17 (left), the spread in $m_{\beta\beta}$ reflects the range of available nuclear-matrix-element calculations for a fixed half-life sensitivity. The lighter shading spans the full set of values considered, while the darker shading indicates the central interval of that set [47]. In this representation, the projected nEXO reach extends well below the corresponding EXO-200 band and reaches the lower part of the inverted-ordering region for favorable matrix-element choices.

Figure 2.17 (right) makes this nuclear-model dependence explicit. Each tick mark corresponds to the $m_{\beta\beta}$ reach obtained from one nuclear-matrix-element calculation for the same assumed $T^{0\nu}_{1/2}$ sensitivity, and the histogram shows how these values are distributed. The vertical dashed line marks the median of the set, and the shaded band indicates the expected $m_{\beta\beta}$ range for inverted ordering. In the nEXO projection, the inferred $m_{\beta\beta}$ reach falls below the lower edge of this band for some nuclear-matrix-element choices, while for others it remains within the band.

### 2.5.6 Running and next-generation $0\nu\beta\beta$ programs

The current and planned experimental landscape pursues two complementary goals: increasing exposure through larger isotope masses and longer livetimes, and reducing backgrounds in a narrow region around $Q_{\beta\beta}$. Table 2.3 summarizes selected running programs and planned next-generation experiments, quoted as projected $T^{0\nu}_{1/2}$ sensitivities at the stated livetimes. Published limits from completed phases are summarized separately in Sec. 1.3.5.

Germanium programs combine excellent intrinsic energy resolution with very low achieved background rates, and the staged LEGEND program builds on GERDA and MAJORANA toward sensitivities beyond $10^{27}$ yr in its current phase [66]. Xenon

| Isotope | Projected $T_{1/2}^{0\nu}$ sensitivity | Experiment | Medium |
|---|---|---|---|
| **Running (projected sensitivity)** | | | |
| $^{76}$Ge | $\gtrsim 10^{27}$ yr (5 yr) | LEGEND-200 [66] | HPGe+LAr |
| **Planned / next-generation (design goals)** | | | |
| $^{76}$Ge | $\gtrsim 1.6 \times 10^{28}$ yr (10 yr) | LEGEND-1000 [63] | HPGe+LAr |
| $^{100}$Mo | $\gtrsim 1.6 \times 10^{27}$ yr (10 yr) | CUPID [67] | scint. bolometers |
| $^{136}$Xe | $\gtrsim 2 \times 10^{27}$ yr (5 yr) | KamLAND2-Zen [68] | Xe-LS |
| $^{136}$Xe | $\gtrsim 6 \times 10^{25}$ yr (3 yr) | NEXT-100 [69] | HPXe TPC |
| $^{136}$Xe | $\gtrsim 1.35 \times 10^{28}$ yr (10 yr) | nEXO [47] | LXe TPC |

Table 2.3: Selected running and planned $0\nu\beta\beta$ experiments and their projected $T_{1/2}^{0\nu}$ sensitivities at the stated livetimes.

TPCs instead emphasize a large homogeneous target, event reconstruction, and scalability. Next-generation tonne-scale designs aim to extend present limits by roughly two orders of magnitude into the $\mathcal{O}(10^{28}\,\mathrm{yr})$ regime, as illustrated by nEXO and LEGEND-1000 [47, 63].

# Chapter 3

# Charge Transport and Liquid Xenon Purity

## Contents


**3.1 Charge Transport in Liquid Xenon . . . . . 47**

3.1.1 O2-equivalent Concentration and Electron Attachment in LXe . . . . . 48

3.1.2 Electron Lifetime Requirement . . . . . 51

3.1.3 Allowed Impurity Source Rate . . . . . 52

3.1.4 Impurity Budgeting . . . . . 56

**3.2 Detector Material Outgassing . . . . . 57**

3.2.1 Gas Sources in Xenon-Contact Materials . . . . . 59

3.2.2 Total Outgassing Model . . . . . 64

**3.3 Measurement Methods . . . . . 67**

3.3.1 Vacuum Chambers . . . . . 68

3.3.2 Liquid Xenon Drift Chambers . . . . . 77

**3.4 Mitigation Techniques . . . . . 78**

3.4.1 Material Choice and Geometry . . . . . 78

3.4.2 Cleaning and Preparation Techniques . . . . . 79

3.4.3 Storage After Cleaning . . . . . 80

Liquid xenon TPCs use a dense, homogeneous medium in which a single energy deposition produces both scintillation and ionization. This makes them powerful rare-event detectors, but it also makes the charge response sensitive to trace chemical impurities in the liquid. Electronegative species can attach drifting electrons and attenuate the charge signal over long drift distances. This chapter examines how charge loss is quantified by the electron lifetime and governed by impurity sources and xenon purification in LXe detectors. The same framework is subsequently applied to establish requirements on detector materials, leaks, xenon handling, and operating procedures, with nEXO as the primary application.

## 3.1 Charge Transport in Liquid Xenon

Electronegative impurities can be introduced into the xenon by outgassing from detector materials, leaks, xenon handling, and residual contamination from the xenon supply chain. Once present in the active volume, these species can capture drifting electrons before they reach the charge readout, as illustrated in Fig. 3.1.

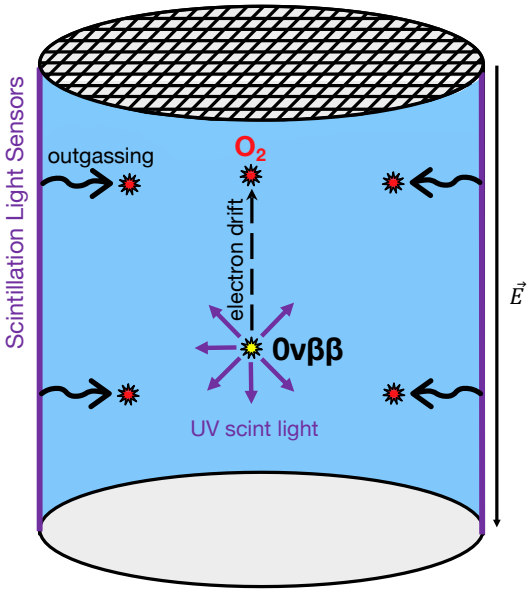


Figure 3.1: Schematic illustration of electron attachment during charge drift in LXe.

For a next-generation $0\nu\beta\beta$ detector, the allowed charge attenuation must be expressed in quantities that can be measured and controlled. The charge-channel requirement is a minimum electron lifetime, which fixes the maximum allowed concentration of electronegative impurities. With xenon recirculation and purification, the same concentration limit can then be converted into an allowed continuous impurity source rate.

Common symbols used in this section are summarized in Table 3.1. Process-specific quantities are defined when they first appear.

| Symbol | Meaning | Unit or convention |
|---|---|---|
| $N_e$ | number of free drifting electrons | – |
| $t_{\mathrm{drift}}$ | electron drift time | s |
| $\tau_e$ | electron lifetime | s |
| $k_S$ | attachment-rate constant for species $S$ | $\mathrm{L\,mol^{-1}\,s^{-1}}$ |
| $c_S$ | molar concentration of species $S$ | $\mathrm{mol\,L^{-1}}$ |
| $c_{\mathrm{O_2,eq}}$ | $O_2$-equivalent concentration | $\mathrm{mol\,L^{-1}}$ |
| $J$ | molar impurity source rate | $\mathrm{mol\,s^{-1}}$ |
| $\mathcal{Q}^{\mathrm{LXe}}$ | LXe-equivalent throughput | $\mathrm{mbar\,L\,s^{-1}}$ |
| $R_{\mathrm{PV}}$ | gas constant in throughput units | $83.14\,\mathrm{mbar\,L\,mol^{-1}\,K^{-1}}$ |
| $F_{\mathrm{LXe}}$ | equivalent liquid recirculation flow | $\mathrm{L\,s^{-1}}$ |
| $r$ | gas recirculation flow | SLPM |
| $\eta$ | one-pass purifier efficiency | – |
| $c^{\mathrm{clean}}$ | purifier-return impurity concentration | $\mathrm{mol\,L^{-1}}$ |

Table 3.1: Common symbols used in the charge-transport and purification model.

### 3.1.1 $O_2$-equivalent Concentration & Electron Attachment in LXe

The quantity relevant to charge collection is not the absolute concentration of a given impurity, but the rate at which that impurity removes drifting electrons. This rate depends on both the impurity concentration and the electron-attachment rate constant.

#### Electron Attachment Rate

For one impurity species $S$, electron attachment is described by

$$\frac{dN_e}{dt} = -k_S c_S N_e. \tag{3.1}$$

After a drift time $t_{\mathrm{drift}}$, the surviving charge is therefore

$$N_e(t_{\mathrm{drift}}) = N_e(0)\exp\left(-k_S c_S t_{\mathrm{drift}}\right). \tag{3.2}$$

This attenuation is usually written in terms of an electron lifetime,

$$N_e(t_{\mathrm{drift}}) = N_e(0)\exp\left(-\frac{t_{\mathrm{drift}}}{\tau_e}\right), \tag{3.3}$$

so that, for one species,

$$\frac{1}{\tau_e} = k_S c_S. \tag{3.4}$$

If several electronegative species are present, their attachment rates add:

$$\frac{1}{\tau_e} = \sum_S k_S c_S. \tag{3.5}$$

A measured electron lifetime is therefore an integrated purity indicator. It reflects the total electron-attachment strength of the impurity mixture, not the concentration of any individual species, unless the mixture composition is independently known.

The main species of practical concern in xenon systems are oxygen and water, which can enter through air exposure, leaks, and material outgassing. Other molecules, such as CO, $CO_2$, nitrogen oxides, or fluorinated species, may also contribute depending on material history and processing.

The attachment rate depends on both species and drift field. Figure 3.2 shows the rates used here at $T = 165\,\mathrm{K}$. The $O_2$, $N_2O$, and $SF_6$ curves are based on LXe measurements from Ref. [70]. In this interpretation, $O_2$ and $SF_6$ decrease with field because their attachment cross sections are largest at low electron energy, while $N_2O$ increases because its attachment cross section peaks near 0.35 eV [70].

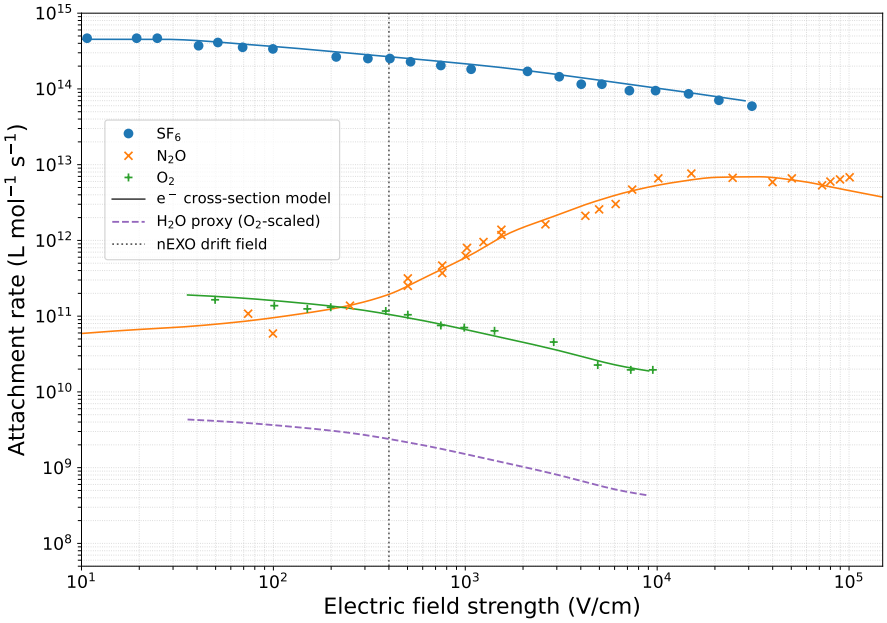


Figure 3.2: Electron attachment-rate constants in LXe at $T = 165\,\mathrm{K}$. The $SF_6$, $N_2O$, and $O_2$ data are from Ref. [70]. The $H_2O$ curve is an order-of-magnitude proxy obtained by scaling the LXe oxygen curve with the low-field $H_2O/O_2$ ratio measured in LAr [71].

No direct LXe measurement of $k_{H_2O}(E)$ comparable to the $O_2$, $N_2O$, and $SF_6$ measurements is available. Since water is commonly observed in vacuum outgassing measurements, an approximate conversion is nevertheless needed. Measurements of $N_2O$ and $SF_6$ in both LAr and LXe show that their attachment-rate ratios relative to oxygen remain comparable between the two liquids, supporting the use of a LAr ratio as an order-of-magnitude proxy [70, 71]. The low-field attachment rates measured

in LAr are

$$k_{O_2}^{LAr} = 4.1^{+1.5}_{-0.9}\ (\mathrm{ms\,ppb})^{-1}, \qquad k_{H_2O}^{LAr} = 0.093^{+0.028}_{-0.033}\ (\mathrm{ms\,ppb})^{-1}. \tag{3.6}$$

Their nominal ratio is

$$\alpha_{H_2O}^{\mathrm{proxy}} \equiv \frac{k_{H_2O}^{LAr}}{k_{O_2}^{LAr}} \simeq 2.3 \times 10^{-2}. \tag{3.7}$$

This ratio is used only as an order-of-magnitude proxy for $k_{H_2O}^{LXe}$. Its uncertainty is not quantified because the reported LAr uncertainty does not include the unknown effects of changing the host liquid.

The rates used at the nominal nEXO drift field, $E_{\mathrm{drift}} = 400\,\mathrm{V\,cm^{-1}}$, are summarized in Table 3.2.

| Species | $k_S(E_{\mathrm{drift}})$ $[10^{11}\,\mathrm{L\,mol^{-1}\,s^{-1}}]$ | $k_S/k_{O_2}$ |
|---|---|---|
| $O_2$ | 1.05 | 1 |
| $H_2O$ | $\sim 0.024$ | $\sim 0.023$ |
| $N_2O$ | 1.94 | 1.85 |
| $SF_6$ | 2660 | 2530 |

Table 3.2: Electron attachment rates at the nominal nEXO drift field, $E_{\mathrm{drift}} = 400\,\mathrm{V\,cm^{-1}}$.

At the nEXO drift field, $N_2O$ attaches electrons at a rate comparable to, but slightly larger than, $O_2$. In contrast, $SF_6$ is more than three orders of magnitude stronger than $O_2$, so even a much smaller concentration would have a large impact on the electron lifetime. The water proxy corresponds to an attachment rate of about 2% of the oxygen rate, but should be interpreted only at the order-of-magnitude level.

### $O_2$-equivalent Concentration

Because attachment rates differ strongly between species, impurity concentrations cannot be compared directly. It is useful to express an impurity mixture as the oxygen concentration that would produce the same total attachment rate:

$$k_{O_2} c_{O_2,\mathrm{eq}} \equiv \sum_S k_S c_S. \tag{3.8}$$

Combining Eq. (3.8) with Eq. (3.5) gives

$$\tau_e = \frac{1}{k_{O_2} c_{O_2,\mathrm{eq}}}. \tag{3.9}$$

The same convention is used for impurity source rates. For a source rate $J_S$ of species $S$, the corresponding $O_2$-equivalent source rate is

$$J_{S,O_2\mathrm{eq}} = \frac{k_S}{k_{O_2}} J_S. \tag{3.10}$$

The ratio $k_S/k_{O_2}$ is evaluated at the relevant drift field. Unless stated otherwise, the values in Table 3.2 are used.

The $O_2$-equivalent scale is a bookkeeping convention based on electron attachment rates. It does not imply that molecular oxygen is the dominant contaminant in a given system. It provides a common basis for comparing impurity concentrations and source rates with different attachment strengths.

### 3.1.2 Electron Lifetime Requirement

The electron lifetime requirement sets how much charge attenuation is allowed over the longest drift time. Individual electrons undergo frequent scattering from xenon atoms and do not travel ballistically; however, their ensemble-averaged drift velocity is parallel to the applied electric field, with drift speed $v_d$. For a drift length $H = 118.3\,\mathrm{cm}$ and $v_d = 1.71\,\mathrm{mm\,\mu s^{-1}}$ at $E_{\mathrm{drift}} = 400\,\mathrm{V\,cm^{-1}}$,

$$t_{\mathrm{drift}}^{\mathrm{max}} = \frac{H}{v_d} \simeq 0.69\,\mathrm{ms}. \tag{3.11}$$

The charge survival over the maximum drift time is

$$\frac{N_e(t_{\mathrm{drift}}^{\mathrm{max}})}{N_e(0)} = \exp\left(-\frac{t_{\mathrm{drift}}^{\mathrm{max}}}{\tau_e}\right). \tag{3.12}$$

Equivalently, a minimum charge survival $f_Q$ requires

$$\tau_e \geq -\frac{t_{\mathrm{drift}}^{\mathrm{max}}}{\ln f_Q}. \tag{3.13}$$

The nEXO detector model uses $\tau_e = 10\,\mathrm{ms}$ as the ideal lifetime, while $\tau_e = 5\,\mathrm{ms}$ is used here as a baseline value for impurity-budget calculations [46]. The corresponding maximum-drift charge survivals are listed in Table 3.3.

| Electron lifetime | $t_{\mathrm{drift}}^{\mathrm{max}}/\tau_e$ | Charge survival | Charge loss |
|---|---|---|---|
| 5 ms | 0.138 | 0.871 | 12.9 % |
| 10 ms | 0.069 | 0.933 | 6.7 % |
| 13.5 ms | 0.051 | 0.950 | 5.0 % |

Table 3.3: Maximum-drift charge attenuation for representative electron lifetimes, using $t_{\mathrm{drift}}^{\mathrm{max}} = 0.69\,\mathrm{ms}$.

A 5 ms lifetime gives about 87 % charge survival over the full drift length, while the 10 ms design value gives about 93 %. A stricter 95 % survival requirement would require $\tau_e \simeq 13.5\,\mathrm{ms}$. For $\tau_e = 10\,\mathrm{ms}$, calibration studies indicate that the associated charge-energy uncertainty can be kept below approximately 0.15 % [46].

Using Eq. (3.9), the lifetime requirement becomes

$$c_{\mathrm{O_2,eq}}^{\mathrm{max}} = \frac{1}{k_{O_2}\tau_e}. \tag{3.14}$$

With $k_{O_2} = 1.05 \times 10^{11}\,\mathrm{L\,mol^{-1}\,s^{-1}}$, the conservative 5 ms requirement gives

$$\boxed{c^{\max}_{O_2,\mathrm{eq}} = 1.90 \times 10^{-9}\,\mathrm{mol\,L^{-1}}} \qquad (\tau_e = 5\,\mathrm{ms}). \tag{3.15}$$

The corresponding mole fraction relative to the enriched xenon inventory is

$$\chi_{O_2,\mathrm{eq}} = \frac{c^{\max}_{O_2,\mathrm{eq}}}{c_{\mathrm{Xe}}} = c^{\max}_{O_2,\mathrm{eq}} \frac{M^{\mathrm{enr}}_{\mathrm{Xe}}}{\rho^{\mathrm{enr}}_{\mathrm{LXe}}}, \tag{3.16}$$

where $c_{\mathrm{Xe}} = \rho^{\mathrm{enr}}_{\mathrm{LXe}}/M^{\mathrm{enr}}_{\mathrm{Xe}}$, $M^{\mathrm{enr}}_{\mathrm{Xe}} \simeq 0.136\,\mathrm{kg\,mol^{-1}}$, and $\rho^{\mathrm{enr}}_{\mathrm{LXe}} = 3.057\,\mathrm{kg\,L^{-1}}$. This gives

$$\boxed{\chi_{O_2,\mathrm{eq}} = 8.5 \times 10^{-11} = 0.085\ \mathrm{ppb}} \qquad (\tau_e = 5\,\mathrm{ms}). \tag{3.17}$$

For the 10 ms design lifetime,

$$\boxed{\chi_{O_2,\mathrm{eq}} = 0.042\ \mathrm{ppb}} \qquad (\tau_e = 10\,\mathrm{ms}). \tag{3.18}$$

The relevant purity scale is therefore below 0.1 ppb $O_2$-equivalent.

### 3.1.3 Allowed Impurity Source Rate

For detector design, the concentration limit must be converted into a source-rate limit. Vacuum-leak and outgassing rates are conventionally expressed as pressure–volume throughputs, typically in $\mathrm{mbar\,L\,s^{-1}}$. A molar impurity source rate $J$ can be written in these units using

$$\mathcal{Q}(T) = J R_{\mathrm{PV}} T. \tag{3.19}$$

Unless stated otherwise, this conversion is evaluated at $T = T_{\mathrm{LXe}} = 165\,\mathrm{K}$, giving an LXe-equivalent throughput.

The xenon recirculation rate is quoted as a gas flow $r$ in standard liters per minute, with standard conditions taken as $T = 273.15\,\mathrm{K}$ and $P = 1\,\mathrm{atm}$. The corresponding molar xenon flow is

$$\dot{n}_{\mathrm{Xe}} = \frac{r}{60\,V_{\mathrm{mol}}}, \tag{3.20}$$

where $V_{\mathrm{mol}} = 22.4\,\mathrm{L\,mol^{-1}}$. Expressed as an equivalent liquid-volume flow,

$$F_{\mathrm{LXe}} = \dot{n}_{\mathrm{Xe}} \frac{M^{\mathrm{enr}}_{\mathrm{Xe}}}{\rho^{\mathrm{enr}}_{\mathrm{LXe}}} = \frac{r}{60\,V_{\mathrm{mol}}} \frac{M^{\mathrm{enr}}_{\mathrm{Xe}}}{\rho^{\mathrm{enr}}_{\mathrm{LXe}}}. \tag{3.21}$$

For the planned nEXO value $r = 350$ SLPM,

$$F_{\mathrm{LXe}} = 1.16 \times 10^{-2}\,\mathrm{L\,s^{-1}}. \tag{3.22}$$

### Dynamic Purification Model

The allowed source rate follows from the impurity balance between continuous sources and purification. Figure 3.3 shows the model used here.

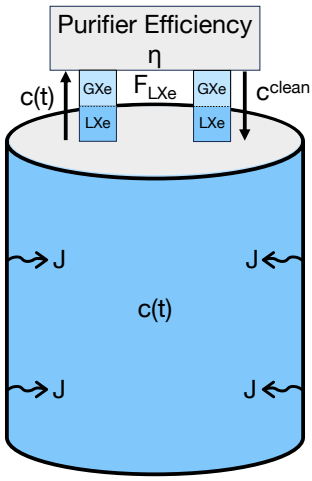


Figure 3.3: Schematic of the dynamic purification model used to relate impurity source rates to the $O_2$-equivalent concentration in LXe.

Let $c(t)$ be the $O_2$-equivalent concentration in the liquid xenon and $J(t)$ the total $O_2$-equivalent molar source rate into the xenon. For a liquid volume $V_{\mathrm{LXe}}$,

$$V_{\mathrm{LXe}}\frac{dc(t)}{dt} = J(t) - \eta F_{\mathrm{LXe}}c(t) + F_{\mathrm{LXe}}c^{\mathrm{clean}}. \tag{3.23}$$

The three terms represent, respectively: (1) impurity injection at rate $J(t)$, (2) removal by the purifier at one-pass efficiency $\eta$, corresponding to the rate $\eta F_{\mathrm{LXe}}c(t)$, and (3) residual impurity returned by the purifier at concentration $c^{\mathrm{clean}}$, corresponding to the rate $F_{\mathrm{LXe}}c^{\mathrm{clean}}$.

For a constant source rate $J(t) = J$, the solution, derived in Appendix F, is

$$c(t) = c_\infty + [c(0) - c_\infty]\exp\left(-\frac{t}{t_{\mathrm{pur}}}\right), \tag{3.24}$$

with

$$t_{\mathrm{pur}} = \frac{V_{\mathrm{LXe}}}{\eta F_{\mathrm{LXe}}} = \frac{t_{\mathrm{rec}}}{\eta}, \tag{3.25}$$

and

$$c_\infty = \frac{J + F_{\mathrm{LXe}}c^{\mathrm{clean}}}{\eta F_{\mathrm{LXe}}}. \tag{3.26}$$

The initial concentration $c(0)$ depends on xenon handling, pre-purification, and detector exposure history. The time-dependent concentration is converted to electron lifetime using Eq. (3.9).

Requiring $c_\infty \leq c^{\mathrm{max}}_{\mathrm{O_2,eq}}$ gives the allowed source rate

$$J^{\mathrm{max}}_{\mathrm{O_2,eq}} = F_{\mathrm{LXe}}\left(\eta c^{\mathrm{max}}_{\mathrm{O_2,eq}} - c^{\mathrm{clean}}\right) = F_{\mathrm{LXe}}\left(\frac{\eta}{k_{\mathrm{O_2}}\tau_e} - c^{\mathrm{clean}}\right). \tag{3.27}$$

Thus the continuous impurity source must fit within the removal capacity of the purification loop. The case $\eta = 1$ corresponds to complete impurity removal in one pass. For the numerical estimates below, $c^{\text{clean}}$ is taken to be negligible.

**N.B. Full Recirculation Time in nEXO**

The full recirculation time is the time needed to process one xenon inventory through the purifier. Using the baseline xenon mass from Chap. 2, $m_{\text{Xe}} = 5.0\,\text{t}$, and the planned nEXO recirculation rate $r = 350$ SLPM,

$$t_{\text{rec}} = \frac{m_{\text{Xe}} V_{\text{mol}}}{M_{\text{Xe}}^{\text{enr}} r} = \frac{5000 \times 22.4}{0.136 \times 350} = 2.35 \times 10^3\,\text{min} = 1.63\,\text{d}. \tag{3.28}$$

This is comparable to the EXO-200 recirculation time of 1.53 d, obtained with $m_{\text{Xe}} \simeq 200\,\text{kg}$ and $r \simeq 15$ SLPM [50]. It achieved electron lifetimes of order 2.5 ms with this recirculation scale [72]. The nEXO recirculation rate of 350 SLPM was chosen to keep a similar full-inventory turnover time.

Using $F_{\text{LXe}} = 1.16 \times 10^{-2}\,\text{L}\,\text{s}^{-1}$, $k_{\text{O}_2} = 1.05 \times 10^{11}\,\text{L}\,\text{mol}^{-1}\,\text{s}^{-1}$, and $\tau_e = 5\,\text{ms}$,

$$J_{\text{O}_2,\text{eq}}^{\max} \simeq 2.2 \times 10^{-11}\,\eta\,\text{mol}\,\text{s}^{-1}. \tag{3.29}$$

In LXe-equivalent pressure–volume units,

$$\mathcal{Q}_{\text{O}_2,\text{eq}}^{\text{LXe}} = J_{\text{O}_2,\text{eq}}^{\max} R_{\text{PV}} T_{\text{LXe}}. \tag{3.30}$$

Combining Eqs. (3.21), (3.27), and (3.30) gives

$$\boxed{\mathcal{Q}_{\text{O}_2,\text{eq}}^{\text{LXe}} \simeq 3.0 \times 10^{-7}\,\eta\,\text{mbar}\,\text{L}\,\text{s}^{-1} \left(\frac{r}{350\ \text{SLPM}}\right)\left(\frac{5\,\text{ms}}{\tau_e}\right)} \tag{3.31}$$

for $k_{\text{O}_2} = 1.05 \times 10^{11}\,\text{L}\,\text{mol}^{-1}\,\text{s}^{-1}$. For 10 ms the limit is smaller by a factor of two:

$$\boxed{\mathcal{Q}_{\text{O}_2,\text{eq}}^{\text{LXe}} \simeq 1.5 \times 10^{-7}\,\eta\,\text{mbar}\,\text{L}\,\text{s}^{-1}} \qquad (\tau_e = 10\,\text{ms},\ r = 350\ \text{SLPM}). \tag{3.32}$$

The liquid purity limit can also be expressed as an equilibrium gas-phase mole-fraction limit using the Henry-law volatility constant

$$K_H^{\text{O}_2} = \frac{x_{\text{O}_2}^{\text{gas}}}{x_{\text{O}_2}^{\text{liquid}}}, \tag{3.33}$$

where $x_{\text{O}_2}^{\text{gas}}$ and $x_{\text{O}_2}^{\text{liquid}}$ are equilibrium mole fractions in the gas and liquid phases. Using $K_H^{\text{O}_2} = 62.5$ for oxygen in xenon [73],

$$x_{\text{O}_2,\max}^{\text{gas}} = K_H^{\text{O}_2} x_{\text{O}_2,\max}^{\text{liquid}}. \tag{3.34}$$

For $\tau_e = 5\,\text{ms}$,

$$x_{\text{O}_2,\max}^{\text{gas}} \simeq 5.3\ \text{ppb}. \tag{3.35}$$

Henry's law relates equilibrium mole fractions in the two phases. In the purification model used here, the allowed source rate is set by the liquid concentration limit and

the recirculation flow [Eq. (3.27)]. Expressing the same purity requirement as a gas-phase mole fraction therefore leaves the source-rate limit in Eq. (3.31) unchanged.

Figure 3.4 illustrates the purification response for different recirculation conditions. The initial condition uses a low-purity LXe lifetime, $\tau_e(0) = 71\,\mu\text{s}$, reported by XENONnT after filling with the purifier units bypassed [74]. This value is not specific to enriched xenon, but it is more conservative than the early EXO-200 enriched-LXe value of about 250 µs measured at low recirculation flow [50]. This corresponds to

$$c(0) = \frac{1}{k_{\text{O}_2}\tau_e(0)} = 1.34 \times 10^{-7}\,\text{mol}\,\text{L}^{-1}. \tag{3.36}$$

The allowed steady-state concentration for the 5 ms requirement is

$$c_\infty^{\max} = c_{\text{O}_2,\text{eq}}^{\max} = 1.90 \times 10^{-9}\,\text{mol}\,\text{L}^{-1}. \tag{3.37}$$

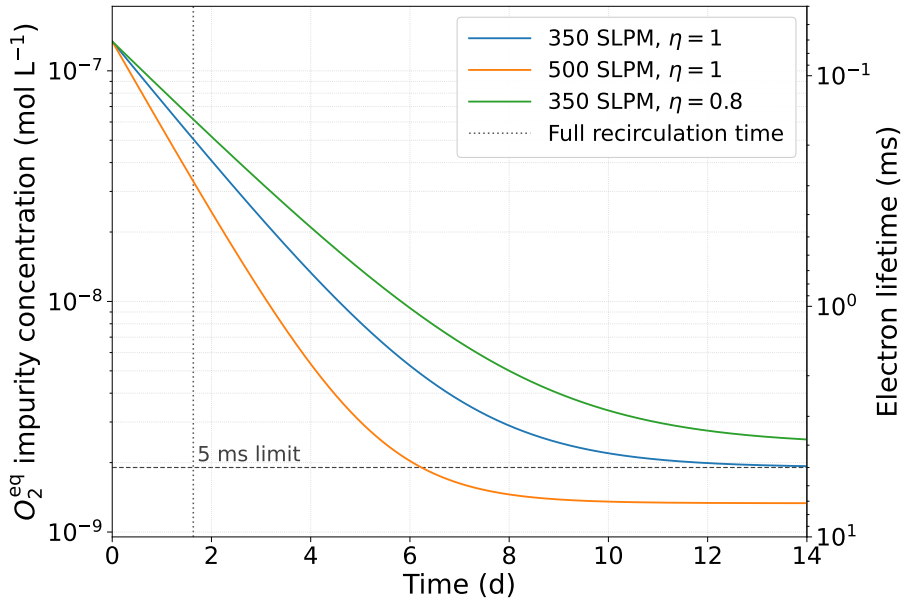


Figure 3.4: Dynamic purification response for an initial concentration corresponding to $\tau_e(0) = 71\,\mu\text{s}$.

The baseline curve uses the allowed source rate from Eq. (3.27), with $r = 350$ SLPM, $c^{\text{clean}} \simeq 0$, and $\eta = 1$. In this case,

$$\frac{c(t)}{c_\infty^{\max}} = 1 + \left[\frac{c(0)}{c_\infty^{\max}} - 1\right] \exp\left(-\frac{t}{t_{\text{rec}}}\right). \tag{3.38}$$

With these values, $c(0)/c_\infty^{\max} \simeq 70$. After one full recirculation time, the concentration is about 27 times the allowed steady-state value; after three recirculation times, it is about 4.5 times this value.

The figure illustrates the two roles of the recirculation flow $F_{\text{LXe}}$: it determines the purification time scale $t_{\text{pur}}$ for approaching equilibrium [Eq. (3.25)] and, at fixed source rate $J$ and purifier conditions, governs the equilibrium concentration $c_\infty$ [Eq. (3.26)]. Increasing the recirculation flow lowers $c_\infty$ and shortens $t_{\text{pur}}$, while

reducing the purifier efficiency raises $c_\infty$ and lengthens $t_{\mathrm{pur}}$. EXO-200 observed a faster-than-linear lifetime improvement with flow in its operating range [75], possibly due to improved mixing and impurity transport at higher flow. The limits derived here instead use the conservative steady-state balance $J \propto F_{\mathrm{LXe}} c$.

### 3.1.4 Impurity Budgeting

The allowed source rate derived above is a detector-level requirement. It must be distributed across the subsystem groups that place materials, interfaces, or internal volumes in contact with liquid or gaseous xenon. This allocation is ongoing work within the collaboration and requires input from subsystem teams to identify xenon-contact components, exposed materials, surface areas, and relevant interfaces.

The impurity budget is organized hierarchically. Each subsystem group $g$ contributes a source rate

$$J_{g,\mathrm{O_2eq}}(t) = \sum_{i \in g} J_{i,\mathrm{O_2eq}}(t), \tag{3.39}$$

where $i$ runs over the components assigned to group $g$. The full detector source rate is

$$J_{\mathrm{tot},\mathrm{O_2eq}}(t) = \sum_{g} J_{g,\mathrm{O_2eq}}(t). \tag{3.40}$$

The detector requirement is

$$J_{\mathrm{tot},\mathrm{O_2eq}}(t) \leq J^{\max}_{\mathrm{O_2,eq}}. \tag{3.41}$$

Table 3.4 summarizes the main subsystem groups and representative xenon-contact components that must be tracked.

| Group | Component classes | Examples of xenon-contact items |
|---|---|---|
| TPC | Active detector | Field cage, charge tiles |
| | HV interfaces | Cables, conduits, feedthroughs |
| Photodetectors | Light sensors | SiPM tiles, interposers |
| | Mechanical supports | Staves, supports, cables, adhesives |
| Xenon system | Purification loop | Pump, purifier, plumbing |
| | Xenon handling | Valves, sensors, storage volumes |
| Charge readout | Cold electronics | ASICs, boards, electronic components |
| | Signal interfaces | Cables, solder, feedthrough interfaces |
| Photon readout | Cold electronics | ASICs, boards, electronic components |
| | Signal interfaces | Cables, solder, feedthrough interfaces |

Table 3.4: Simplified grouping of xenon-contact components used to organize the electronegative-impurity source budget within the collaboration.

This budgeting step is needed to connect the detector-level purity requirement to component-level material studies. Once the xenon-contact inventory is defined, each component source rate must be estimated and the sum compared with Eq. (3.41). The next section develops the outgassing model used for this estimate.

## 3.2 Detector Material Outgassing

The impurity budget developed in Sec. 3.1.4 requires a source rate for each xenon-contact component. In detector materials, gases can be present as free gas in internal volumes, molecules adsorbed on surfaces, or molecules absorbed in the bulk. Their release into the xenon volume is referred to as outgassing. It depends on the material, exposed area, geometry, temperature, cleaning, storage history, air exposure, and time under vacuum or in xenon.

Throughout this section, source rates are expressed as LXe-equivalent pressure–volume throughputs, using

$$\mathcal{Q}^{\mathrm{LXe}} = J R_{\mathrm{PV}} T_{\mathrm{LXe}}, \tag{3.42}$$

where $J$ is a molar source rate and $R_{\mathrm{PV}} = 83.14\,\mathrm{mbar\,L\,mol^{-1}\,K^{-1}}$. Common symbols used in the outgassing model are summarized in Table 3.5; only process-specific quantities are introduced again in the text.

| Symbol | Meaning | Unit or convention |
|---|---|---|
| $\mathcal{Q}^{\mathrm{LXe}}$ | LXe-equivalent throughput | $\mathrm{mbar\,L\,s^{-1}}$ |
| $J$ | molar source rate | $\mathrm{mol\,s^{-1}}$ |
| $A$ | emitting or permeating area | $\mathrm{m^2}$ |
| $d$ | thickness or diffusion length | m |
| $T_m$ | material temperature | K |
| $T_{\mathrm{LXe}}$ | LXe conversion temperature | 165 K |
| $R_{\mathrm{PV}}$ | gas constant in throughput units | $83.14\,\mathrm{mbar\,L\,mol^{-1}\,K^{-1}}$ |
| $R_{\mathrm{g}}$ | molar gas constant | $8.314\,\mathrm{J\,mol^{-1}\,K^{-1}}$ |
| $N_A$ | Avogadro constant | $6.022 \times 10^{23}\,\mathrm{mol^{-1}}$ |
| $D(T_m)$ | diffusion coefficient | $\mathrm{m^2\,s^{-1}}$ |
| $c_0$ | initial bulk concentration | $\mathrm{m^{-3}}$ |
| $C_{0,m}$ | initial surface density of population $m$ | $\mathrm{m^{-2}}$ |
| $k_m(T_m)$ | first-order desorption rate constant | $\mathrm{s^{-1}}$ |

Table 3.5: Common symbols used in the material outgassing source model.

Molecules can be released from the material itself, from the external environment through an interface, from the surface, or from the bulk, as illustrated in Fig. 3.5. Leaks are not a material-release process, but they add gas to the same impurity budget. The main gas-release processes relevant to vacuum systems are:

- **Vaporization** occurs when molecules of the material itself leave the surface. It is controlled by the vapor pressure of the material and is negligible for the low-vapor-pressure detector materials considered here at LXe temperature.
- **Permeation** occurs when molecules pass through a material from one side to the other. It can be important for elastomers or thin barriers exposed to

a concentration gradient, but it is not expected to dominate for the internal nEXO TPC because the xenon-contact boundary is mainly metallic and the active xenon is enclosed by the TPC vessel described in Chap. 2.

- **Desorption** is the release of molecules adsorbed on a surface, such as water or atmospheric gases accumulated during air exposure. It depends strongly on surface history, cleaning, and time under vacuum.
- **Diffusion** is the transport of dissolved molecules from the bulk of a material to an exposed surface, where they are released into the surrounding volume. The process is diffusion-limited when transport through the bulk is slower than release at the surface. It is particularly relevant for polymers, epoxies, and other materials that can absorb gases during manufacturing or air exposure.
- **Leaks** introduce gas through openings or trapped internal volumes. Their contribution depends on the geometry of seals, welds, feedthroughs, and plumbing connections, and can be reduced with welded joints or all-metal seals.

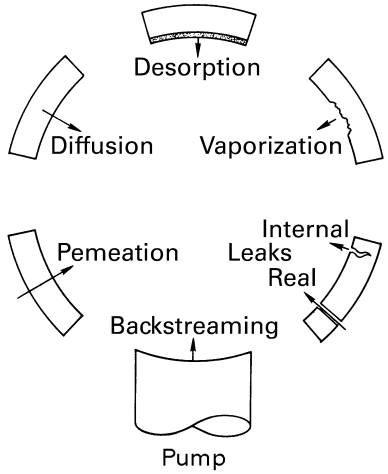


Figure 3.5: Sources of outgassing. Reproduced with authorization from Ref. [76] Copyright © 2024 by John Wiley & Sons, Inc. All rights reserved.

Figure 3.6 shows the qualitative sequence of pressure-limiting processes during pump-down. The initial free gas is removed rapidly, while later times are limited by slower release from surfaces and bulk materials.

Before xenon filling, vacuum pumping and compatible bake-out reduce the free gas and surface gas load. After filling, residual material release continues, but the concentration reached in LXe is set by the balance between sources, gas–liquid partitioning, and purification. For the internal nEXO material budget, the dominant material terms are expected to be desorption and diffusion. Vaporization and permeation are kept as limiting cases, and leaks are treated separately.

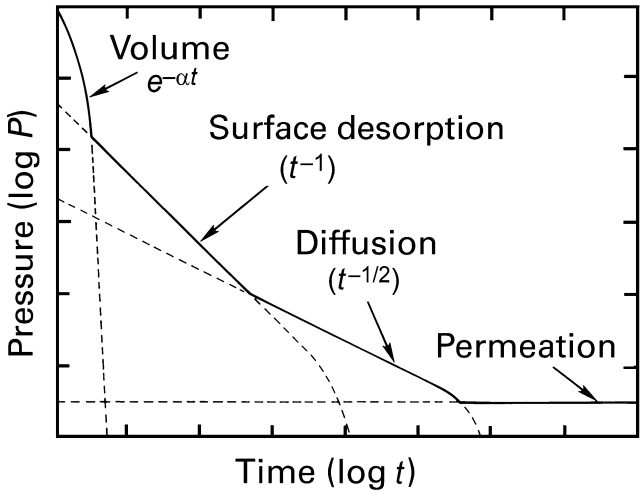


Figure 3.6: Rate-limiting processes during the pumping of a vacuum chamber. Reproduced with authorization from Ref. [76] Copyright © 2024 by John Wiley & Sons, Inc. All rights reserved.

### 3.2.1 Gas Sources in Xenon-Contact Materials

#### Vaporization

Vaporization is the thermally stimulated transfer of atoms or molecules from a condensed material into the vapor phase. For a pure material evaporating freely into vacuum, the Hertz–Knudsen relation gives the maximum molecular emission rate [76],

$$J_{\mathrm{vap}} \leq J_{\mathrm{vap}}^{\max} = 2.63 \times 10^{24} \frac{P_{\mathrm{vap}} A}{\sqrt{M T_m}}, \tag{3.43}$$

where $J_{\mathrm{vap}}$ is the actual molecular emission rate, $J_{\mathrm{vap}}^{\max}$ is its free-evaporation upper bound in molecules per second, $P_{\mathrm{vap}}$ is in Pa, $A$ is in $\mathrm{m}^2$, $M$ is in $\mathrm{g\,mol^{-1}}$, and $T_m$ is in K.

Over a limited temperature range, the vapor pressure can often be represented by

$$\ln\left(\frac{P_{\mathrm{vap}}}{P_0}\right) = -\frac{\Delta H_{\mathrm{vap}}}{R_{\mathrm{g}} T_m} + C, \tag{3.44}$$

where $P_0 = 1\,\mathrm{Pa}$, $\Delta H_{\mathrm{vap}}$ is the molar enthalpy of vaporization, and $C$ is material dependent. The exponential dependence on $1/T_m$ suppresses vaporization at cryogenic temperature.

The corresponding upper bound on the LXe-equivalent throughput corresponding to Eq. (3.43) is

$$\mathcal{Q}_{\mathrm{vap}}^{\mathrm{LXe,max}} = \frac{J_{\mathrm{vap}}^{\max}}{N_A} R_{\mathrm{PV}} T_{\mathrm{LXe}}, \tag{3.45}$$

or, for $T_{\mathrm{LXe}} = 165\,\mathrm{K}$, this gives

$$\boxed{\mathcal{Q}_{\mathrm{vap}}^{\mathrm{LXe,max}} \simeq 6.0 \times 10^4 \frac{P_{\mathrm{vap}} A}{\sqrt{M T_m}} \quad [\mathrm{mbar\,L\,s^{-1}}]} \tag{3.46}$$

Vaporization is not expected to contribute significantly to the electronegative-impurity budget of the internal nEXO TPC. Structural metals have negligible vapor pressure at LXe temperature, and evaporation of a detector material would not primarily release the molecular electronegative species, such as $O_2$ or $H_2O$, that control electron attachment. For polymers and epoxies, the relevant low-temperature sources are instead adsorbed surface species and absorbed bulk molecules.

### Permeation

Permeation is transport through a material separating two gas reservoirs. It can be relevant for seals, feedthroughs, thin barriers, or gas-handling interfaces, but it is not expected to dominate for the main internal nEXO TPC materials, which are not used as barriers between xenon and an external impurity reservoir.

For molecular permeation, the steady-state throughput is proportional to the partial-pressure difference. For dissociative hydrogen permeation through metals, the driving term is instead the difference in square roots of the partial pressures. With $p_\mathrm{u} > p_\mathrm{d}$, $\Delta p = p_\mathrm{u} - p_\mathrm{d}$, and $\Delta\sqrt{p} = \sqrt{p_\mathrm{u}} - \sqrt{p_\mathrm{d}}$, the two limits are [76]

$$\boxed{\mathcal{Q}_\mathrm{perm} = 10\,\frac{A}{d}\begin{cases} K_p^\mathrm{diss}\Delta\sqrt{p}, & \text{dissociative,} \\ K_p^\mathrm{mol}\Delta p, & \text{molecular.} \end{cases}} \tag{3.47}$$

The factor 10 converts $\mathrm{Pa\,m^3\,s^{-1}}$ to $\mathrm{mbar\,L\,s^{-1}}$. The coefficients $K_p^\mathrm{diss}$ and $K_p^\mathrm{mol}$ have different dimensions because the driving terms are different.

For molecular permeation,

$$K_p^\mathrm{mol} = DS, \qquad K_p^\mathrm{mol}(T_m) = K_0 \exp\!\left(-\frac{E_p}{R_\mathrm{g} T_m}\right), \tag{3.48}$$

where $S$ is the solubility, $K_0$ is the permeability prefactor, and $E_p$ is the activation energy for permeation. For an initially gas-free slab exposed to a constant upstream concentration, the permeation time lag is

$$t_\mathrm{lag} = \frac{d^2}{6D}. \tag{3.49}$$

This quantity is obtained from the asymptotic cumulative permeation curve. If a permeation throughput is quoted at a reference temperature $T_\mathrm{ref}$, the corresponding LXe-equivalent throughput is

$$\mathcal{Q}_\mathrm{perm}^\mathrm{LXe} = \mathcal{Q}_\mathrm{perm}^{(T_\mathrm{ref})}\frac{T_\mathrm{LXe}}{T_\mathrm{ref}}. \tag{3.50}$$

Metal permeation mainly concerns hydrogen, which is not the dominant electron-attaching impurity in LXe. Molecular permeation can matter locally at polymeric seals or gas-system interfaces, but for the internal detector material model it is treated as a subdominant or interface-specific contribution.

### Desorption

Desorption is the release of atoms or molecules that were previously adsorbed on a material surface. Surface binding is usually classified into two limiting cases:

- **Physisorption:** van der Waals binding, with $E_{\mathrm{des}} < 40\,\mathrm{kJ\,mol^{-1}}$.
- **Chemisorption:** chemical bonds, with $E_{\mathrm{des}} \sim 80\,\mathrm{kJ\,mol^{-1}}$ to $800\,\mathrm{kJ\,mol^{-1}}$.

Larger desorption energies give longer surface residence times and therefore slower removal. Water bound to metal surfaces can have $E_{\mathrm{des}}$ of order $1 \times 10^2\,\mathrm{kJ\,mol^{-1}}$, making adsorbed $H_2O$ an important long-term gas load after air exposure [76].

Different desorption orders describe different surface regimes. Zero-order desorption applies to multilayers and gives an approximately constant rate until the surface reservoir is depleted; it is not used here because pump-down and baking should remove such layers before TPC filling. First-order desorption applies to molecular adsorbates below one monolayer, with a rate proportional to the remaining surface coverage, and is used here for species such as $H_2O$ and $O_2$. Second-order desorption is more relevant to dissociative adsorption and recombination of small atoms, such as hydrogen on metals, and is thus not included for the molecular electronegative impurities considered here.

For sub-monolayer molecular coverage, first-order desorption gives

$$k_m(T_m) = \nu_0 \exp\left(-\frac{E_{\mathrm{des},m}}{R_{\mathrm{g}} T_m}\right), \quad \tau_m(T_m) = \frac{1}{k_m(T_m)} = \tau_0 \exp\left(\frac{E_{\mathrm{des},m}}{R_{\mathrm{g}} T_m}\right). \tag{3.51}$$

Here $E_{\mathrm{des},m}$ is the desorption energy of population $m$, $\nu_0 = 1/\tau_0 \sim 1 \times 10^{13}\,\mathrm{s^{-1}}$, and $R_{\mathrm{g}}$ is replaced by $k_B$ if the energy is given per molecule.

The theoretical LXe-equivalent specific throughput from a distribution of first-order surface populations is

$$\boxed{q_{\mathrm{des}}^{\mathrm{th,LXe}}(t) = \frac{R_{\mathrm{PV}} T_{\mathrm{LXe}}}{N_A} \sum_m C_{0,m} k_m(T_m) \exp[-k_m(T_m) t]\,.} \tag{3.52}$$

The total contribution is $\mathcal{Q}_{\mathrm{des}}^{\mathrm{th,LXe}} = A q_{\mathrm{des}}^{\mathrm{th,LXe}}$, with $A$ expressed in the same area units as $C_{0,m}$. This microscopic model is useful for showing the dependence on $E_{\mathrm{des}}$ and $T_m$, but real pump-down curves can deviate because of readsorption processes, near-surface diffusion, and surface history [76].

A practical pump-down description is therefore often used instead:

$$\boxed{q_{\mathrm{des}}^{\mathrm{emp}}(t) = q_0 \left(\frac{t_0}{t}\right)^{\alpha}, \qquad t \geq t_0.} \tag{3.53}$$

For water-dominated, unbaked metal surfaces at room temperature, a typical scale is $q_0 \sim 1 \times 10^{-8}\,\mathrm{mbar\,L\,s^{-1}\,cm^{-2}}$ at $t_0 = 1\,\mathrm{h}$, with $\alpha$ often close to one, although the value depends strongly on surface preparation and exposure history [76].

Equation (3.53) is an empirical representation of Eq. (3.52). A real surface contains a distribution of residence times: fast populations are depleted first, and

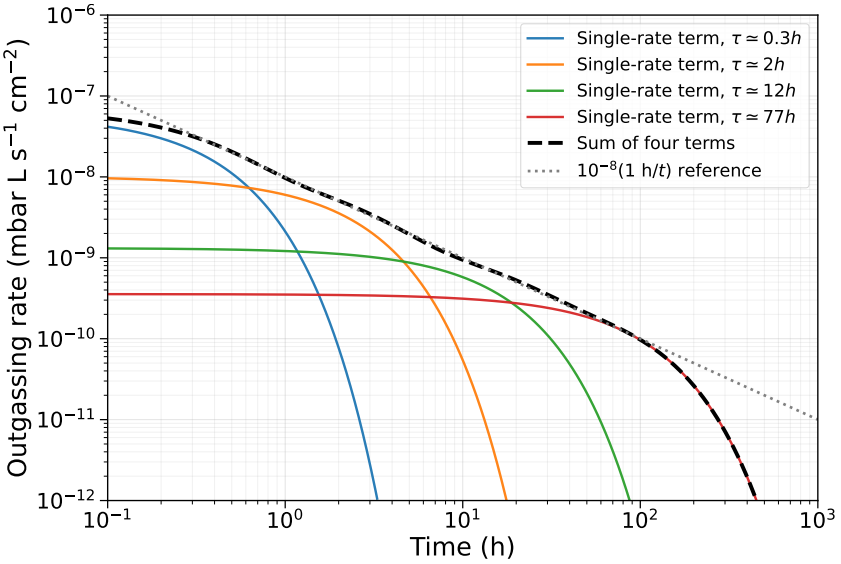


Figure 3.7: Illustrative sum of first-order desorption populations compared with an empirical $t^{-1}$ reference.

slower populations dominate later. Their sum can approximate a power law over the pump-down interval, as illustrated in Fig. 3.7.

For the internal nEXO TPC, desorption is mainly important for metallic surfaces during room-temperature pump-down. It can be reduced by vacuum pumping and material-compatible baking before filling. At LXe temperature, the desorption constants are strongly suppressed, but a small slowly varying contribution can remain over long times.

### Diffusion

Diffusion releases species initially dissolved or absorbed in the bulk of a material. A concentration gradient drives molecules to the xenon-facing surface, where they are removed. If surface removal is fast compared with bulk transport, the release is diffusion-limited. This case is especially relevant for polymers and epoxies exposed to air during fabrication, storage, or handling.

For one-dimensional transport,

$$\frac{\partial c}{\partial t} = D(T_m)\frac{\partial^2 c}{\partial x^2}, \tag{3.54}$$

where $c(x,t)$ is the molecular concentration in the material. The diffusion coefficient is commonly written as

$$D(T_m) = D_0 \exp\left(-\frac{E_D}{R_g T_m}\right), \tag{3.55}$$

with prefactor $D_0$ and activation energy $E_D$.

The initial concentration depends on exposure history and solubility. For a material exposed to air at 1 atm,

$$c_0 = S\alpha_{\mathrm{air}}\frac{N_A}{V_{\mathrm{mol}}^{\mathrm{STP}}}, \tag{3.56}$$

where $S$ is the solubility for the pure gas at 1 atm, $\alpha_{\text{air}}$ is the gas abundance in air, and $V_{\text{mol}}^{\text{STP}}$ is the molar volume at STP. The derivation is given in App. G.1.

For a slab with uniform initial concentration and zero concentration at the exposed surfaces, the LXe-equivalent diffusion throughput is

$$\boxed{\mathcal{Q}_{\text{diff}}^{\text{LXe}}(t) = \frac{c_0 A}{N_A} R_{\text{PV}} T_{\text{LXe}} F_D(t).} \tag{3.57}$$

The finite-slab solution, derived in App. G.2, gives

$$F_D(t) = \frac{4D}{d} \sum_{n=0}^{\infty} \exp\left[ -\left( \frac{\pi(2n+1)}{d} \right)^2 Dt \right]. \tag{3.58}$$

For one-dimensional Fickian diffusion in a slab with uniform initial concentration, constant $D$, and zero concentration at both surfaces, $A$ includes both emitting faces. The characteristic diffusion time is

$$\tau_D = \frac{d^2}{\pi^2 D}. \tag{3.59}$$

At early times, $t \lesssim 0.5\tau_D$, only the near-surface region is depleted, and

$$F_D(t) \simeq \sqrt{\frac{D}{\pi t}}. \tag{3.60}$$

At later times, $t \gtrsim 0.5\tau_D$, depletion of the finite reservoir makes the first term of the finite-slab solution dominant, and the release becomes exponential,

$$F_D(t) \simeq \frac{4D}{d} \exp\left( -\frac{\pi^2 Dt}{d^2} \right). \tag{3.61}$$

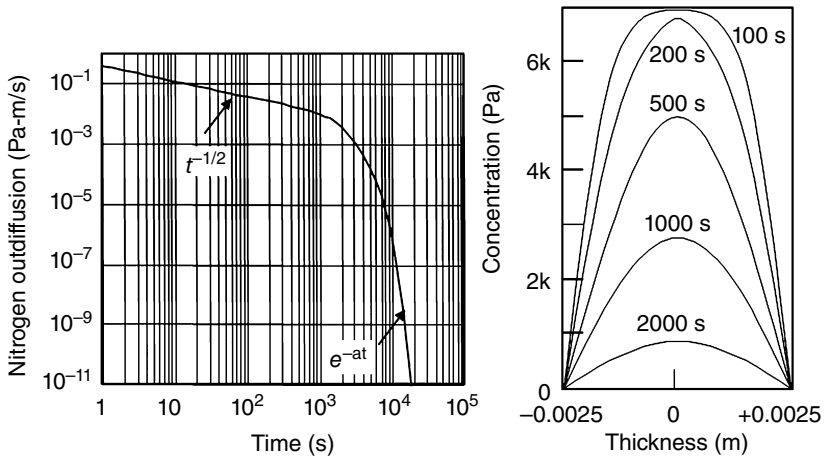


Figure 3.8: Diffusion-limited outgassing and concentration profiles for nitrogen in a 5 mm silicone rubber slab at 25 °C. Reproduced with authorization from Ref. [76] Copyright © 2024 by John Wiley & Sons, Inc. All rights reserved.

Figure 3.8 shows this evolution: an initial $t^{-1/2}$ decrease while the depletion region grows into the material, followed by an exponential fall once the finite slab thickness is sampled.

Long-duration pump-down measurements of PEEK, Kapton, and Vespel showed deviations from the ideal finite-slab solution at very long times. Ref. [77] therefore introduced the following empirical three-regime parameterization:

$$F_D^{\mathrm{emp}}(t) = \begin{cases} \sqrt{\dfrac{D}{\pi t}}, & t \le 0.5\tau_D, \\ \dfrac{4D}{d}\exp\!\left(-\dfrac{\pi^2 D t}{d^2}\right), & 0.5\tau_D < t \le 3\tau_D, \\ \dfrac{1}{6D^2 d}\left(\dfrac{d^2}{\pi t}\right)^3, & t > 3\tau_D. \end{cases} \tag{3.62}$$

The first two branches correspond to the short- and long-time approximations of the classical Fickian finite-slab solution. The $t^{-3}$ branch was introduced empirically in Ref. [77] to reproduce the slower decrease measured for $t > 3\tau_D$ and should be validated experimentally. The corresponding throughput is obtained by replacing $F_D(t)$ with $F_D^{\mathrm{emp}}(t)$ in Eq. (3.57).

Diffusion is most relevant for polymers and epoxies. For dense metals, bulk transport of electronegative molecules is usually negligible compared with surface desorption; hydrogen is the main exception, but it is not the dominant electron-attaching impurity in LXe.

#### Leaks

Leaks are gas-flow paths through seals, welds, feedthroughs, valves, or plumbing interfaces. Unlike desorption or diffusion, an inward leak is approximately constant in time as long as the pressure boundary conditions remain unchanged.

For an incoming gas containing species $i$ with a mole fraction $x_i$, the LXe-equivalent leak source can be obtained from the standard throughput relations [76]:

$$\mathcal{Q}_{\mathrm{leak},i}^{\mathrm{LXe}} = x_i\,\mathcal{L}_{\mathrm{in}}\frac{T_{\mathrm{LXe}}}{T_{\mathrm{meas}}}, \qquad \mathcal{L}_{\mathrm{in}} = 10\,V\dot{P} \simeq 10\,C_\ell \Delta P. \tag{3.63}$$

Here $\mathcal{L}_{\mathrm{in}}$ is the total incoming-gas throughput measured at $T_{\mathrm{meas}}$, $V\dot{P}$ is obtained from a rate-of-rise measurement, $C_\ell$ is the leak-path conductance, and $\Delta P$ is the pressure drop. The factor 10 converts $\mathrm{Pa\,m^3\,s^{-1}}$ to $\mathrm{mbar\,L\,s^{-1}}$.

For an atmospheric leak at 20 °C and 50% relative humidity, $x_{\mathrm{H_2O}} \simeq 1.15 \times 10^{-2}$ and $x_{\mathrm{O_2}} \simeq 0.21$. If the outside of the leak path is purged with nitrogen, the same equation applies using the impurity composition of the purge gas.

### 3.2.2 Total Outgassing Model

For one component and one impurity species, the full material source can be written as

$$\mathcal{Q}_{\mathrm{mat}}^{\mathrm{LXe}}(t) = \mathcal{Q}_{\mathrm{des}}^{\mathrm{LXe}}(t) + \mathcal{Q}_{\mathrm{diff}}^{\mathrm{LXe}}(t) + \mathcal{Q}_{\mathrm{perm}}^{\mathrm{LXe}}(t) + \mathcal{Q}_{\mathrm{vap}}^{\mathrm{LXe}}(t). \tag{3.64}$$

For the internal material budget, the practical model retains only the desorption and diffusion terms, since vaporization is negligible at LXe temperature and permeation is not expected to be a dominant impurity source in the detector configuration:

$$\boxed{\mathcal{Q}^{\mathrm{LXe}}_{\mathrm{mat}}(t) \simeq \mathcal{Q}^{\mathrm{LXe}}_{\mathrm{des}}(t) + \mathcal{Q}^{\mathrm{LXe}}_{\mathrm{diff}}(t).} \tag{3.65}$$

Interface leaks are added separately. The detector-level $O_2$-equivalent source is then

$$\mathcal{Q}^{\mathrm{LXe}}_{\mathrm{det,O_2eq}}(t) = \sum_{i,S} \frac{k_S}{k_{\mathrm{O_2}}} \mathcal{Q}^{\mathrm{LXe}}_{i,S}(t) + \sum_{\ell,S} \frac{k_S}{k_{\mathrm{O_2}}} \mathcal{Q}^{\mathrm{LXe}}_{\mathrm{leak},\ell,S}(t), \tag{3.66}$$

where $i$ indexes material components, $\ell$ indexes leak or interface sources, and $S$ indexes impurity species.

### Physics-Based Model

The physics-based model combines Fickian diffusion from the bulk with first-order desorption from the surface. For one component and one impurity species,

$$\boxed{\mathcal{Q}^{\mathrm{LXe}}_{\mathrm{phys}}(t) = \frac{A R_{\mathrm{PV}} T_{\mathrm{LXe}}}{N_A} \left[ c_0 F_D(t; T_m) + \sum_m C_{0,m} k_m(T_m) \exp[-k_m(T_m) t] \right].} \tag{3.67}$$

The first term is diffusion and the second is desorption. The diffusion factor is given by Eq. (3.58), with the diffusion coefficient evaluated at the material temperature, $D = D(T_m)$. The temperature dependences of $D(T_m)$ and $k_m(T_m)$ are given by Eqs. (3.55) and (3.51), respectively.

This model is useful when material-specific diffusion and desorption parameters are available. For bake-out or cooldown histories, $T_m$ can be evaluated as a function of time. Its main limitation is that $c_0$, $D(T_m)$, $C_{0,m}$, and $E_{\mathrm{des},m}$ are strongly material- and history-dependent.

### Empirical Pump-Down Model

The empirical model uses measured pump-down behavior for desorption and a three-regime description for diffusion-limited polymer outgassing. For one component and one impurity species,

$$\boxed{\mathcal{Q}^{\mathrm{LXe}}_{\mathrm{emp}}(t) = A \left[ \frac{R_{\mathrm{PV}} T_{\mathrm{LXe}}}{N_A} c_0 F_D^{\mathrm{emp}}(t; T_m) + q_0^{\mathrm{LXe}} \left( \frac{t_0}{t} \right)^{\alpha} \right], \qquad t \geq t_0.} \tag{3.68}$$

The first term is diffusion and the second is empirical desorption. The diffusion factor is given by Eq. (3.62), with the diffusion coefficient evaluated at the material temperature, $D = D(T_m)$, and therefore $\tau_D = d^2/[\pi^2 D(T_m)]$.

In practice, Eq. (3.68) can be fitted to outgassing data, or reduced to a single term when one process dominates. Metal samples are often described by the desorption

power law, while polymer samples can be dominated by diffusion. If $q_0$ and $\alpha$ are extracted from a total polymer outgassing measurement, the diffusion term should not be added again unless the surface and bulk contributions have been separated.

### Implementation and Validation

Table 3.6 summarizes the inputs needed for the two model families. At fixed temperature, the diffusion model requires $c_0$, $D(T_m)$, and geometry. Desorption requires either surface-population parameters for the physics-based model, or $q_0$ and $\alpha$ for the empirical model. Extrapolation from room temperature to LXe temperature requires temperature-dependent measurements.

| | | Model type | |
|---|---|---|---|
| Category | Input | Physics-based | Empirical |
| Geometry | $A, d$ | yes | yes |
| Temperature | $T_m$ | yes | yes |
| Diffusion | $c_0, D(T_m)$ | yes | yes |
| Desorption surface populations | $C_{0,m}, \tau_m(T_m)$ | yes | – |
| Desorption linear fit | $q_0, \alpha$ | – | yes |
| Temperature extrapolation | $D_0, E_D, \nu_0, E_{\mathrm{des},m}$ | yes | diffusion only |

Table 3.6: Inputs used by the physics-based and empirical outgassing models.

Figure 3.9 gives an illustrative comparison of the two model families.

The diffusion example uses water release from a Kapton slab with $d = 0.125\,\mathrm{mm}$ and $A = 200\,\mathrm{cm}^2$. The diffusion coefficient and initial moisture content are taken from the fitted average Kapton values reported by Sammartano et al. [77]. The stainless-steel example uses $A = 1.5\,\mathrm{m}^2$ and a water-desorption normalization chosen to place the curve in the same range as the Kapton examples. These normalizations are not material requirements; they are used only to compare the time dependence of the different model terms.

The physics-based and empirical desorption curves are close because a broad distribution of first-order surface time constants can reproduce an approximately $t^{-1}$ pump-down law. The diffusion curves agree through the initial and intermediate regimes, and differ mainly at long times when the finite Kapton reservoir is depleted in the exact slab solution. In the total source rate, this late-time difference is masked by the stainless-steel desorption component. The comparison shows that similar pump-down curves can arise from different mechanisms, so material type, geometry, and exposure history are needed to assign a measured source rate to desorption or diffusion.

The inputs $D(T_m)$, $k_m(T_m)$, $q_0$, and $\alpha$ can be measured on representative samples using RGA or rate-of-rise methods. The resulting model should then be checked, when possible, against liquid-xenon purity or electron-lifetime measurements.

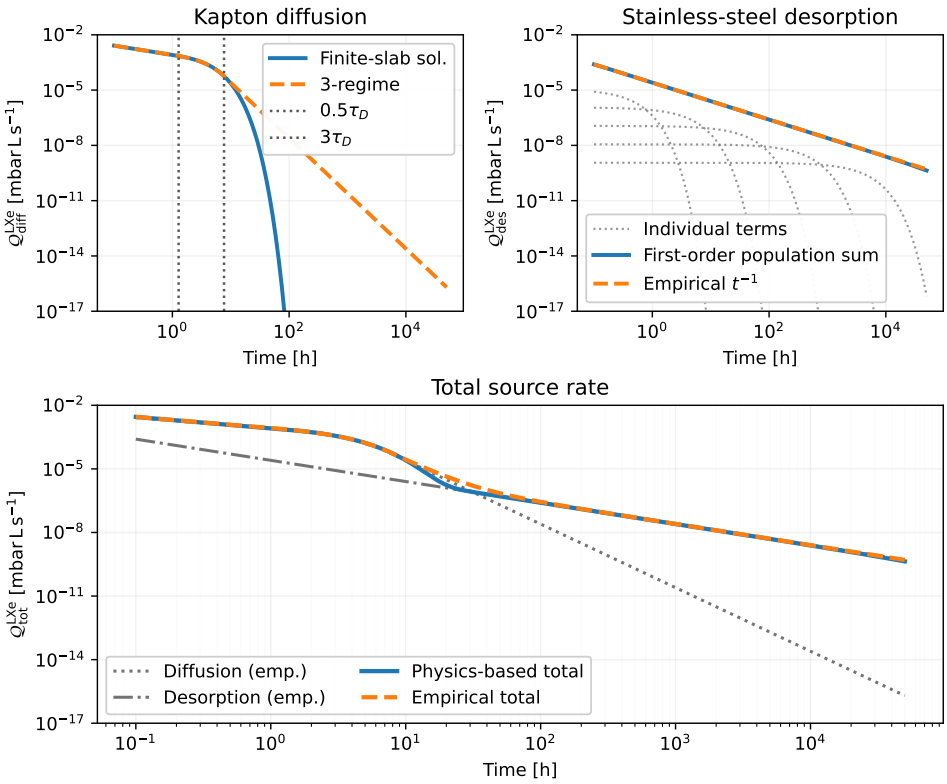


Figure 3.9: Illustrative comparison of Kapton diffusion and stainless-steel desorption source models, converted to LXe-equivalent pressure–volume throughput. The Kapton diffusion parameters are source-informed, while the normalizations are tuned to compare the model behavior.

**Other Impurity Sources** The models above describe impurity release from detector materials and interfaces, but they do not cover all possible electronegative contaminants. Additional sources can arise from the xenon supply and enrichment chain, and from chemical or process-induced residues introduced during fabrication, cleaning, storage, or filling. Enriched xenon can carry trace contaminants from isotope-separation equipment, including fluorinated lubricant residues or species such as $SF_6$, which would be important even at very low concentration because of their large electron-attachment rates [72]. These contaminants are expected to be reduced by dedicated xenon pre-purification and by recirculation through getters. No persistent electron-lifetime limitation from such species was observed in EXO-200.

## 3.3 Measurement Methods

The source terms in Sec. 3.2 must be constrained with measurements on representative detector materials. Vacuum measurements isolate a sample in a controlled chamber and identify the gas species released as a function of time and temperature. Liquid-xenon measurements instead observe the integrated effect of all impurity sources through the electron lifetime. The vacuum method is therefore best

suited to material screening and model-parameter extraction, while liquid-xenon tests provide the closest validation of the detector-relevant impurity budget.

### 3.3.1 Vacuum Chambers

Vacuum outgassing measurements place a material sample in a pumped chamber and record the gas load released by the sample. Several vacuum outgassing setups are operated within the nEXO collaboration. This section focuses on the Yale setup because it is the data set analyzed in this work. The measurements were performed by David Moore's group at Yale, and the analysis presented here was carried out in collaboration with that group.

A residual gas analyzer (RGA) separates the pressure into mass channels, while thermometers and heater controls define the material temperature. The measured quantity is a partial pressure. To compare with the source models of Sec. 3.2.2, the pressure is converted into a gas-specific throughput.

#### Yale outgassing setup

The functional layout of the Yale setup is shown in Fig. 3.10.

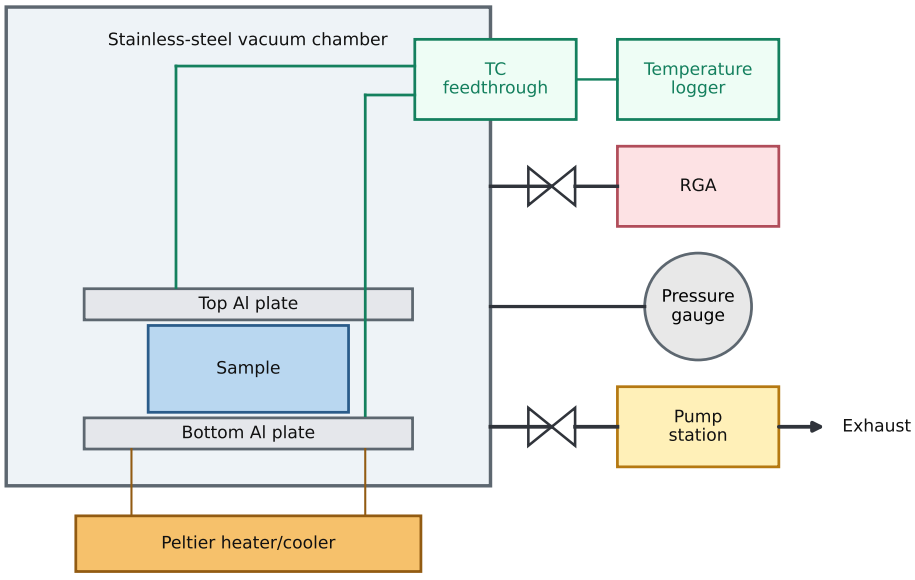


Figure 3.10: Functional schematic of the Yale vacuum outgassing setup used in this analysis, based on Ref. [72]. The drawing is not to scale.

The central element is a stainless-steel ConFlat chamber, approximately 20 cm in diameter and 12 cm high, connected to a turbomolecular pump through a valved pumping line. The empty chamber reaches a base pressure of order $5 \times 10^{-8}$ mbar. At the pressures considered here, the gas flow is assumed to be molecular. The conductance of the fixed pumping-line geometry is therefore taken to be pressure-independent during a measurement, but gas-dependent. Using the measured oxygen

conductance $C_{O_2} = 10\,\mathrm{L\,s^{-1}}$ [72] and the molecular-flow scaling $C_I \propto M_I^{-1/2}$ at fixed temperature [78], the adopted conductances are

$$C_{O_2} = 10\,\mathrm{L\,s^{-1}}, \qquad C_{H_2O} = C_{O_2}\sqrt{\frac{M_{O_2}}{M_{H_2O}}} \simeq 13.3\,\mathrm{L\,s^{-1}}. \tag{3.69}$$

A pressure gauge monitors the total chamber pressure, while a residual gas analyzer (RGA), connected through a separate valved side port, measures the mass-resolved gas composition.

The sample sits inside the vacuum volume between two polished aluminum plates. The plates are thermally coupled to a Peltier heater/cooler attached below the chamber. Two K-type thermocouples measure the sample temperature from the top and bottom sides and exit through a thermocouple feedthrough to a temperature logger. The analysis uses the mean of the two thermocouple readings as the sample temperature.

The usual procedure is to pump the chamber for about 12 h before heating, then increase the temperature in 10 °C steps up to about 50 °C, holding each step for a few hours. The RGA takes full scans from 0 to 100 amu about every 30 s. Other runs use linear temperature ramps. The data contain partial pressures for $H_2$, $H_2O$, $N_2$, $O_2$, and $CO_2$, together with the total pressure and the mean sample temperature.

For each selected RGA pressure channel, the gas load is computed from

$$\mathcal{Q}^{\mathrm{vac}}(t) = C_I\left[P^{\mathrm{sample}}(t) - P^{\mathrm{bg}}(t)\right], \qquad [\mathcal{Q}^{\mathrm{vac}}] = \mathrm{mbar\,L\,s^{-1}}, \tag{3.70}$$

where $C_I$ is the gas-specific pumping-line conductance and $P^{\mathrm{bg}}(t)$ is the blank-chamber partial pressure measured with the same temperature evolution as the sample run. The specific outgassing rate can be written as $q^{\mathrm{vac}}(t) = \mathcal{Q}^{\mathrm{vac}}(t)/A_s$, where $A_s$ is the exposed sample area. The geometry convention used here removes the bottom support-contact face from $A_s$.

### Samples and selected runs

The campaign tested several samples, including PTFE/Teflon, VESPEL, and MasterBond EP29LPSP epoxy. These sample geometries are shown in Fig. 3.11.

The PTFE/Teflon sample is not shown because it has the same disk geometry as the VESPEL sample, with the dimensions listed in Table 3.7.

| Material | Geometry | Diameter / side (cm) | Thickness (cm) | $A_s$ (cm$^2$) |
|---|---|---|---|---|
| PTFE | disk | $7.680 \pm 0.002$ | $2.032 \pm 0.002$ | $95.35 \pm 0.06$ |
| VESPEL | disk | $5.094 \pm 0.002$ | $1.272 \pm 0.002$ | $40.74 \pm 0.04$ |
| Epoxy | 8 slabs | $(2.522 \times 2.521) \pm 0.002$ | $0.207 \pm 0.002$ | $67.57 \pm 0.17$ |

Table 3.7: Sample geometry and exposed area used for the Yale fits.

The bottom support-contact face is removed from the exposed area because it rests on the lower aluminum plate. The upper aluminum thermal-contact piece only

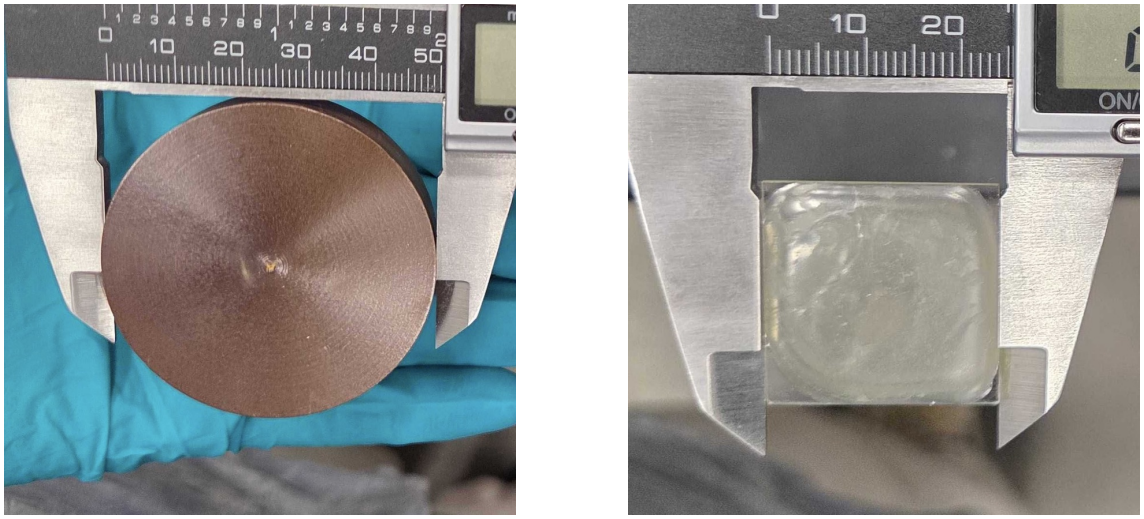

**(a)** VESPEL disk **(b)** MasterBond epoxy slab

Figure 3.11: Photographs of two Yale outgassing samples. The PTFE sample has the same disk geometry as the VESPEL sample, with a larger diameter and thickness.

partly covers the top sample face, and is therefore not removed from the exposed sample area.

These materials were selected because they are representative of polymeric or adhesive components considered for xenon-contact regions of nEXO. PTFE was tested as a reference fluoropolymer, since it has been commonly used in LXe detectors for reflective surfaces, although the current nEXO design minimizes the amount of plastic in contact with the LXe. VESPEL was tested as a candidate for small insulating or field-cage spacer parts. MasterBond EP29LPSP was tested as a low-outgassing epoxy candidate for encapsulation of charge-readout cables and support assemblies [46].

The runs shown in this section are representative of the measurements performed for each material. Multiple runs were taken to compare results and test different temperature profiles, including stepwise heating and temperature ramps.

### Fit definitions

Polymer outgassing is expected to be dominated by diffusion from the bulk. The data are therefore fit first with diffusion models, while a desorption component can be added if diffusion alone does not describe the pressure trend well. Two diffusion descriptions are used: the finite-slab solution from the physics-based model and the three-regime approximation from the empirical model. For one pressure channel, the fitted diffusion contribution is written generically as

$$\mathcal{Q}_{\mathrm{diff}}^{\mathrm{vac}}(t) = A_s c_0^{\mathrm{eff}} F_D^{\mathrm{ramp}}(t; T_m), \tag{3.71}$$

where $c_0^{\mathrm{eff}}$ is the fitted initial gas inventory density for the chosen diffusion model. The pressure compared with the RGA measurement is

$$P_{\mathrm{diff}}(t) = \frac{\mathcal{Q}_{\mathrm{diff}}^{\mathrm{vac}}(t)}{C_I}. \tag{3.72}$$

Each fit uses the same Arrhenius functional form, written relative to room temperature,

$$D(T_m) = D_{298} \exp\left[-\frac{E_D}{k_B}\left(\frac{1}{T_m} - \frac{1}{298.15\,\mathrm{K}}\right)\right], \tag{3.73}$$

which is equivalent to the Arrhenius form in Eq. (3.55), with the activation energy written per molecule in eV; this is why $k_B$ is used instead of $R_g$. Since the Yale measurements are not isothermal, the constant-temperature diffusion exposure $D(T_m)t$ is replaced by

$$\Lambda(t) = \Lambda_0 + \int_{t_{\mathrm{start}}}^{t} D[T_m(t')]\, dt'. \tag{3.74}$$

This is valid because $D$ varies only with the measured sample temperature. The integral accounts for the diffusion accumulated over the full temperature history, while $\Lambda_0$ accounts for the period before $t_{\mathrm{start}}$.

The parameters are fitted simultaneously with a least-squares regression. This is possible because they affect the pressure trace in different ways. The normalization parameters set the overall pressure scale, the diffusion or desorption rates control how fast the pressure changes with time, and the activation energies control how strongly the pressure responds to the temperature steps. These different time and temperature dependences allow the fit to separate the parameters reasonably well, although some correlations can remain. The degree of separation depends on the time range covered by each run. In particular, $c_0$ and $D_{298}$ remain strongly correlated when the measurements mainly cover the early diffusion regime, as discussed below.

**Physics-based diffusion.** For the physics-based fit, $F_D^{\mathrm{ramp}}$ is the finite-slab diffusion factor from Eq. (3.58), with the replacement $D(T_m)t \to \Lambda(t)$. The diffusion series is evaluated to numerical convergence. The reported physics-based parameters are $D_{298}$, $E_D$, and $c_0^{\mathrm{eff}}$.

**Empirical diffusion.** A second fit is performed as a cross-check using the diffusion part of the empirical pump-down model in Eq. (3.68). The same non-isothermal correction is used as for the physics-based fit. In the finite-slab model, the temperature history appears through the product $D(T_m)t$, which can be replaced directly by $\Lambda(t)$. In the empirical model, Eq. (3.62) is written in terms of $t$, $\tau_D$, and regime boundaries such as $t \leq 0.5\tau_D$. To keep that form, the elapsed time is replaced by the diffusion-equivalent time

$$t^{\mathrm{ramp}}(t) = \frac{\Lambda(t)}{D[T_m(t)]}. \tag{3.75}$$

The empirical diffusion factor used in the fit is therefore Eq. (3.62), evaluated with $D(T_m) \to D[T_m(t)]$, $t \to t^{\mathrm{ramp}}(t)$, and $\tau_D \to d^2/\{\pi^2 D[T_m(t)]\}$. The empirical fit parameters are $D_{298}$, $E_D$, $c_0^{\mathrm{eff}}$, and the initial-exposure offset, but they are used only as a cross-check of the pressure trend.

**Desorption addition.** If diffusion alone does not describe a pressure trace, the physics-based fit can add the first-order desorption term from Eq. (3.67). The general model allows a sum over reservoirs, but the fit uses one reservoir; its inventory $C_0$ and pressure-conversion factors are absorbed into $A_{\mathrm{des}}$. The time dependence is therefore fit as

$$P^{\mathrm{des}}(t) = A_{\mathrm{des}} k[T_m(t)] \exp\left[-\int_{t_{\mathrm{start}}}^{t} k[T_m(t')]\, dt'\right], \tag{3.76}$$

with

$$k(T_m) = k_{298} \exp\left[-\frac{E_{\mathrm{des}}}{k_B}\left(\frac{1}{T_m} - \frac{1}{298.15\,\mathrm{K}}\right)\right], \tag{3.77}$$

and $\tau_{\mathrm{des},298} = 1/k_{298}$. In the final fits this term is needed only for the PTFE $H_2O$ trace. The desorption parameters are $A_{\mathrm{des}}$, $k_{298}$, $E_{\mathrm{des}}$, and the derived time constant $\tau_{\mathrm{des},298}$. In the empirical comparison, desorption is treated instead with the power-law term $q_0(t_0/t)^{\alpha}$ from Eq. (3.68), with fitted parameters $q_0$ and $\alpha$.

### Results

The Yale pressure traces are fit with the diffusion models defined above, with a desorption term added only where diffusion alone does not describe the pressure evolution. The results shown here use a small set of runs selected because they have usable blank-chamber measurements with compatible temperature histories. Other Yale runs are still being analyzed, but require additional blank-chamber data following the same temperature trends before the same background subtraction can be applied.

The inputs listed in Table 3.6 can be used with the fitted values reported below: $D_{298}$ and $E_D$ define $D(T_m)$ through Eq. (3.73). The central values use the mean of the two thermocouple readings. The quoted uncertainties combine the fit uncertainties with the systematic uncertainty from temperature non-uniformity across the sample [72]. The latter is estimated by refitting the model using each thermocouple channel in turn and using the envelope of the resulting fit parameters as a systematic band; the two contributions are combined in quadrature. Additional systematic uncertainties associated with pumping-line conductance, species-dependent RGA sensitivity, and the reproducibility of the background subtraction are not included in the quoted uncertainties and should be addressed in a future analysis.

Figure 3.12 shows the representative pressure behavior. The PTFE $O_2$ channel illustrates the diffusion-only case also obtained for VESPEL and epoxy, while the PTFE $H_2O$ channel shows the case where desorption is needed.

The first 3 h of each run is excluded from the fits because the blank-chamber measurements show non-negligible early-time pressure variations, consistent with chamber-wall outgassing before the background stabilizes.

The step-like response of the pressure to the temperature evolution is reproduced by the diffusion model for $O_2$. For $H_2O$, the same temperature dependence is present, but diffusion alone misses part of the slow evolution of the trace. This motivates the first-order desorption component retained for PTFE water. The corresponding fit-quality metrics are summarized in Table 3.8.

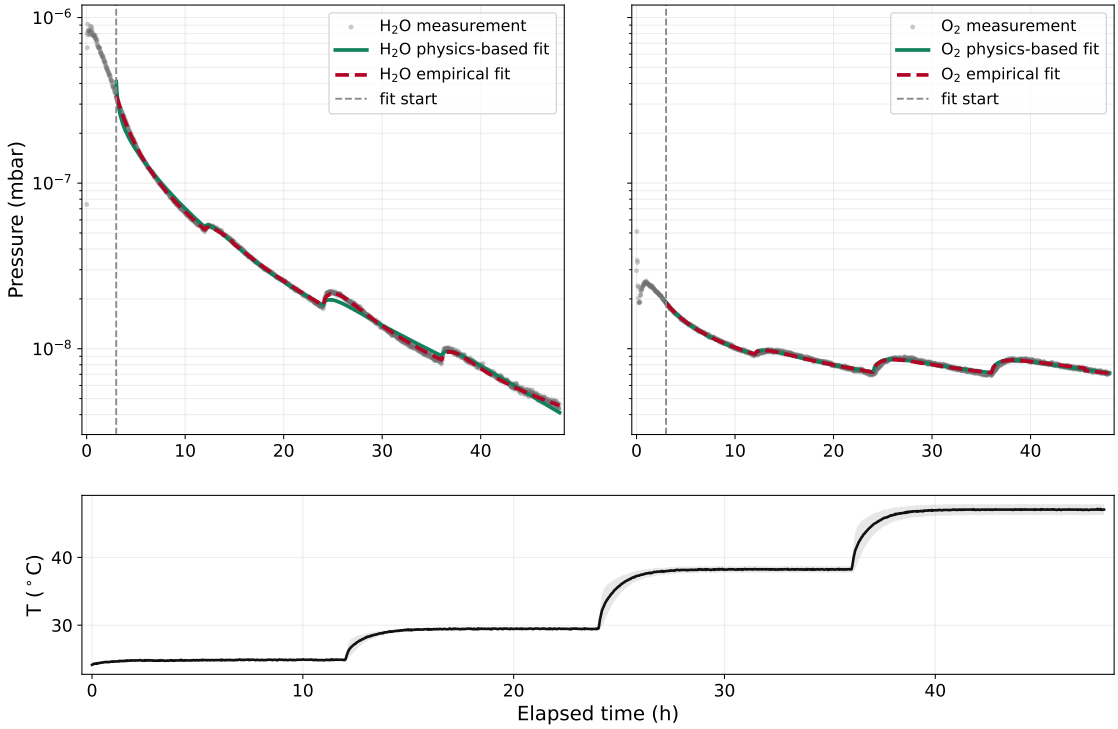


Figure 3.12: PTFE Yale outgassing fits. The $O_2$ channel is fit with diffusion only. The $H_2O$ channel requires the diffusion plus first-order desorption model.

| Material | Gas | Model | $R^2$ |
|---|---|---|---|
| PTFE | $H_2O$ | diffusion + desorption | 0.998 |
| | $O_2$ | diffusion | 0.990 |
| VESPEL | $H_2O$ | diffusion | 0.979 |
| | $O_2$ | diffusion | 0.930 |
| Epoxy | $H_2O$ | diffusion | 0.996 |
| | $O_2$ | diffusion | 0.762 |

Table 3.8: Model choice and fit quality for the selected Yale outgassing fits.

The fit-quality values are high for all channels except epoxy $O_2$, showing that the selected models generally reproduce the main time and temperature dependence of the measurements. Visually, the fitted curves also follow the pressure trends well. Diffusion alone describes all channels except PTFE $H_2O$, where the first-order desorption term is retained. The lower $R^2$ for epoxy $O_2$ comes mainly from the mid-temperature step, where the pressure evolution deviates slightly from the diffusion trend; the fitted curve nevertheless remains close to the data, with residuals smaller than the pressure uncertainty band. The PTFE $H_2O$ component decomposition is shown in Fig. 3.13.

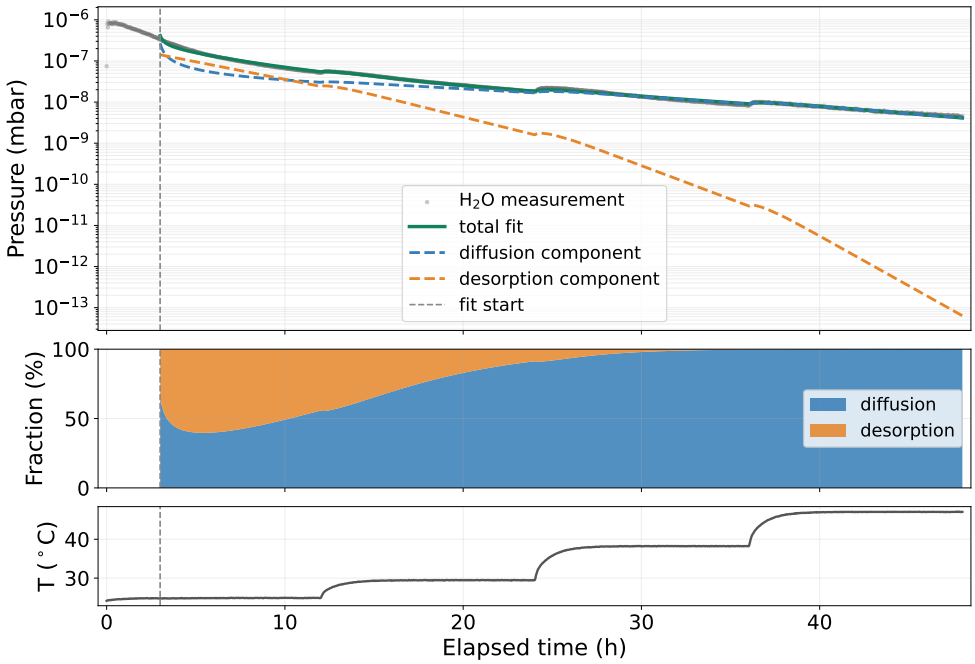


Figure 3.13: PTFE $H_2O$ fit components.

Figure 3.13 decomposes the fitted PTFE $H_2O$ pressure into the diffusion and desorption terms of the selected model. In this fit, desorption is most visible near the beginning of the fitted window, then rapidly decreases as the diffusion component becomes dominant through the later temperature steps. This early water contribution is plausibly related to sample preparation or storage, during which the PTFE could have adsorbed moisture before the measurement. This split depends on the applied fit model and should not be interpreted as a unique material fraction. The fitted diffusion variables are collected in Table 3.9.

Table 3.9 reports $c_0$ in pressure-equivalent vacuum units, rather than as a molecular density; this keeps the normalization tied to the measured RGA pressure and the gas-specific pumping-line conductance $C_I$.

The water fits give the clearest diffusion trends, while the VESPEL and epoxy $O_2$ fits give $D_{298}$ and $c_0$ with large uncertainties because the background-subtracted oxygen signal is small. Their $O_2$ activation energies are better constrained because the temperature dependence is still visible. Stronger oxygen signals, possibly from larger samples or higher temperatures, would improve the measurement precision.

| Material | Gas | $D_{298}$ [$\mathrm{cm^2\,s^{-1}}$] | $E_D$ [eV] | $c_0$ [$\mathrm{mbar\,L\,cm^{-3}}$] |
|---|---|---|---|---|
| PTFE | $H_2O$ | $\left(5.92^{+0.51}_{-0.27}\right) \times 10^{-6}$ | $0.175^{+0.021}_{-0.044}$ | $\left(5.65^{+0.36}_{-0.18}\right) \times 10^{-4}$ |
| | $O_2$ | $\left(1.13^{+0.10}_{-0.12}\right) \times 10^{-6}$ | $0.238^{+0.013}_{-0.015}$ | $\left(3.33^{+0.22}_{-0.14}\right) \times 10^{-4}$ |
| VESPEL | $H_2O$ | $1.54 \times 10^{-8} \pm 7.78 \times 10^{-4}$ † | $0.374^{+0.011}_{-0.014}$ | $0.532 \pm 1.34 \times 10^{4}$ † |
| | $O_2$ | $6.15 \times 10^{-9} \pm 5.99 \times 10^{-4}$ † | $0.421^{+0.013}_{-0.019}$ | $1.46 \times 10^{-3} \pm 71.3$ † |
| Epoxy | $H_2O$ | $6.98 \times 10^{-10} \pm 3.99 \times 10^{-5}$ † | $0.736^{+0.006}_{-0.006}$ | $0.633 \pm 1.81 \times 10^{4}$ † |
| | $O_2$ | $1.67 \times 10^{-9} \pm 3.03 \times 10^{-4}$ † | $0.441^{+0.010}_{-0.010}$ | $1.29 \times 10^{-3} \pm 117$ † |

Table 3.9: Final Yale outgassing fit results. Daggers mark early-regime fits with unresolved $c_0$–$D_{298}$ separation. Uncertainties combine local fit and thermocouple estimates; the large daggered uncertainties do not define reliable individual parameter ranges.

Compared with published values, the fitted PTFE $O_2$ and VESPEL $H_2O$ diffusion coefficients are within the same broad order of magnitude [79]. The fitted epoxy water value is lower than some generic epoxy moisture-diffusion values, which can still be plausible as water transport in epoxy depends strongly on cure, absorbed inventory, and sample history [80].

In both the VESPEL and epoxy runs, the $H_2O$ and $O_2$ measurements mainly cover the early diffusion regime, which constrains $c_0\sqrt{D_{298}}$ and leaves $c_0$ and $D_{298}$ strongly correlated. These four gas-specific fits are marked in Table 3.9. With controlled sample conditioning and known pump-down histories, $c_0$ and $D_{298}$ could be better separated by using thinner samples or longer measurements to capture the transition to finite-size depletion, or by independently measuring the gas inventory.

**Diffusion prefactor versus activation energy.** The room-temperature diffusion coefficient is convenient for quoting the Yale fits because the measurements are close to room temperature. However, outgassing predictions require the temperature dependence of the diffusion coefficient. The same fits are therefore rewritten in the conventional Arrhenius form by converting $D_{298}$ into

$$D_0 = D_{298} \exp\left(\frac{E_D}{k_B\, 298.15\,\mathrm{K}}\right). \tag{3.78}$$

This is the same diffusion law as Eq. (3.73), rewritten with the standard prefactor.

The $D_0$–$E_D$ plane is useful because polymer diffusion often follows a compensation trend: larger activation energies are paired with larger prefactors [81]. For simple gases, the comparison is made by grouping published values for $N_2$, $O_2$, $CO_2$, and $H_2$ by polymer class. PTFE is compared to semi-crystalline polymers, while VESPEL and epoxy are compared to glassy polymers. Water is shown separately because moisture diffusion depends more strongly on sample preparation and storage history, so it is compared with published moisture-diffusion values [80]. Only Yale points from runs with reliable background subtraction are overlaid here; additional points can be added when matching blank measurements are available. The

strong $c_0$–$D_{298}$ correlation in the daggered fits also affects the interpretation of $D_0$, calculated using Eq. (3.78); these points are distinguished by hollow markers.

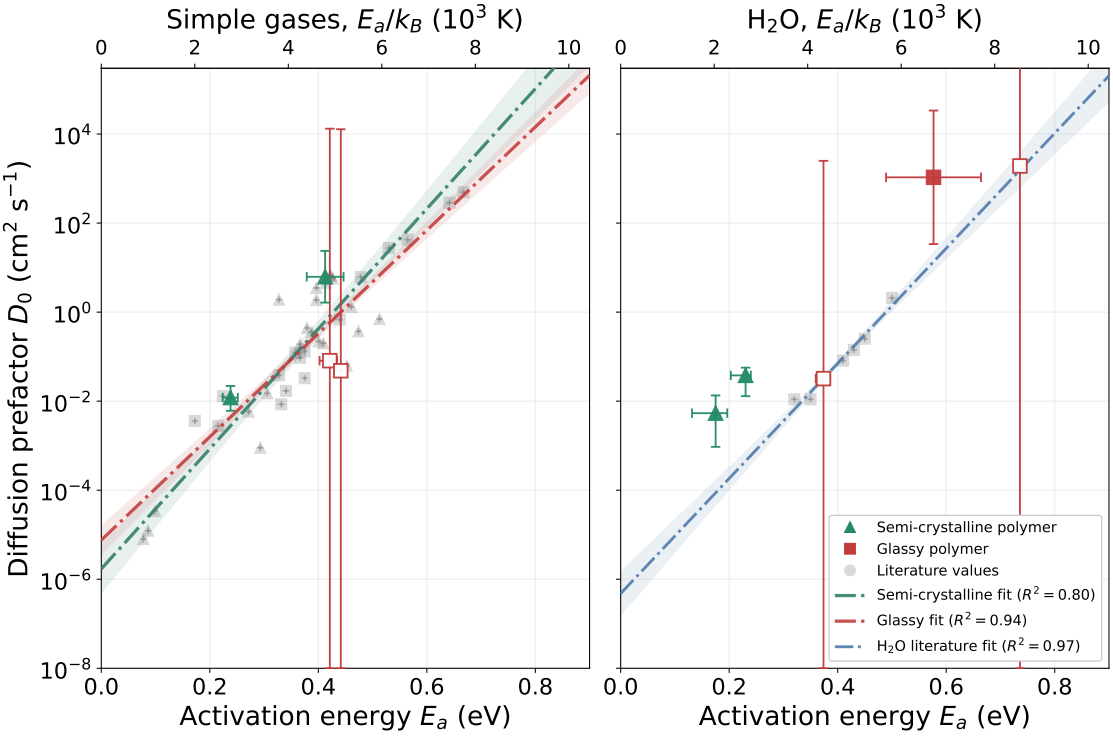


Figure 3.14: Diffusion prefactor $D_0$ versus activation energy for the Yale fits and literature data. Simple gases include $N_2$, $O_2$, $CO_2$, and $H_2$. Yale points are excluded from the literature fits. Hollow Yale markers identify the four fits marked with daggers in Table 3.9, where $c_0$ and $D_{298}$ are strongly correlated. The large $D_0$ uncertainties result from weakly constrained diffusion normalizations and the exponential dependence of $D_0$ on $E_D$.

The lines in Fig. 3.14 are least-squares fits to literature values only, allowing comparison with the values obtained from Yale data. With $X = (E_D/k_B)/(10^3\ \mathrm{K})$ and $D_0$ in $\mathrm{cm^2\,s^{-1}}$, the fitted relations are

$$\begin{aligned}
\log_{10} D_0 &= (1.162 \pm 0.130)\, X - (5.767 \pm 0.565), && \text{semi-crystalline, simple gases,}\\
\log_{10} D_0 &= (1.000 \pm 0.069)\, X - (5.121 \pm 0.337), && \text{glassy, simple gases,}\\
\log_{10} D_0 &= (1.114 \pm 0.105)\, X - (6.321 \pm 0.506), && \text{glassy, } H_2O.
\end{aligned} \tag{3.79}$$

The coefficient uncertainties are one-sigma standard errors from the fits.

The PTFE $O_2$ points lie slightly above the semi-crystalline fit but follow the same broad compensation trend as the literature values. For the daggered VESPEL and epoxy fits, both the $H_2O$ and $O_2$ points show large vertical uncertainties because their short-time pressure traces mainly constrain $c_0\sqrt{D_{298}}$. The small background-subtracted oxygen signals further reduce the precision of the $O_2$ fits, whose fitted values remain close to the glassy-polymer scale.

In the $H_2O$ panel, the daggered VESPEL and epoxy fit values lie close to the published moisture-diffusion epoxy trend and its extrapolation. The PTFE points and the additional VESPEL water point follow the same trend, although they are slightly above the literature line.

These comparisons support using the obtained fit equations as inputs for electronegative outgassing budgets. More values could improve confidence in these results and allow semi-crystalline and glassy polymer trends to be separated for $H_2O$.

### 3.3.2 Liquid Xenon Drift Chambers

Liquid-xenon drift chambers provide a complementary measurement to vacuum outgassing chambers. Vacuum measurements isolate a material sample, identify released gas species, and constrain diffusion or desorption parameters. Liquid-xenon measurements instead test the integrated detector-relevant effect: whether impurities released by a sample reduce the electron lifetime in LXe. They are therefore sensitive to effects that are difficult to isolate in vacuum, including impurity dissolution in liquid xenon, transport to the active region, sample preparation, cryogenic operation, and electron attachment in the detector medium.

Within the nEXO collaboration, liquid-xenon drift chambers or purity monitors are operated at SLAC, Stanford, and Yale. The Stanford purity monitor is used here as an example. It is designed to measure the electron lifetime in LXe while material samples are installed near the drift region [82].

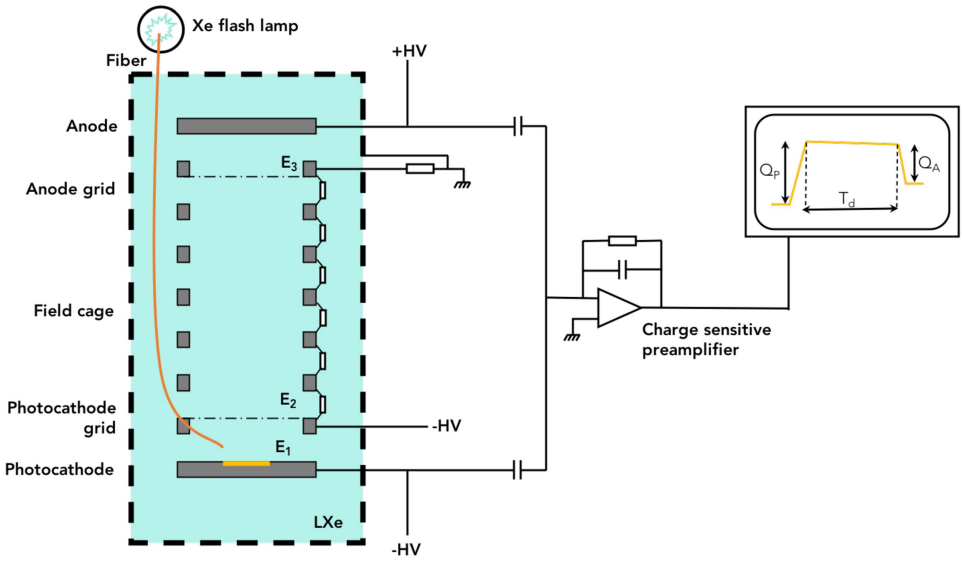


Figure 3.15: Schematic of the Stanford liquid-xenon purity monitor used to measure electron lifetime in LXe. Reproduced with permission from Marie Vidal.

Figure 3.15 shows the basic measurement principle. A xenon flash lamp sends ultraviolet light through a fiber onto a gold-coated photocathode, producing an

initial charge signal $Q_P$. The electrons then drift through liquid xenon over a known drift time $t_d$, and the surviving charge signal $Q_A$ is measured at the anode. Since $Q_P$ and $Q_A$ are proportional to the number of electrons before and after the drift region, Eq. (3.3) can be written as

$$\frac{Q_A}{Q_P} = \exp\left(-\frac{t_d}{\tau_e}\right). \tag{3.80}$$

Solving for $\tau_e$ gives the purity-monitor lifetime estimator,

$$\tau_e = -\frac{t_d}{\ln(Q_A/Q_P)}. \tag{3.81}$$

The drift time is set by the drift length and field-dependent drift velocity, as in Eq. (3.11). If several electronegative species contribute, their attachment rates add according to Eq. (3.5).

The Stanford purity monitor has a 12 cm central drift region, with field rings used to keep the drift field uniform up to about $400\,\mathrm{V\,cm^{-1}}$ [82]. The photocathode and anode are separated from the central drift region by two Frisch grids (a wire grid placed in front of an electrode to reduce the signal induced by electrons while they are still far from that electrode). Material samples can be installed in holders outside the field cage to test their electronegative out-diffusion into LXe.

These measurements do not replace vacuum outgassing tests. They usually do not identify which species causes the lifetime degradation, and the result depends on the full xenon-handling and purification history. The outgassing models developed here can help interpret the observed electron lifetimes by connecting them to RGA scans taken during pump-down before the cells are filled with xenon. Their strength is that they directly test the detector-relevant observable, $\tau_e$, in liquid xenon.

## 3.4 Mitigation Techniques

The goal of mitigation is to make xenon-contact materials contribute as little as possible to the detector-level source defined in Eq. (3.66). In practice, this means choosing materials with small impurity reservoirs, reducing unnecessary exposed material, removing surface contamination before installation, and keeping parts clean during assembly.

### 3.4.1 Material Choice and Geometry

#### Material choice

Material selection is the first handle for controlling outgassing. Metals, ceramics, and glasses are generally preferred over polymers, elastomers, oils, and greases, since they usually have lower outgassing rates [83]. Polymers and adhesives are still needed for insulation, cables, feedthroughs, or mechanical support, but their use should remain limited to cases where no simpler low-outgassing material can provide the same function. This approach is already part of the nEXO design. The detector

minimizes the amount of these materials in contact with xenon and accounts for their contribution in the impurity budget.

#### Geometry

Geometry also affects outgassing by setting the exposed surface area and the volume that can store impurities. The main quantities to reduce are:

- surface area in contact with xenon;
- polymer and adhesive thickness;
- closed holes and trapped pockets;

This is especially important for diffusion-limited sources: thinner polymer parts are easier to degas and contain less impurity. Enclosed regions should be avoided when possible. A typical example is a screw tightened into a hole that does not go through the part, leaving a small trapped volume behind it. If such features are unavoidable, they should include a clear vent path so that trapped gas can be removed during pump-down.

### 3.4.2 Cleaning and Preparation Techniques

Before installation, components can be cleaned, pumped, and baked to reduce the impurities they release in xenon. These steps act on different parts of the outgassing model in Sec. 3.2. Cleaning mainly removes residues left on the surface by machining, handling, and air exposure. Vacuum pump-down removes free gas and weakly adsorbed molecules. Bake-out, when compatible with the component, accelerates desorption and can also reduce the bulk reservoir in thin materials.

The following subsections describe the main preparation steps used to reduce these contributions before detector assembly.

#### Metal surface finishing

For metal parts, the surface finish can affect how much contamination remains after cleaning. A rough surface has more sites where water, dust, or machining residues can stay attached. Mechanical polishing smooths the surface by abrasion, while electropolishing removes a thin surface layer with an electrochemical process, leaving a smoother and cleaner metal surface [83].

#### Vacuum pump-down

Vacuum pump-down removes gas and weakly adsorbed molecules after cleaning. It is especially useful with RGA monitoring, since it shows whether water, oxygen, or solvent residues are still being released from the sample.

Pumping alone is not enough for thick polymers or epoxies. In these materials, impurities can remain trapped in the bulk and must first diffuse to the surface before

they can be removed. The diffusion term in Eqs. (3.67) and (3.68) can therefore remain relevant for a long time even under vacuum.

#### Bake-out

Bake-out is the strongest preparation step when the component can tolerate it. Heating accelerates desorption and diffusion through the temperature dependence in Eq. (3.55), so it can reduce both surface contamination and bulk impurity reservoirs before xenon exposure.

The bake method must be chosen component by component. Bare metal parts can usually tolerate higher temperatures than cables, epoxies, feedthroughs, sensors, or electronics. For sensitive assemblies, a lower-temperature vacuum bake for a longer time is usually safer than a high temperature bake that could damage materials.

### 3.4.3 Storage After Cleaning

After cleaning, pump-down, or bake-out, parts should not be left exposed to air. They should be handled with low-residue gloves and clean tools, then kept in clean, sealed containers under dry nitrogen to limit the re-adsorption of atmospheric water before installation. The container and purge line must also be clean and dry; otherwise storage itself can become a source of contamination.

Ideally, the measured sample should be in the same physical and chemical state as the component as installed. If a part is cleaned, baked, stored, or handled differently between the outgassing measurement and detector installation, the fitted parameters in Eqs. (3.67) and (3.68) may no longer accurately describe the installed component's outgassing behavior. This traceability information should be documented for each xenon-contact component in the impurity budget.

# Chapter 4

# Background Mitigation with Cryogenic Shields

## Contents


**4.1 Background Model . . . . . 82**
4.1.1 Internal Background Sources . . . . . 82
4.1.2 Background Calculation Method . . . . . 84
4.1.3 Reference Background Budget . . . . . 88
**4.2 Cryogenic Fluorinated Liquid Shield (HFE) . . . . . 90**
4.2.1 HFE Properties, Radiopurity, and Shielding Role . . . . . 90
4.2.2 Ultra-Radiopure Nickel Cryostat . . . . . 92
**4.3 Internal Backgrounds vs. HFE Thickness . . . . . 95**
4.3.1 HFE . . . . . 96
4.3.2 Cryostat Vessels . . . . . 100
4.3.3 Water Shield . . . . . 103
4.3.4 Other Components . . . . . 107
4.3.5 Updated Background Budget . . . . . 112
**4.4 Possible Design Optimizations . . . . . 114**
4.4.1 Reduced HFE Configuration . . . . . 114
4.4.2 Improved Water Shielding with a Smaller Outer Vessel . . 121
4.4.3 Cylindrical Cryostat . . . . . 123

The earlier cryostat design used carbon-fiber-composite shells with titanium liners because sufficiently radiopure composite materials were available and the vessels could be fabricated underground [46]. However, manufacturing these large composite vessels would have been challenging, and subsequent radiopurity studies showed that their residual contamination could still make a significant contribution to the background budget. More recently, ultra-radiopure nickel was identified as a promising alternative for the cryostat vessels [84], with a substantially lower expected background contribution.

Because the cryostat is now much cleaner, the baseline HFE shielding requirement can be reassessed. Reducing the HFE inventory could lower the overall cost and detector size, simplifying construction, but would also weaken the attenuation of nearby and external radioactive sources. This chapter introduces the background model and uncertainty treatment used to quantify this trade-off, then examines the shielding role of the HFE volume and the background contribution of the nickel cryostats. The dependence of the main detector background contributions on HFE thickness is evaluated to determine how far the cryogenic shielding configuration can be reduced without significantly degrading the background level or $0\nu\beta\beta$ sensitivity.

## 4.1 Background Model

The detector background model includes intrinsic and distributed sources such as $2\nu\beta\beta$, radon activity in xenon, activation products, solar-neutrino scatters, and residual cosmogenic contributions, introduced in Chapter 2. The present chapter focuses on radiogenic backgrounds from detector materials and surrounding structures, since these depend directly on material choice, cryostat design, and shielding geometry. The corresponding model is used here to quantify these contributions, construct a reference background budget, and compare alternative shielding configurations.

### 4.1.1 Internal Background Sources

Internal background sources include both bulk contamination in solid detector components and mobile radioactive species transported into internal fluid volumes, in contrast to environmental backgrounds originating outside the detector. The dominant source terms are the $^{238}$U and $^{232}$Th decay chains, together with $^{40}$K and $^{60}$Co in solid materials, and $^{222}$Rn and $^{42}$Ar/$^{42}$K in internal fluids [47]. Their background contribution is set by the contaminant inventory, half-life, and emitted radiation. The activity and specific activity are given by

$$A = \lambda N = \frac{\ln 2}{T_{1/2}} N, \qquad a = \frac{A}{m} = \frac{\ln 2}{T_{1/2}} \frac{cN_A}{M}, \tag{4.1}$$

where $N$ is the number of radioactive nuclei, $m$ is the sample mass, $c$ is the isotope mass concentration in kg/kg, $N_A$ is the Avogadro constant, and $M$ is the isotope molar mass in kg/mol. With $T_{1/2}$ in seconds, $a$ is expressed in Bq/kg. In particular,

$1\,\mathrm{fg/g} = 10^{-15}\,\mathrm{kg/kg}$. The resulting specific activities are used below to calculate expected background rates.

For the long-lived U and Th chains, the relevant MeV $\gamma$ rays are emitted mainly by daughter isotopes, whereas radiopurity inputs are often expressed in terms of the parents. Inferring daughter activities from parent concentrations assumes secular equilibrium: the parent half-life must greatly exceed those of the relevant daughters, sufficient time must have elapsed for daughter ingrowth, and the chain must remain closed to selective removal or addition of its members. Along an unbranched decay sequence, daughter production then balances decay, giving

$$A_{\mathrm{parent}} \simeq A_{\mathrm{daughter}}. \tag{4.2}$$

Branching fractions are included in the parent-normalized hit efficiencies defined below.

Material processing or purification can temporarily or persistently alter these activity ratios. The time required to restore equilibrium depends on the sub-chain considered. For example, following radon removal, $^{226}$Ra and its short-lived progeny through $^{214}$Bi approach equilibrium within about 38 d, corresponding to ten $^{222}$Rn half-lives, provided radium remains present and radon and its progeny are retained [85]. This short timescale does not apply to equilibrium between $^{238}$U and $^{226}$Ra, which involves much longer-lived intermediate isotopes.

Table 4.1 highlights the source categories most relevant to the reconstructed MeV-scale spectrum.

| Source | State | Half-life | Relevant $\gamma$-ray(s) [keV] | BR [%] |
|---|---|---|---|---|
| $^{232}$Th ($^{208}$Tl) | solid | $1.40 \times 10^{10}$ yr | 2615 | 99.75 |
| $^{238}$U ($^{214}$Bi) | solid | $4.47 \times 10^{9}$ yr | 1764, 2204, 2448 | 15.4, 4.9, 1.5 |
| $^{222}$Rn ($^{214}$Bi) | gas | 3.82 d | 1764, 2204, 2448 | 15.4, 4.9, 1.5 |
| $^{40}$K | solid | $1.25 \times 10^{9}$ yr | 1461 | 10.55 |
| $^{42}$Ar ($^{42}$K) | gas | 32.9 yr | 1525 | 18.1 |

Table 4.1: Internal radioactive source categories considered in this chapter and the isotopes most relevant to the reconstructed energy spectrum [47].

This is especially relevant in the $0\nu\beta\beta$ region of interest around $Q_{\beta\beta} = 2458\,\mathrm{keV}$:

- $^{208}$Tl is the dominant natural $\gamma$-ray source because its 2615 keV line lies above $Q_{\beta\beta}$ and can therefore populate the ROI through Compton scattering and partial energy deposition. This behavior is illustrated in Fig. 2.12, whose right panel shows the $^{232}$Th contribution extending across the ROI.
- $^{214}$Bi is also important since its highest-intensity lines extend up to 2448 keV, just below $Q_{\beta\beta}$. Although no single main line exceeds the ROI energy, these emissions populate the spectrum up to its lower edge and can leak into the ROI through the finite energy resolution or through decays in which several emitted

$\gamma$ rays deposit energy in the detector. This is likewise visible in Fig. 2.12, where the $^{238}$U contribution reaches the ROI region.

- $^{222}$Rn is treated separately from $^{238}$U because, as a gas, it can emanate from solids, migrate through gas spaces, and dissolve into xenon or HFE. Its daughters, including $^{214}$Bi, may then decay in fluid volumes or on internal surfaces rather than at the site of the original bulk contamination.
- $^{40}$K and $^{42}$Ar/$^{42}$K are more relevant to the broader MeV-scale spectrum than to the final ROI budget. $^{40}$K contributes mainly below the ROI through its 1461 keV line, while $^{42}$Ar/$^{42}$K is retained because noble contaminants can be transported into internal fluid volumes and decay closer to the sensitive region.

Other isotopes are neglected because their contribution to the present study is expected to be negligible, due to low activity, short half-life, insufficiently penetrating radiation, or negligible inventory in the subsystems considered. In particular, $^{210}$Po is not included as a direct internal $\gamma$-ray background source, since its main relevance is indirect, through $\alpha$-induced neutron production after deposition of radon daughters on material surfaces [46].

The relevant subsystems are those whose mass, proximity, or fluid coupling make them non-negligible internal sources: the TPC vessel and nearby detector hardware, the cryostat vessels, the HFE volume, xenon and gas-phase regions, and selected support or service components close to the cryostat. Their relative importance is set by both activity and geometry. Components close to the active xenon can contribute despite modest mass, while more distant structures contribute only if their larger inventory compensates for attenuation in the intervening xenon, HFE, vessel walls, or water. The internal background budget can therefore be written as

$$B_{\text{int}} = \sum_c B_c, \tag{4.3}$$

where $B_c$ is the contribution of component $c$. This component-level decomposition is used in the following sections to identify the dominant terms and to evaluate their dependence on shielding thickness and cryostat geometry [47].

### 4.1.2 Background Calculation Method

For a detector component $i$ and isotope or decay-chain parent $j$, the background contribution is determined from three inputs: the component mass $m_i$ [kg], the specific activity $a_{ij}$ [Bq kg$^{-1}$], and the parent-normalized hit efficiency $\varepsilon_{ij}$, defined as the expected number of events reconstructed in the ROI and within the inner 2 t fiducial xenon mass per parent decay.

The nominal background contribution is then

$$B_{ij} = m_i \, a_{ij} \, \varepsilon_{ij}, \tag{4.4}$$

where $\varepsilon_{ij}$ has units of cts/(FWHM $\cdot$ 2 t), corresponding to the expected number of counts per parent decay within one FWHM around $Q_{\beta\beta}$ in the central 2 tonne

xenon mass. This inner-2 tonne rate provides a common reference for comparing background contributions; the full multiparameter sensitivity analysis is described in Sec. 2.5.4. The quantity $B_{ij}$ therefore has units of cts/(FWHM $\cdot$ 2 t $\cdot$ s), and the corresponding annual contribution is

$$B_{ij}^{\mathrm{yr}} = S_{\mathrm{yr}}\, m_i\, a_{ij}\, \varepsilon_{ij}, \qquad S_{\mathrm{yr}} = 365.25 \times 24 \times 3600, \tag{4.5}$$

with units of cts/(FWHM $\cdot$ 2 t $\cdot$ yr).

The activity inputs $a_{ij}$ are taken from dedicated radiopurity assays of materials, fluids, and selected assemblies, including HPGe $\gamma$-ray spectrometry, mass spectrometry, neutron activation analysis, and radon emanation measurements where relevant [47]. ICP-MS measures isotope concentrations, commonly those of $^{238}$U and $^{232}$Th, whereas HPGe spectrometry measures $\gamma$-emitting progeny and constrains the corresponding sub-chain activities. Where both measurements are available, comparing parent and daughter activities also provides a check of secular equilibrium [86].

Following the nEXO background model, secular equilibrium is assumed for bulk U/Th contamination in HFE and solid components, relating parent activities to those of $^{214}$Bi and $^{208}$Tl with the branching correction defined below. This approach is supported by EXO-200, where assay-based background predictions were broadly consistent with data [47]. Radon and additional $^{210}$Po contributions are treated separately. Each adopted assay result is converted to a specific activity $a_{ij}$ and an associated uncertainty $\sigma_{a_{ij}}$.

The hit efficiencies are obtained from detector Monte Carlo simulations in the full geometry of the configuration under study. Figure 4.1 shows a Geant4 rendering of the simulated detector configuration used to propagate radioactive decays through the cryostat, shielding volumes, and central TPC region.



Figure 4.1: Geant4 rendering of the detector geometry showing the nested cryostat and shielding volumes together with the central TPC region.

The hit-efficiency calculation is then summarized schematically in Fig. 4.2: decays are generated in the selected source component, transported through the detec-

tor geometry, converted into detector observables, and passed through reconstruction and analysis selections.

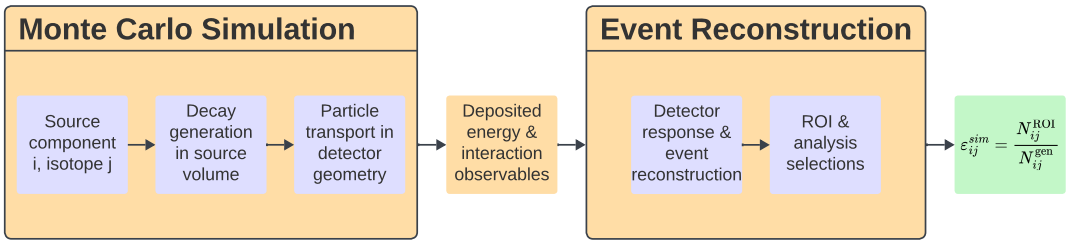


Figure 4.2: Schematic illustration of the simulation and reconstruction chain used to derive the hit efficiency for each component–isotope pair.

For each component–isotope pair $(i, j)$, a set of decays of the simulated isotope is generated in the corresponding source volume and propagated through the detector geometry shown in Fig. 4.1. After detector response, event reconstruction, fiducial selection to the inner 2 t of xenon, and the full set of analysis selections defining the $0\nu\beta\beta$ search region, the simulated-isotope hit efficiency is defined as

$$\varepsilon_{ij}^{\mathrm{sim}} = \frac{N_{ij}^{\mathrm{ROI}}}{N_{ij}^{\mathrm{gen}}}, \tag{4.6}$$

where $N_{ij}^{\mathrm{gen}}$ and $N_{ij}^{\mathrm{ROI}}$ denote, respectively, the number of generated decays and the number of reconstructed events surviving all selections.

Because the dominant $\gamma$-ray background in the ROI is generally produced by specific late-chain daughters, the Monte Carlo is performed for these isotopes rather than for the full parent decay chain. In the present study, the simulated daughters are $^{208}$Tl for the $^{232}$Th chain and $^{214}$Bi for the $^{238}$U chain. The efficiency entering the background budget is therefore normalized back to the parent activity. If $b_{ij}$ denotes the branching factor relating parent isotope $j$ to the simulated daughter contribution used in the model, the parent-normalized hit efficiency is

$$\varepsilon_{ij} = b_{ij}\, \varepsilon_{ij}^{\mathrm{sim}}. \tag{4.7}$$

For the $^{232}$Th chain, this normalization includes the branching fraction $b_{\mathrm{Th}} = 0.3594$, corresponding to the 35.94 % $\alpha$-decay branch of $^{212}$Bi that produces $^{208}$Tl. For the $^{238}$U chain, $^{214}$Bi is reached without a significant competing branch, so $b_{\mathrm{U}} \simeq 1$ [85]. Unless stated otherwise in this chapter, the parent-normalized hit efficiencies used in the calculations are listed in Appendix C.1.1 and Appendix C.1.2.

A complete background budget also requires an uncertainty for each line, arising from both the assay input and the finite Monte Carlo statistics used to determine the efficiency. The quantities $B_{ij}$ and $\sigma_{ij}$ are first obtained within the usual Gaussian approximation. Treating the assay and Monte Carlo statistical contributions as independent, the one-$\sigma$ uncertainty on the line $(i, j)$ follows from linear propagation of Eq. (4.4),

$$\sigma_{ij} = \sqrt{\left(m_i\, \varepsilon_{ij}\, \sigma_{a_{ij}}\right)^2 + \left(m_i\, a_{ij}\, \sigma_{\varepsilon_{ij}}\right)^2}. \tag{4.8}$$

The calculation of $\sigma_{\varepsilon_{ij}}$ from binomial counting statistics is summarized in Appendix A.1.

At this stage, each budget line is described by a Gaussian central value $B_{ij}$ and standard deviation $\sigma_{ij}$. A naive Gaussian model,

$$X_{ij} \sim \mathcal{N}\left(\mu_{ij}, \sigma_{ij}^2\right), \qquad \mu_{ij} = B_{ij}, \tag{4.9}$$

would, however, assign nonzero probability to negative background rates. Since negative rates are unphysical, the distribution is instead truncated at zero, so that only $X_{ij} \geq 0$ is retained.

It is convenient to express the truncation in terms of the dimensionless variable

$$z_{ij} = \frac{\mu_{ij}}{\sigma_{ij}}, \tag{4.10}$$

which measures how many standard deviations the nominal rate lies above the physical boundary at zero. Introducing the standard normal probability density and cumulative distribution functions,

$$\phi(z) = \frac{1}{\sqrt{2\pi}}\, e^{-z^2/2}, \qquad \Phi(z) = \int_{-\infty}^{z} \phi(u)\, du, \tag{4.11}$$

and the Mills ratio

$$\lambda(z) = \frac{\phi(z)}{\Phi(z)}, \tag{4.12}$$

the mean and variance of the truncated variable $X_{ij} \mid X_{ij} \geq 0$ can be written analytically. Additional properties of these functions are shown in Appendix A.2, and the derivation of the truncated moments is given in Appendix A.3. The variance expression follows the standard result for a lower-truncated normal distribution [87].

The mean of the truncated Gaussian is

$$\mathbb{E}[X_{ij} \mid X_{ij} \geq 0] = \mu_{ij} + \sigma_{ij}\, \lambda(z_{ij}), \tag{4.13}$$

and its variance is

$$\mathrm{Var}(X_{ij} \mid X_{ij} \geq 0) = \sigma_{ij}^2 \left[1 - z_{ij}\lambda(z_{ij}) - \lambda^2(z_{ij})\right]. \tag{4.14}$$

The corresponding truncated-Gaussian spread, denoted TG-spread in the following, is the standard deviation of the truncated distribution,

$$u_{ij}^{\mathrm{TG}} = \sigma_{ij}\sqrt{1 - z_{ij}\lambda(z_{ij}) - \lambda^2(z_{ij})}. \tag{4.15}$$

This prescription shifts the mean upward relative to the naive Gaussian when the zero boundary removes a non-negligible fraction of the distribution, and simultaneously reduces the uncertainty. In the limit $z_{ij} \gg 1$, the truncation becomes negligible and the usual Gaussian expressions are recovered.

Each component–isotope line is therefore represented by the truncated-Gaussian expectation value and TG-spread of its annual background contribution. Using the conversion factor $S_{\mathrm{yr}}$, these are defined as

$$\overline{B}_{ij}^{\mathrm{yr}} = S_{\mathrm{yr}}\, \mathbb{E}[X_{ij} \mid X_{ij} \geq 0], \tag{4.16}$$

and

$$u_{ij}^{\mathrm{yr}} = S_{\mathrm{yr}}\, u_{ij}^{\mathrm{TG}}, \tag{4.17}$$

both expressed in cts/(FWHM · 2 t · yr). An equivalent form of these expressions, written in terms of exp and erf and convenient for numerical implementation, is given in Appendix A.4.

These quantities constitute the basic entries of the internal background budget discussed in Sec. 4.1.3.

For the component-scan plots shown later in this chapter, the shaded bands indicate the $1\sigma$ uncertainty on the fitted attenuation curve. In the simplest case used here, the background evolution with shielding thickness is modeled as an exponential,

$$f(x) = A\, e^{-\mu x}, \tag{4.18}$$

where $x$ is the scanned geometry variable, $A$ is a normalization constant, and $\mu$ is the effective attenuation coefficient extracted from the fit. The fit returns the best-fit values $\hat{A}$ and $\hat{\mu}$, together with their covariance matrix

$$C = \begin{pmatrix} C_{AA} & C_{A\mu} \\ C_{A\mu} & C_{\mu\mu} \end{pmatrix}, \tag{4.19}$$

which encodes both the variance of each parameter and their correlation.

The uncertainty on the fitted curve at each value of $x$ is then obtained by propagating the uncertainties on $A$ and $\mu$,

$$\sigma_f^2(x) \simeq \mathbf{J}(x)\, C\, \mathbf{J}^{\mathsf{T}}(x), \tag{4.20}$$

where $\mathbf{J}(x)$ is the vector of derivatives of the fitted curve with respect to the fit parameters,

$$\mathbf{J}(x) = \left( \frac{\partial f}{\partial A}, \frac{\partial f}{\partial \mu} \right)_{\hat{A},\hat{\mu}} = \left( e^{-\mu x},\ -Axe^{-\mu x} \right)_{\hat{A},\hat{\mu}}. \tag{4.21}$$

This gives

$$\sigma_f^2(x) = C_{AA}e^{-2\mu x} - 2C_{A\mu}Axe^{-2\mu x} + C_{\mu\mu}A^2x^2e^{-2\mu x}. \tag{4.22}$$

The upper and lower edges of the plotted $1\sigma$ band are then defined as

$$f_{\mathrm{hi}}(x) = f(x; \hat{A}, \hat{\mu}) + \sigma_f(x), \qquad f_{\mathrm{lo}}(x) = f(x; \hat{A}, \hat{\mu}) - \sigma_f(x). \tag{4.23}$$

For fit models more complex than a single attenuation exponential, the same method is used: the covariance matrix returned by the fit is propagated through the fitted function using the corresponding derivatives with respect to its parameters.

### 4.1.3 Reference Background Budget

The general background model and its relation to the projected $0\nu\beta\beta$ sensitivity were introduced in Chapter 2. The present section uses that framework as the reference point for the cryogenic-shield study and focuses on the intrinsic-radioactivity

contribution, which is the part of the budget most directly affected by the cryostat material, HFE thickness, and nearby detector geometry.

Using the line-by-line annual contributions defined in Sec. 4.1.2, the baseline total background is

$$B_{\mathrm{tot}}^{\mathrm{yr}} \simeq 0.55 \text{ cts}/(\mathrm{FWHM} \cdot 2\,\mathrm{t} \cdot \mathrm{yr}).$$

This value includes the intrinsic radiogenic background together with the other background sources illustrated in Fig. 2.13. It is of the same order as the inner-2 t ROI background scale corresponding to the published $T_{1/2}^{0\nu} \simeq 1.35 \times 10^{28}$ yr sensitivity discussed in Sec. 2.5.4. The present budget is used here as a conservative reference, since further reductions remain possible through improved radiopurity inputs and detector-design optimization, as discussed below.

Within that total, the intrinsic-radioactivity term contains the main design handles considered in this study. Its component-level breakdown is shown in Fig. 4.3.

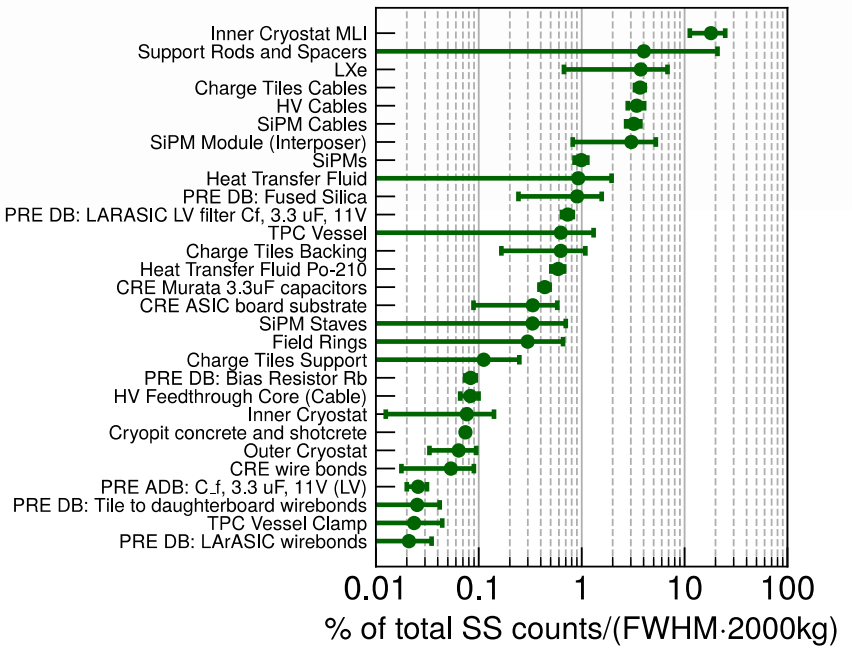


Figure 4.3: Component-level intrinsic-radioactivity budget in the inner 2000 kg and within one FWHM around $Q_{\beta\beta}$. Updated from [47].

The corresponding total intrinsic radiogenic background contribution is

$$B_{\mathrm{int}}^{\mathrm{yr}} \simeq 0.26 \pm 0.043 \text{ cts}/(\mathrm{FWHM} \cdot 2\,\mathrm{t} \cdot \mathrm{yr}),$$

corresponding to about 47% of the total background budget.

Compared with earlier configurations, the updated intrinsic budget is more distributed. A key change is the replacement of the carbon-fiber cryostat vessels by ultra-radiopure nickel, which strongly reduces the vessel contribution and motivates the study developed in the following sections. The largest remaining entries are

1. the inner-cryostat MLI,
2. the inner TPC components,
3. the TPC-support components, such as HV cables and HFE.

The prominence of the inner-cryostat MLI should be interpreted cautiously, since it is shown here as a conservative worst-case contribution and had not yet been optimized in either mass or radiopurity. More generally, the intrinsic background is now distributed among vessel-adjacent structures, inner-TPC elements, nearby services, and shielding fluids, rather than being driven primarily by the cryostat vessels.

This distribution motivates the component-level treatment used in the remainder of the chapter. The next section focuses on the HFE volume and cryostat vessels, both as shielding elements and as source terms whose contributions evolve with the detector geometry.

## 4.2 Cryogenic Fluorinated Liquid Shield (HFE)

The cryogenic shield around the TPC plays both a thermal and a shielding role. In the baseline design, the active xenon is enclosed within nested cryostat vessels and surrounded by a large volume of fluorinated heat-transfer fluid. This configuration attenuates external $\gamma$-rays and provides thermal stability [46]. In this chapter, the HFE volume and cryostat vessels are treated together because increasing the HFE improves shielding but also increases the size, mass, and intrinsic background of the inner cryostat vessel.

### 4.2.1 HFE Properties, Radiopurity, and Shielding Role

In the baseline design, the shielding fluid is HFE-7200. It is selected because it provides a highly radiopure cryogenic bath around the TPC while remaining liquid over the full operating range and offering efficient attenuation of external MeV $\gamma$-rays and neutrons [46]. Its molecular formula is $C_4F_9OC_2H_5$, usually written $C_6H_5F_9O$.

The radiopurity of the fluid is a key design input, since the HFE is deployed in large quantity close to the active xenon. The available PNNL assay results for NOVEC HFE-7200 are summarized in Table 4.2.

| Isotope | Assay result | Activity [Bq kg$^{-1}$] |
|---|---|---|
| $^{232}$Th | $< 1.3\,\mathrm{fg\,g^{-1}}$ | $< 5.3 \times 10^{-9}$ |
| $^{238}$U | $< 4.3\,\mathrm{fg\,g^{-1}}$ | $< 5.3 \times 10^{-8}$ |

Table 4.2: Rounded 90% C.L. PNNL assay limits for NOVEC HFE-7200, reported in the nEXO radioassay compilation [88]. The calculation uses zero central values and Gaussian widths of $3.257 \times 10^{-9}$ and $3.233 \times 10^{-8}$ Bq/kg for Th and U, respectively.

These limits are sufficiently low that HFE-7200 can be treated primarily as a shielding medium rather than as a dominant intrinsic source term. Its residual contribution is then driven mainly by its deployed mass and position in the detector model.

The main physical properties relevant to the present study are listed in Table 4.3. The attenuation coefficients are quoted at $\sim 2.5\,\mathrm{MeV}$, since this is a representative energy for shielding studies near the ROI.

| Symbol | Property | At | Value |
|---|---|---|---|
| — | Boiling point | 1 bar | $350\,\mathrm{K}$ |
| — | Freezing point | 1 bar | $135\,\mathrm{K}$ |
| — | Vapor pressure | $298\,\mathrm{K}$ | $109\,\mathrm{mmHg}$ |
| $\rho$ | Density | $170\,\mathrm{K}$ | $1.73\,\mathrm{g\,cm^{-3}}$ |
| $c_p$ | Specific heat | $298\,\mathrm{K}$ | $1.21\,\mathrm{kJ\,kg^{-1}\,K^{-1}}$ |
| $\mu/\rho$ | Mass attenuation coefficient | $2.5\,\mathrm{MeV}$ | $4.0 \times 10^{-2}\,\mathrm{cm^2\,g^{-1}}$ |
| $\mu$ | Linear attenuation coefficient | $165\,\mathrm{K}$, $2.5\,\mathrm{MeV}$ | $6.7 \times 10^{-2}\,\mathrm{cm^{-1}}$ |

Table 4.3: Physical properties of HFE-7200 relevant to the present study, from the vendor's spec sheet.

Several properties in Table 4.3 are important for the present study. The low freezing point keeps HFE-7200 liquid over the detector operating range, while the relatively large density for an organic fluid gives it useful shielding power. Its vapor pressure is also substantial, showing that the fluid is fairly volatile at room temperature. In practice, however, the main engineering constraint at cryogenic temperature is not freezing itself, but the strong increase in viscosity well before the freezing point. This complicates cooldown and recirculation, and is one of the motivations for the dedicated HFE recirculation studies described in Chapter 5.

From the attenuation coefficients in Table 4.3, the linear coefficient follows from $\mu = (\mu/\rho)\rho$ using $\rho \simeq 1.73\,\mathrm{g\,cm^{-3}}$, which gives $\mu \simeq 6.7 \times 10^{-2}\,\mathrm{cm^{-1}}$ at $2.5\,\mathrm{MeV}$. The corresponding attenuation length is about $14.8\,\mathrm{cm}$. For comparison, ice at the same $\gamma$-ray energy has an attenuation length of about $25\,\mathrm{cm}$. HFE-7200 therefore provides local shielding against external MeV $\gamma$-rays.

The minimum HFE thickness requirement can be written in terms of the attenuation law,

$$T(t) = \frac{I(t)}{I_0} = e^{-\mu t}, \tag{4.24}$$

where $T$ is the transmitted fraction through a thickness $t$. Limiting the transmitted fraction to $\lesssim 0.5\%$ ensures that external $\gamma$-ray backgrounds remain subdominant in the overall background budget. Requiring a $\sim 2.5\,\mathrm{MeV}$ $\gamma$-ray to be attenuated to this level gives

$$T(t_{\mathrm{min}}) \lesssim 5 \times 10^{-3}, \qquad t_{\mathrm{min}} \gtrsim \frac{\ln(200)}{\mu}. \tag{4.25}$$

For $\mu \sim 6.7 \times 10^{-2}\,\mathrm{cm^{-1}}$, this gives a characteristic minimum thickness of order $0.8\,\mathrm{m}$, consistent with the baseline requirement of about $76\,\mathrm{cm}$.

However, the HFE thickness is not uniform, because the baseline geometry places a cylindrical TPC inside spherical cryostat vessels, following historical mechanical

design constraints. A simple geometric study is given in Appendix B. For the baseline dimensions, the HFE thickness ranges from about $t_{\min}$ to 1053 mm, with a geometric mean thickness of about 968 mm. The attenuation-equivalent thickness is slightly smaller, about 946 mm, because $\gamma$-ray attenuation depends exponentially on path length. The resulting mean transmission at 2.5 MeV is $\langle T \rangle \simeq 1.69 \times 10^{-3}$, or about 0.17%, comfortably below the design requirement.

The mean thickness characterizes the geometry, while the attenuation-equivalent thickness characterizes its mean shielding performance. These quantities are summarized in Table 4.4. Other baseline detector parameters are given in Chapter 2.

| Symbol | Parameter | Value |
|---|---|---|
| $m_{\mathrm{HFE}}$ | Baseline HFE mass | 32 t |
| $V_{\mathrm{HFE}}$ | Baseline HFE volume | 18.5 $\mathrm{m}^3$ |
| $t_{\min}$ | Minimum thickness requirement | 760 mm |
| $t_{\max}$ | Geometric maximum thickness | 1053 mm |
| $\langle t \rangle$ | Mean thickness | 968 mm |
| $\delta_{\mathrm{att}}$ | Attenuation-equivalent thickness | 946 mm |
| $T_{\mathrm{req}}$ | Transmission requirement at 2.5 MeV | $\leq 0.5\,\%$ |
| $\langle T \rangle$ | Mean transmission at 2.5 MeV | 0.17 % |

Table 4.4: Geometrical and shielding parameters of the baseline HFE layer. The mean-thickness quantities are derived in Appendix B.

The HFE is continuously recirculated through an external $LN_2$-driven heat exchanger during cooldown and operation, with a nominal mass flow rate of up to $\sim 0.3\,\mathrm{kg\,s^{-1}}$ [46]. This loop is used to cool the inner cryostat and to remove the steady heat load, while the same fluid also transfers pressure loads from the TPC vessel to the cryostat. Because the HFE inventory is large and the fluid becomes increasingly viscous at low temperature, its circulation is a significant engineering constraint. These issues are addressed experimentally in Chapter 5, which presents the dedicated HFE recirculation setup developed for this purpose.

### 4.2.2 Ultra-Radiopure Nickel Cryostat

Because the cryostat vessels are among the most massive structures close to the active xenon, their material choice directly affects the intrinsic background budget. The earlier configuration used carbon-fiber composite shells with titanium liners [47], whereas the updated baseline adopts spherical all-nickel vessels. This change is motivated primarily by radiopurity considerations, since it strongly suppresses the vessel contribution. It also simplifies fabrication, since the vessels can be manufactured on the surface as metallic panels and then formed and welded, rather than assembled underground from layered composite materials.

The cryostat remains a vacuum-insulated two-vessel system with nominal diameters of about 3.4 m for the inner vessel and 4.5 m for the outer vessel, both supported

from the upper structure, as shown in Fig. 4.4.

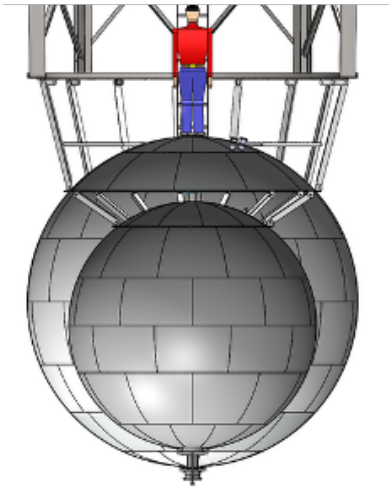

Figure 4.4: Cutaway view of the cryostat region, showing the nested spherical cryostat vessels surrounding the TPC and HFE volume and suspended from the upper support structure.

In the baseline spherical layout, the outer vessel is vertically offset with respect to the inner vessel, so the HFE feedthrough below the inner vessel sets the minimum steel-to-steel clearance,

$$t_{\mathrm{vac,min}} = 126\,\mathrm{mm}, \tag{4.26}$$

The adopted masses, thicknesses, and radioassay inputs for the two cryostat configurations are summarized in Table 4.5. For the earlier design, the CFC shell activities are obtained by combining the resin and fiber contributions into a single shell activity. In the nickel design, the adopted values correspond to the chemical-vapor-deposition (CVD) nickel assay inputs used in the updated model. The background contributions quoted below were derived using the calculation method defined in Sec. 4.1.2, using the corresponding masses, activities, and parent-normalized hit efficiencies for the cryostat components.

The impact of this material change is shown more directly in Table 4.6, which compares the vessel-related intrinsic background contributions obtained from the background model. In the earlier configuration, the IV shell and liner together contribute

$$\begin{aligned} B_{\mathrm{IV}}^{\mathrm{CFC}} &= (1.34 \pm 0.95) \times 10^{-2} + (9.22 \pm 3.02) \times 10^{-3} \\ &= (2.26 \pm 1.00) \times 10^{-2}\ \mathrm{cts/(FWHM \cdot 2\,t \cdot yr)}, \end{aligned} \tag{4.27}$$

while the corresponding nickel IV vessel contributes

$$B_{\mathrm{IV}}^{\mathrm{Ni}} = (5.63 \pm 2.34) \times 10^{-5}\ \mathrm{cts/(FWHM \cdot 2\,t \cdot yr)}.$$

This corresponds to an IV reduction factor of about 400. Similarly, the OV shell and liner contribution changes from

$$\begin{aligned} B_{\mathrm{OV}}^{\mathrm{CFC}} &= (2.17 \pm 1.66) \times 10^{-2} + (7.47 \pm 4.63) \times 10^{-3} \\ &= (2.92 \pm 1.72) \times 10^{-2}\ \mathrm{cts/(FWHM \cdot 2\,t \cdot yr)}, \end{aligned} \tag{4.28}$$

| Design | Component | Mass | Thickness | Specific activity | |
|---|---|---|---|---|---|
| | | [kg] | [mm] | $^{232}$Th [µBq/kg] | $^{238}$U [µBq/kg] |
| CFC | IV CFC shell | 823 | 10 | $123 \pm 82$ | $239 \pm 100$ |
| | IV Ti liner | 323 | 2 | $230 \pm 20$ | $0 \pm 90$ |
| | OV CFC shell | 2700 | 20 | $123 \pm 82$ | $239 \pm 100$ |
| | OV Ti liner | 859 | 3 | $230 \pm 20$ | $0 \pm 90$ |
| Nickel | IV vessel | 1682 | 5 | $0.264 \pm 0.118$ | $0 \pm 0.743$ |
| | OV vessel | 5705 | 10 | $0.264 \pm 0.118$ | $0 \pm 0.743$ |

Table 4.5: Adopted masses, thicknesses, and specific activities for the cryostat vessel materials used in the earlier CFC+titanium-liner configuration and in the updated all-nickel configuration.

to

$$B_{\mathrm{OV}}^{\mathrm{Ni}} = (8.20 \pm 3.16) \times 10^{-5}\ \mathrm{cts/(FWHM \cdot 2\,t \cdot yr)},$$

corresponding to an OV reduction factor of about 360. Summing both vessels, the total vessel contribution decreases from

$$B_{\mathrm{vessels}}^{\mathrm{CFC}} = (5.18 \pm 1.99) \times 10^{-2}\ \mathrm{cts/(FWHM \cdot 2\,t \cdot yr)}$$

to

$$B_{\mathrm{vessels}}^{\mathrm{Ni}} = (1.38 \pm 0.39) \times 10^{-4}\ \mathrm{cts/(FWHM \cdot 2\,t \cdot yr)},$$

that is, a total reduction factor of about 370.

| Design | Part | Background | | Total |
|---|---|---|---|---|
| | | [cts/(FWHM · 2 t · yr)] | % of alloc. | [cts/(FWHM · 2 t · yr)] |
| CFC | IV shell | $(1.34 \pm 0.95) \times 10^{-2}$ | 69% | $(5.18 \pm 1.99) \times 10^{-2}$ |
| | IV liner | $(9.22 \pm 3.02) \times 10^{-3}$ | | |
| | OV shell | $(2.17 \pm 1.66) \times 10^{-2}$ | | |
| | OV liner | $(7.47 \pm 4.63) \times 10^{-3}$ | | |
| Nickel | IV | $(5.63 \pm 2.34) \times 10^{-5}$ | 0.18% | $(1.38 \pm 0.39) \times 10^{-4}$ |
| | OV | $(8.20 \pm 3.16) \times 10^{-5}$ | | |

Table 4.6: Comparison of the vessel-related intrinsic background contributions for the earlier CFC+titanium-liner configuration and the updated all-nickel configuration. The cryostat allocation is 0.075 cts/(FWHM · 2 t · yr).

Figure 4.5 places this comparison in the context of the full intrinsic background model. In the CFC-based configuration, the cryostat vessels are among the dominant contributors to the total budget. Once the vessels are replaced by ultra-radiopure nickel, their contribution is strongly suppressed and the intrinsic budget becomes

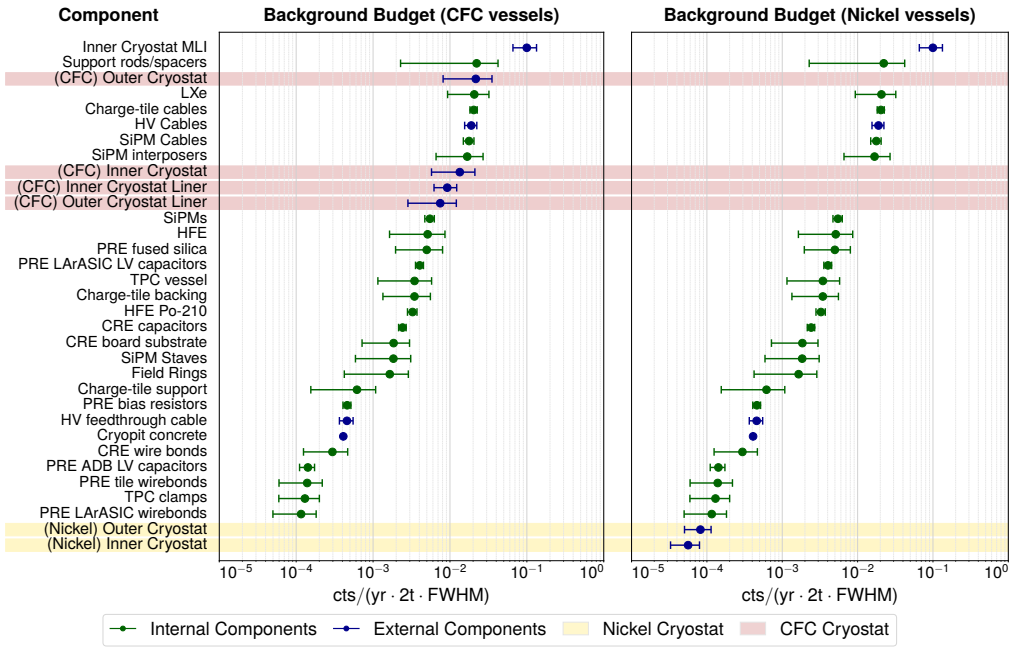


Figure 4.5: Component-by-component intrinsic background budget for the earlier CFC+titanium-liner cryostat configuration and the updated all-nickel configuration.

more distributed across other nearby components, including the inner cryostat MLI, support and service structures, and the HFE region.

In the updated design, the cryostat allocation is 0.075 cts/(FWHM · 2 t · yr). Relative to this allowance, the earlier CFC+titanium-liner configuration corresponds to about 69% of the cryostat budget, whereas the all-nickel design corresponds to only about 0.18%. The cryostat shells therefore no longer dominate the intrinsic background model in the nickel baseline.

This change also modifies the shielding problem considered in the rest of this chapter. In the earlier CFC-based configuration, the HFE shield partly compensated a comparatively large vessel source term. Once the vessels are replaced by ultra-radiopure nickel, the relevant optimization is instead set by the balance among several subdominant sources close to the TPC. For this reason, the scans presented below take the all-nickel cryostat as the updated baseline configuration.

## 4.3 Internal Backgrounds vs. HFE Thickness

This section studies how reduced HFE thickness affects radiogenic backgrounds from detector materials external to the TPC vessel. The aim is to determine how much shielding can be removed before the corresponding background increase becomes significant.

The study uses the Geant4-based detector model introduced earlier. For each scanned configuration, only the HFE thickness and the corresponding inner-cryostat radius are changed, while the source terms, isotope assumptions, and analysis selections are kept fixed. The comparison therefore isolates the shielding role of the

HFE. The overall scan workflow is summarized in Fig. 4.2.

Because the probability that a decay occurring in an external component produces a count in the ROI is small, the simulated samples typically contain between $10^9$ and $10^{11}$ decays per configuration. These scans were run on the Lawrence Livermore National Laboratory (LLNL) computing clusters, and a single configuration typically required a few days of computing time. To reduce the simulation cost, the following optimizations are applied for particles produced outside the TPC:

1. electrons are not tracked once their energy falls below the ROI threshold,
2. $\gamma$ rays are terminated once their energy falls below the ROI threshold,
3. only events depositing more than 700 keV in the TPC are retained.

These choices are suitable for comparing relative hit efficiencies in the ROI, but they modify the detailed reconstructed spectrum and are therefore not intended for constructing full sensitivity models.

### 4.3.1 HFE

The HFE-7200 volume is the closest large external medium surrounding the TPC vessel. It is introduced primarily as a cryogenic and radiological shield, but its own background contribution must also be evaluated because of its large mass and proximity to the active xenon. Reducing the HFE shield therefore has two competing effects: it weakens the attenuation of external backgrounds, but it also reduces the amount of HFE that can contribute as a source term itself.

In the geometry scans considered here, the HFE inventory is varied through the inner-cryostat radius $R_{\mathrm{IV}}$. The corresponding HFE volume is parameterized as the volume inside the spherical inner cryostat minus an internal volume that does not contain HFE,

$$V_{\mathrm{HFE}}(R_{\mathrm{IV}}) = \frac{4\pi}{3} R_{\mathrm{IV}}^3 - V_{\mathrm{det}}, \tag{4.29}$$

where $V_{\mathrm{det}}$ denotes the detector volume enclosed by the inner cryostat and displaced from the HFE bath. In this conversion, $V_{\mathrm{det}}$ accounts for the TPC envelope together with nearby detector parts and subcomponents. Since these internal structures are unchanged across the scan, $V_{\mathrm{det}}$ is taken to be independent of $R_{\mathrm{IV}}$. The HFE mass is then

$$m_{\mathrm{HFE}}(R_{\mathrm{IV}}) = \rho_{\mathrm{HFE}}\, V_{\mathrm{HFE}}(R_{\mathrm{IV}}), \tag{4.30}$$

with $\rho_{\mathrm{HFE}} = 1.73\,\mathrm{t/m^3}$. Fixing the parameterization to the baseline design at $R_{\mathrm{IV}} = 1691\,\mathrm{mm}$ and $m_{\mathrm{HFE}} = 31.81\,\mathrm{t}$ gives

$$V_{\mathrm{det}} = \frac{4\pi}{3} R_{\mathrm{IV}}^3 - \frac{m_{\mathrm{HFE}}}{\rho_{\mathrm{HFE}}} \simeq 1.87\,\mathrm{m^3}. \tag{4.31}$$

This relation is used below to convert the scanned values of $R_{\mathrm{IV}}$ into HFE mass.

Three source models are considered for the HFE contribution. The first includes only bulk $^{232}$Th and $^{238}$U contamination in the HFE. The second adds dissolved $^{222}$Rn. The third includes an additional $^{210}$Po-related term. These cases are treated separately because they do not scale identically with HFE mass.

For source terms distributed throughout the HFE volume, increasing the HFE mass has two competing effects. It increases the total source mass, but it also increases the average distance between the decay location and the active xenon. The resulting background contribution is therefore expected to rise more slowly than linearly with mass and can approach a saturation-like behavior once self-shielding becomes effective. The resulting dependence on HFE mass is shown in Fig. 4.6.

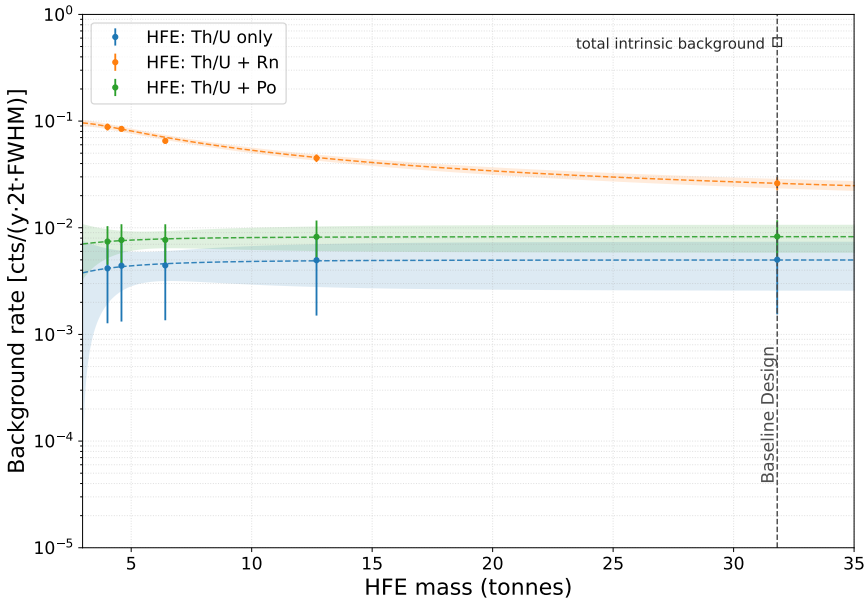


Figure 4.6: HFE-related background contribution as a function of HFE mass for three source models: bulk Th/U only, bulk Th/U plus radon, and bulk Th/U plus Po-related activity. Points are MC-based estimates. Dashed curves use fitted normalizations and offsets at fixed $\mu_{\mathrm{HFE}}$, with the radon contribution normalized to the baseline allocation. Bands show propagated $1\sigma$ uncertainties from the fits and radon inputs.

### Th/U contribution

The bulk Th/U-only contribution remains at the level of a few $10^{-3}$ cts/(FWHM·2 t·yr) and varies only weakly with HFE mass, showing that self-shielding compensates most of the increase in source material. To describe this trend, the background contribution from uniformly distributed bulk activity in the HFE, denoted $B_{\mathrm{bulk}}$, is modeled as

$$B_{\mathrm{bulk}}(R_{\mathrm{IV}}) = B_0 + A \int_{R_0}^{R_{\mathrm{IV}}} 4\pi r^2 \, f_\Omega(r) \, T_{\mathrm{hit}}(r; \mu_{\mathrm{HFE}}) \, dr, \tag{4.32}$$

where $A$ is a normalization constant and $B_0$ accounts for the contribution from the HFE already present below the lower bound $R_0$ of the fitted range. In the scanned range, $R_{\mathrm{IV}}$ remains larger than the distance from the TPC center to its corner, so increasing $R_{\mathrm{IV}}$ adds a full spherical shell of HFE and the corresponding differential volume element is $4\pi r^2 dr$.

The function $f_\Omega(r)$ describes the purely geometric acceptance of a source element at radius $r$ toward the finite cylindrical TPC, while $T_{\rm hit}(r;\mu_{\rm HFE})$ describes the associated self-attenuation of $\gamma$ rays in the HFE. The attenuation term is written as

$$T_{\rm hit}(r;\mu_{\rm HFE}) = e^{-\mu_{\rm HFE}\ell_{\rm eff}(r)}, \tag{4.33}$$

where $\ell_{\rm eff}(r)$ is the HFE path length for rays emitted at radius $r$ that reach the TPC, and $\mu_{\rm HFE}(E_\gamma)$ is the energy-dependent linear attenuation coefficient of HFE. For the $\sim 2.5\,\mathrm{MeV}$ $\gamma$ rays considered here, it is fixed to

$$\mu_{\rm HFE} = 6.7440 \times 10^{-3}\ \mathrm{mm}^{-1}, \tag{4.34}$$

corresponding to HFE-7200 at LXe temperature [89].

The geometric acceptance $f_\Omega(r)$ is determined using a dedicated Monte Carlo simulation of the cylindrical TPC with its nominal dimensions. For each shell radius, emission points are sampled uniformly over the spherical shell, and rays are emitted isotropically into the inward hemisphere. A total of $6 \times 10^5$ rays are generated at each of 22 equally spaced radii between 0.95 and 1.70 m. The resulting inward-hemisphere acceptance, $G(r) = \Omega/(2\pi)$, is fitted over this range with the empirical form $A/r^2 + B/r^3$. Converting to the full-sphere acceptance, $f_\Omega(r) = G(r)/2$, gives

$$f_\Omega(r) \simeq \frac{1}{2}\left(\frac{0.196\ \mathrm{m}^2}{r^2} + \frac{0.099\ \mathrm{m}^3}{r^3}\right), \qquad 0.95\ \mathrm{m} \le r \le 1.70\ \mathrm{m}. \tag{4.35}$$

A ray is accepted if it intersects the cylindrical TPC. The $1/r^2$ dependence follows the inverse-square scaling of the solid angle in the far field, while the $1/r^3$ term captures the main finite-size correction at smaller radii.

### $^{210}$Po contribution

An additional $^{210}$Po-related term is included in the HFE study to represent the radon-daughter $(\alpha, n)$ background associated with the vessel/HFE region. In this mechanism, the decay of $^{210}$Po emits a $\sim 5.3\,\mathrm{MeV}$ $\alpha$ particle, which can interact with nearby low-$Z$ nuclei in the HFE and produce a neutron. The neutron can then propagate through the surrounding HFE, reach the xenon, and generate a background count either through direct interactions or through subsequent capture-induced activity. In the baseline geometry, the adopted contribution is

$$B_{^{210}\mathrm{Po}} = (3.26 \pm 0.46) \times 10^{-3}\ \mathrm{cts}/(\mathrm{FWHM} \cdot 2\,\mathrm{t} \cdot \mathrm{yr}).$$

This value is derived from a dedicated collaboration study of $^{210}$Po-induced neutron backgrounds, which expresses the effect in terms of an allowable $^{210}$Po activity. In the present scan, this term is kept fixed at its baseline value. HFE self-shielding makes the neutron background only weakly sensitive to the removal of HFE located far from the TPC when the inner-vessel radius is reduced. Unlike the bulk Th/U contribution, it is not modeled as a source distributed throughout the full HFE volume.

### $^{222}$Rn contribution

The HFE contribution including dissolved $^{222}$Rn increases more rapidly as the HFE mass is reduced and remains the dominant HFE-related term over the scanned range. The value adopted at the baseline design point is not a measured $^{222}$Rn activity, but a design-limit background allocation. Radon in the HFE region is associated with several nearby sources, including calibration components, TPC supports and conduits immersed in HFE, the HFE pump and associated piping, feedthroughs, and the inner-vessel surface and ports. To describe its evolution with geometry, the total HFE-related background is written as

$$B(R_{\mathrm{IV}}) = B_0 + B_{\mathrm{Th/U}}(R_{\mathrm{IV}}) + B_{\mathrm{Rn}}(R_{\mathrm{IV}}), \tag{4.36}$$

where $B_0$ is a radius-independent offset and $B_{\mathrm{Th/U}}$ is the bulk Th/U contribution introduced above.

The radon term is modeled with the same geometric and attenuation kernel as the Th/U component,

$$B_{\mathrm{Rn}}(R_{\mathrm{IV}}) = A_{\mathrm{Rn}}(R_{\mathrm{IV}}) \int_{R_{\mathrm{min}}}^{R_{\mathrm{IV}}} 4\pi r^2 \, f_\Omega(r) \, T_{\mathrm{hit}}(r; \mu_{\mathrm{HFE}}) \, dr, \tag{4.37}$$

but with a radius-dependent normalization

$$A_{\mathrm{Rn}}(R_{\mathrm{IV}}) = \frac{N_{\mathrm{other}}^{\mathrm{Rn}} + N_{\mathrm{IV}}^{\mathrm{Rn}} \left(\frac{R_{\mathrm{IV}}}{R_0}\right)^2}{V_{\mathrm{HFE}}(R_{\mathrm{IV}})}. \tag{4.38}$$

Here $R_0$ is the baseline inner-vessel radius, $V_{\mathrm{HFE}}(R_{\mathrm{IV}})$ is the HFE volume defined above, $N_{\mathrm{other}}^{\mathrm{Rn}}$ represents the radon activity from the non-IV sources listed above, and $N_{\mathrm{IV}}^{\mathrm{Rn}}$ the part associated with the inner-vessel surface. The factor $(R_{\mathrm{IV}}/R_0)^2$ accounts for the change in inner-vessel surface area, while $1/V_{\mathrm{HFE}}(R_{\mathrm{IV}})$ accounts for the change in dissolved-radon concentration. Because the HFE volume decreases faster than the inner-vessel surface area, the radon concentration and corresponding background increase as $R_{\mathrm{IV}}$ decreases.

Deposited-energy spectra around the ROI can also be compared for each tested inner-cryostat radius. Figure 4.7 shows the reconstructed energy spectra for HFE-related $^{238}$U- and $^{232}$Th-chain backgrounds as the inner-cryostat radius is reduced.

The energy spectra show that, as the HFE quantity is reduced, the overall rate increases because less shielding remains between the HFE source volume and the active xenon. For the bulk Th/U and $^{210}$Po terms, however, this increase in transmitted rate does not translate into a strong change in the corresponding background contribution, since it is largely compensated by the simultaneous reduction in HFE source mass.

The main design implication is instead set by the radon-related term. In the present study, its absolute baseline value is taken from the default-design background allocation rather than from a direct measurement, so the relevant result is not the absolute level itself but its relative evolution with reduced HFE volume. Over the scanned range, the radon-related contribution increases by at most about a factor of

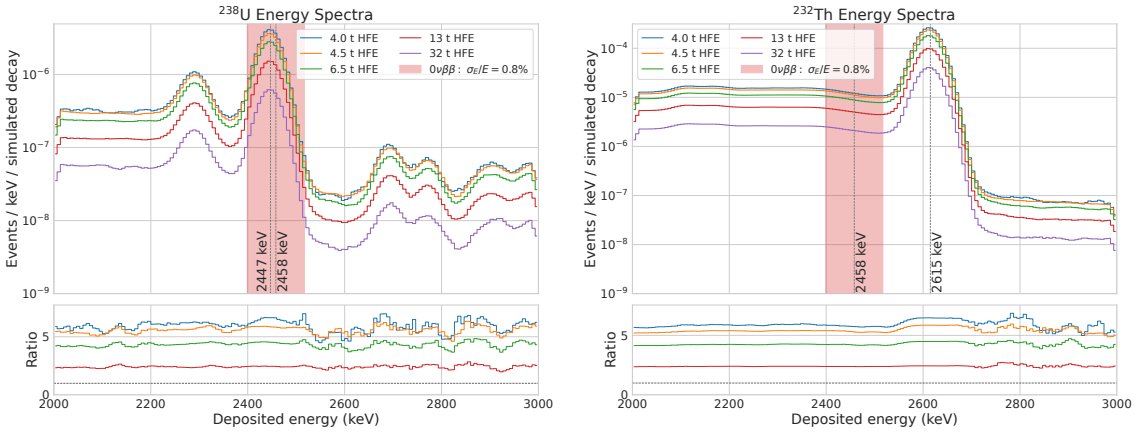


(a) $^{238}$U-chain HFE spectrum (b) $^{232}$Th-chain HFE spectrum

Figure 4.7: Reconstructed energy spectra from HFE-related backgrounds for several inner-cryostat radii. The lower panels show the ratio to the baseline-radius spectrum. Reducing the HFE thickness increases the overall rate, while preserving the main spectral structures associated with the radiogenic source term.

4. This shows that reduced-HFE options are constrained mainly by the radon-related scaling, whereas the bulk intrinsic HFE terms remain subdominant throughout the scan.

### 4.3.2 Cryostat Vessels

The cryostat vessels are the largest metallic structures outside the HFE shield and remain among the closest radiogenic sources surrounding the active xenon volume. In the present scan, the vessel specific activities and wall thicknesses are kept fixed while the inner-vessel radius $R_{\mathrm{IV}}$ is varied, so that the evolution includes both the change in HFE shielding and the reduction in inner-vessel mass. A smaller cryostat could in principle also allow thinner vessels, but that separate effect is considered in the next subsection.

Reducing the HFE quantity changes both the amount of shielding between the inner vessel and the TPC and the inner-vessel source mass. The dominant effect is therefore the change in $\gamma$-ray attenuation through the intervening HFE. The resulting IV and OV background contributions are shown in Fig. 4.8.

Both trends are well described over the scanned range by an exponential attenuation model,

$$B_{\mathrm{vessel}}(R_{\mathrm{IV}}) = N_{\mathrm{vessel}}\, e^{-\mu_{\mathrm{vessel}} R_{\mathrm{IV}}}, \tag{4.39}$$

where $N_{\mathrm{vessel}}$ is a normalization constant and $\mu_{\mathrm{vessel}}$ is an effective attenuation slope. In Fig. 4.8, the horizontal axis is expressed as the equivalent HFE mass for consistency with the HFE scan, but the fit itself is performed as a function of $R_{\mathrm{IV}}$, since this directly controls the HFE thickness between the inner vessel and the TPC.

For the nickel cryostat, the fitted slopes are

$$\mu_{\mathrm{IV}} = (6.37 \pm 0.86) \times 10^{-3}\ \mathrm{mm}^{-1}, \qquad \mu_{\mathrm{OV}} = (6.14 \pm 0.79) \times 10^{-3}\ \mathrm{mm}^{-1}. \tag{4.40}$$

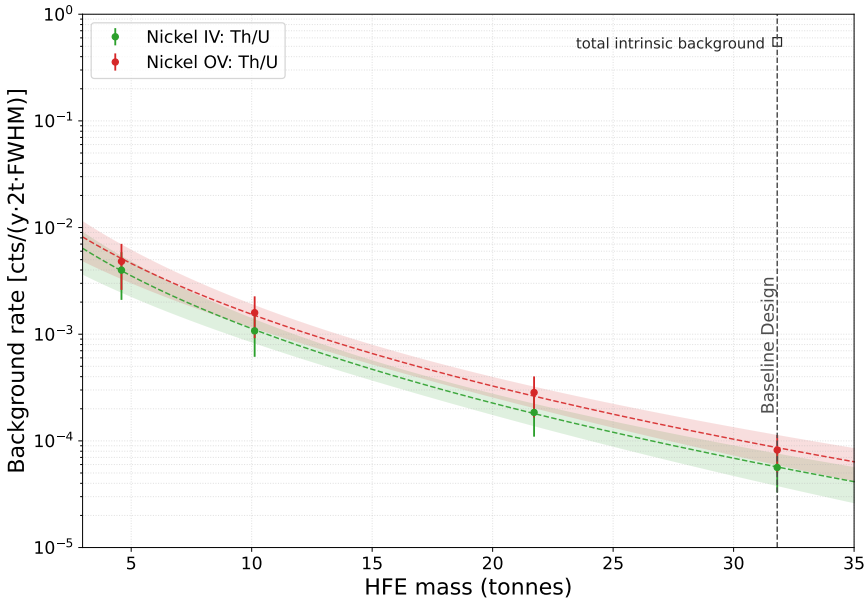


Figure 4.8: Intrinsic background contribution from the nickel inner vessel and outer vessel as a function of HFE mass. Points are MC-based estimates; dashed curves show exponential fits in $R_{\mathrm{IV}}$ with free normalization and slope. Bands show $1\sigma$ uncertainties propagated from the fit covariances.

These values are compatible with the HFE attenuation coefficient introduced earlier, which indicates that the observed evolution is dominated by $\gamma$-ray attenuation in the HFE.

The separate $^{232}$Th and $^{238}$U components follow the same pattern. For the IV, the background is split into a $^{232}$Th contribution of about 55% and a $^{238}$U contribution of about 45%. Fitting the two isotope components separately gives

$$\mu_{\mathrm{IV}}^{\mathrm{Th}} = (5.96 \pm 0.81) \times 10^{-3}\ \mathrm{mm}^{-1}, \qquad \mu_{\mathrm{IV}}^{\mathrm{U}} = (6.77 \pm 1.53) \times 10^{-3}\ \mathrm{mm}^{-1}. \quad (4.41)$$

The $^{238}$U component is therefore slightly steeper than the $^{232}$Th component, consistent with the lower characteristic $\gamma$-ray energies in the $^{238}$U chain. The OV shows the same qualitative behavior, so only the IV decomposition is quoted here.

For reference, Appendix C.1.3 compares the inner-vessel hit efficiency in the baseline geometry to that obtained when the HFE volume is replaced by vacuum. The corresponding equivalent HFE thicknesses are

- $(982 \pm 80)$ mm for the $^{238}$U chain, consistent with the attenuation-equivalent thickness $\delta_{\mathrm{att}} = 946$ mm listed in Table 4.4;
- $(756 \pm 51)$ mm for the $^{232}$Th chain, which is instead close to the minimum HFE thickness.

This difference reflects the distinct origin of ROI events for each chain: for $^{238}$U, the surviving background is governed primarily by transmission through the full HFE layer, whereas for $^{232}$Th the ROI is populated mainly by the $^{208}$Tl Compton

continuum, so photons scattered within the HFE are not fully removed from the background-producing population. This is nevertheless consistent with the HFE-thickness scans discussed here. The direct comparison with and without HFE probes the total suppression produced by the full baseline HFE volume, including the effect of its non-uniform thickness. By contrast, the scan slope is extracted from nearby configurations in which the HFE thickness is changed only gradually. It therefore reflects mainly the incremental attenuation of the surviving high-energy $^{208}$Tl $\gamma$-ray population, which is why the fitted slope can still remain close to the characteristic attenuation coefficient of a $\sim 2.5\,\mathrm{MeV}$ $\gamma$ ray in HFE.

Figure 4.9 compares the reconstructed IV spectra for representative HFE quantities.

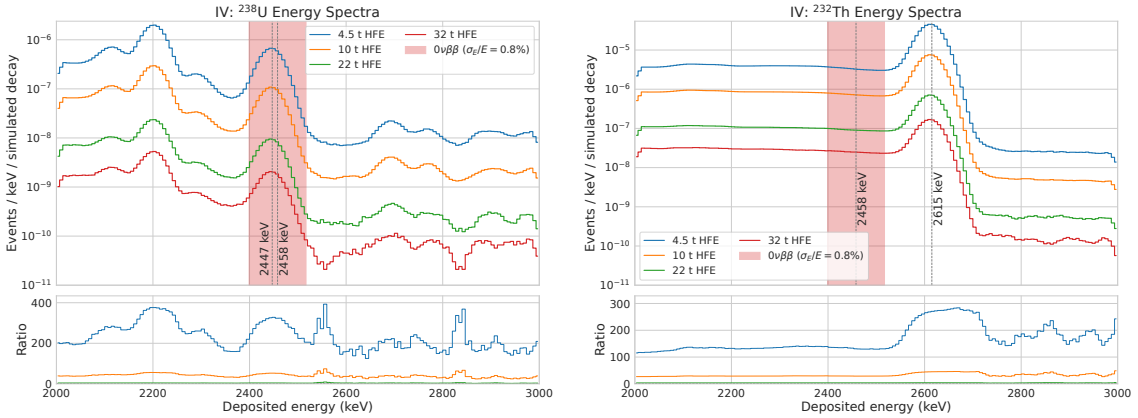


(a) $^{238}$U-chain IV spectrum (b) $^{232}$Th-chain IV spectrum

Figure 4.9: Reconstructed IV energy spectra for representative HFE quantities. The lower panels show the ratio to the baseline 32 t HFE configuration.

In both decay chains, reducing the HFE mass increases the transmitted rate. The dominant effect is therefore the strong rise in transmitted intensity as the shielding is reduced.

Figure 4.10 illustrates the effect of the topology selection by comparing the IV spectra before and after the DNN $> 0.88$ requirement.

In both decay chains, the DNN cut suppresses the vessel background by more than an order of magnitude over most of the energy range. The surviving events are concentrated more strongly in the single-site-like part of the spectrum, near the main $\gamma$-ray peaks, while the broad continuum is strongly reduced. Topology discrimination therefore provides an important secondary handle for rejecting vessel backgrounds.

Even in reduced-HFE configurations, the combined IV and OV contribution remains nearly two orders of magnitude below the total intrinsic background budget. It nevertheless follows a clear exponential dependence on HFE quantity, well captured by an attenuation law with a slope compatible with $\mu_{\mathrm{HFE}}$. The vessel background is therefore not the term that sets the minimum acceptable HFE quantity in the present study, although it remains a sensitive probe of the shielding performance.

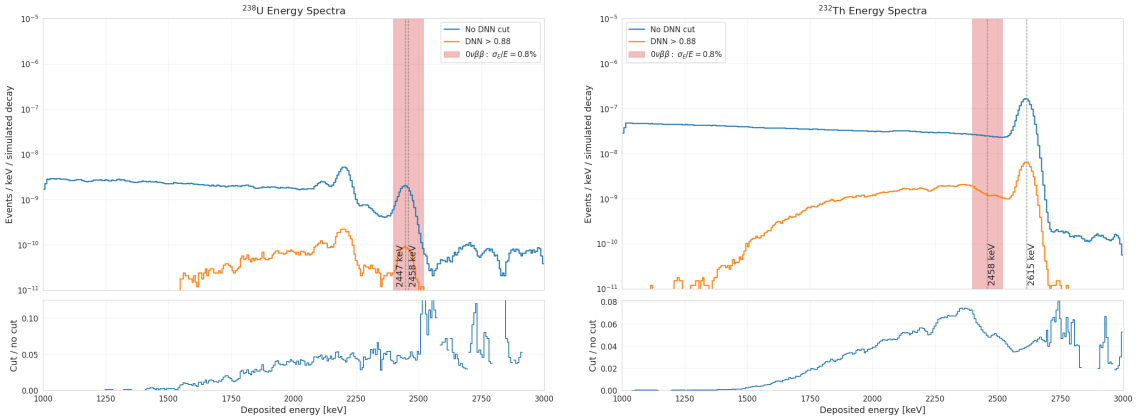


(a) $^{238}$U-chain IV spectrum with and without DNN cut

(b) $^{232}$Th-chain IV spectrum with and without DNN cut

Figure 4.10: Reconstructed IV energy spectra before and after the DNN $> 0.88$ requirement. The lower panels show the ratio of the selected spectrum to the spectrum without the DNN cut.

### 4.3.3 Water Shield

The water shield is much farther from the active xenon than the HFE and cryostat vessels, but its very large mass makes it a possible distributed background source. In the Geant4 geometry used here, the cylindrical water interior has a diameter of 12.9 m and a height of 13.7 m. Subtracting the spherical cryostat ($R_{\mathrm{OV}} = 2230$ mm) gives a water mass of approximately 1.75 kt. The water system is also designed to operate as an active Cherenkov veto, but the present subsection considers only the intrinsic radiogenic contribution from the water itself.

The adopted water-shield inputs for the two explicit MC geometries are summarized in Table 4.7. The activity inputs are the SNO+ water-shield assay values [90], while the hit efficiencies are the parent-normalized MC values used in the present study. The quoted efficiency uncertainties are propagated binomial counting uncertainties. For the baseline $^{238}$U point, no event survives the full selection, so a 90% C.L. upper limit is quoted. Other water radioassay results considered for comparison are listed in Table C.4 of Appendix C.2. A later SNO+ publication reports order-of-magnitude lower activities after improvements to the water purification system, but only for the active-volume water, so those values are not adopted for the present outer-detector estimate.

An earlier dedicated nEXO water-shield study estimated that recoil-driven emanation from the stainless-steel tank would produce 262 $^{222}$Rn atoms/day in the water, corresponding to about 1447 atoms in steady state for the full tank volume. Converting this steady-state inventory to activity gives

$$A_{\mathrm{Rn}}^{\mathrm{water}} = \frac{\lambda N_{\mathrm{Rn}}}{M_{\mathrm{water}}} \simeq 1.73 \times 10^{-9}\ \mathrm{Bq/kg}, \tag{4.42}$$

using $T_{1/2}(^{222}\mathrm{Rn}) = 3.82$ d and the baseline water mass. This is orders of magnitude below the adopted U/Th activity scale. In addition, $^{222}$Rn in the outer-detector

| $R_{\mathrm{IV}}$ [mm] | $m_{\mathrm{HFE}}$ [t] | Isotope | Activity [Bq/kg] | Hit efficiency [cts/(FWHM · 2 t)] | Total simulated |
|---|---|---|---|---|---|
| 1026 | 4.73 | $^{232}$Th | $(3.93 \pm 0.14) \times 10^{-7}$ | $(2.16 \pm 0.88) \times 10^{-10}$ | $10^{10}$ |
| | | $^{238}$U | $(1.98 \pm 0.39) \times 10^{-6}$ | $(1.00 \pm 1.00) \times 10^{-10}$ | |
| 1691 | 31.60 | $^{232}$Th | $(3.93 \pm 0.14) \times 10^{-7}$ | $(7.19 \pm 5.08) \times 10^{-12}$ | $10^{11}$ |
| | | $^{238}$U | $(1.98 \pm 0.39) \times 10^{-6}$ | $< 2.30 \times 10^{-11}$ | |

Table 4.7: Adopted activity inputs and parent-normalized hit efficiencies for the two explicit water-shield MC geometries. The $^{238}$U value at $R_{\mathrm{IV}} = 1691$ mm is a 90% C.L. upper limit.

water can be maintained below $9 \times 10^{-9}$ Bq/kg through purification [47]. The displayed water curves are therefore shown for the Th/U contribution only.

The outer-detector water system includes recirculation, purification, and monitoring, with a nominal flow of order 100 L/min, corresponding to recirculation of the full water inventory in about 12 days [46]. The water contribution discussed here should therefore be regarded as a conservative radiopurity input for the shielding study rather than as a background term expected to grow during nominal purified operation.

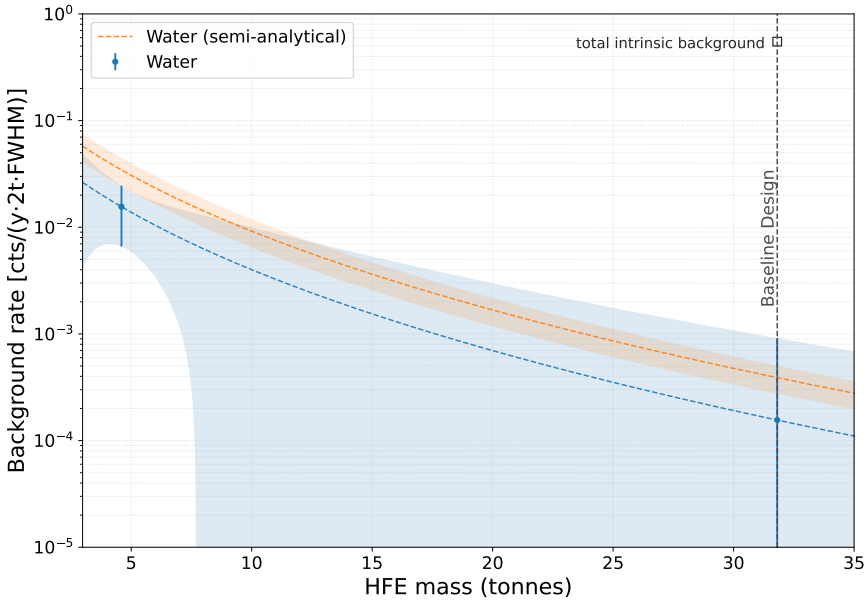


Figure 4.11: Water-shield background contribution as a function of HFE mass. Points are MC-based estimates. Dashed curves show an exponential fit with free normalization and slope (blue) and a semi-analytical prediction normalized to baseline OV simulations with fixed attenuation coefficients (orange). Bands show propagated $1\sigma$ fit uncertainties (blue) and activity and efficiency uncertainties (orange).

Figure 4.11 shows that the direct MC estimate is limited by low statistics, since the water shield is both distant from the TPC and strongly self-shielding. A semi-

analytical model was therefore developed to describe the same trend with reduced statistical limitations.

### Monte Carlo points and fitted trend

Even for the most reduced tested geometry, corresponding to only about 4.7 t of HFE, the surviving water contribution remains extremely small. The origin of these events is illustrated in Fig. 4.12.

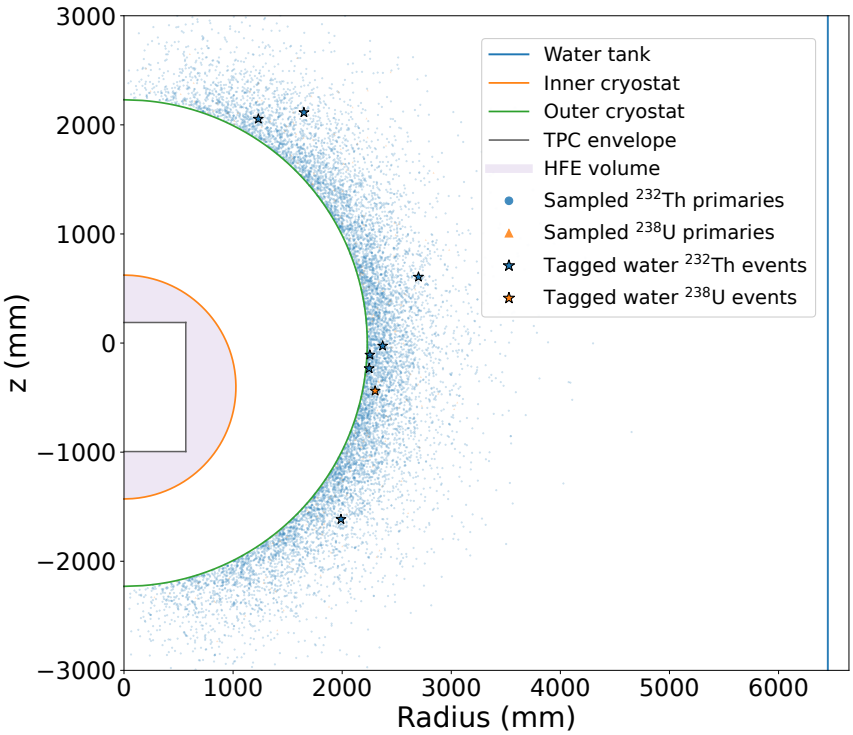


Figure 4.12: TPC-depositing events from water and tagged events producing near-ROI backgrounds.

Figure 4.12 shows that only decays occurring close to the OV deposit energy in the TPC, directly reflecting the strong self-attenuation of water. The tagged near-ROI sample contains seven $^{232}$Th events and one $^{238}$U event; this imbalance is consistent with the higher-energy $\gamma$ line of the $^{232}$Th chain, which is more likely to survive transport through the intervening water and HFE. These rare background-producing primaries are even more concentrated near the OV-facing side of the water volume, showing that the water background is dominated by a thin inner layer.

This behavior is consistent with the attenuation of MeV $\gamma$ rays in water together with the large source-to-TPC distance. Using the linear attenuation coefficient of water at the relevant energy scale, $\mu_{\text{water}} = 4.5 \times 10^{-2}$ cm$^{-1}$ [89], the transmitted fraction after a water thickness $d$ is

$$T(1\,\text{m}) = e^{-4.5} \simeq 1.1 \times 10^{-2}, \tag{4.43}$$

corresponding to only about 1% transmission per meter of water. Thus, even the first few tens of centimeters already provide substantial attenuation.

The MC trend is described by an empirical attenuation law,

$$B^{\mathrm{MC}}_{\mathrm{water}}(R_{\mathrm{IV}}) = N_{\mathrm{water}} e^{-\mu^{\mathrm{fit}}_{\mathrm{water}} R_{\mathrm{IV}}}, \tag{4.44}$$

where $N_{\mathrm{water}}$ is a normalization constant and $\mu^{\mathrm{fit}}_{\mathrm{water}}$ an effective attenuation slope. The fit gives

$$\mu^{\mathrm{fit}}_{\mathrm{water}} = 6.92 \times 10^{-3}\ \mathrm{mm}^{-1}, \tag{4.45}$$

which is compatible with the HFE attenuation coefficient introduced earlier.

### Semi-analytical model

The semi-analytical model keeps the activity inputs and the background formalism of Sec. 4.1.2 unchanged, and replaces only the geometry-dependent efficiency by a water-averaged efficiency.

For isotope $k$, the parent-normalized efficiency is written as

$$\bar{\varepsilon}_{\mathrm{water},k}(R_{\mathrm{IV}}, R_{\mathrm{OV}}) = \varepsilon_{\mathrm{OV},k}(R_{\mathrm{OV}})\, T_{\mathrm{HFE}}(R_{\mathrm{IV}})\, \frac{2\pi}{V_{\mathrm{water}}} \times \int_{-H_{\mathrm{tank}}/2}^{H_{\mathrm{tank}}/2} \int_{0}^{R_{\mathrm{tank}}} f_{\Omega,\mathrm{OV}}(s)\, e^{-\mu_{\mathrm{water}}(s - R_{\mathrm{OV}})}\, r\, dr\, dz, \tag{4.46}$$

with

$$s = \sqrt{r^2 + z^2}. \tag{4.47}$$

Here $\mu_{\mathrm{water}}$ is the linear attenuation coefficient in water at the relevant $\gamma$-ray energy, $V_{\mathrm{water}}$ is the water volume, $f_{\Omega,\mathrm{OV}}(s)$ describes the geometric acceptance of a source point at distance $s$, and $T_{\mathrm{HFE}}(R_{\mathrm{IV}})$ accounts for the change in attenuation through the HFE layer.

The reference efficiency $\varepsilon_{\mathrm{OV},k}(R^0_{\mathrm{OV}})$ is the probability per parent decay in the OV of producing an event passing the analysis selection. It is obtained from the baseline OV-source simulation, with $R^0_{\mathrm{OV}} = 2230\,\mathrm{mm}$ and $R^0_{\mathrm{IV}} = 1691\,\mathrm{mm}$. For a different OV radius, its geometric dependence is approximated by inverse-square scaling,

$$\varepsilon_{\mathrm{OV},k}(R_{\mathrm{OV}}) = \varepsilon_{\mathrm{OV},k}(R^0_{\mathrm{OV}}) \left(\frac{R^0_{\mathrm{OV}}}{R_{\mathrm{OV}}}\right)^2, \tag{4.48}$$

In the HFE-mass scan, $R_{\mathrm{OV}} = R^0_{\mathrm{OV}}$, so this geometric scaling factor equals unity; it is retained for the smaller-OV study below. Changes in HFE shielding relative to the baseline IV radius, $R^0_{\mathrm{IV}} = 1691\,\mathrm{mm}$, are accounted for by

$$T_{\mathrm{HFE}}(R_{\mathrm{IV}}) = \exp\left[-\mu_{\mathrm{HFE}}(R_{\mathrm{IV}} - R^0_{\mathrm{IV}})\right]. \tag{4.49}$$

The geometric factor is taken as

$$f_{\Omega,\mathrm{OV}}(s) = \left(\frac{R_{\mathrm{OV}}}{s}\right)^2 \Theta(s - R_{\mathrm{OV}}), \tag{4.50}$$

where $\Theta$ is the Heaviside step function restricting source points to the water outside the OV. The factor $(R_{\mathrm{OV}}/s)^2$ accounts for the lower geometric acceptance of water

sources farther from the detector. The exponential accounts for attenuation through the water between the source point and the OV surface.

The statistical uncertainty on the baseline OV efficiency for isotope $k$ is taken as

$$\sigma_{\varepsilon,k} = \sqrt{\frac{\varepsilon_{\mathrm{OV},k}(R^0_{\mathrm{OV}})\, b_k}{N_{\mathrm{OV}}}}, \tag{4.51}$$

with $b_k$ the corresponding parent-to-daughter normalization factor and $N_{\mathrm{OV}}$ the number of simulated OV decays. This uncertainty is propagated through the same multiplicative factors entering Eq. (4.46), and the isotope-by-isotope background uncertainties are then combined in quadrature.

This model reproduces the same qualitative picture as the MC tagging study: the contribution is dominated by a thin water layer adjacent to the OV, while deeper regions are exponentially suppressed. In the baseline configuration, the cumulative form of Eq. (4.46) gives a 90% containment thickness of about 0.51 m, showing that the water background is controlled mainly by the first $\sim 50$ cm of the tank.

The semi-analytical model reproduces the MC trend in Fig. 4.11 within the statistical uncertainty of the simulated points. The water contribution increases by at most about two orders of magnitude when going from the baseline geometry to a strongly reduced-HFE configuration. Even in that case, it remains an order of magnitude under the total intrinsic background. Adopting more recent UHP-water assay scale would likely reduce this contribution by at least another order of magnitude.

### 4.3.4 Other Components

Beyond the HFE volume, cryostat vessels, and water shield, the remaining external components are expected to stay subdominant in the intrinsic background budget. The most relevant example considered here is the transition hardware in the water tank.

#### Transition Box

The transition hardware is part of the readout chain and is one of the few service-connected assemblies outside the cryostat that remains relatively close to the TPC. In the baseline design, it includes two CRE transition boxes for the 120 charge modules, split into two groups of 60, together with two PRE transition boxes. These elements are placed in the water tank, about 1 m from the outer cryostat, to keep the readout transition and power regulation closer to the TPC and reduce pickup on the chain [46].

In the present study, the transition boxes are represented by two subcomponents: a stainless-steel enclosure and an internal PCB assembly. The box dimensions are taken to be approximately 45 cm × 30 cm × 30 cm. The adopted masses, activities, and hit efficiencies are summarized in Table 4.8.

The PCB hit efficiencies are taken to be equal to those of the enclosing box. This is a conservative assumption, since the PCBs are in reality smaller than the

| $R_{\mathrm{IV}}$ [mm] | Part | Qty. | Mass [kg] | Isotope | Activity [Bq/kg] | Hit efficiency [cts/(FWHM · 2 t)] |
|---|---|---|---|---|---|---|
| 1026 | Box | 4 | 5.00 | $^{232}$Th | $(-0.95 \pm 0.68) \times 10^{-3}$ | $(2.88 \pm 1.02) \times 10^{-11}$ |
| | Box | 4 | 5.00 | $^{238}$U | $(-0.13 \pm 0.92) \times 10^{-3}$ | $< 1.14 \times 10^{-11}$ |
| | PCB | 4 | 0.25 | $^{232}$Th | $7.40 \pm 0.74$ | $(2.88 \pm 1.02) \times 10^{-11}$ |
| | PCB | 4 | 0.25 | $^{238}$U | $7.39 \pm 0.74$ | $< 1.14 \times 10^{-11}$ |
| 1691 | Box | 4 | 5.00 | $^{232}$Th | $(-0.95 \pm 0.68) \times 10^{-3}$ | $< 4.10 \times 10^{-12}$ |
| | Box | 4 | 5.00 | $^{238}$U | $(-0.13 \pm 0.92) \times 10^{-3}$ | $< 1.14 \times 10^{-11}$ |
| | PCB | 4 | 0.25 | $^{232}$Th | $7.40 \pm 0.74$ | $< 4.10 \times 10^{-12}$ |
| | PCB | 4 | 0.25 | $^{238}$U | $7.39 \pm 0.74$ | $< 1.14 \times 10^{-11}$ |

Table 4.8: Material inputs and hit efficiencies adopted for the transition-box. Steel activities are the collaboration Alabama assay estimates and $1\sigma$ uncertainties before the nonnegative truncated-Gaussian treatment. When no event survives the full selection, a one-sided 68% C.L. upper limit is quoted.

box itself. Dedicated Monte Carlo simulations were performed for $R_{\mathrm{IV}} = 1026\,\mathrm{mm}$ and $R_{\mathrm{IV}} = 1691\,\mathrm{mm}$, with $10^{11}$ generated decays for each configuration.

In the baseline design, no simulated transition-box event survives the full selection. The corresponding hit efficiencies are therefore constrained by the upper limits in Table 4.8, rather than established to be zero. In the reduced-HFE configuration, the contribution becomes visible. The resulting evolution is shown in Fig. 4.13.

To describe this trend, the transition-box background is modeled, as for the previous components, with an exponential attenuation law in the HFE thickness. In this case, however, the attenuation coefficient is fixed to the HFE value for a $\sim 2.5\,\mathrm{MeV}$ $\gamma$ ray in order to avoid a large uncertainty band driven by the baseline point, whose central value is zero. With this choice, the resulting evolution remains compatible with the simulated background values within their uncertainties.

The two explicit Monte Carlo background points are summarized in Table 4.9.

| $R_{\mathrm{IV}}$ [mm] | $m_{\mathrm{HFE}}$ [t] | Component | Background [cts/(FWHM · 2 t · yr)] | Model value [cts/(FWHM · 2 t · yr)] |
|---|---|---|---|---|
| 1026 | 4.60 | Transition box | $(6.713 \pm 2.911) \times 10^{-3}$ | $(6.711 \pm 2.910) \times 10^{-3}$ |
| 1691 | 31.81 | Transition box | $(0.000 \pm 1.702) \times 10^{-3}$ | $(0.0757 \pm 0.0328) \times 10^{-3}$ |

Table 4.9: Transition-box background values for the two MC geometries together with the corresponding values of the fixed-slope attenuation model.

The quoted contribution corresponds to the sum of the two subcomponents over the four transition elements. The quoted model uncertainties are the $1\sigma$ confidence-band half-widths of the fitted mean curve.

Within this model, the transition-box contribution increases by about two orders of magnitude between the baseline design radius and the smallest tested radius, and

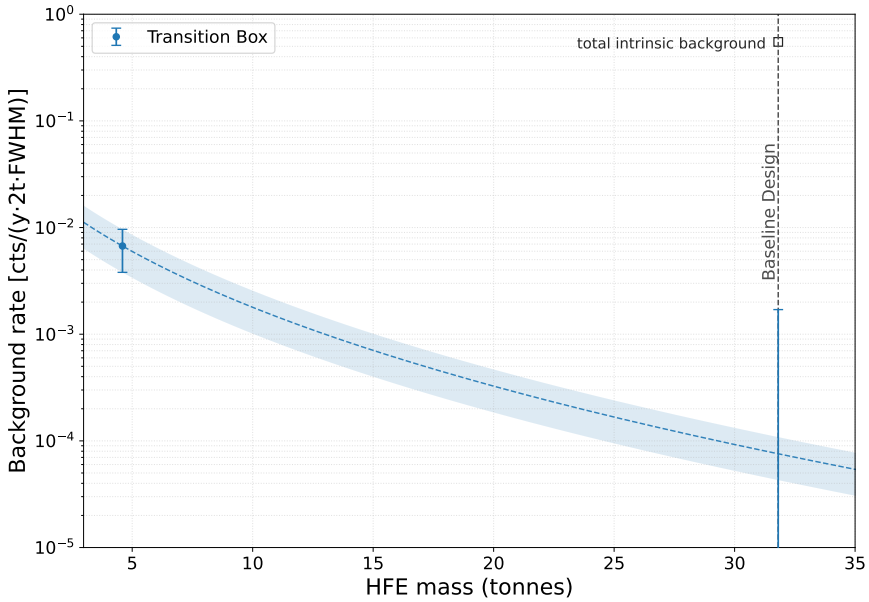


Figure 4.13: Transition-box background contribution as a function of HFE mass. Points are MC-based estimates. The dashed curve shows the fixed-slope attenuation model with fitted normalization and $\mu$ fixed to the HFE attenuation coefficient at $\sim 2.5\,\mathrm{MeV}$. The band shows the $1\sigma$ uncertainty from the fitted normalization.

can become non-negligible. If needed, this contribution could be reduced further by placing the transition boxes deeper in the water shield, thereby increasing their shielding while still allowing a reduced-HFE configuration.

### Supports, Superstructure & Rock

Other structures outside the HFE volume were also checked, including the IV and OV supports, the personnel platform, the superstructure above the cryostat (all visible in Fig. 4.4), and the surrounding outer-detector structures represented here by the OD tank, PMTs and the cryopit concrete/shotcrete. These components are farther from the active xenon than the cryostat vessels and HFE region, but their large masses can still make them relevant once the HFE shield is reduced.

For the nickel support structures, the activity values are the same as those adopted for the nickel cryostat vessels. For the stainless-steel structures, the activities used in the present study are summarized in Table 4.10.

| Material | $^{232}$Th [Bq/kg] | $^{238}$U [Bq/kg] |
|---|---|---|
| Stainless steel | $(4.90 \pm 0.50) \times 10^{-4}$ | $(2.70 \pm 0.30) \times 10^{-4}$ |

Table 4.10: NIRONIT stainless-steel activities used in the present study [91].

These values are consistent with low-background stainless-steel assay scales used in rare-event experiments [91]. For comparison, the GERDA stainless-steel values

used in other collaboration calculations are more stringent, with $^{238}\mathrm{U} < 0.86\,\mathrm{mBq/kg}$ and $^{232}\mathrm{Th} < 0.24\,\mathrm{mBq/kg}$ [91], but these are only upper limits.

The baseline masses and parent-normalized hit efficiencies adopted for the support related external structures are summarized in Table 4.11.

| Component | Material | Mass [kg] | Hit efficiency [cts/(FWHM · 2 t)] | |
|---|---|---|---|---|
| | | | $^{232}$Th | $^{238}$U |
| IV support | Ni | 127.74 | $(3.59 \pm 3.59) \times 10^{-11}$ | $< 1.14 \times 10^{-10}$ |
| OV support | Ni | 623 | $< 4.10 \times 10^{-11}$ | $< 1.14 \times 10^{-10}$ |
| Platform | SS | 210 | $(3.59 \pm 1.14) \times 10^{-10}$ | $(1.00 \pm 1.00) \times 10^{-10}$ |
| Superstructure | SS | 2777 | $< 4.10 \times 10^{-12}$ | $< 1.14 \times 10^{-11}$ |

Table 4.11: Baseline masses and hit efficiencies for support structures. Entries with no surviving events are quoted as one-sided 68% C.L. upper limits.

The corresponding simulations use $10^{10}$ generated primaries for the IV support, OV support, and personnel platform, and $10^{11}$ for the superstructure.

The corresponding background contributions are given in Table 4.12. Independent collaboration estimates for the OD hardware and the cryopit are also included in the baseline background budget. These terms come from dedicated $\gamma$-background studies of the cryopit rock, concrete, and shotcrete, and of outer-detector hardware including the PMTs, their cables and mounts, and the stainless-steel water tank. In the present work, they are treated as imported conservative estimates rather than re-derived from explicit component-level hit-efficiency calculations.

| Component | Background [cts/(FWHM · 2 t · yr)] |
|---|---|
| IV support | $(3.82 \pm 3.26) \times 10^{-8}$ |
| OV support | $(0.00 \pm 1.28) \times 10^{-7}$ |
| Personnel platform | $(1.35 \pm 0.41) \times 10^{-3}$ |
| Superstructure | $(0.00 \pm 1.94) \times 10^{-4}$ |
| OD tank | $5.0 \times 10^{-5}$ |
| OD PMTs | $5.0 \times 10^{-5}$ |
| Cryopit concrete/shotcrete | $4.1 \times 10^{-4}$ |

Table 4.12: Baseline background contributions adopted for the support-related and outer-detector structures discussed in this subsection. The OD tank, OD PMTs, and cryopit values are collaboration independent estimates.

The IV support, OV support, and superstructure remain negligible in the present model, while the personnel platform is the dominant support-related contribution. The support masses may vary slightly with the cryostat geometry and therefore modify their background contributions. This effect is not scaled here, since the support structures could be redesigned for each configuration.

### MLI

The multi-layer insulation (MLI) wrapped around the outer surface of the inner cryostat vessel was the largest single intrinsic-radiogenic contributor in the conservative background allocation when evaluated with the older MLI efficiency assumption. In the present model, it is treated as a five-layer aluminized-PET superinsulation blanket around the IV, following the EXO-200-based inputs adopted in the cryostat design studies [46]. In that configuration, the radiative heat loss through the vacuum insulation is kept below about 100 W [46].

The adopted specific activities are

$$a_{\mathrm{Th}}^{\mathrm{MLI}} = 0.00 \pm 1.01 \times 10^{-2}\ \mathrm{Bq/kg}, \qquad a_{\mathrm{U}}^{\mathrm{MLI}} = (5.79 \pm 0.47) \times 10^{-2}\ \mathrm{Bq/kg}, \tag{4.52}$$

which gives a summed specific activity

$$a_{\Sigma}^{\mathrm{MLI}} = a_{\mathrm{Th}}^{\mathrm{MLI}} + a_{\mathrm{U}}^{\mathrm{MLI}} = (5.79 \pm 1.11) \times 10^{-2}\ \mathrm{Bq/kg}. \tag{4.53}$$

For a total MLI mass of 6.5 kg, this corresponds to a total activity

$$A_{\Sigma}^{\mathrm{MLI}} = m_{\mathrm{MLI}}\, a_{\Sigma}^{\mathrm{MLI}} = (3.76 \pm 0.72) \times 10^{-1}\ \mathrm{Bq}. \tag{4.54}$$

Using the older MLI hit efficiency assumption, this activity gave

$$B_{\mathrm{MLI}}^{0,\mathrm{old}} = (9.98 \pm 3.38) \times 10^{-2}\ \mathrm{cts/(FWHM \cdot 2\,t \cdot yr)}. \tag{4.55}$$

Since the MLI is installed on the outer surface of the inner cryostat vessel, we now instead estimate its background using the updated inner-cryostat-vessel hit efficiency. With this assumption, the same activity gives

$$B_{\mathrm{MLI}}^{0,\mathrm{IV}} = (1.31 \pm 0.29) \times 10^{-2}\ \mathrm{cts/(FWHM \cdot 2\,t \cdot yr)}. \tag{4.56}$$

As a reference, the charge-tile-cable background is

$$B_{\mathrm{ref}} = (2.04 \pm 0.22) \times 10^{-2}\ \mathrm{cts/(FWHM \cdot 2\,t \cdot yr)}. \tag{4.57}$$

With the updated IV-efficiency estimate, the MLI contribution is no longer the dominant intrinsic-radiogenic background in the model. It remains one of the larger individual contributors, but its revised value is below the charge-tile-cable reference contribution.

For the scaling studies with the inner-vessel radius, we scale the MLI mass with the inner-vessel surface area and use the evolution of the inner-cryostat-vessel hit efficiency to determine its background contribution.

Both the required MLI mass and the adopted assay values can still be optimized. A dedicated thermal study is needed to determine the minimum number of layers compatible with the cryogenic requirements, while updated radiopurity measurements are needed to establish a more precise MLI background for the current design.

### 4.3.5 Updated Background Budget

The updated external-component inputs are shown in Fig. 4.14. The red markers correspond to components outside the HFE volume, while the orange marker corresponds to the HFE contribution itself.

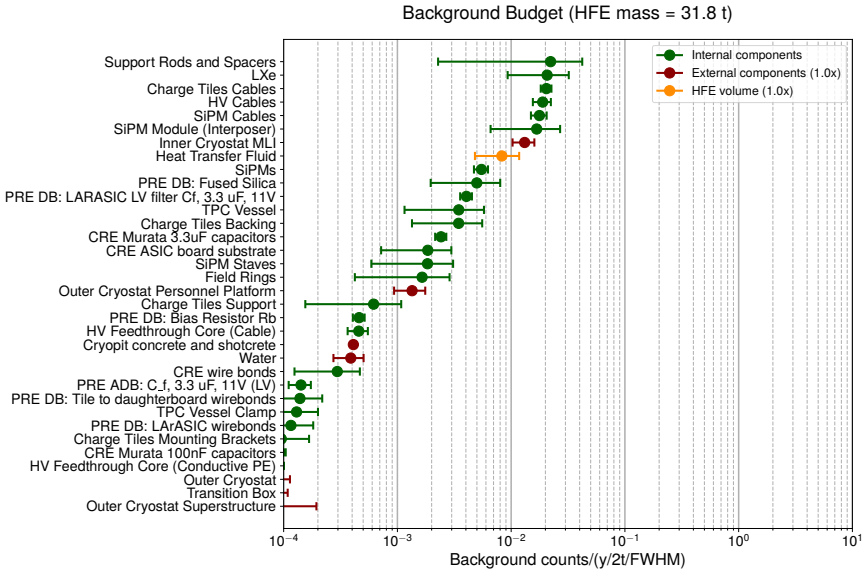


Figure 4.14: Updated component background contribution for the baseline design.

With the corrected external-component inputs, but keeping the previous baseline MLI contribution unchanged, the intrinsic radiogenic baseline background would change only marginally, from

$$B^{31.8\,\mathrm{t}}_{\mathrm{int,\,collab}} = 0.2584 \pm 0.0429 \ \mathrm{cts/(FWHM \cdot 2\,t \cdot yr)} \tag{4.58}$$

to

$$B^{31.8\,\mathrm{t}}_{\mathrm{int,\,updated}} = 0.2595 \pm 0.0429 \ \mathrm{cts/(FWHM \cdot 2\,t \cdot yr)}, \tag{4.59}$$

corresponding to a relative change of +0.4%, well below the quoted uncertainty. When the MLI contribution is instead evaluated with the updated inner-cryostat-vessel hit efficiency, the baseline estimate becomes

$$B^{31.8\,\mathrm{t}}_{\mathrm{int,\,updated}} = 0.1729 \pm 0.0265 \ \mathrm{cts/(FWHM \cdot 2\,t \cdot yr)}, \tag{4.60}$$

a decrease of 33.1% relative to the collaboration implementation. This difference is driven by the revised MLI estimate, while the remaining external/HFE updates are small at the baseline geometry.

To estimate the corresponding reduced-HFE budgets, the components outside the HFE region are propagated with the same HFE-attenuation model used earlier in this section, which was shown to reproduce the dedicated Monte Carlo trends for the vessel- and water-dominated terms. The HFE contribution itself is scaled with the source-dependent evolution obtained in Sec. 4.3.1. The resulting component rankings are shown in Fig. 4.15, and the gray markers indicate the collaboration baseline reference values.

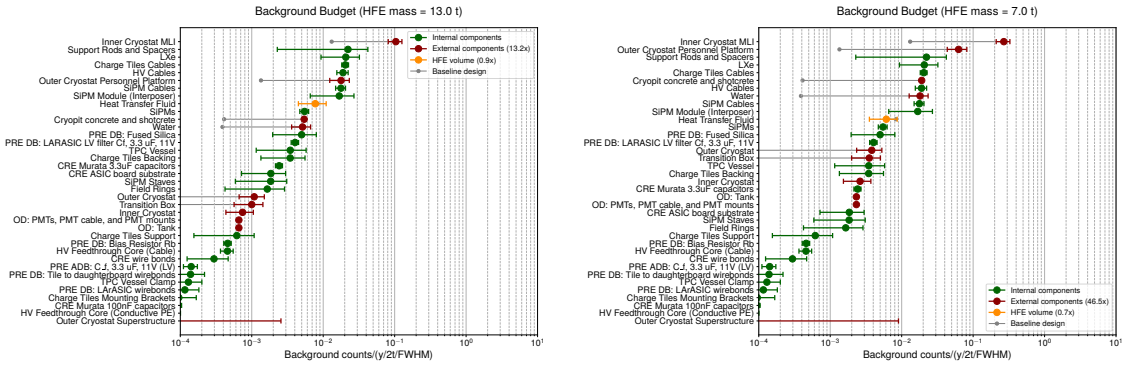


(a) Recommended, $m_{\mathrm{HFE}} = 13.0\,\mathrm{t}$ (b) Aggressive, $m_{\mathrm{HFE}} = 7.0\,\mathrm{t}$

Figure 4.15: Evolution of the radiogenic background contribution with reduced HFE configurations. Red markers correspond to components outside the HFE volume, orange markers to the HFE contribution itself, and gray markers to the collaboration baseline reference where shown.

The summed intrinsic radiogenic contribution from the external/HFE component set is summarized in Table 4.13. In this comparison, the MLI mass is scaled with the inner-vessel surface area, and its background contribution follows the evolution of the inner-cryostat-vessel hit efficiency.

| Configuration | Total intrinsic background [cts/(FWHM · 2 t · yr)] | | External/HFE contribution [cts/(FWHM · 2 t · yr)] | |
|---|---|---|---|---|
| | Value | Change | Value | Change |
| Baseline | $0.2584 \pm 0.0429$ | – | $0.1094 \pm 0.0340$ | – |
| Updated baseline | $0.1729 \pm 0.0265$ | $-33.1\%$ | $0.0239 \pm 0.0045$ | $-78.2\%$ |
| 13 t HFE | $0.2932 \pm 0.0351$ | $+13.5\%$ | $0.1443 \pm 0.0236$ | $+31.8\%$ |
| 7 t HFE | $0.5384 \pm 0.0676$ | $+108.3\%$ | $0.3894 \pm 0.0623$ | $+255.9\%$ |

Table 4.13: Summary of the total intrinsic radiogenic background and of the external/HFE contribution for the different configurations.

Table 4.13 shows that the updated baseline is lower than the collaboration implementation because of the revised MLI estimate. For reduced HFE inventories, however, the external/HFE contribution grows rapidly. At 13 t HFE, the total intrinsic radiogenic background is 13.5% above the collaboration baseline, while the 7 t case gives an increase of 108.3%. The corresponding change in the total background and its impact on sensitivity are discussed more precisely next in Sec. 4.4.

These external/HFE sums correspond to about 14%, 49%, and 72% of the total intrinsic radiogenic contribution for the updated baseline, 13 t, and 7 t configurations, respectively. As the HFE shield is reduced, the MLI, personnel platform, cryopit concrete, and water contributions become major, or near-major, terms in the external budget. By contrast, the cryostat vessels and OD hardware remain comparatively small contributors throughout the scan. The other support-related

structures stay negligible at the level of their central values, although the uncertainties associated with the outer-cryostat superstructure broaden substantially in the reduced-HFE configurations and reach non-negligible levels.

## 4.4 Possible Design Optimizations

In the current baseline design, the cryogenic shield is defined by the requirement that the HFE bath provide a minimum thickness of about 76 cm from the edge of the TPC in all directions, which corresponds to an HFE inventory of about 32 t in the reference geometry. The results of Sec. 4.3 show, however, that in the updated nickel design the background is no longer dominated by a single cryostat-related term. Instead, the remaining contribution is distributed among the HFE region, inner cryostat structures, nearby detector components, and more distant shielding volumes. The optimization problem is therefore no longer simply to maximize shielding thickness, but to determine how far the cryogenic envelope can be reduced relative to this baseline requirement before the associated increase in radiogenic background becomes significant.

### 4.4.1 Reduced HFE Configuration

Two reduced-HFE configurations are retained for further study and design optimization: a recommended configuration with 13 t of HFE, and an aggressive configuration with 7 t of HFE. Their geometric parameters and approximate external attenuation factors are summarized in Table 4.14.

| Configuration | $m_{\mathrm{HFE}}$ [t] | $V_{\mathrm{HFE}}$ [m$^3$] | $R_{\mathrm{IV}}$ [mm] | $m_{\mathrm{HFE}}/m^0_{\mathrm{HFE}}$ | $f_{\mathrm{ext}}$ |
|---|---|---|---|---|---|
| Baseline | 31.8 | 18.38 | 1691 | 1.000 | 1.0 |
| Recommended | 13.0 | 7.51 | 1308 | 0.409 | 13.2 |
| Aggressive | 7.0 | 4.05 | 1122 | 0.220 | 46.5 |

Table 4.14: Baseline and reduced-HFE candidate configurations considered for the design optimization study. The corresponding inner-vessel radii are shown together with the approximate external attenuation factor $f_{\mathrm{ext}}$.

Relative to the baseline, the recommended and aggressive configurations reduce the HFE mass by 59.1% and 78.0%, respectively. The corresponding inner-vessel radius decreases from 1691 mm to 1308 mm and 1122 mm, that is, by 22.6% and 33.7%. The attenuation factors in Table 4.14 already show that the shielding penalty grows rapidly as the HFE layer is reduced.

The component-by-component evolution of the external contributions studied in this chapter is shown together in Fig. 4.16 with the HFE masses corresponding to the proposed designs.

Table 4.15 summarises the evolution of both the total intrinsic background and the total background for each configuration relative to the pre-update baseline.

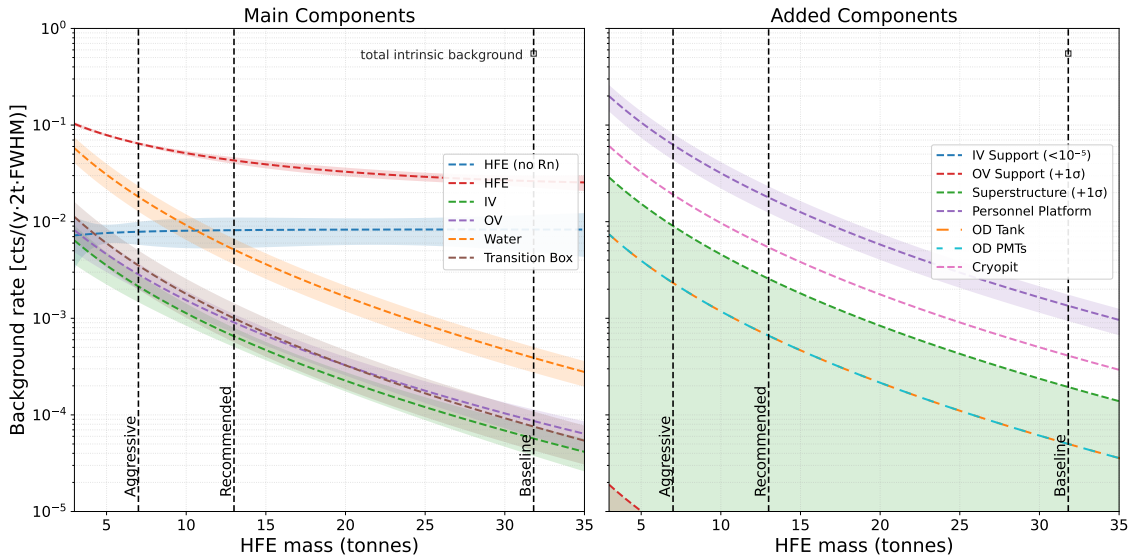


Figure 4.16: Background contribution of the studied external components as a function of HFE mass. The vertical dashed lines indicate the aggressive, recommended, and baseline configurations.

The total intrinsic background decreases by 33.1% for the updated baseline, mainly because of the revised MLI estimate. It then rises by 13.5% for the recommended 13 t configuration and by 108.3% for the aggressive 7 t configuration, both relative to the pre-update baseline. Because the fixed non-intrinsic and non-signal invariant contribution,

$$B_{\text{fixed}} = 0.2941 \text{ cts}/(\text{FWHM} \cdot 2\,\text{t} \cdot \text{yr}), \tag{4.61}$$

is held fixed in this study, the total background varies more moderately: −15.5% for the updated baseline, +6.3% for the recommended configuration, and +50.7% for the aggressive one. More dedicated studies would be needed to check whether other background classes would also vary under these design changes.

| Configuration | Total intrinsic background [cts/(FWHM · 2 t · yr)] | | Total background [cts/(FWHM · 2 t · yr)] | |
|---|---|---|---|---|
| | Value | Change | Value | Change |
| Baseline | $0.2584 \pm 0.0429$ | – | $0.5525 \pm 0.0450$ | – |
| Updated baseline | $0.1729 \pm 0.0265$ | −33.1% | $0.4670 \pm 0.0297$ | −15.5% |
| 13 t HFE | $0.2932 \pm 0.0351$ | +13.5% | $0.5874 \pm 0.0377$ | +6.3% |
| 7 t HFE | $0.5384 \pm 0.0676$ | +108.3% | $0.8325 \pm 0.0689$ | +50.7% |

Table 4.15: Summary of the total intrinsic background and total background for each configuration.

Using the sensitivity-scaling approximation from Eq. (2.12),

$$T_{1/2}^{0\nu} \propto B^{-0.28}, \tag{4.62}$$

the background variations can be converted into approximate relative changes in the $0\nu\beta\beta$ half-life sensitivity. The updated baseline lies only about 7% below the studied background range, making this modest extrapolation reasonable for an approximate estimate given the weak background dependence of the fitted relation.

Taking the baseline total background to be $B_0 = 0.5525$ SS cts/(FWHM $\cdot$ 2 t $\cdot$ yr) and adopting the reference sensitivity $T^{0\nu}_{1/2,0} = 1.35 \times 10^{28}$ yr [47], the resulting approximate sensitivities are summarized in Table 4.16.

| Configuration | $B/B_0$ | $T^{0\nu}_{1/2}/T^{0\nu}_{1/2,0}$ | $T^{0\nu}_{1/2}$ [yr] |
|---|---|---|---|
| Baseline | 1.000 | 1.000 | $1.35 \times 10^{28}$ |
| Updated baseline | 0.845 | 1.048 | $1.42 \times 10^{28}$ |
| 13 t HFE | 1.063 | 0.983 | $1.33 \times 10^{28}$ |
| 7 t HFE | 1.507 | 0.892 | $1.20 \times 10^{28}$ |

Table 4.16: Approximate change in $0\nu\beta\beta$ half-life sensitivity derived from the total-background scaling $T^{0\nu}_{1/2} \propto B^{-0.28}$, using the baseline value $T^{0\nu}_{1/2,0} = 1.35 \times 10^{28}$ yr.

Table 4.16 shows that the impact on sensitivity is weaker than the corresponding change in background, as expected from the scaling in Eq. (2.12). The updated baseline gives a slightly improved sensitivity because of the reduced background. For the recommended 13 t configuration, the increase in total background translates into only about a 1.7% reduction in $T^{0\nu}_{1/2}$ sensitivity relative to the pre-update baseline. For the aggressive 7 t option, the expected degradation is larger, at about 10.8%.

### Thinner Cryostat Vessels

A reduced-HFE configuration also permits thinner cryostat vessels. This matters because the vessel contribution depends both on the shielding between the vessel and the TPC and on the vessel source mass itself. The fixed-thickness scans of Sec. 4.3.2 already include the reduction in vessel mass associated with the smaller vessel surface at fixed wall thickness. The optimization considered here therefore accounts only for the additional reduction obtained when the wall thickness itself is allowed to scale with radius.

For the inner vessel, the wall thickness of a spherical shell under pressure follows the hoop-stress relation [92]:

$$\sigma_{\theta,\mathrm{sph}} = \frac{P\,R}{2\,t_{\mathrm{sph}}} \quad \Longrightarrow \quad t_{\mathrm{sph}} = \frac{P\,R}{2\,\sigma_{\mathrm{allow}}}, \tag{4.63}$$

where $P$ is the internal pressure, $R$ the mean shell radius, and $\sigma_{\mathrm{allow}}$ the allowable membrane stress. At fixed design pressure and allowable stress, this implies $t_{\mathrm{sph}} \propto R$. The present study therefore uses the scaling

$$t_{\mathrm{IV}}(R_{\mathrm{IV}}) = t^0_{\mathrm{IV}}\,\frac{R_{\mathrm{IV}}}{R^0_{\mathrm{IV}}}, \tag{4.64}$$

with

$$t_{\mathrm{IV}}^{0} = 5\,\mathrm{mm}, \qquad R_{\mathrm{IV}}^{0} = 1691\,\mathrm{mm}. \tag{4.65}$$

This is used here as a mechanical parameterization for the background study; final vessel dimensions would require dedicated engineering validation.

Assuming fixed material density, the optimized-thickness vessel mass then scales as

$$m_{\mathrm{IV}}(R_{\mathrm{IV}}) = m_{\mathrm{IV}}^{0} \left( \frac{R_{\mathrm{IV}}}{R_{\mathrm{IV}}^{0}} \right)^{3}, \tag{4.66}$$

with

$$m_{\mathrm{IV}}^{0} = 1681.6\,\mathrm{kg}. \tag{4.67}$$

For comparison, a fixed-thickness spherical shell scales at first order as $m_{\mathrm{IV}}^{\mathrm{fixed}} \propto R_{\mathrm{IV}}^{2}$. The resulting evolution of $t_{\mathrm{IV}}$ and $m_{\mathrm{IV}}$ across the scanned HFE range is shown in Fig. 4.17. For the two reduced-HFE configurations, this gives

$$t_{\mathrm{IV}}(13\,\mathrm{t}) = 3.87\,\mathrm{mm}, \qquad m_{\mathrm{IV}}(13\,\mathrm{t}) \simeq 779\,\mathrm{kg}, \tag{4.68}$$

and

$$t_{\mathrm{IV}}(7\,\mathrm{t}) = 3.32\,\mathrm{mm}, \qquad m_{\mathrm{IV}}(7\,\mathrm{t}) \simeq 491\,\mathrm{kg}. \tag{4.69}$$

The IV mass is thus reduced to 46.3% and 29.2% of its baseline value in the recommended and aggressive configurations, respectively.

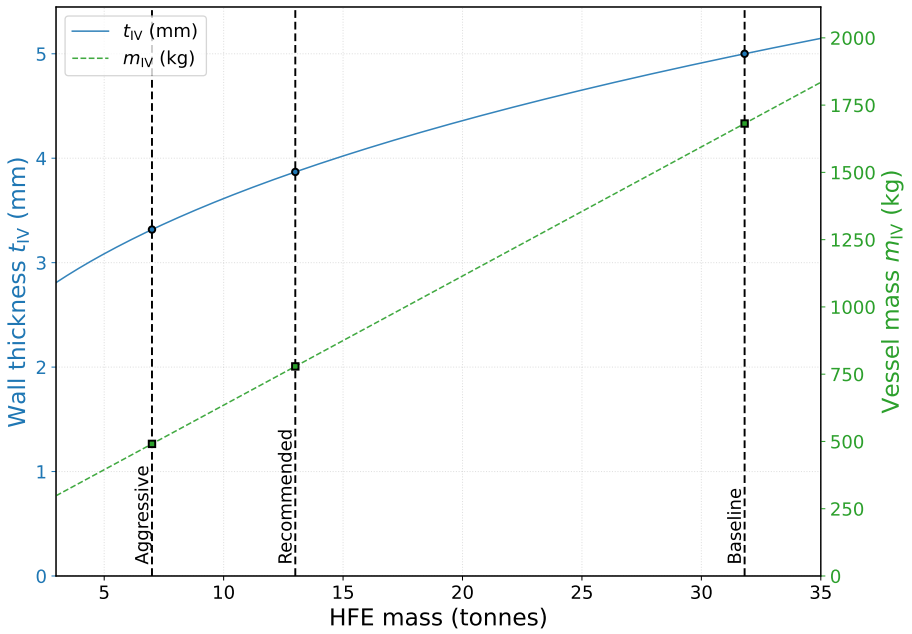


Figure 4.17: Inner-vessel wall thickness and vessel mass obtained from the radius-scaling model.

This mass reduction directly lowers the intrinsic IV source term. Because the fixed-thickness IV background curve from Sec. 4.3.2 already includes the radius dependence of the IV mass at fixed thickness, the optimized-thickness correction

must be applied as the ratio of the optimized-thickness and fixed-thickness mass scalings,

$$B_{\mathrm{IV}}^{\mathrm{thin}}(R_{\mathrm{IV}}) = B_{\mathrm{IV}}^{\mathrm{fixed}}(R_{\mathrm{IV}}) \frac{m_{\mathrm{IV}}^{\mathrm{thin}}(R_{\mathrm{IV}})}{m_{\mathrm{IV}}^{\mathrm{fixed}}(R_{\mathrm{IV}})} \simeq B_{\mathrm{IV}}^{\mathrm{fixed}}(R_{\mathrm{IV}}) \left( \frac{R_{\mathrm{IV}}}{R_{\mathrm{IV}}^{0}} \right), \tag{4.70}$$

where the last step uses $m_{\mathrm{IV}}^{\mathrm{fixed}} \propto R_{\mathrm{IV}}^{2}$ together with Eq. (4.66). The resulting evolution is shown in Fig. 4.18.

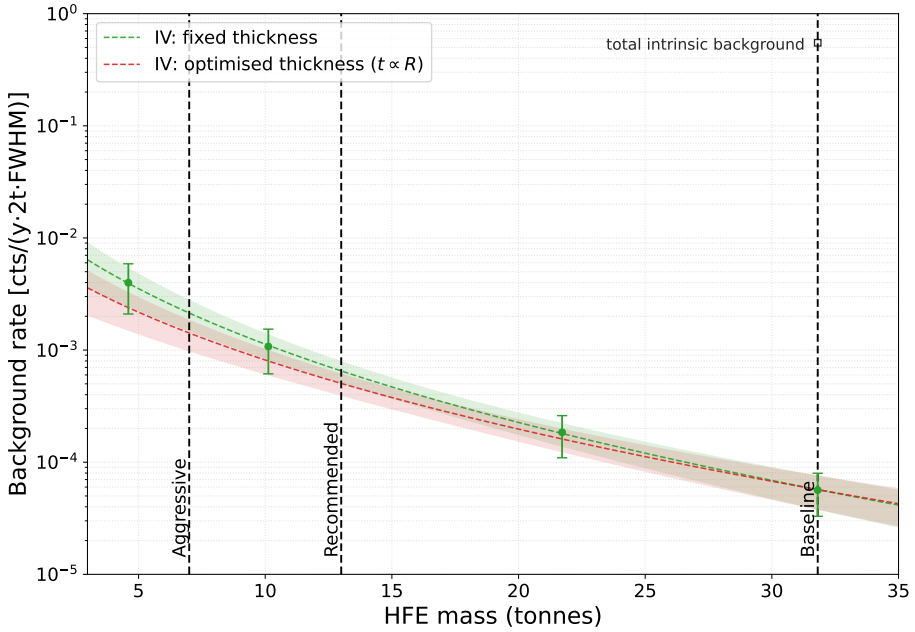


Figure 4.18: Inner-vessel background contribution as a function of HFE mass for the fixed-thickness model and for the optimized-thickness scaling $t \propto R$.

The quantitative effect at the two reduced-HFE design points is summarized in Table 4.17. At 13 t, the IV contribution is reduced from $6.52 \times 10^{-4}$ to $5.04 \times 10^{-4}$ cts/(FWHM · 2 t · yr), corresponding to a 22.6% reduction. At 7 t, it decreases from $2.14 \times 10^{-3}$ to $1.42 \times 10^{-3}$ cts/(FWHM · 2 t · yr), corresponding to a 33.7% reduction.

Allowing the IV to become thinner partly compensates the background increase associated with reduced HFE shielding. The compensation is moderate because the fixed-thickness curve already contains the radius-dependent decrease of the IV mass at fixed wall thickness; the optimized-thickness model adds only the extra $R_{\mathrm{IV}}/R_{\mathrm{IV}}^{0}$ suppression. The transmitted IV background still rises as the HFE layer is reduced, but the increase is mitigated by the smaller vessel mass. This remains a first-order correction rather than a final mechanical design result, but it shows that a reduced-HFE configuration is somewhat less penalizing than the fixed-thickness scan alone would suggest.

The same optimization logic can also be applied to the outer vessel if the OV radius is reduced together with the overall cryostat size. That case is considered separately in the following subsection.

| Configuration | $B_{\mathrm{IV}}^{\mathrm{fixed}}$ | $B_{\mathrm{IV}}^{\mathrm{thin}}$ | Reduction |
|---|---|---|---|
| Recommended (13 t) | $6.52 \times 10^{-4}$ | $5.04 \times 10^{-4}$ | −22.6% |
| Aggressive (7 t) | $2.14 \times 10^{-3}$ | $1.42 \times 10^{-3}$ | −33.7% |

Table 4.17: Inner-vessel background contribution at the recommended and aggressive reduced-HFE configurations for the fixed-thickness and optimized-thickness models. Background rates are given in cts/(FWHM · 2 t · yr).

### Cold Mass

The HFE bath around the TPC is not only a radiation shield but also a thermal buffer. The TPC must be maintained close to its operating temperature of about 165 K, with a stability requirement at the level of ±1 K, while the HFE inventory provides the large thermal inertia needed to smooth temperature gradients across the thin TPC vessel and to keep the xenon liquid through temporary losses of cooling power [46].

For a passive warm-up estimate, the relevant quantity is the heat capacity of the cold mass that follows the TPC temperature. For a set of cold components with masses $m_i$ and specific heats $c_{p,i}$, the thermal energy associated with a temperature change $\Delta T$ is

$$E_{1\mathrm{K}} = \Delta T \sum_i m_i c_{p,i}. \tag{4.71}$$

Using $\Delta T = 1\,\mathrm{K}$, $E_{1\mathrm{K}}$ provides a convenient measure of thermal inertia. In the present estimate, the sum includes the HFE inventory, 5 t of LXe, and the radius-scaled nickel inner vessel. The HFE-7200 specific heat is estimated at 165 K using the approximate temperature-dependent model described in Sec. 5.1.2, giving $c_p \simeq 828\,\mathrm{J\,kg^{-1}\,K^{-1}}$. The LXe and nickel specific heats used are $339\,\mathrm{J\,kg^{-1}\,K^{-1}}$ and $330\,\mathrm{J\,kg^{-1}\,K^{-1}}$, respectively, with the latter obtained by linear interpolation of the NIST-JANAF values at 100 K and 200 K [93].

The same energy scale can be converted into the time required for a 1 K temperature rise under the nEXO heat leaks. For a fixed parasitic heat load $\dot{Q}$,

$$t_{1\mathrm{K}} = \frac{E_{1\mathrm{K}}}{\dot{Q}}. \tag{4.72}$$

Using the nEXO steady-state heat-loss estimate $\dot{Q} = 490\,\mathrm{W}$ [46], the 5 t LXe inventory alone corresponds to 1.70 MJ/K, or 0.96 h for a 1 K passive warm-up.

The resulting passive warm-up time is shown in Fig. 4.19. The curve labelled "With HFE" includes the summed contribution from the HFE, the LXe, and the radius-scaled nickel inner vessel, while the component curves show the LXe and nickel contributions separately. The vertical lines indicate the baseline, recommended, and aggressive HFE configurations.

The corresponding values for the baseline, recommended, and aggressive configurations are summarized in Table 4.18.

Table 4.18 shows that the HFE remains the dominant contributor to the thermal inertia of the cold system in all three configurations. Even in the aggressive design,

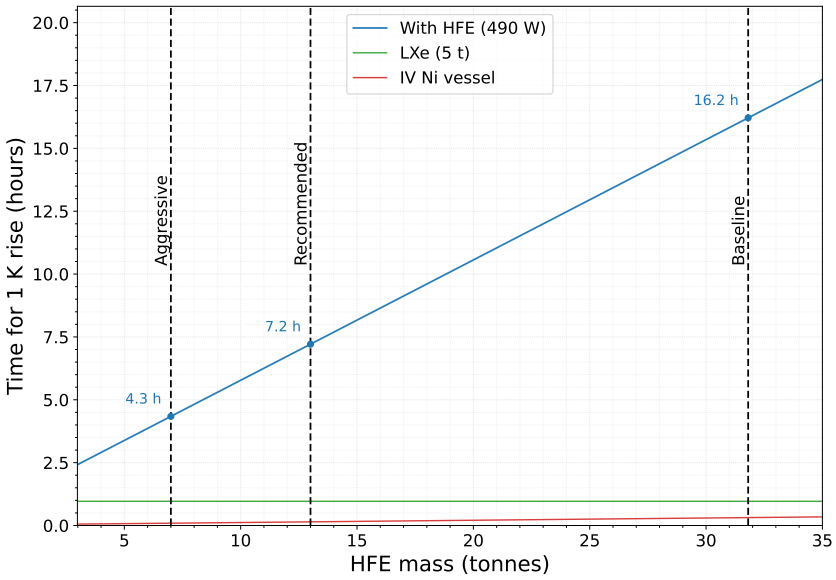


Figure 4.19: Time required for a 1 K temperature rise as a function of HFE mass, assuming the nEXO steady-state heat leak of 490 W.

| Design | $m_{\mathrm{HFE}}$ [t] | $E_{1\mathrm{K}}$ [MJ] | $t_{1\mathrm{K}}$ [h] | vs baseline | vs 5 t LXe |
|---|---|---|---|---|---|
| Baseline | 31.8 | 28.6 | 16.2 | — | ×16.9 |
| Recommended | 13.0 | 12.7 | 7.2 | −56% | ×7.5 |
| Aggressive | 7.0 | 7.7 | 4.3 | −73% | ×4.5 |

Table 4.18: Thermal energy required for a 1 K temperature rise and corresponding passive warm-up time for the baseline, recommended, and aggressive configurations.

the total cold capacity is 7.7 MJ/K, corresponding to a passive 1 K warm-up time of about 4.3 h at the assumed nEXO heat leak. This is still about 4.5 times the 5 t LXe reference alone.

From the cryogenic point of view, lowering the HFE cold mass is favorable for cooldown and the total refrigeration burden, but it also reduces the passive thermal buffer against interruptions in cooling. The recommended configuration gives a 1 K warm-up time of about 7.2 h, while removing most of the HFE relative to the baseline and keeping the increase in external intrinsic background modest. The aggressive configuration yields a further reduction in HFE mass, but with both a shorter passive warm-up time and a substantially larger shielding penalty.

### 4.4.2 Improved Water Shielding with a Smaller Outer Vessel

At fixed $R_{\mathrm{IV}}$, reducing the outer-vessel radius decreases the cryostat size while increasing the water thickness between the OV and the tank wall. This is potentially advantageous because it lowers the OV mass and can improve shielding against source terms external to the cryostat without changing the HFE inventory. The relevant question is then whether the intrinsic contributions from the OV and from the water remain stable, or are even reduced, when $R_{\mathrm{OV}}$ is decreased.

For the OV itself, the leading behavior follows from

$$B_{\mathrm{OV}} \propto M_{\mathrm{OV}}\,\varepsilon_{\mathrm{OV}}. \tag{4.73}$$

For a thin spherical shell of fixed thickness,

$$M_{\mathrm{OV}} \propto R_{\mathrm{OV}}^2, \tag{4.74}$$

while, at fixed HFE shielding, the geometric part of the hit efficiency scales approximately as

$$\varepsilon_{\mathrm{OV}} \propto \frac{1}{R_{\mathrm{OV}}^2}. \tag{4.75}$$

To first order, these two factors cancel, so the fixed-thickness OV background is expected to depend only weakly on $R_{\mathrm{OV}}$. If the OV thickness is also allowed to scale as $t_{\mathrm{OV}} \propto R_{\mathrm{OV}}$, then $M_{\mathrm{OV}} \propto R_{\mathrm{OV}}^3$, and the OV contribution correspondingly decreases for smaller radii.

This behavior is consistent with the dedicated tests performed at fixed $R_{\mathrm{IV}} = 1226$ mm, corresponding to $m_{\mathrm{HFE}} \approx 10$ t. The derived hit efficiencies are listed in Table 4.19, and the corresponding OV background values in Table 4.20.

Reducing $R_{\mathrm{OV}}$ from 2230 mm to 1765 mm increases the hit efficiency for both chains, consistent with the larger solid angle subtended by the TPC. The effect is larger than the corresponding change in the total OV background because the smaller vessel surface also reduces the OV source mass.

Reducing $R_{\mathrm{OV}}$ from 2230 mm to 1765 mm changes the fixed-thickness OV contribution by only 7.6%, while the inclusion of the thickness optimization gives a total reduction of 26.9% relative to the baseline.

| $R_{\mathrm{OV}}$ [mm] | Isotope | Hit efficiency [cts/(FWHM · 2 t)] | Error [cts/(FWHM · 2 t)] |
|---|---|---|---|
| 2230 | $^{232}$Th | $1.73 \times 10^{-8}$ | $7.88 \times 10^{-10}$ |
| | $^{238}$U | $7.10 \times 10^{-9}$ | $8.43 \times 10^{-10}$ |
| 1765 | $^{232}$Th | $2.70 \times 10^{-8}$ | $9.84 \times 10^{-10}$ |
| | $^{238}$U | $1.05 \times 10^{-8}$ | $1.02 \times 10^{-9}$ |

Table 4.19: OV hit efficiencies at fixed $R_{\mathrm{IV}} = 1226\,\mathrm{mm}$ for the baseline and smaller-OV configurations.

| $R_{\mathrm{OV}}$ [mm] | $t_{\mathrm{OV}}$ [mm] | Background [cts/(FWHM · 2 t · yr)] | Reduction vs. baseline |
|---|---|---|---|
| 2230 | 10.00 | $(1.5916 \pm 0.6735) \times 10^{-3}$ | — |
| 1765 | 10.00 (fixed) | $(1.4704 \pm 0.6140) \times 10^{-3}$ | −7.6% |
| | 7.91 (optimized) | $(1.1638 \pm 0.4860) \times 10^{-3}$ | −26.9% |

Table 4.20: OV intrinsic background at fixed $R_{\mathrm{IV}} = 1226\,\mathrm{mm}$ for the baseline and smaller-OV configurations. The optimized-thickness values use the scaling $t_{\mathrm{OV}} \propto R_{\mathrm{OV}}$.

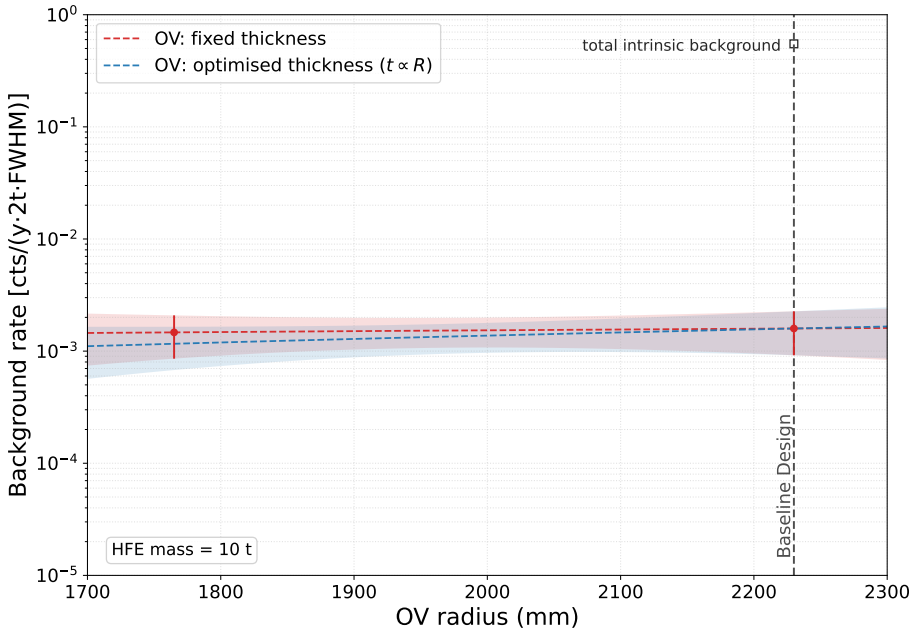


Figure 4.20: Outer-vessel intrinsic background as a function of $R_{\mathrm{OV}}$ at fixed $R_{\mathrm{IV}} = 1226\,\mathrm{mm}$ ($m_{\mathrm{HFE}} \approx 10\,\mathrm{t}$). The red curve shows the fixed-thickness case, while the blue curve includes the optimized-thickness scaling $t_{\mathrm{OV}} \propto R_{\mathrm{OV}}$. The vertical dashed line indicates the baseline design.

The water contribution can be treated with the semi-analytical model introduced in Sec. 4.3.3. At fixed $R_{\mathrm{IV}}$, its $R_{\mathrm{OV}}$ dependence can be written as

$$B_{\mathrm{water}}(R_{\mathrm{OV}}) \propto M_{\mathrm{water}}(R_{\mathrm{OV}}) \left(\frac{R_{\mathrm{OV}}^{0}}{R_{\mathrm{OV}}}\right)^{2} F(R_{\mathrm{OV}}), \tag{4.76}$$

where $F(R_{\mathrm{OV}})$ averages the product of the geometric acceptance and attenuation factors over the water volume, as defined in Eq. (4.46).

The intrinsic water contribution for the two OV configurations is summarized in Table 4.21. The change is negligible over the range considered here.

| $R_{\mathrm{OV}}$ [mm] | $B_{\mathrm{water}}$ [cts/(FWHM · 2 t · yr)] | Error [cts/(FWHM · 2 t · yr)] | Change vs. baseline |
|---|---|---|---|
| 2230 | $8.95 \times 10^{-3}$ | $2.65 \times 10^{-3}$ | — |
| 1765 | $8.93 \times 10^{-3}$ | $2.64 \times 10^{-3}$ | $-0.24\%$ |

Table 4.21: Semi-analytical intrinsic water background at fixed $R_{\mathrm{IV}} = 1226\,\mathrm{mm}$ ($m_{HFE} \approx 10$ t) for the baseline and smaller-OV configurations.

This near-constancy follows the same logic as for the OV itself. Because of self-attenuation, only the water close to the OV contributes appreciably to the background. When $R_{\mathrm{OV}}$ is reduced, an additional shell of water is added inward, but its geometric acceptance toward the TPC scales approximately as $1/R_{\mathrm{OV}}^{2}$, while the corresponding shell mass scales as $R_{\mathrm{OV}}^{2}$. To first order, these effects compensate, so the intrinsic water contribution remains nearly unchanged.

The smaller OV nevertheless improves shielding against source terms external to the detector. Shrinking $R_{\mathrm{OV}}$ from 2230 mm to 1765 mm adds

$$\Delta x = 46.5\,\mathrm{cm} \tag{4.77}$$

of water between the cryostat and the tank wall. Using the attenuation coefficient introduced earlier for 2.5 MeV $\gamma$ rays in water, this corresponds to an additional suppression factor

$$\exp(-\mu_{\mathrm{water}}\Delta x) = \exp\left[-(4.5\ \mathrm{m}^{-1}) \times 0.465\,\mathrm{m}\right] \simeq 0.12, \tag{4.78}$$

that is, a reduction by a factor of about 8 for source terms that must cross this added water layer.

A smaller OV therefore does not significantly penalize the detector-intrinsic background model. The intrinsic water term remains essentially constant, while the added water thickness provides stronger shielding against backgrounds originating outside the cryostat.

### 4.4.3 Cylindrical Cryostat

The baseline cryostat design uses spherical vessels because this geometry minimizes wall stress and vessel mass for a given pressure requirement, which was crucial for the

original CFC-vessel design. Now that the nickel design is the default, a cylindrical alternative is worth considering, since it could simplify fabrication and reduce the HFE inventory by matching the cylindrical TPC geometry more closely and by maintaining the required minimum HFE thickness around the TPC. Figure 4.21 compares the baseline spherical layout to the cylindrical option considered here.

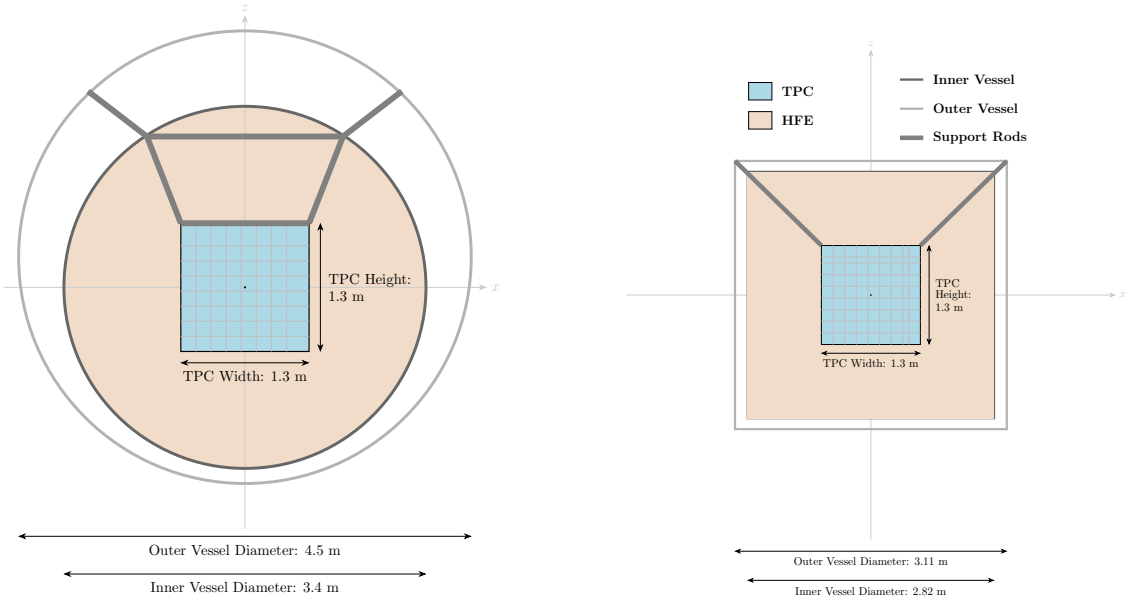


(a) Spherical cryostat (baseline)

(b) Cylindrical cryostat

Figure 4.21: Schematic representations of the TPC and cryostat geometries for the baseline spherical design and the cylindrical cryostat option.

### HFE quantity

Using the same minimum HFE requirement as in the baseline design, the cylindrical inner vessel, with flat ends, is taken to enclose the TPC with a uniform radial and axial clearance of 760 mm. For the rounded reference TPC dimensions ($R_{\mathrm{TPC}} = 650\,\mathrm{mm}$, $H_{\mathrm{TPC}} = 1300\,\mathrm{mm}$), this gives

$$R_{\mathrm{IV}}^{\mathrm{cyl}} = 1410\,\mathrm{mm}, \qquad H_{\mathrm{IV}}^{\mathrm{cyl}} = 2820\,\mathrm{mm}. \tag{4.79}$$

Because the vessel now follows the TPC profile, the HFE thickness is much more uniform than in the spherical case. The corresponding HFE volume is therefore reduced to about $15.9\,\mathrm{m}^3$, or

$$m_{\mathrm{HFE}}^{\mathrm{cyl}} \simeq 27.5\,\mathrm{t},$$

which is about 14% below the spherical baseline. This simplified volume estimate subtracts only the TPC envelope and neglects other displaced volumes.

This reduction in HFE inventory comes with a modest shielding penalty. Relative to the spherical baseline, the cylindrical option gives a smaller mean-equivalent attenuation thickness and therefore a larger average transmission for 2.5 MeV $\gamma$ rays. The mean transmission increases from about 0.17% in the spherical case to

about 0.35% in the cylindrical one. The cylindrical geometry therefore remains close to the design shielding target, but no longer benefits from the additional average shielding provided by the spherical envelope.

### Outer-vessel size

The cylindrical option is constructed by preserving the baseline minimum IV–OV vacuum-gap requirement,

$$t_{\mathrm{vac,min}} = 126\,\mathrm{mm}.$$

Keeping the outer vessel concentric with the inner vessel then gives

$$R_{\mathrm{OV}}^{\mathrm{cyl}} = R_{\mathrm{IV}}^{\mathrm{cyl}} + t_{\mathrm{vac,min}} = 1.410\,\mathrm{m} + 0.126\,\mathrm{m} = 1.536\,\mathrm{m}, \tag{4.80}$$

$$H_{\mathrm{OV}}^{\mathrm{cyl}} = H_{\mathrm{IV}}^{\mathrm{cyl}} + 2\,t_{\mathrm{vac,min}} = 2.820\,\mathrm{m} + 2 \times 0.126\,\mathrm{m} = 3.07\,\mathrm{m}. \tag{4.81}$$

If more clearance is needed for supports, service lines, or cryogenic feedthroughs, the radius and height can both be increased.

Relative to the spherical baseline, the cylindrical option therefore reduces the overall cryostat size. For the inner vessel, both the radius and the total height decrease by about 17%, while for the outer vessel the corresponding reductions are about 32%.

### Vessel thickness

The side-wall thickness of a cylindrical shell under pressure follows the hoop-stress relation [92]:

$$\sigma_{\theta,\mathrm{cyl}} = \frac{P\,R}{t_{\mathrm{cyl}}} \quad \Longrightarrow \quad t_{\mathrm{cyl}} = \frac{P\,R}{\sigma_{\mathrm{allow}}}, \tag{4.82}$$

where $P$ is the internal pressure, $R$ the mean shell radius, and $\sigma_{\mathrm{allow}}$ the allowable membrane stress. Comparing this expression with Eq. (4.63) shows that, at fixed radius and allowable stress,

$$t_{\mathrm{cyl}} = 2\,t_{\mathrm{sph}}. \tag{4.83}$$

For this preliminary comparison, the present estimate assumes cylindrical side-wall thicknesses twice the baseline spherical thicknesses:

$$t_{\mathrm{cyl,\,inner}} = 2 \times 5\,\mathrm{mm} = 10\,\mathrm{mm}, \qquad t_{\mathrm{cyl,\,outer}} = 2 \times 10\,\mathrm{mm} = 20\,\mathrm{mm}. \tag{4.84}$$

The flat endcaps are assumed to have the same thicknesses as the spherical vessels (5 mm for the inner vessel and 10 mm for the outer vessel). With this parameterization, the estimated nickel masses become

$$M_{\mathrm{IV}}^{\mathrm{cyl}} \simeq 2.61\,\mathrm{t}, \qquad M_{\mathrm{OV}}^{\mathrm{cyl}} \simeq 6.24\,\mathrm{t}, \tag{4.85}$$

to be compared with about 1.6 t and 5.71 t for the spherical baseline. These values are only preliminary and do not include any detailed analysis of endplate bending, buckling or stiffening, but they are sufficient to illustrate the background trade-off for these assumed thicknesses.

### Background contribution

Monte Carlo studies used the spherical baseline geometry to determine the reference hit efficiencies $\varepsilon_{0,i}^{\mathrm{sph}}$ (cts/(FWHM·2 t)) for each isotope $i$. To obtain the corresponding cylindrical-baseline efficiencies, these values are first rescaled by the ratio of the mean 2.5 MeV transmission:

$$\varepsilon_{0,i}^{\mathrm{cyl}} = \varepsilon_{0,i}^{\mathrm{sph}} \times \frac{\mathcal{T}_{\mathrm{cyl}}}{\mathcal{T}_{\mathrm{sph}}} = \varepsilon_{0,i}^{\mathrm{sph}} \times \frac{0.35\%}{0.17\%} \approx 2.10\,\varepsilon_{0,i}^{\mathrm{sph}}, \tag{4.86}$$

where $\mathcal{T}_{\mathrm{sph}} = 0.17\,\%$ and $\mathcal{T}_{\mathrm{cyl}} = 0.35\,\%$ are the mean transmissions for $t_{\mathrm{HFE,min}} = 760\,\mathrm{mm}$. This rescaling considers only the change in mean HFE transmission and is therefore approximate. A dedicated Monte Carlo simulation would be needed for a more accurate estimate.

For a given HFE thickness, the background contribution is then scaled using the attenuation law with the HFE coefficient defined earlier. At each $t$, the corresponding vessel mass is written as

$$M_j(t) = \rho_{\mathrm{Ni}}\Big[V_{\mathrm{side},j}(t) + V_{\mathrm{caps},j}(t)\Big], \tag{4.87}$$

and the same mean background rate and TG-spread uncertainty prescription defined earlier in the chapter is used.

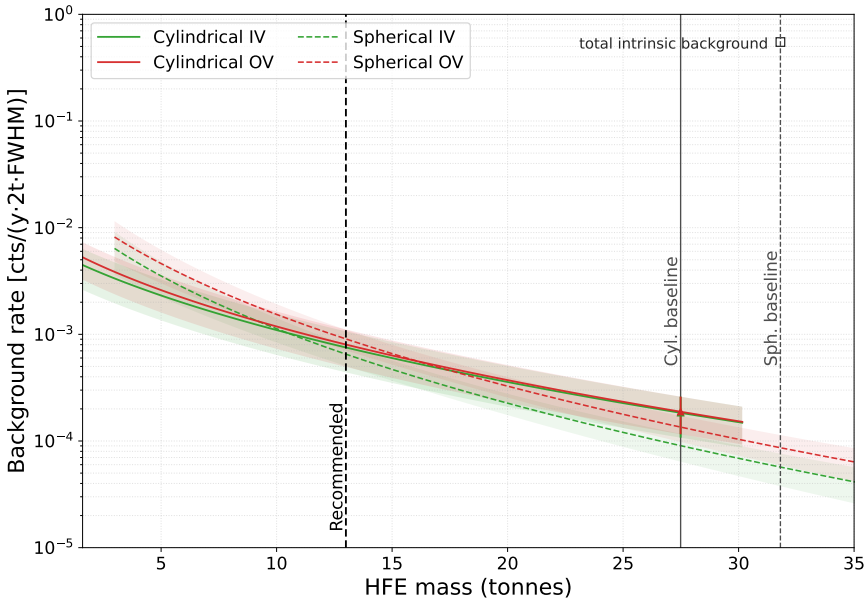


Figure 4.22: Background contribution from the inner and outer vessels as a function of HFE mass for the cylindrical cryostat option, compared with the corresponding spherical-vessel background curves.

The main parameters of the two options are summarized in Table 4.22.

The cylindrical design offers advantages in terms of geometric compactness and fabrication simplicity, and it reduces the baseline HFE inventory by several tonnes. At the 76 cm HFE baseline, the thicker cylindrical vessels and their larger mass

| **Parameter** | **Spherical design** | | **Cylindrical design** | |
|---|---|---|---|---|
| **HFE layer** | | | | |
| Minimum thickness [m] | 0.76 | | 0.76 | |
| Maximum thickness [m] | 1.05 | | 1.08 | |
| HFE volume [$m^3$] | 18.5 | | 15.9 | |
| HFE mass at baseline [t] | 32 | | 27.5 | |
| Mean transmission at baseline | 0.17% | | 0.35% | |
| **Vacuum gap** | | | | |
| Minimum thickness [mm] | 126 | | 126 | |
| **Vessel properties** | **IV** | **OV** | **IV** | **OV** |
| Radius [m] | 1.69 | 2.25 | 1.41 | 1.54 |
| Height [m] | 3.38 | 4.50 | 2.82 | 3.07 |
| Wall thickness [mm] | 5 | 10 | 10 | 20 |
| Endcap thickness [mm] | – | – | 5 | 10 |
| Nickel mass [t] | 1.60 | 5.71 | 2.61 | 6.24 |
| Vessel background at baseline | baseline | baseline | ×3.3 | ×2.3 |

Table 4.22: Comparison of the main geometrical, shielding, and vessel-background parameters for the spherical baseline and the cylindrical cryostat option. The baseline vessel-background scaling refers to the 76 cm HFE configuration.

increase the corresponding vessel-background contribution relative to the spherical design, by about a factor of 3 for the inner vessel and about a factor of 2 for the outer vessel. However, when both designs are compared at the proposed 13 t HFE inventory, their vessel-background contributions are comparable. For smaller HFE inventories, the spherical-vessel contribution increases more rapidly and becomes larger than the cylindrical-vessel contribution.

# Chapter 5

# Characterization of Cryogenic Hydrofluoroether Flow

## Contents


**5.1 Cooling Hydrofluoroether Fluids . . . . . 130**

5.1.1 Thermophysical Properties of HFE . . . . . 130

5.1.2 Differential Scanning Calorimetry Measurements . . . . . 134

**5.2 UMass HFE Recirculation System . . . . . 137**

5.2.1 Piping and Instrumentation Diagram . . . . . 139

5.2.2 Cryogenic Recirculation Pump . . . . . 142

5.2.3 Sensor Suite . . . . . 144

5.2.4 Thermal Insulation . . . . . 146

5.2.5 Liquid-Nitrogen Heat Exchanger . . . . . 149

**5.3 Support Infrastructure . . . . . 154**

5.3.1 HFE Reservoir . . . . . 155

5.3.2 Fluid Manifold . . . . . 158

5.3.3 Gas Trap . . . . . 159

5.3.4 Feed and Return Lines . . . . . 160

**5.4 Slow-Control System . . . . . 163**

5.4.1 Electrical Architecture . . . . . 164

5.4.2 Control Logic . . . . . 168

5.4.3 Data Acquisition and Logging . . . . . 169

**5.5 Commissioning and Performance Tests . . . . . 170**

5.5.1 Room-Temperature Pump Commissioning . . . . . 170

5.5.2 Thermocouple Calibration . . . . . 174

5.5.3 Heat-Exchanger Performance . . . . . 178

5.5.4 Leak-Tightness Tests . . . . . 182

5.5.5 Initial System Fill . . . . . 185
**5.6 Analysis of Cryogenic Runs . . . . . 187**
5.6.1 System Performance . . . . . 188
5.6.2 Pump Performance . . . . . 194
5.6.3 Cryogenic HFE Behavior . . . . . 198
**5.7 Future Developments . . . . . 202**
5.7.1 Controls and Monitoring . . . . . 202
5.7.2 HFE Mixtures . . . . . 202

This chapter examines the cryogenic recirculation of hydrofluoroether fluids for large liquid-xenon detectors. As discussed in Chap. 2, the nEXO detector geometry includes a surrounding HFE volume that acts as the immediate cryogenic medium around the TPC. In the baseline nEXO cryogenic scheme, this fluid is cooled by recirculation through an external heat exchanger. This differs from EXO-200, which operated with a smaller HFE volume cooled by static liquid-nitrogen heat-exchanger plates rather than by recirculation.

The viability of this approach depends on whether the fluid can be cooled, circulated, and handled reliably near operating temperature, where its properties differ substantially from their room-temperature values. In particular, previous studies showed a strong increase in viscosity as the temperature decreased, while operation near phase-transition regimes can further affect pump behavior, heat exchange, and fluid transport. To study these issues, a dedicated HFE recirculation system was developed at UMass. This chapter presents the motivation for these studies, the design of the apparatus, and the main results from commissioning and cryogenic tests.

Hydrofluoroether fluids are used industrially as heat-transfer and cleaning fluids because they are electrically insulating, non-flammable under normal handling conditions, chemically stable, and compatible with many metals and hard plastics.

## 5.1 Cooling Hydrofluoroether Fluids

The main challenge is not only to cool the HFE, but to do so while maintaining stable flow and avoiding operating conditions that can compromise the recirculation loop. Earlier tests within the collaboration were therefore carried out to identify the main limitations of cryogenic HFE circulation.

A first exploratory cryogenic recirculation test was performed at LLNL using a centrifugal pump. That test ended after cavitation damaged the pump internals and caused the pump head to fail mechanically. Cavitation occurs when the local pressure near the impeller falls below the fluid vapor pressure, causing vapor bubbles to form. As these bubbles are carried into regions of higher pressure, they collapse abruptly and produce localized pressure shocks. This can erode the impeller surfaces, induce vibration, reduce pump performance, and eventually cause mechanical failure. Because HFE has a high vapor pressure, it is especially prone to this effect. This result motivated the use of pump technologies less susceptible to cavitation, in particular gear pumps.

### 5.1.1 Thermophysical Properties of HFE

The two hydrofluoroethers considered for the nEXO cryogenic shield and for this recirculation study are HFE-7000 and HFE-7200. Their chemical formulas are $C_3F_7OCH_3$ for HFE-7000 and $C_4F_9OC_2H_5$ for HFE-7200. In the detector model used in this dissertation, HFE-7200 is the baseline cryogenic shielding fluid, while

HFE-7000 remains relevant as a lower-viscosity comparison fluid and as a possible component of future mixtures. HFE-7200 was used as the working fluid for the recirculation studies presented in this chapter because its higher boiling point and lower room-temperature vapor pressure make laboratory handling easier. The thermophysical properties discussed here are taken from the manufacturer documentation for the two fluids [94, 95], supplemented by low-temperature data transmitted internally by 3M.

Table 5.1 summarizes the room-temperature properties most relevant to cryogenic cooling and recirculation, with water included for comparison. Viscosity is expressed throughout as the kinematic viscosity $\nu$, with $1\,\mathrm{cSt} = 1\,\mathrm{mm^2/s} = 10^{-6}\,\mathrm{m^2/s}$. Source values reported as dynamic viscosity $\mu$ are converted using $\nu = \mu/\rho$, where $\rho$ is the fluid density and $1\,\mathrm{cP} = 1\,\mathrm{mPa\,s}$.

| Property at 25 °C | Water | HFE-7000 | HFE-7200 |
|---|---|---|---|
| Chemical formula | $H_2O$ | $C_3F_7OCH_3$ | $C_4F_9OC_2H_5$ |
| Boiling point | 100 °C | 34 °C | 76 °C |
| Freezing point | 0 °C | −122 °C | −138 °C |
| Density | $997\,\mathrm{kg\,m^{-3}}$ | $1400\,\mathrm{kg\,m^{-3}}$ | $1430\,\mathrm{kg\,m^{-3}}$ |
| Water solubility in fluid | — | ∼60 ppmw | 92 ppmw |
| Vapor pressure | 3.17 kPa | 65 kPa | 14.5 kPa |
| Kinematic viscosity | 0.89 cSt | 0.32 cSt | 0.43 cSt |
| Heat of vaporization | $2440\,\mathrm{kJ\,kg^{-1}}$ | $142\,\mathrm{kJ\,kg^{-1}}$ | $\sim 126\,\mathrm{kJ\,kg^{-1}}$ |
| Specific heat | $4180\,\mathrm{J\,kg^{-1}\,K^{-1}}$ | $1300\,\mathrm{J\,kg^{-1}\,K^{-1}}$ | $\sim 1210\,\mathrm{J\,kg^{-1}\,K^{-1}}$ |

Table 5.1: Representative room-temperature properties of water, HFE-7000, and HFE-7200. The HFE values are taken from the manufacturer documentation [94, 95].

Compared with water, both hydrofluoroethers have much lower specific heat and latent heat of vaporization, but they remain liquid to much lower temperature and are electrically insulating. Between the two HFE candidates, HFE-7000 is the less viscous fluid at low temperature, while HFE-7200 is less volatile at room temperature. The lower vapor pressure of HFE-7200 reduces evaporative losses and provides additional margin against cavitation during laboratory recirculation studies.

For low-temperature flow, the dominant practical effect is the strong rise in viscosity as the fluids are cooled. The low-temperature viscosity data transmitted by 3M, together with Seeton-model fits [96], are shown in Fig. 5.1.

The Seeton model is an empirical correlation used to describe the temperature dependence of liquid kinematic viscosity over a wide temperature range. In the form used here,

$$\ln\Big[\ln\Big(\nu + 0.7 + e^{-\nu} K_0(\nu + 1.244067)\Big)\Big] = A - B\ln(T_K), \tag{5.1}$$

where $T_K$ is the temperature in kelvin, $\nu$ is the kinematic viscosity in cSt, $K_0$ is the

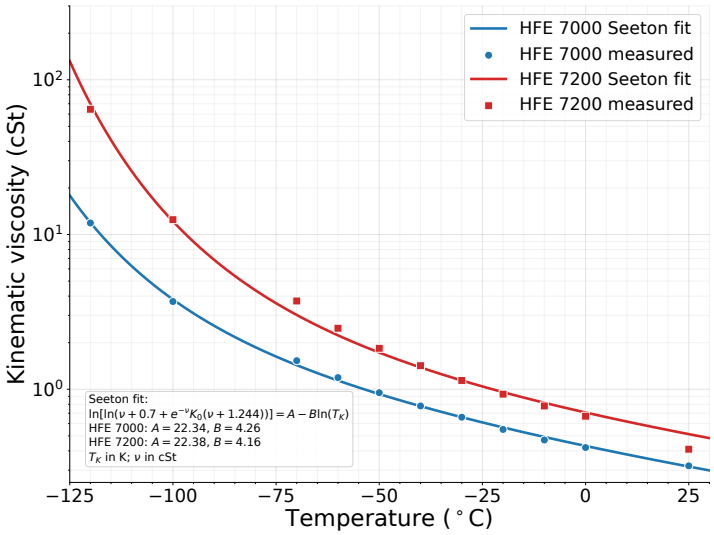


Figure 5.1: Kinematic viscosity of HFE-7000 and HFE-7200 as a function of temperature, compiled from manufacturer data, together with Seeton-model fits.

modified Bessel function of the second kind of order zero, and $A$ and $B$ are empirical fit parameters [96]. For the fits shown in Fig. 5.1, the extracted parameters are $A = 22.34$ and $B = 4.26$ for HFE-7000, and $A = 22.38$ and $B = 4.16$ for HFE-7200.

For both fluids, the viscosity increases rapidly as the temperature decreases. This viscosity increase constrains cryogenic recirculation, since it directly affects pressure drop, achievable flow rate, pump load, and the margin against cavitation or flow instability.

Density and vapor pressure are shown in Fig. 5.2.

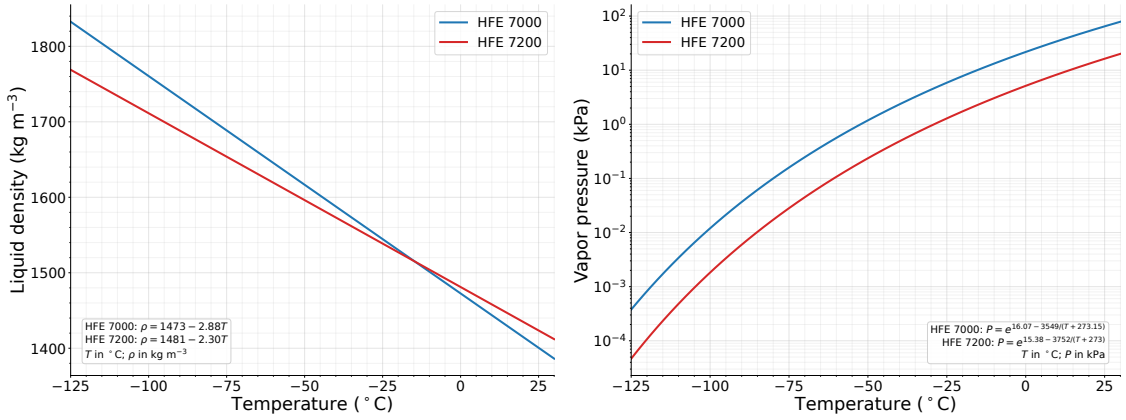


Figure 5.2: Density (left) and vapor pressure (right) of HFE-7000 and HFE-7200 as functions of temperature, from manufacturer [94, 95].

For each fluid, the density and vapor-pressure curves were calculated using the temperature-dependent equations reported in the corresponding manufacturer data sheet [94, 95].

In both cases, the density increases approximately linearly as the temperature is reduced, while the vapor pressure falls rapidly. The lower vapor pressure of HFE-

7200 is advantageous for fluid handling and pump operation, but it does not remove the hydraulic penalty associated with the low-temperature viscosity increase.

For HFE-7000, the manufacturer documentation also provides temperature dependent parameterizations for the thermal conductivity and specific heat, shown in Fig. 5.3 [94].

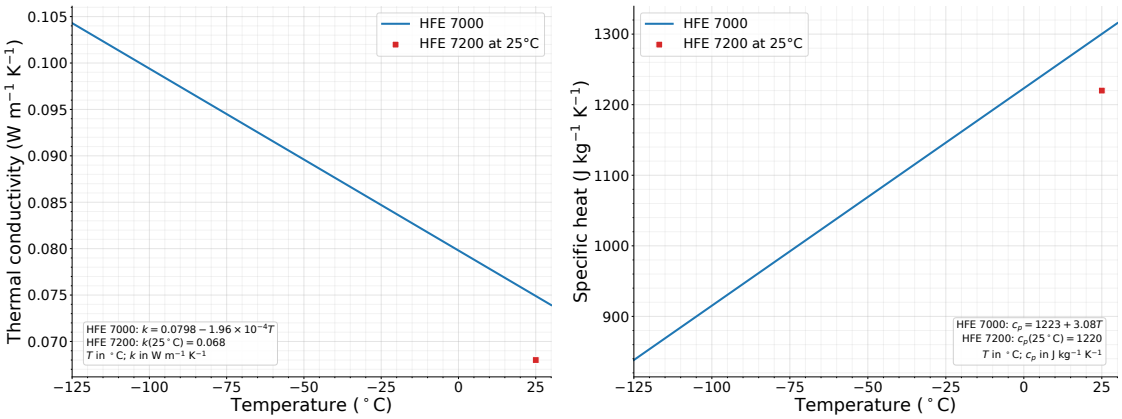


Figure 5.3: Thermal conductivity (left) and specific heat (right) of HFE-7000 as functions of temperature, evaluated from manufacturer correlations [94]. For HFE-7200, only room-temperature values were available.

Over the range relevant to cryogenic operation, the HFE-7000 thermal conductivity decreases approximately linearly with temperature, while the specific heat increases linearly. At 25 °C, the HFE-7000 values are $k = 0.075\,\mathrm{W\,m^{-1}\,K^{-1}}$ and $c_p = 1300\,\mathrm{J\,kg^{-1}\,K^{-1}}$. For HFE-7200, the corresponding room-temperature values are $k \approx 0.068\,\mathrm{W\,m^{-1}\,K^{-1}}$ and $c_p \approx 1210\,\mathrm{J\,kg^{-1}\,K^{-1}}$. These quantities enter cooldown estimates and heat-exchanger calculations, but in the present system the dominant low-temperature effect remains the viscosity increase rather than a large change in bulk heat capacity or thermal conductivity.

Both fluids are electrically insulating, chemically stable, non-corrosive, and non-ozone-depleting under normal handling conditions. Their environmental impact is nevertheless not negligible. The quoted 100-year global-warming potentials are about 530 for HFE-7000 and 55 for HFE-7200 [94, 95]. On a mass basis, this means that the emission of 1 kg of HFE-7000 has the same integrated warming effect as about 530 kg of $CO_2$, while 1 kg of HFE-7200 corresponds to about 55 kg of $CO_2$. HFE-7200 is therefore about an order of magnitude less impactful than HFE-7000, but both fluids require careful containment and recovery to minimize losses.

Materials compatibility is another practical consideration for the recirculation loop. The manufacturer documentation reports compatibility with common metals and many hard plastics, while fluorinated polymers, silicones, and some elastomers can absorb the fluid and swell under long exposures [94, 95]. This motivates the use of all-metal plumbing where possible and careful seal selection for cryogenic service.

### 5.1.2 Differential Scanning Calorimetry Measurements

Differential scanning calorimetry (DSC) measures the differential power required to keep a sample and an inert reference at the same temperature during a controlled temperature ramp [97]. Away from phase transitions, the signal is dominated by the smooth heat-capacity difference between them, while transitions appear as additional heat-flow features. With the convention used here, exothermic features are plotted upward and endothermic features downward.

The former HFE manufacturer, 3M, reported three low-temperature features for HFE-7200: a glass-like transition near −167 °C, a cold-crystallization exotherm near −120 °C, and a melting endotherm near −100 °C. The vendor trace was digitized from the data sheet and corrected by subtracting a linear baseline fitted over −75 °C to 0 °C. It is used here as the reference for the cold-dip measurements.

A DSC-like curve was reconstructed from the passive warm-up of an approximately 15 mL HFE-7200 sample after immersion in $LN_2$. The apparatus, shown in Fig. 5.4, consisted of a glass test tube instrumented with a thermocouple immersed in the liquid. The tube was plunged into $LN_2$, allowed to cool, then withdrawn and left to warm slowly inside insulation. The raw temperature trace was smoothed with a 10 s centered rolling mean before computing the temperature rate by finite differences,

$$\dot{T}(t) = \frac{T_{\mathrm{smooth}}(t + \Delta t) - T_{\mathrm{smooth}}(t - \Delta t)}{2\Delta t}. \tag{5.2}$$

The apparent heat capacity of the filled test tube was modeled as

$$C_{\mathrm{app}}(T) = C_{\mathrm{glass}} + m\, c_p^{\mathrm{HFE}}(T), \tag{5.3}$$

where $C_{\mathrm{glass}}$ is obtained from the glass mass and the specific heat of borosilicate glass. The HFE-7200 heat capacity $c_p^{\mathrm{HFE}}(T)$ is treated as an approximate temperature-dependent input, anchored to the room-temperature HFE-7200 value and scaled using the HFE-7000 temperature dependence. The corresponding specific heat flow is

$$\frac{q_{\mathrm{meas}}(T)}{m} = -\frac{C_{\mathrm{app}}(T)\,\dot{T}}{m}. \tag{5.4}$$

During passive warm-up, $\dot{T} > 0$, so the smooth heating contribution is negative with this convention. The raw warm-up power is therefore shown as $-q_{\mathrm{meas}}/m$.

Unlike a true DSC measurement, the cold-dip measurement has no reference cell to cancel the smooth heat input. The passive heat leak from the surroundings must therefore be modeled and subtracted before interpreting the residual structures. As an empirical baseline, the heat leak into the tube is assumed to scale with the temperature difference between the environment and the sample, as expected from Newton's law of cooling [98]. Dividing by the HFE mass and absorbing the geometry and surroundings into a run-dependent coefficient gives

$$\frac{q_{\mathrm{bg}}(T)}{m} = -\,k_{\mathrm{run}}\,(T_{\mathrm{room}} - T)\,, \tag{5.5}$$

where $k_{\mathrm{run}}$ is obtained independently for each run from a fit to $q_{\mathrm{meas}}/m$ over the feature-free interval $-75\,^{\circ}\mathrm{C}$ to $0\,^{\circ}\mathrm{C}$. The minus sign follows the convention of Eq. (5.4). The baseline-subtracted signal is then defined as

$$\frac{q_{\mathrm{event}}(T)}{m} = \frac{q_{\mathrm{bg}}(T)}{m} - \frac{q_{\mathrm{meas}}(T)}{m}. \tag{5.6}$$

With this sign convention, an exothermic cold-crystallization event releases latent heat and increases the sample warm-up rate above its expected baseline value. Since $q_{\mathrm{meas}}/m = -C_{\mathrm{app}}\dot{T}/m$, the increase in $\dot{T}$ makes $q_{\mathrm{meas}}/m$ more negative than $q_{\mathrm{bg}}/m$, so Eq. (5.6) gives $q_{\mathrm{event}}/m > 0$. The event therefore appears as an upward peak, consistent with the exothermic-upward convention. Conversely, an endothermic transition slows the warm-up and produces a negative peak.

The random thermocouple noise was estimated run-by-run from the median absolute deviation of the raw-minus-smoothed residuals, giving $\sigma_T \simeq 0.04\,^{\circ}\mathrm{C}$. The corresponding uncertainties on the temperature rate and heat flow are

$$\sigma_{\dot{T}} \simeq \frac{\sigma_T}{W_{\mathrm{smooth}}}, \qquad \sigma_{q/m} = \frac{C_{\mathrm{app}}(T)}{m}\,\sigma_{\dot{T}}, \tag{5.7}$$

with $W_{\mathrm{smooth}} = 10\,\mathrm{s}$. Seven runs were recorded between April 8 and April 23, 2026. The two April 14 runs were retained for the final DSC-like comparison because they showed the most consistent behavior through the transition region.

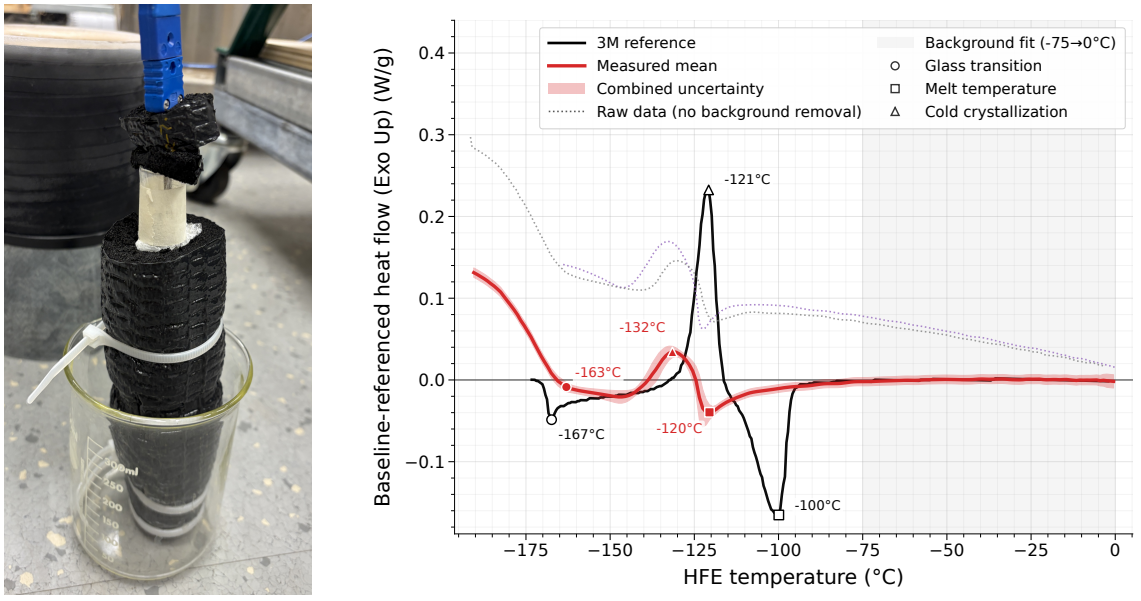


(a) (b)

Figure 5.4: DSC-like characterization of HFE-7200. (a) Tube and thermocouple arrangement used for the cold-dip measurement. (b) Baseline-subtracted heat-flow proxy compared with the digitized 3M DSC reference.

The cold-dip data reproduce the main low-temperature structure reported by 3M, although the individual feature temperatures do not all agree at the same level. The extracted transition temperatures are summarized in Table 5.2.

| Feature | 3M DSC reference [°C] | Cold-dip measurement [°C] |
|---|---|---|
| Glass-like transition, $T_g$ | $-167$ | $-163 \pm 6$ |
| Cold crystallization, $T_{cc}$ | $-120$ | $-131 \pm 1$ |
| Melting, $T_m$ | $-100$ | $-120 \pm 2$ |

Table 5.2: Low-temperature transitions of HFE-7200 from the 3M DSC reference and cold-dip measurements.

The same phase behavior can also be observed qualitatively during direct $LN_2$ immersion tests. Figure 5.5 shows HFE-7200 at three representative temperatures spanning the liquid, onset of crystallization, and glass-like regimes.

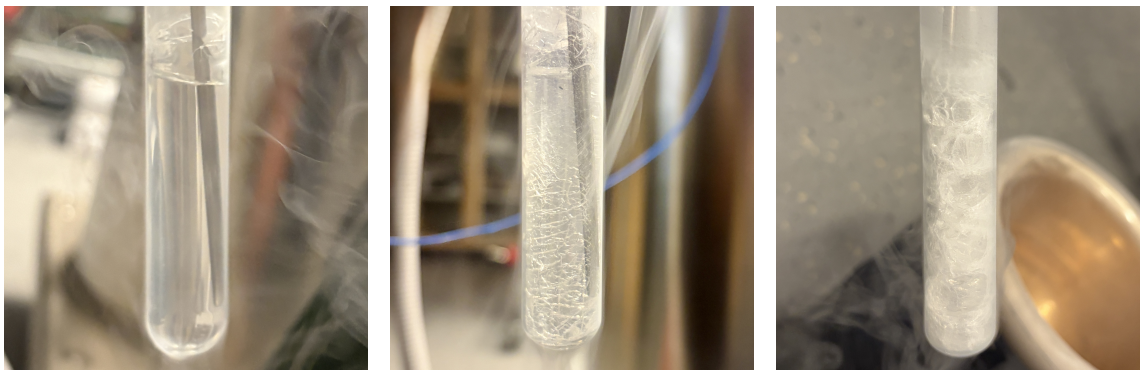

(a) $-110\,°C$; liquid. (b) $-160\,°C$; crystal/solid. (c) $-188\,°C$; glass-like phase.

Figure 5.5: Visual appearance of HFE-7200 after immersion in liquid nitrogen at three representative temperatures. The thermocouple used for the measurement is visible as a stainless-steel rod.

Near the LXe operating temperature, $T_{\mathrm{LXe}} \simeq -108\,°C$, HFE-7200 remained liquid but was visually much more viscous than at room temperature. During warm-up tests, the fluid behaved like a thick syrup near this temperature and became noticeably more mobile after only a small increase in temperature. This qualitative observation is consistent with the steep low-temperature rise in viscosity shown in Fig. 5.1.

The glass-like transition is observed at $T_g = -163 \pm 6\,°C$, consistent with the 3M value within the run-to-run spread. The positive feature at $T_{cc} = -131 \pm 1\,°C$ is assigned to the cold-crystallization exotherm, while the negative feature at $T_m = -120 \pm 2\,°C$ is assigned to melting. Both features are shifted to lower temperatures relative to the 3M reference. The latter occurs near the cold-crystallization temperature reported by 3M, but its endothermic sign supports its interpretation as melting rather than as a second crystallization feature.

This shift may partly reflect the uncertain purity of the sample used for the dip test. The tested fluid was spare HFE-7200 with an uncertain handling history. Impurities are known to modify crystallization behavior through both thermodynamic effects, such as changes in phase equilibria, and kinetic effects, such as changes in

nucleation [99]. The measured $T_{cc}$ and $T_m$ should therefore be treated as sample- and history-dependent transition temperatures rather than fixed material constants. Future measurements will use higher-purity HFE-7200 and controlled HFE mixtures. As discussed later in this chapter, mixtures may provide a practical way to lower the crystallization temperature and reduce the viscosity, in the same way that impurities can shift phase behavior.

The LXe operating temperature is $-108\,^{\circ}\mathrm{C}$. This is close to the transition region observed for HFE-7200 and only $\sim 13\,^{\circ}\mathrm{C}$ above the crystallization temperature measured in 3M's DSC. HFE-7200 cooling must therefore be closely controlled to avoid partial solidification during cooldown and recirculation.

## 5.2 UMass HFE Recirculation System

The UMass cryogenic HFE recirculation system was designed and assembled between summer 2025 and early 2026, with mechanical-design contributions from Graeme Sullivan. The apparatus is a laboratory-scale test stand for the hydraulic and thermal issues associated with recirculating HFE near LXe temperature. It was not designed as a radiopure detector subsystem. Instead, the component choices were driven by cryogenic reliability, accessibility, instrumentation coverage, and the ability to change operating conditions during commissioning.

The principal requirements are summarized in Table 5.3. The temperature range extends down to the LXe operating temperature in order to probe the transition region discussed in Sec. 5.1.2. The pressure requirement is specified as the maximum pump differential pressure across the recirculation loop.

| Requirement | Design value |
|---|---|
| Minimum HFE temperature | $165\,\mathrm{K}$ $(-108\,^{\circ}\mathrm{C})$ |
| Maximum pump differential pressure | $\Delta P_{\mathrm{pump,max}} = 10\,\mathrm{bar}$ |
| Maximum HFE volume flow | $\dot{V}_{\mathrm{HFE,max}} = 4\,\mathrm{L\,min^{-1}}$ |
| Cooling method | Single-pass $LN_2$ heat exchanger |

Table 5.3: Design operating requirements for the UMass HFE recirculation system.

The system was designed to address the following operating goals:

1. cool HFE to LXe temperature under controlled recirculation;
2. identify freezing or crystallization signatures during cooldown;
3. measure pump performance as a function of temperature, pressure, and flow;
4. test alternative HFE compositions and mixtures.

A simplified CAD model of the cold recirculation loop is shown in Fig. 5.6.

The model shows the heat-exchanger tank, HFE pump, flow meter, bypass, gas trap, and main cryogenic isolation valves. In the orientation shown, the pump circulates HFE counter-clockwise. The bypass provides a parallel path around the tank; with both branches open, flow divides according to their hydraulic impedances. The

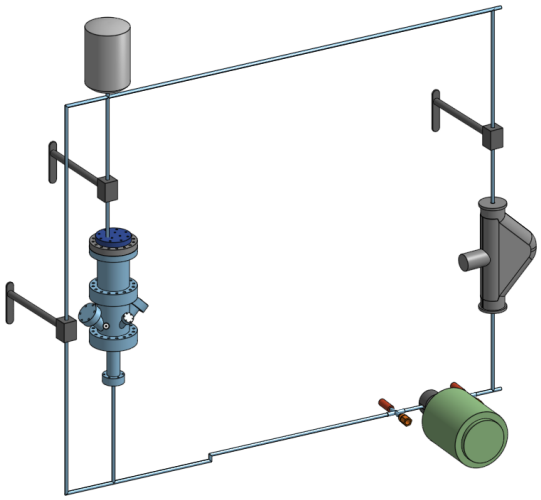

Figure 5.6: Simplified CAD model of the UMass HFE cold recirculation loop, showing the heat-exchanger tank, pump, flow meter, tank bypass, gas-trap, and valves.

tank path can be isolated when cooling is unnecessary or when partial solidification or increased HFE viscosity restricts flow during cooldown. Space and connectors on the right were reserved for a future auxiliary branch without rebuilding the primary frame. The installed cold-loop envelope is approximately 1.35 m tall and 1.22 m wide, with the bypass extending the layout by about 18 cm on the left. The assembled system before final insulation is shown in Fig. 5.7.




Figure 5.7: Front view of the assembled UMass HFE recirculation system before final insulation. A short tubing section was insulated during insulation tests.

The heat-exchanger tank, pump, flow meter, and principal HFE plumbing are

mounted on a common Unistrut support frame. A short tubing section is already insulated in the photograph because insulation tests were performed before the final wrap was installed. The remaining visible components are described in the following sections.

### 5.2.1 Piping and Instrumentation Diagram

The complete piping and instrumentation diagram (P&ID) is shown in Fig. 5.8. The P&ID is the reference for the component labels used in the slow-control interface and in the data analysis. Line colors distinguish the HFE, $LN_2$, gaseous-nitrogen, vacuum, and vent circuits, and the diagram assigns names to the valves, pressure sensors, thermocouples, flow meter, feedthroughs, and transfer connections.

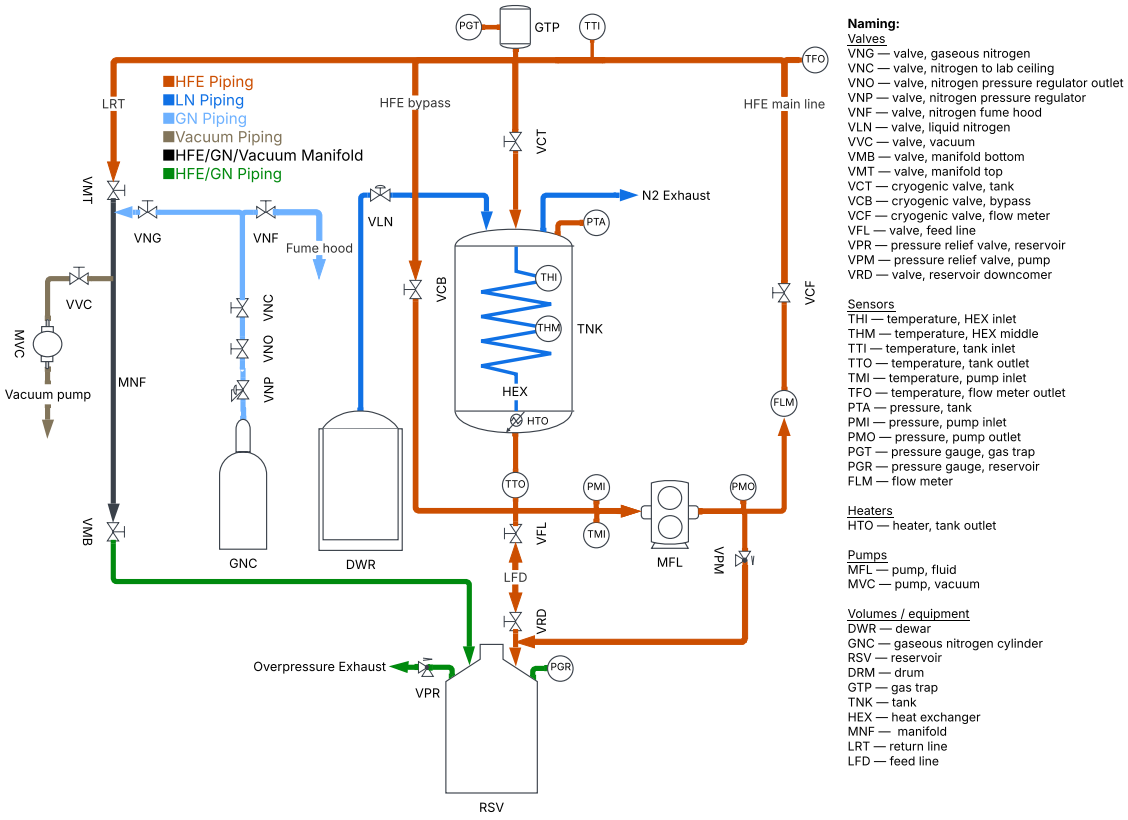


Figure 5.8: Piping and instrumentation diagram of the UMass HFE recirculation system. Line colors distinguish the HFE, $LN_2$, gaseous-nitrogen and vacuum circuits.

The system uses both vacuum and nitrogen pressure for fluid handling. Before filling, the HFE loop is evacuated to remove residual nitrogen from purging, or air and water vapor if the system has been opened during commissioning. The HFE reservoir, labelled RSV in the P&ID, is then pressurized with dry nitrogen to transfer liquid into the evacuated loop. Emptying is performed by gravity where possible, followed by a controlled nitrogen overpressure of the loop relative to the reservoir to recover the remaining fluid. These operations were formalized in a step-by-step checklist requiring pressure, valve-state, and fill-volume checks before each transfer. The nitrogen side of the system is supplied from the laboratory gas infrastructure,

which is connected to a nitrogen cylinder through ceiling ports, and purge or vent lines are routed through the fume hood.

The system is operated as a closed, dry circuit to limit volatile HFE loss and contamination from laboratory air. The room-temperature vapor pressures summarized in Table 5.1 imply that small leaks can produce measurable fluid loss during filling, transfer, or warm operation, while the finite water solubility of the fluids allows air exposure to introduce moisture into the HFE and onto internal surfaces [94, 95]. During cooldown, this moisture can freeze into ice, obstruct narrow passages, and provide uncontrolled nucleation sites. The loop is therefore evacuated before filling, handled with dry nitrogen, and leak checked before cryogenic operation.

### Tubing and Fittings

The installed HFE plumbing contains approximately 5.5 m of tubing, including the 1.75 m bypass. The tank path used for the pressure-drop estimate is approximately 3.75 m long. Since the HFE circulates in a closed loop and the pump inlet and outlet are taken at the same elevation, the static-head term cancels over one complete circuit. The pump head is therefore set by pipe friction and by minor losses from bends, valves, contractions, and expansions.

The tubing-size calculation is described in App. D. It uses the Darcy–Weisbach pressure-loss relation for incompressible single-phase flow, with HFE-7200 properties evaluated at the cold design point. Figure 5.9 shows the calculated pressure drop at $\dot{V}_{\mathrm{HFE}} = 4\,\mathrm{L\,min^{-1}}$ and $-110\,^{\circ}\mathrm{C}$ as a function of tubing inner diameter.

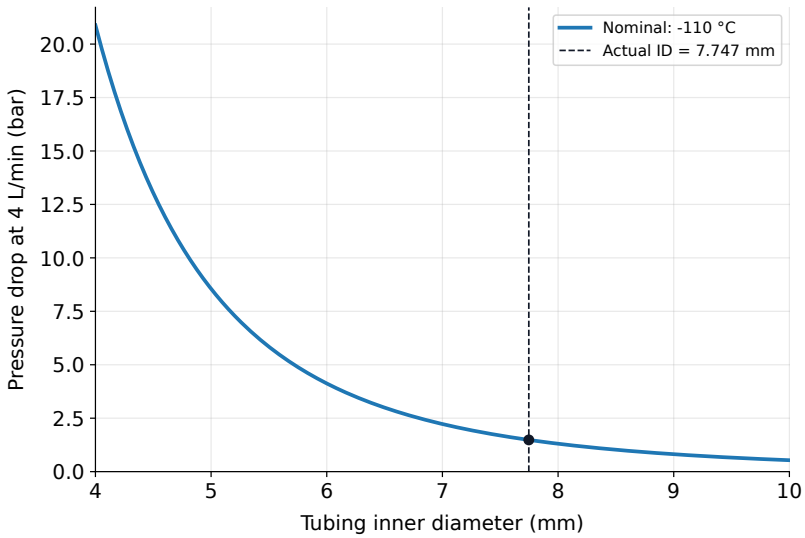


Figure 5.9: Calculated HFE-7200 pressure drop through the tank path as a function of tubing inner diameter. The calculation uses $\dot{V}_{\mathrm{HFE}} = 4\,\mathrm{L\,min^{-1}}$, $T = -110\,^{\circ}\mathrm{C}$, and the loss model described in App. D. The vertical line indicates the installed tubing inner diameter used in the model.

At fixed flow rate, the laminar straight-tube pressure drop scales approximately as $D_{\mathrm{ID}}^{-4}$, making small tubing unfavorable at low temperature when the HFE viscosity is high. Since 0.25 in-OD tubing left little margin relative to the 10 bar pump

differential-pressure requirement, the loop was built with 3/8-in.-OD stainless-steel tubing, corresponding to $D_{\mathrm{ID}} = 7.747\,\mathrm{mm}$. The installed tubing length, including the bypass, is approximately 5.5 m, giving a volume of about 260 mL. At the cold design point, HFE-7200 has $\rho = 1734\,\mathrm{kg\,m^{-3}}$ and $\nu = 28.35\,\mathrm{cSt}$. For $\dot{V}_{\mathrm{HFE}} = 4\,\mathrm{L\,min^{-1}}$, this gives $Re \simeq 386$, confirming laminar flow. Including straight-tube and minor losses, the calculated pressure drop through the tank path is $\Delta P = 1.48\,\mathrm{bar}$, well below the pump limit.

The HFE plumbing uses stainless-steel tubing and metal-gasket face-seal fittings (VCR) wherever possible, providing tight seals that are important for limiting HFE vapor leaks. Threaded NPT interfaces were used only where required by commercial components, on the reservoir and gas trap, and were placed on gas-side connections. The heat-exchanger tank was a spare ultra-high-vacuum vessel available in the laboratory. After subtracting the volume displaced by the immersed $LN_2$ heat exchanger, it provides an available HFE volume of approximately 2.43 L. The vessel has four side ConFlat feedthrough ports, four welded VCR tube stubs on the top flange, and one welded VCR tube stub at the bottom.

### Valves

The system uses three classes of valves:

1. cryogenic manual ball valves in the cold HFE loop;
2. room-temperature manual valves on the warm transfer and gas-handling lines;
3. an electrically actuated valve on the $LN_2$ supply.

This separation ensures that each valve is operated within its specified temperature and pressure range.

**Cryogenic valves** The cold-loop isolation valves are cryogenic three-piece floating ball valves manufactured by Habonim. They are specified for cryogenic service and have a pressure class well above the 10 bar maximum pump differential pressure of the HFE loop. Their role is to select flow through the heat-exchanger tank, through the bypass, or through both paths. The extended bonnet keeps the stem seal away from the cold HFE volume, reducing the risk of icing or seal degradation during actuation.

**Warm manual valves** Room-temperature manual valves are stainless-steel ball valves manufactured by Swagelok and are used on the gas-handling, vacuum, vent, and HFE-transfer lines. They are rated up to approximately 172 bar at room temperature, which is well above the warm handling-system pressures, but their specified temperature range does not extend to the cold-loop design temperature. They are therefore excluded from the cryogenic HFE path.

**$LN_2$ valve** The $LN_2$ heat-exchanger supply is controlled by a normally closed direct-acting 2/2-way plunger valve manufactured by Bürkert. The valve is media-separated by stainless-steel bellows, which thermally isolate the solenoid coil from

the cryogenic flow path and reduce the risk of actuator freezing during $LN_2$ operation. It is rated to a pressure up to 10 bar. Because the valve is direct acting, it does not require a minimum pressure drop to actuate. This was preferred over the one-way actuating valve used on the laboratory LXe system, which could occasionally remain stuck under certain $LN_2$ flow conditions.

The component labeled VNP in the P&ID is a nitrogen pressure regulator; the label is kept only for consistency with the operating checklist and slow-control interface.

### 5.2.2 Cryogenic Recirculation Pump

The pump is the central active component of the recirculation loop. It must operate over a wide range of HFE viscosity, remain compatible with a closed and leak-tight fluid boundary, and provide sufficient differential pressure to overcome the cold-loop hydraulic losses described in App. D. These requirements motivated the use of a positive-displacement gear pump rather than a centrifugal pump.

The difference between the two operating principles is illustrated in Fig. 5.10.

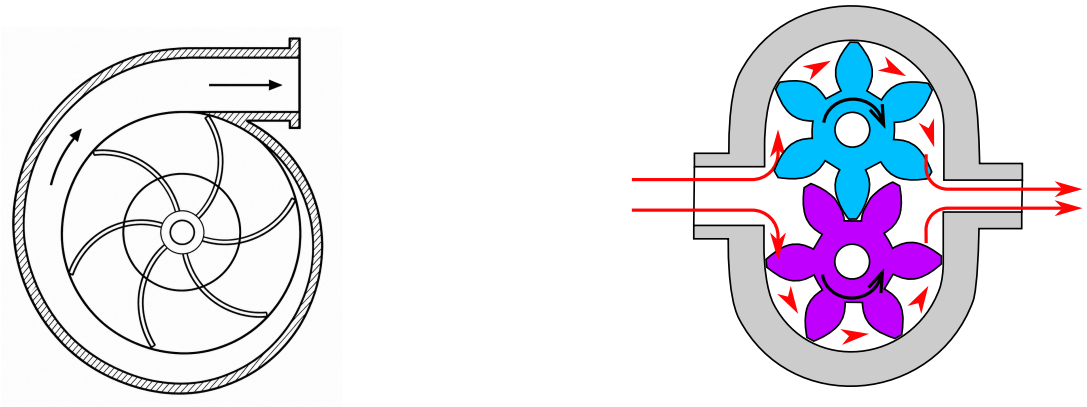

(a) Centrifugal pump.

(b) External gear pump.

Figure 5.10: Working principles of centrifugal and external gear pumps, adapted from Richards [100] and Rbalieiro [101]; the latter under CC BY-SA 4.0.

**Centrifugal pump** A centrifugal pump adds energy to the liquid through a rotating impeller and is well suited to low-viscosity fluids at moderate pressure rise. Its performance, however, is sensitive to cavitation when the local pressure near the impeller falls below the fluid vapor pressure. This is a concern for HFE operation, especially during warm filling or pump start-up when the vapor pressure is highest. Previous collaboration tests with a centrifugal pump ended with cavitation damage, reinforcing the choice of a pump technology less sensitive to this type of failure.

**Gear pump** An external gear pump instead transports fluid by trapping fixed volumes between the gear teeth and the pump housing. The volumetric flow is

set primarily by the rotation speed, with slip losses that depend on viscosity and pressure difference. This positive-displacement behavior is better matched to the expected low-temperature operating regime, where the HFE viscosity increases rapidly. The lower internal flow velocities also reduce the tendency to produce the strong local pressure depressions characteristic of centrifugal impellers.

The selected pump is a Gather magnetically coupled external gear pump specified for HFE-7000 and HFE-7200 service. The operating specifications are summarized in Table 5.4.

| Quantity | Specification |
|---|---|
| Fluid compatibility | HFE-7000 and HFE-7200 |
| Temperature range | $-110\,^{\circ}\mathrm{C}$ to $30\,^{\circ}\mathrm{C}$ |
| Differential pressure | up to 10 bar |
| Volume flow | $0.5\,\mathrm{L\,min^{-1}}$ to $4.0\,\mathrm{L\,min^{-1}}$ |
| Pump type | Magnetically coupled external gear pump |

Table 5.4: Operating specifications of the selected HFE recirculation pump.

This choice satisfies the two main requirements of the recirculation loop: hydraulic margin at low temperature and a leak-tight fluid boundary.

The maximum flow rate matches the hydraulic design point used in Sec. 5.2.1, while the 10 bar differential-pressure capability provides margin above the calculated 1.48 bar cold-loop pressure drop for the tank path.

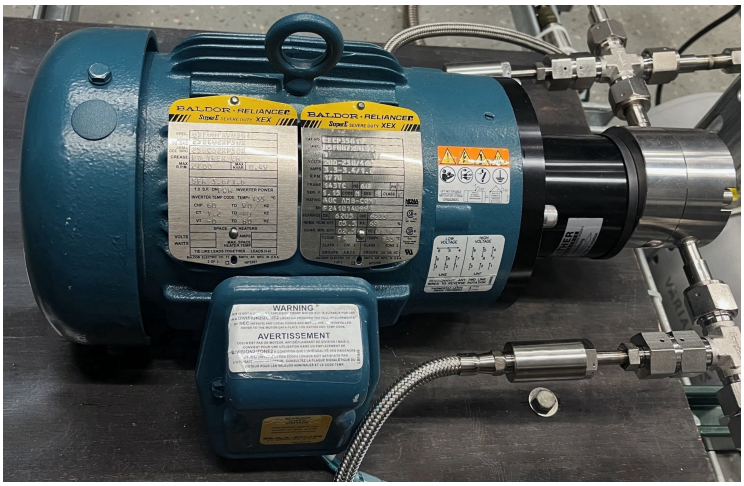


Figure 5.11: Magnetically coupled external gear pump installed in the UMass HFE recirculation system. The pump head is connected to the HFE loop through metal-gasket VCR fittings.

The magnetic coupling improves HFE containment by transmitting torque across a sealed boundary, avoiding a rotating shaft seal through the pump housing. This removes a leak path from the closed HFE loop. The pump head uses stainless-steel wetted parts, nickel-alloy gears, carbon slide bearings, and 0.5 in VCR process connections, allowing direct integration into the metal-gasket HFE plumbing.

The same pump principle and vendor family are adopted in the current nEXO cryogenic design, with a full-scale HFE volume flow up to $10\,\mathrm{L\,min^{-1}}$ [46]. The UMass system therefore tests the same pump technology at lower flow rate, while preserving the key constraints of cryogenic HFE recirculation.

The pump was installed at the bottom of the cold loop. Figure 5.11 also shows the four-way VCR adapters at the pump inlet and outlet, which provide local pressure and temperature measurements for monitoring the pump differential pressure during cooldown and flow tests. The pump speed is controlled by a variable-frequency drive and monitored by the slow-control system described in Sec. 5.4.

### 5.2.3 Sensor Suite

The recirculation loop is instrumented to monitor the local thermal and hydraulic state of the HFE during filling, cooldown, and recirculation. The primary measurements are temperature, pressure, and flow. Together, they are used to identify cooldown gradients and localized heat loads, estimate the pump differential pressure, monitor the approach to high-viscosity or phase-transition regimes, and measure the flow conditions. Unless stated otherwise, the specifications quoted below are the vendor technical-data values for the installed sensor models.

#### Thermocouples and Pressure Sensors

The system is instrumented with six thermocouples, three pressure transducers, and two mechanical pressure gauges. The Type-T thermocouples and pressure transducers used on the cold loop are shown in Fig. 5.12. All thermocouples are read out through thermocouple amplifiers in the electronics system.

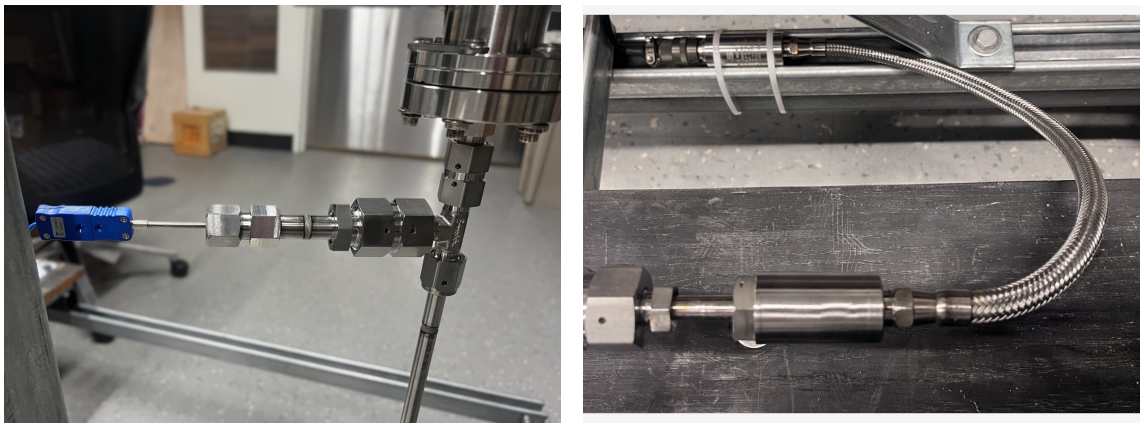

(a) Thermocouple probes. (b) Pressure transducers.

Figure 5.12: Temperature and pressure sensors used to instrument the HFE recirculation loop.

**Thermocouples** Thermocouples measure temperature through the thermoelectric voltage generated at the junction of two dissimilar metals. The four cold-loop

probes are TC Measurement Type-T thermocouples, using copper and constantan conductors. Type-T thermocouples are appropriate for the cryogenic range of interest and are specified over approximately −200 °C to 350 °C. The two thermocouples inside the heat-exchanger tank are Dwyer Omega Type-K thermocouples, using chromel and alumel conductors, with a broader specified range extending from approximately −200 °C to above 1000 °C.

The four Type-T probe thermocouples are installed directly in the HFE loop: at the tank outlet (TTO), upstream of the pump (TMI), downstream of the flow meter (TFO), and upstream of the tank (TTI). The probes are 3.18 mm-diameter 304-stainless-steel encased thermocouples with insulated junctions. The probe length is 15.2 cm (except for TTI, where a 30.5 cm probe is used to account for the longer feedthrough geometry). Each probe is inserted through a TC Measurement Spectite compression-style feedthrough with PTFE sealant, rated up to about 200 barg. The rigid probe body keeps the sensor tip fixed near the tube center, where it samples the flowing HFE.

The two Type-K thermocouples are installed inside the heat-exchanger tank using a spare ConFlat thermocouple feedthrough. These PFA-coated flexible probes are positioned near the $LN_2$ heat-exchanger coil to monitor local cooling and possible ice or frozen-HFE buildup. THM is located lower in the tank near the lower/middle part of the coil before the tube turns upward through the center; its tip points inward and is approximately 0.3 cm from the coil. THI is located near the $LN_2$ inlet region, with its tip also pointing inward and approximately 1 cm from the coil.

**Pressure sensors** Three American Sensing pressure transducers are installed on the cold loop: in the heat-exchanger tank (PTA), at the pump inlet (PMI), and at the pump outlet (PMO). They are sealed-gauge sensors with a 0 barg to 10 barg range, 0 V to 5 V output, 1/4-in. VCR process connection, and cryogenic operation down to −110 °C for the installed configuration. Their wetted material is Inconel 718, a nickel-based alloy used here as a cryogenic-compatible metallic surface in contact with the HFE.

These pressure sensors provide the pump differential pressure during cooldown, bypass operation, and flow tests. Two Swagelok Grade A pressure gauges are also installed on the gas trap (PGT) and HFE reservoir (PGR). They cover approximately −1.0 barg to 4.1 barg and provide a local visual check of vacuum, purge pressure, and reservoir pressure during manual operations. For this range, the Grade A accuracy is about ±0.05 bar near mid-scale and ±0.10 bar near the ends.

### Flow Meter

The HFE flow rate is measured with a Coriolis mass flow meter installed in the cold recirculation loop, shown in Fig. 5.13. A Coriolis meter was selected because it is compatible with cryogenic operation and measures mass flow directly, making it well suited to HFE as its density and viscosity change during cooldown.

The installed instrument is a cryogenic Krohne flow meter with a stainless-steel




Figure 5.13: Coriolis mass flow meter installed in the HFE recirculation loop.

dual-tube sensor. It uses 1/2-in. flanged connections sealed with PTFE gaskets and bolted flange joints. The vendor specifies cryogenic operation down to −196 °C and a process-pressure rating of 19 bar for the installed configuration. The meter was mounted vertically to allow self-draining when the system is emptied.

The instrument provides three primary measurements:

1. mass flow rate, $\dot{m}_{\mathrm{HFE}}$, measured directly from the Coriolis phase shift, with an accuracy of ±0.1%;
2. density, $\rho_{\mathrm{HFE}}$, inferred from the vibration frequency of the measuring tubes, with an accuracy of $\pm 1\,\mathrm{kg\,m^{-3}}$;
3. process temperature, measured internally by the flow-meter sensor, with an accuracy of $\pm 0.5\,^{\circ}\mathrm{C} \pm 0.5\%$.

The volume flow used in the hydraulic analysis is then calculated from

$$\dot{V}_{\mathrm{HFE}} = \frac{\dot{m}_{\mathrm{HFE}}}{\rho_{\mathrm{HFE}}}. \tag{5.8}$$

The simultaneous density and temperature measurements also provide diagnostics for changes in fluid state or increasing viscosity during cryogenic operation.

### 5.2.4 Thermal Insulation

The cold parts of the HFE system are covered with removable insulation, as shown in Fig. 5.14.

The insulation is not glued to the system. It is held in place with zip ties and can be removed for inspection, leak checking, or hardware changes, then reinstalled for cryogenic operation. Its measured performance during cryogenic operation is discussed in Sec. 5.6.

Three insulation materials were used, depending on the component geometry:

1. flexible rubber-foam tube insulation for the HFE piping and $LN_2$ line;
2. flexible rubber-foam sheet insulation for the tank and flow meter;

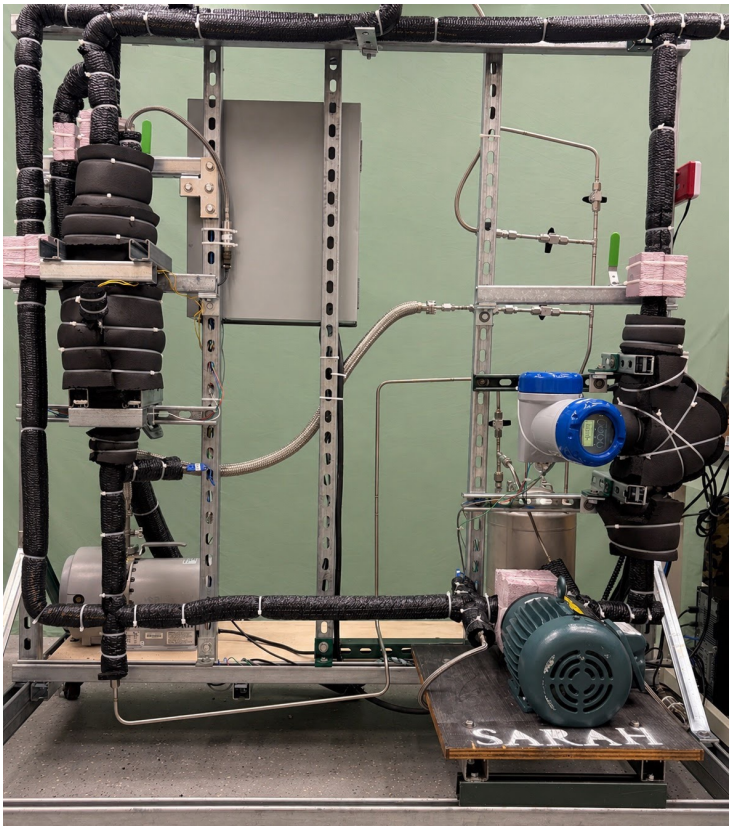


Figure 5.14: Front view of the HFE recirculation system after installation of the removable thermal insulation.

3. carved rigid XPS foam for the pump and cryogenic valves.

### Piping

The HFE piping was insulated with McMaster-Carr flexible Buna-N/PVC rubber-foam tube insulation. The installed tubing insulation has a 25.4 mm (1-in.) wall thickness and an inner diameter matched to the tubing outer diameter, providing good surface contact and reducing the volume where humid air could condense or freeze on the tube wall. Its listed temperature range is approximately $-183\,^{\circ}\mathrm{C}$ to $104\,^{\circ}\mathrm{C}$, and its thermal conductivity is $k = 0.036\,\mathrm{W\,m^{-1}\,K^{-1}}$.

For pipe insulation, the conductive heat leak is estimated from the radial thermal resistance for one-dimensional cylindrical conduction [98],

$$R_{\mathrm{cyl}} = \frac{\ln(r_o/r_i)}{2\pi k L}, \qquad \dot{Q}_{\mathrm{cyl}} = \frac{\Delta T}{R_{\mathrm{cyl}}}, \tag{5.9}$$

where $k$ is the insulation thermal conductivity, $L$ is the insulated length, and $r_i$ and $r_o$ are the inner and outer insulation radii. For the installed 3/8-in.-OD tubing, the insulation radii are $r_i = 4.76\,\mathrm{mm}$ and $r_o = 30.16\,\mathrm{mm}$. With $L = 5.5\,\mathrm{m}$, $T_\infty = 25\,^{\circ}\mathrm{C}$, and $T_c = -110\,^{\circ}\mathrm{C}$, the temperature difference is

$$\Delta T = T_\infty - T_c = 135\,\mathrm{K}. \tag{5.10}$$

The corresponding insulation resistance is

$$R_{\text{ins}} = \frac{\ln(30.16/4.76)}{2\pi(0.036\,\text{W m}^{-1}\,\text{K}^{-1})(5.5\,\text{m})} = 1.48\,\text{K W}^{-1}, \tag{5.11}$$

giving

$$\dot{Q}_{\text{piping}} \simeq \frac{135\,\text{K}}{1.48\,\text{K W}^{-1}} = 91\,\text{W}. \tag{5.12}$$

The stainless-steel tube-wall resistance is negligible compared with the insulation resistance for this estimate.

The same insulation material was also used on the $LN_2$ line. This line can locally approach the $LN_2$ temperature near the dewar outlet, below the lower rating of the insulation. Small heat leaks on the $LN_2$ line are not expected to dominate the HFE cooling performance.

### Tank and Flow Meter

The heat-exchanger tank and the Coriolis flow meter were insulated with McMaster-Carr Buna-N/PVC rubber-foam sheets. The sheets are 25.4 mm (1-in.) thick and could be cut to fit around the irregular tank, feedthrough, and flow-meter geometries. Their listed temperature range is approximately −183 °C to 110 °C, which covers the HFE operating temperature. For this sheet insulation, the listed $R$-value is $R$-4, corresponding to an area-normalized thermal resistance

$$R'' \simeq 4\ \text{ft}^2\,^\circ\text{F h BTU}^{-1} \simeq 0.704\,\text{m}^2\,\text{K W}^{-1}. \tag{5.13}$$

For an approximately flat insulated surface, the conductive heat leak through the insulation is estimated from the one-dimensional thermal-resistance form of Fourier's law [98],

$$\dot{Q} \simeq \frac{A\Delta T}{R''}, \tag{5.14}$$

where $A$ is the insulated area, $\Delta T$ is the temperature difference between the room and the cold surface, and $R''$ is the area-normalized thermal resistance. Using $T_\infty = 25\,^\circ\text{C}$ and $T_c = -110\,^\circ\text{C}$, $\Delta T = 135\,\text{K}$. With the areas used in the heat-leak estimate, this gives approximately

$$\dot{Q}_{\text{tank}} \simeq 53\,\text{W}, \qquad \dot{Q}_{\text{FM}} \simeq 31\,\text{W}. \tag{5.15}$$

Multiple layers were added around selected parts of the tank to reduce local heat input and improve coverage around feedthroughs.

### Pump and Cryogenic Valves

The pump and cryogenic valves were insulated with carved rigid XPS foam. This material is a 25.4 mm (1-in.) thick closed-cell polystyrene board with a listed $R$-value of $R$-5, a minimum compressive strength of 103 kPa, and low water absorption. Its rigidity made it useful for forming removable pieces around the pump body and valve bonnets, where flexible sheet insulation did not conform cleanly. It is not

specified as cryogenic insulation, but it is external to the HFE boundary and is not in contact with the fluid.

The listed $R$-value corresponds to an area-normalized thermal resistance

$$R'' \simeq 5\ \mathrm{ft^2\,^\circ F\,h\,BTU^{-1}} \simeq 0.881\ \mathrm{m^2\,K\,W^{-1}}. \tag{5.16}$$

Using the same flat-surface approximation as Eq. (5.14), with $T_\infty = 25\,^\circ\mathrm{C}$, $T_c = -110\,^\circ\mathrm{C}$, and the pump/valve insulated area used in the heat-leak estimate, the corresponding pump heat leak is

$$\dot{Q}_{\mathrm{pump}} \simeq \frac{A_{\mathrm{pump}}\Delta T}{R''} \simeq 14\,\mathrm{W}. \tag{5.17}$$

The cryogenic-valve heat leaks were not treated separately in this estimate because their exposed areas are small compared with the pump and tank areas, and their contribution is expected to be subdominant.

**Combined heat leak** Combining the insulated tank, flow meter, pump, and HFE piping gives the estimated parasitic heat load

$$\dot{Q}_{\mathrm{leak}} = \dot{Q}_{\mathrm{tank}} + \dot{Q}_{\mathrm{FM}} + \dot{Q}_{\mathrm{pump}} + \dot{Q}_{\mathrm{piping}} \simeq 53 + 31 + 14 + 91 = 189\,\mathrm{W}. \tag{5.18}$$

This value is used as an order-of-magnitude design estimate; the heat load is evaluated experimentally from the cryogenic runs in Sec. 5.6.

### 5.2.5 Liquid-Nitrogen Heat Exchanger

The HFE is cooled by a single-pass $LN_2$ heat exchanger immersed in the HFE tank. The large temperature difference between boiling nitrogen, near $-196\,^\circ\mathrm{C}$, and the HFE operating point makes the exchanger geometry important. A compact in-line exchanger could provide large heat-transfer area, but would also increase the risk of locally cooling HFE-7200 into its crystallization region near $-120\,^\circ\mathrm{C}$.

The UMass system therefore uses the tank HFE inventory as the bulk fluid, with $LN_2$ flowing through an immersed coil. This shell-side-like geometry provides thermal inertia around the cold tube surface and reduces the risk of rapid bulk freezing. Commercial non-inline exchangers with similar geometry were considered, but available options did not meet the cleanliness and integration requirements of the HFE system, so a custom coil was built to fit inside the tank. Liquid nitrogen is supplied from a pressurized dewar through the normally closed $LN_2$ valve described in Sec. 5.2.1, whose installed configuration is rated to 10 bar. The dewar pressure drives the $LN_2$ flow through the narrow heat-exchanger tubing and therefore controls the cooling power. Commissioning tests indicate an approximately linear increase of cooling power with dewar pressure over the tested range, up to the 10 bar valve rating. After passing through the exchanger, nitrogen exits through an open exhaust routed into the laboratory fume-hood vent.

### Preliminary Design

The liquid-nitrogen heat exchanger was sized with a simplified HFE-side heat-transfer model, described in App. E. The calculation estimates the tube length required to remove the expected parasitic heat load without driving the HFE-side tube-wall temperature below a conservative freezing limit. The main assumptions are summarized in Table 5.5. The heat-leak value is a rounded conservative estimate based on the insulation calculation discussed in Sec. 5.2.4.

| Quantity | Value |
|---|---|
| Target HFE bulk temperature | $T_{\text{target}} = -110\,^{\circ}\text{C}$ |
| Minimum wall temperature | $T_{\text{freeze}} = -121\,^{\circ}\text{C}$ |
| Ambient temperature | $T_{\text{amb}} = 25\,^{\circ}\text{C}$ |
| Design heat leak | $\dot{Q}_{\text{leak}} = 200\,\text{W}$ |
| Tube outside diameter | $d_o = 6.35\,\text{mm}$ |
| HFE-side coefficient | $h_{\text{HFE}} = 250\,\text{W}\,\text{m}^{-2}\,\text{K}^{-1}$ |

Table 5.5: Design point used for the preliminary $LN_2$ heat-exchanger sizing calculation.

The calculation is a first-order sizing estimate. In the real heat exchanger, $LN_2$ boils inside the tube, the coil temperature is not uniform, the nitrogen flow conditions evolve during operation, and HFE can freeze locally on the cold surface. The wall temperature in Table 5.5 is therefore best interpreted as a HFE-side surface temperature, rather than as the local $LN_2$ temperature. This approximation is closest to an actively regulated case, such as operation with high-pressure cold nitrogen gas or an $LN_2$ control loop that keeps the surface temperature between the HFE target temperature and the onset of freezing.

For a tube of outside diameter $d_o$ and length $L$, the simplified HFE-side heat-removal rate is

$$\dot{Q}_{\text{HX}} = h_{\text{HFE}} \pi d_o L \left(T_{\text{bulk}} - T_{\text{wall}}\right), \tag{5.19}$$

using the Newton-law form for convective heat transfer [98]. At the limiting design point, $T_{\text{bulk}} = T_{\text{target}}$ and $T_{\text{wall}} = T_{\text{freeze}}$, giving

$$L_{\text{req}} = \frac{\dot{Q}_{\text{leak}}}{\pi d_o h_{\text{HFE}} \left(T_{\text{target}} - T_{\text{freeze}}\right)} = 3.65\,\text{m}. \tag{5.20}$$

The value $h_{\text{HFE}} = 250\,\text{W}\,\text{m}^{-2}\,\text{K}^{-1}$ was obtained from a conservative HFE-side estimate based on the Churchill–Bernstein correlation. The low-temperature $Pr$ and $k$ inputs were taken from Graham Corporation helical heat-exchanger tests, as detailed in App. E [102].

The cooling is intended to be dominated by convection from the bulk HFE to the cold tube surface. HFE-7200 has a low thermal conductivity: scaling the HFE-7000 temperature dependence to the HFE-7200 room-temperature value gives $k_{7200}(-110\,^{\circ}\text{C}) \simeq 0.095\,\text{W}\,\text{m}^{-1}\,\text{K}^{-1}$. This is comparable to paper, cardboard, or

low-conductivity wood, and is about a factor of six below water. A stagnant or solid HFE layer on the tube would therefore add a significant thermal resistance. For a layer of thickness $\delta$,

$$h_\delta \simeq \frac{k_{7200}}{\delta}. \tag{5.21}$$

Thus, $\delta = 0.5\,\mathrm{mm}$ gives $h_\delta \simeq 190\,\mathrm{W\,m^{-2}\,K^{-1}}$, while $\delta = 1\,\mathrm{mm}$ gives a value of $h_\delta \simeq 95\,\mathrm{W\,m^{-2}\,K^{-1}}$. Even a thin layer can therefore strongly reduce heat transfer to the tube. This effect can partly self-limit further local freezing, but it also reduces cooling performance. The desired operating condition is therefore to keep the heat-exchanger surface between the HFE target temperature and the freezing region.

The corresponding helical layout is shown in Fig. 5.15.

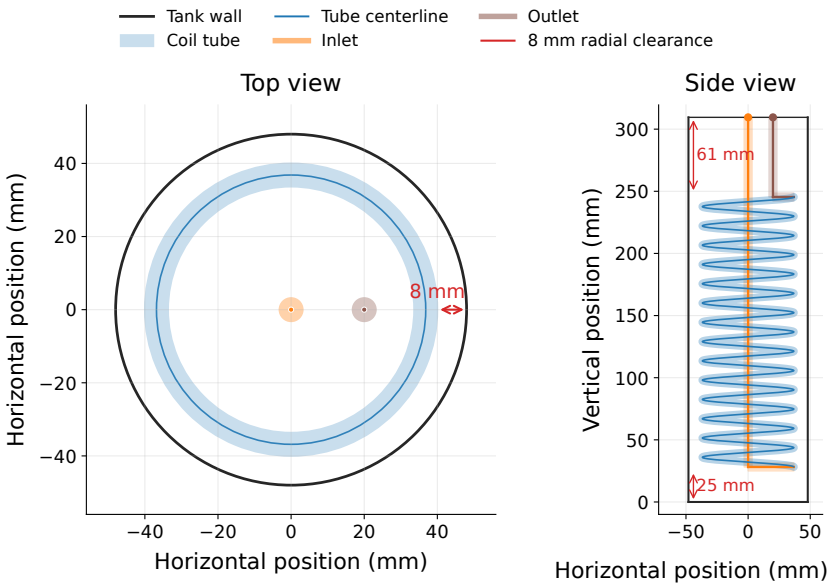


Figure 5.15: Preliminary helical layout used to package the required $LN_2$ heat-exchanger length inside the HFE tank.

The available tank body is 309.5 mm high with a 96 mm inner diameter. An 80 mm-diameter coil envelope leaves an 8 mm radial clearance. A 14-turn coil with a 15.52 mm pitch provides the required tube length while maintaining an axial tube-to-tube gap of 9.17 mm.

### Manufacturing

The heat-exchanger coil was manufactured from 1/4-in.-OD, 0.049 in-wall 304L stainless-steel tubing. This tubing size was chosen to balance heat-transfer area, bendability, and the available space inside the tank. Its smaller outer diameter, compared with the 3/8-in.-OD HFE loop tubing, allows a compact helical coil to fit inside the 96 mm-ID tank body. The relatively thick wall also adds some thermal mass and conductive resistance between the $LN_2$ and the HFE, providing a small buffer between the $LN_2$ temperature and the warmer HFE-side surface temperature targeted during cooldown.

The final coil was made from approximately 6.1 m (20 ft) of tubing, exceeding the 3.65 m minimum length estimated in Sec. 5.2.5. The additional length increases the available heat-transfer area and provides margin against the simplified sizing model. The coil diameter was set to approximately 80 mm, leaving about 8 mm radial clearance to the tank wall. The coil descends helically, turns inward near the bottom, and returns upward through a straight central section, so that both tube ends remain accessible at the tank feedthroughs.

The tube ends were terminated with 1/4-in. VCR glands, connecting to the tank feedthroughs. The manufactured heat exchanger is shown in Fig. 5.16.

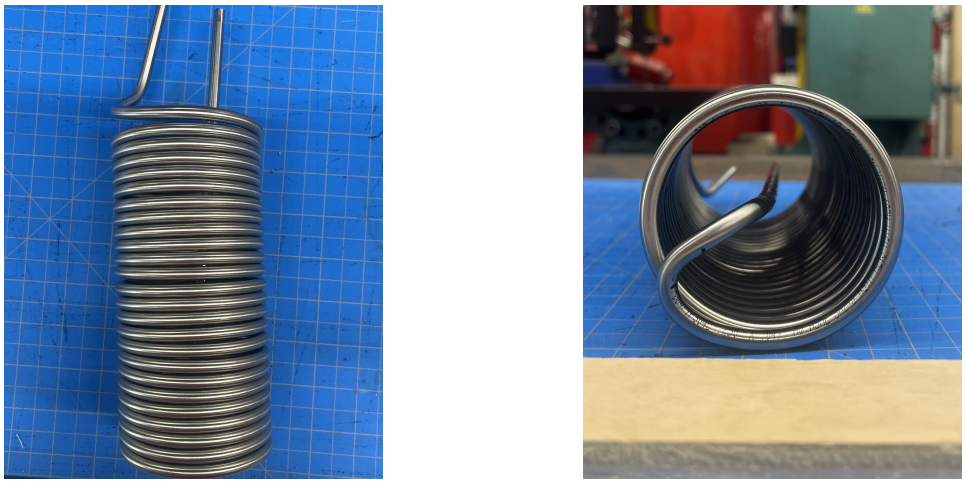

(a) Side view. (b) Top view.

Figure 5.16: Manufactured $LN_2$ heat-exchanger coil before installation.

The $LN_2$ flow direction was selected during commissioning (see Sec. 5.5.3). A counter-flow configuration was first tested, with the $LN_2$ inlet connected to the downcomer and the outlet connected to the top of the coil. This configuration is thermally efficient, since the HFE encounters a progressively colder heat-exchanger surface as it cools. However, it also places the coldest heat-exchanger surface near the coldest HFE, increasing the risk of local HFE freezing. The final configuration therefore uses the top of the coil as the $LN_2$ inlet and the downcomer as the outlet. This configuration is less aggressive thermally, but safer during cooldown: the coldest $LN_2$ first encounters warmer HFE, while the colder HFE later encounters a tube surface that has been warmed by nitrogen evaporation.

**Spacer** A spacer was added to keep the $LN_2$ coil centered inside the HFE tank. Without this constraint, the suspended coil could shift and contact the tank wall, creating a direct cold path to the vessel rather than cooling primarily through the surrounding HFE. The spacer, shown in Fig. 5.17, was 3D printed from ABS with 50% infill and designed with a low profile, rounded edges, and a central opening to preserve HFE flow toward the lower part of the tank.

ABS compatibility was checked with HFE-immersion and cold-stress tests. After approximately one week in HFE, an ABS test piece showed dimensional changes

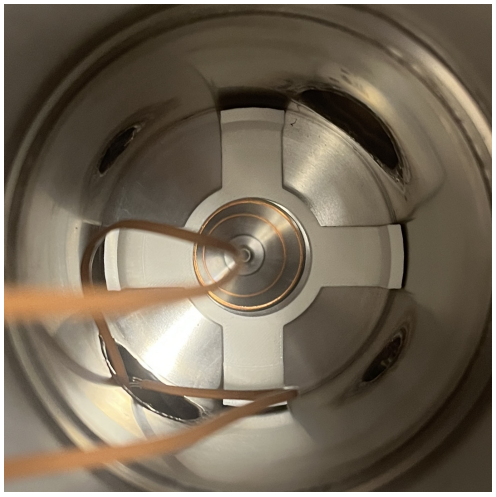

Figure 5.17: ABS spacer installed at the bottom of the HFE tank to keep the $LN_2$ coil centered away from the vessel wall. The brown PFA-coated thermocouples used to monitor the heat-exchanger temperature are also visible.

below 0.6% and no increase in brittleness. Separate cold-stress tests, performed after $LN_2$ immersion, showed no failure under moderate handling loads. These checks do not constitute a full material qualification, but they were sufficient for the spacer's limited role in this system.

### Heaters

Two flexible Omega polyimide heaters provide auxiliary thermal control in the cryogenic system. Both heaters are self-adhesive, 25.4 mm wide, 304.8 mm long, and rated for 30 W. Their purpose is to add controlled heat where it can improve temperature regulation or nitrogen-flow control. Their locations and roles are summarized in Table 5.6.

| | Tank heater | $LN_2$ outlet heater |
|---|---|---|
| Status | Installed | Planned |
| Location | HFE tank bottom | $LN_2$ outlet line |
| Size | 25.4 mm wide × 304.8 mm long | |
| Power | 30 W | |
| Heater type | Omega self-adhesive polyimide flexible heater | |
| Adhesive operating range | −40 °C to 149 °C | |
| Purpose | Warm the tank outlet<br>Avoid cooling overshoots | Warm the nitrogen outlet<br>Test $LN_2$ flow regulation |

Table 5.6: Auxiliary Omega polyimide heaters used or planned for thermal control in the HFE recirculation system.

The installed tank heater can be turned on during cooldown or steady operation to add a controlled heat load near the tank outlet. This provides a way to recover

from excessive cooling and maintain the HFE closer to a chosen set point, especially near the transition region where temperature overshoot can lead to partial freezing.

The planned $LN_2$ outlet heater will be used to test an additional control handle on the nitrogen side. By heating the gas leaving the coil, it can increase the outlet-side pressure and help regulate the $LN_2$ flow through the heat exchanger. Since parts of the system can be colder than the adhesive operating range during operation, the heaters are treated as external control elements rather than cryogenic-qualified structural components.

## 5.3 Support Infrastructure

The rear side of the apparatus contains the support infrastructure for filling, draining, purging, and monitoring the cold HFE loop. This side of the system is shown in Fig. 5.18.




Figure 5.18: Rear view of the HFE recirculation system, showing the main support infrastructure for fluid handling and slow control.

The main support components are:

1. the HFE reservoir (RSV);
2. the gas and fluid manifold (MNF);
3. the vacuum pump (MVC);
4. the feed (LFD) and return lines (LRT) connecting the support infrastructure to the cold loop;
5. the gas trap (GTP), not visible in Fig. 5.18;

6. the electronics enclosure.

The rear side also provides access to the cryogenic valve arms and their green manual handles. The HFE reservoir, its scale, and the vacuum pump are mounted together on a plywood support attached to the main frame. Since the frame is mounted on wheels, this arrangement allows the full system, including its handling infrastructure, to be moved as a single assembly when needed.

During cryogenic operation, the $LN_2$ dewar is placed near the rear side of the system and connected to the heat-exchanger supply line. The dewar is installed on a scale connected to the electronics system, allowing the $LN_2$ consumption to be monitored during cooldown and steady-operation tests.

### 5.3.1 HFE Reservoir

The HFE reservoir (RSV), shown in Fig. 5.19, stores the working HFE inventory between tests and provides the pressure boundary used for filling and emptying the cold loop. The reservoir is a McMaster-Carr 11.3 L stainless-steel pressurized liquid-dispensing tank with four 1/4-in. female NPT ports and a maximum pressure rating of approximately 12.8 barg. This rating is well above the small nitrogen overpressures used during normal HFE transfers.




Figure 5.19: HFE reservoir installed on the rear side of the recirculation system. The reservoir is mounted on a scale to monitor the HFE inventory during filling and recovery.

The reservoir ports are connected to the manifold (top reservoir port), the feed line (reservoir liquid downcomer), the reservoir pressure gauge (PGR), and the reservoir pressure-relief valve (VPR). The downcomer reaches near the bottom of the tank so that liquid HFE can be transferred rather than only gas from the headspace. The top port allows the reservoir to be vented, or pressurized with nitrogen.

The RSV is mounted on a scale, with a 68 kg capacity and 0.1 kg readout increments. The scale is used to follow the HFE inventory during transfer, filling, and

recovery.

**Initial HFE transfer** The delivered HFE-7200 was supplied in the original TMC shipping drum, with an initial measured mass of $22.6 \pm 0.1$ kg, corresponding to about $20.8 \pm 0.1$ kg of HFE after subtracting the empty drum mass. This HFE was transferred into the RSV and a separate storage drum (DRM). The transfer was performed under nitrogen purge to minimize contact with laboratory air. A prepared transfer line was first used, but after the plastic funnel on the shipping drum cracked, the transfer was completed by open pouring. The final recovered quantities are summarized in Table 5.7.

| Vessel | Final full mass [kg] | HFE mass [kg] | HFE volume [L] |
|---|---|---|---|
| RSV | $20.4 \pm 0.1$ | $13.7 \pm 0.1$ | $9.61 \pm 0.07$ |
| DRM | $13.4 \pm 0.1$ | $6.8 \pm 0.1$ | $4.77 \pm 0.07$ |
| Total recovered | $33.8 \pm 0.14$ | $20.5 \pm 0.14$ | $14.38 \pm 0.10$ |

Table 5.7: HFE quantities recovered after the initial transfer from the shipping drum to the system reservoir and storage drum. The uncertainties correspond to the 0.1 kg scale precision propagated to the HFE volume using the room-temperature HFE-7200 density.

After transfer, RSV and DRM were left slightly above atmospheric pressure with nitrogen.

**Pressure monitoring and relief** The RSV pressure is monitored locally with the mechanical gauge PGR. The reservoir is protected by the VPR relief valve, a Generant relief valve set to open at 2.1 barg. This set point is well below the reservoir pressure rating and provides protection against accidental over-pressurization during nitrogen-assisted transfers.

**Reservoir seal selection** Because the RSV is used for HFE storage and transfer, the lid seal must be both compatible with HFE and compliant enough to seal the reservoir lid. Four seal options were considered, as summarized in Table 5.8. The original reservoir gasket is an EPDM (ethylene-propylene-diene monomer rubber) pressure seal. This gasket is well matched to the reservoir lid geometry, but it is not the most conservative choice for long-term HFE exposure because elastomers can absorb fluorinated fluids and swell or soften over time [95].

The other three seals were purchased separately to explore different compromises between HFE compatibility and sealing performance. PTFE (polytetrafluoroethylene) was considered because of its chemical inertness and low extractables, but is quite rigid. Viton/FKM and FEP-encapsulated silicone represent intermediate choices: Viton/FKM is a compliant fluorinated elastomer, while the FEP jacket

provides a stronger fluoropolymer barrier at the cost of reduced conformity to the lid. The qualitative comparison is summarized in Table 5.8.

| Seal option | HFE compatibility | Expected sealing |
|---|---|---|
| Original EPDM pressure seal | Fair | Good |
| Viton/FKM | Good | Good |
| FEP-encapsulated silicone | Very good | Fair |
| PTFE | Very good | Poor |

Table 5.8: Qualitative comparison of reservoir lid seal options considered for HFE storage.

Three of the tested seals are shown in Fig. 5.20. The PTFE gasket was too rigid to seal reliably in this lid geometry and was not retained for leak testing.




Figure 5.20: Reservoir lid seals tested for HFE storage: Viton/FKM, original EPDM pressure seal, and FEP-encapsulated silicone.

The seals were compared with pressure-decay tests of the closed RSV. The absolute pressure evolution was fitted with

$$P_{\mathrm{abs}}(t) = P_{\mathrm{atm}} + A\exp(kt), \qquad P_{\mathrm{atm}} = 1.013\,25\,\mathrm{bar}, \tag{5.22}$$

where a negative $k$ corresponds to pressure loss. The fitted decay constant was converted to an HFE-7200 vapor throughput,

$$Q = V_{\mathrm{RSV}}(-k)P_{\mathrm{vap}}(T)\frac{1000}{3600}, \tag{5.23}$$

with $Q$ in $\mathrm{mbar\,L\,s^{-1}}$, $V_{\mathrm{RSV}}$ in L, $k$ in $\mathrm{h^{-1}}$, and $P_{\mathrm{vap}}$ in bar [103].

The liquid-equivalent HFE loss was then obtained from the ideal-gas law. The pressure-volume throughput can be related to the molar leak rate by

$$\dot{n} = \frac{Q_{\mathrm{SI}}}{R(T + 273.15)}. \tag{5.24}$$

Since $Q$ is expressed in $\mathrm{mbar\,L\,s^{-1}}$,

$$Q_{\mathrm{SI}} = 0.1\,Q, \tag{5.25}$$

because 1 mbar L s$^{-1}$ = 0.1 Pa m$^3$ s$^{-1}$. The molar loss rate is therefore

$$\dot{n} = \frac{0.1\,Q}{R(T + 273.15)}. \tag{5.26}$$

The corresponding liquid-equivalent volume loss rate is

$$\dot{V}_{\mathrm{liq}} = \dot{n}\frac{M}{\rho(T)} = \frac{0.1\,Q}{R(T + 273.15)}\frac{M}{\rho(T)}, \tag{5.27}$$

where $\dot{V}_{\mathrm{liq}}$ is in m$^3$ s$^{-1}$, $M = 0.264\,\mathrm{kg\,mol^{-1}}$ is the molar mass of HFE-7200, and $\rho(T)$ is the HFE-7200 liquid density [95]. For reporting in L yr$^{-1}$, this rate is multiplied by $1000\,t_{\mathrm{yr}}$, with $t_{\mathrm{yr}} = 365.25\,\mathrm{day}$.

The ideal-gas law is used here only to convert the low-pressure HFE vapor throughput into a molar loss rate. This conversion should be interpreted as a conservative gas-side HFE-vapor-equivalent estimate. It assumes that the headspace remains saturated with HFE vapor and that the leak conductance measured with nitrogen also applies to HFE vapor. Under normal gas-side leakage, this likely overestimates the HFE loss if the heavier HFE vapor has a lower conductance than nitrogen. The comparison is shown in Fig. 5.21.

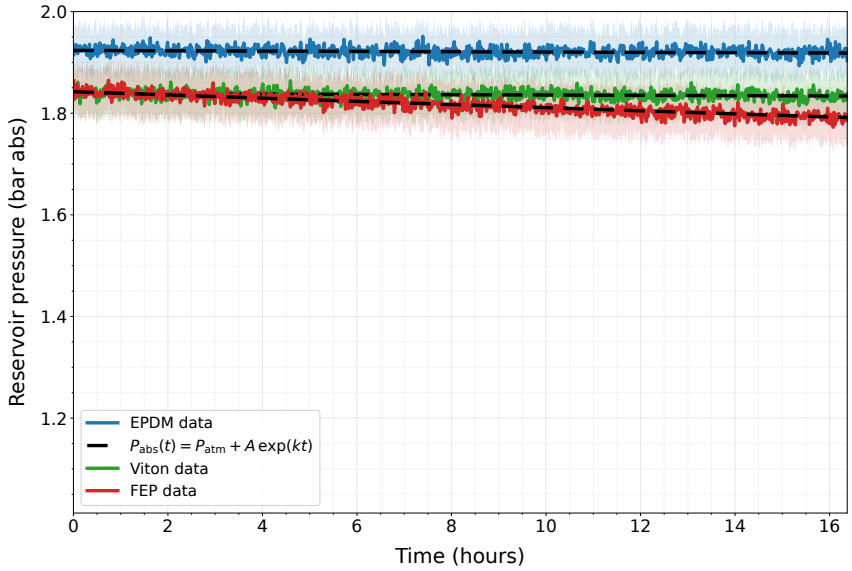


Figure 5.21: Reservoir pressure-relaxation comparison for the tested lid seals.

The corresponding extracted leak properties are summarized in Table 5.9.

The FEP-encapsulated seal produced the largest resolved loss, about 10 times the Viton/FKM best-fit value. The original EPDM seal did not show a resolved pressure drop in this data set, but its long-term HFE compatibility is less favorable. Viton/FKM was therefore selected for the reservoir lid as the best compromise between chemical compatibility and measured sealing performance.

### 5.3.2 Fluid Manifold

The fluid manifold (MNF) is the gas-handling interface used to apply either vacuum or dry nitrogen pressure to the HFE reservoir and to the system. It contains four

| Seal | $T$ [°C] | $k$ [$h^{-1}$] | HFE loss [$L\,yr^{-1}$] |
|---|---|---|---|
| EPDM | 20.736 | not resolved | $\leq 0.091$ (95% CL) |
| Viton/FKM | 20.774 | $(-3.65 \pm 2.10) \times 10^{-4}$ | $0.036 \pm 0.021$ |
| FEP-encapsulated silicone | 20.466 | $(-3.86 \pm 0.23) \times 10^{-3}$ | $0.376 \pm 0.022$ |

Table 5.9: Pressure-relaxation results for the reservoir lid seals. The EPDM data set did not show a resolved endpoint pressure drop, so only a 95% confidence-level upper limit is quoted.

room-temperature manual valves: VMT and VMB connect the manifold to the gas trap and reservoir headspace, respectively, while VVC connects it to the vacuum pump and VNG to the nitrogen line. This arrangement allows the reservoir and gas-trap sides of the system to be evacuated, vented, or pressurized independently. The resulting pressure differences are used to fill the cold loop from the reservoir, return HFE to the reservoir after a run, and purge residual gas or vapor from the system.

Although the manifold is primarily a gas-handling volume, liquid HFE can also enter it after cold recirculation when extra liquid inventory is intentionally left in the gas trap, as discussed in Sec. 5.3.3. This is acceptable because the manifold remains connected to the reservoir through the transfer path and can be drained back to the RSV after operation.

**Vacuum pump** The manifold is connected to a Varian dry scroll pump. The pump has a pumping speed of $110\,L\,min^{-1}$ and a specified ultimate pressure of $6.6 \times 10^{-2}$ mbar. In the HFE system, it is used to evacuate the system before filling, remove residual nitrogen after purging, and generate the pressure difference needed for pressure-driven HFE transfer. Since the pump is a dry scroll pump, no pump oil can backstream into the HFE plumbing.

**Nitrogen line** Dry nitrogen is supplied from an ultra-high-purity nitrogen cylinder through a pressure regulator. The cylinder is a 49 L high-pressure steel cylinder with a service pressure of about 165 barg. The regulated outlet is connected to the system through the laboratory ceiling line, which also provides a routed connection to the fume hood. This configuration allows the manifold to supply dry nitrogen for purging, reservoir pressurization, and controlled emptying, while also allowing gas to be vented safely through the hood rather than into the room.

### 5.3.3 Gas Trap

The gas trap (GTP), shown in Fig. 5.22, is installed at the top of the HFE system and provides the overhead volume used during filling, pressure adjustment, and cooldown. The installed vessel is made of stainless steel, with a capacity of 3 L, a wall thickness of 2 mm, and a maximum pressure of 12 bar.

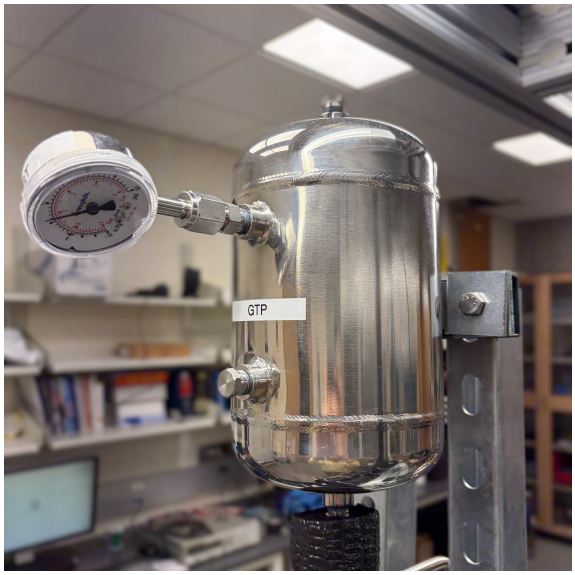


Figure 5.22: Gas trap installed at the top of the HFE system. The vessel provides the overhead volume used during filling, pressure adjustment, and cooldown.

The gas trap is connected to the upper part of the cold loop through an NPT-to-VCR adapter and a VCR tee. The same tee connects the trap to the return line (LRT) and to the gas-handling manifold through VMT. A mechanical pressure gauge (PGT) is mounted on the trap through an NPT port to provide a local readout of the overhead pressure. Two additional NPT ports are plugged, but remain available for future additions, such as a dedicated nitrogen line for dynamic overhead-pressure regulation.

During filling, liquid HFE is pushed from the reservoir through the feed line and into the system. When the liquid reaches the gas trap, bubbling is observed as HFE displaces gas in the return line, with VMT closed to isolate the manifold. During cooldown, part of the room-temperature HFE initially present in the gas trap is drawn into the cold loop as the HFE density increases. This keeps the tank and cold-loop tubing filled while preserving a gas headspace.

### 5.3.4 Feed and Return Lines

The feed and return lines connect the HFE reservoir to the cold recirculation loop. They are used during filling, emptying, and recovery operations; during cryogenic recirculation, the liquid inventory is isolated in the cold loop. The feed line (LFD) is connected to the RSV downcomer, so that liquid HFE is drawn from the bottom of the reservoir. The return line (LRT) connects the upper part of the cold loop and the gas trap back to the RSV through the manifold.

The cold-loop volume that must remain filled during operation does not include the feed and return lines, since these lines are isolated after filling. It includes the heat-exchanger tank, the cold-loop tubing, and the small internal volumes of the pump, flow meter, and feedthrough tubing:

$$V_{\mathrm{cold}} = V_{\mathrm{tank,HFE}} + V_{\mathrm{loop}} + V_{\mathrm{aux}} = 2.43\,\mathrm{L} + 0.260\,\mathrm{L} + 0.115\,\mathrm{L} = 2.81\,\mathrm{L}. \tag{5.28}$$

Here $V_{\mathrm{aux}}$ accounts for the estimated pump, flow-meter, and feedthrough-tubing hold-up volumes. The feed and return lines are nevertheless filled during transfer and must be included in the mass removed from the reservoir:

$$V_{\mathrm{lines}} = V_{\mathrm{LFD}} + V_{\mathrm{LRT}} = 0.099\,\mathrm{L} + 0.071\,\mathrm{L} = 0.170\,\mathrm{L}. \tag{5.29}$$

To keep the cold loop filled after cooling to $-110\,^{\circ}\mathrm{C}$, the required HFE mass is set by the cold density,

$$m_{\mathrm{cold}} = \rho_{7200}(-110\,^{\circ}\mathrm{C})V_{\mathrm{cold}} \simeq \left(1.73\,\mathrm{kg\,L^{-1}}\right)(2.81\,\mathrm{L}) = 4.9\,\mathrm{kg}. \tag{5.30}$$

At room temperature, this same mass occupies

$$V_{\mathrm{fill}}(25\,^{\circ}\mathrm{C}) = \frac{m_{\mathrm{cold}}}{\rho_{7200}(25\,^{\circ}\mathrm{C})} \simeq 3.40\,\mathrm{L}. \tag{5.31}$$

The difference,

$$V_{\mathrm{GT,liq}} = V_{\mathrm{fill}}(25\,^{\circ}\mathrm{C}) - V_{\mathrm{cold}} \simeq 0.59\,\mathrm{L}, \tag{5.32}$$

is the room-temperature HFE volume that must initially sit in the gas trap to compensate for the density increase during cooldown. This corresponds to

$$m_{\mathrm{GT,liq}} = \rho_{7200}(25\,^{\circ}\mathrm{C})V_{\mathrm{GT,liq}} \simeq 0.84\,\mathrm{kg}. \tag{5.33}$$

Including the feed and return lines, the total volume transferred from the RSV during a full cryogenic fill is

$$V_{\mathrm{transfer}} = V_{\mathrm{fill}}(25\,^{\circ}\mathrm{C}) + V_{\mathrm{lines}} \simeq 3.57\,\mathrm{L}, \tag{5.34}$$

corresponding to a reservoir mass decrease of about 5.1 kg.

The filling pressure is set by two constraints. First, the RSV pressure must lift the HFE column to the gas trap. Neglecting line losses,

$$P_{\mathrm{RSV}} - P_{\mathrm{GT}} \geq \rho g \Delta z, \tag{5.35}$$

where all pressures are gauge pressures and $\Delta z$ is the height difference between the reservoir liquid level and the gas trap. For $\Delta z \simeq 1.85\,\mathrm{m}$,

$$\rho g \Delta z \simeq \left(1430\,\mathrm{kg\,m^{-3}}\right)\left(9.81\,\mathrm{m\,s^{-2}}\right)(1.85\,\mathrm{m}) \simeq 0.26\,\mathrm{bar}. \tag{5.36}$$

Thus, for a desired gas-trap overhead pressure $P_{\mathrm{GT}}$,

$$P_{\mathrm{RSV}} \simeq P_{\mathrm{GT}} + 0.26\,\mathrm{bar}, \tag{5.37}$$

before adding margin for valve restrictions and transient losses.

Second, if the system is sealed during filling, the gas initially present in the system is compressed into the remaining gas volume in the gas trap. With a total gas-trap volume $V_{\mathrm{GT}} = 3.0\,\mathrm{L}$, the initial gas volume is

$$V_{\mathrm{gas,0}} = V_{\mathrm{cold}} + V_{\mathrm{lines}} + V_{\mathrm{GT}} = 2.81\,\mathrm{L} + 0.170\,\mathrm{L} + 3.0\,\mathrm{L} = 5.98\,\mathrm{L}. \tag{5.38}$$

The final gas volume is

$$V_{\mathrm{gas},f} = V_{\mathrm{GT}} - V_{\mathrm{GT,liq}} = 3.0\,\mathrm{L} - 0.59\,\mathrm{L} = 2.41\,\mathrm{L}. \tag{5.39}$$

Assuming isothermal compression, the initial absolute pressure to set in the system is

$$P_{\mathrm{sys},0,\mathrm{abs}} = P_{\mathrm{GT,abs}} \frac{V_{\mathrm{gas},f}}{V_{\mathrm{gas},0}}. \tag{5.40}$$

For example, to obtain $P_{\mathrm{GT}} = 1\,\mathrm{barg}$ after filling, $P_{\mathrm{GT,abs}} = 2.013\,\mathrm{bar}$, giving

$$P_{\mathrm{sys},0,\mathrm{abs}} \simeq (2.013\,\mathrm{bar})\,\frac{2.41\,\mathrm{L}}{5.98\,\mathrm{L}} = 0.81\,\mathrm{bar}, \tag{5.41}$$

or about $-0.20\,\mathrm{barg}$. The corresponding reservoir pressure is

$$P_{\mathrm{RSV}} \simeq 1\,\mathrm{barg} + 0.26\,\mathrm{bar} = 1.26\,\mathrm{barg}. \tag{5.42}$$

| Category | Quantity | Value |
|---|---|---|
| Volumes | Tank HFE volume | $V_{\mathrm{tank,HFE}} \simeq 2.43\,\mathrm{L}$ |
| | Cold-loop tubing volume | $V_{\mathrm{loop}} = 0.260\,\mathrm{L}$ |
| | Pump, flow-meter, feedthroughs | $V_{\mathrm{aux}} \simeq 0.115\,\mathrm{L}$ |
| | Cold-loop operating volume | $V_{\mathrm{cold}} \simeq 2.81\,\mathrm{L}$ |
| | Gas-trap liquid margin | $V_{\mathrm{GT,liq}} \simeq 0.59\,\mathrm{L}$ (0.84 kg) |
| | Room-temperature fill volume | $V_{\mathrm{fill}} \simeq 3.40\,\mathrm{L}$ |
| | Feed and return line volume | $V_{\mathrm{lines}} = 0.170\,\mathrm{L}$ |
| | Total transferred amount | $V_{\mathrm{trans.}} \simeq 3.57\,\mathrm{L}$ (5.1 kg) |
| Static head | Height to gas trap | $\Delta z \simeq 1.85\,\mathrm{m}$ |
| | Hydrostatic $\Delta P$ | $\rho g \Delta z \simeq 0.26\,\mathrm{bar}$ |
| | Density used | $\rho_{7200}(25\,^{\circ}\mathrm{C}) \simeq 1.43\,\mathrm{kg\,L^{-1}}$ |
| Example | Target gas-trap pressure | $P_{\mathrm{GT}} = 1\,\mathrm{barg}$ |
| | Initial system pressure | $P_{\mathrm{sys},0} \simeq -0.20\,\mathrm{barg}$ |
| | Reservoir pressure | $P_{\mathrm{RSV}} \simeq 1.26\,\mathrm{barg}$ |

Table 5.10: HFE volumes and pressure scale used to fill the cold loop from the reservoir. The example pressures correspond to a target gas-trap overhead pressure of 1 barg after filling, neglecting line losses.

**Filling the system** Before filling, the system is evacuated or set to the desired initial pressure through the manifold. The RSV headspace is then pressurized with dry nitrogen, and the feed path from the RSV downcomer to the cold loop is opened. The pressure difference pushes liquid HFE through LFD and into the loop. The reservoir scale is used to monitor the transferred mass. Filling is stopped when the desired transferred mass is reached and liquid is present in the gas trap, typically indicated by bubbling as liquid displaces gas in the return line.

**Emptying the system** Emptying is performed in two steps. First, the reservoir and cold loop are connected so that the bulk liquid returns to the RSV by gravity. The reservoir mass is monitored until it reaches a stable value. A small amount of HFE can remain in low points of the loop, so a second pressure-assisted step is used: dry nitrogen is applied to the system side while the reservoir is kept at lower pressure, pushing the remaining liquid back through the feed path into the RSV. Residual HFE vapor can then be removed by cycling the system between dry nitrogen purge and vacuum. This final purge is kept short and is performed only after liquid recovery, to minimize HFE venting.

**Pump pressure-relief valve** A Generant pressure-relief valve is installed downstream of the gear pump to protect it from excessive differential pressure. It is connected to the end of the feed line, close to the RSV downcomer port, so that overpressure at the pump outlet can be relieved toward the reservoir side. This is important during cold operation, when the HFE viscosity increases strongly and a partial blockage, closed valve, or local freezing could raise the pump outlet pressure. The relief valve is set to 10 bar, matching the pump differential-pressure limit, and provides a hardware protection layer in addition to the slow-control interlocks described in Sec. 5.4.

## 5.4 Slow-Control System

The HFE recirculation system is operated through a dedicated slow-control system for sensor readout, actuator control, data logging, and interlocks. Since the relevant time scales are set by cryogenic flow and thermal equilibration, a 1 Hz cadence is sufficient for stable monitoring and reproducible operation. The system records the HFE temperatures, pressures, flow-meter quantities, pump-drive state, $LN_2$ valve state, heater state, and control set points. The control and telemetry architecture is shown in Fig. 5.23.

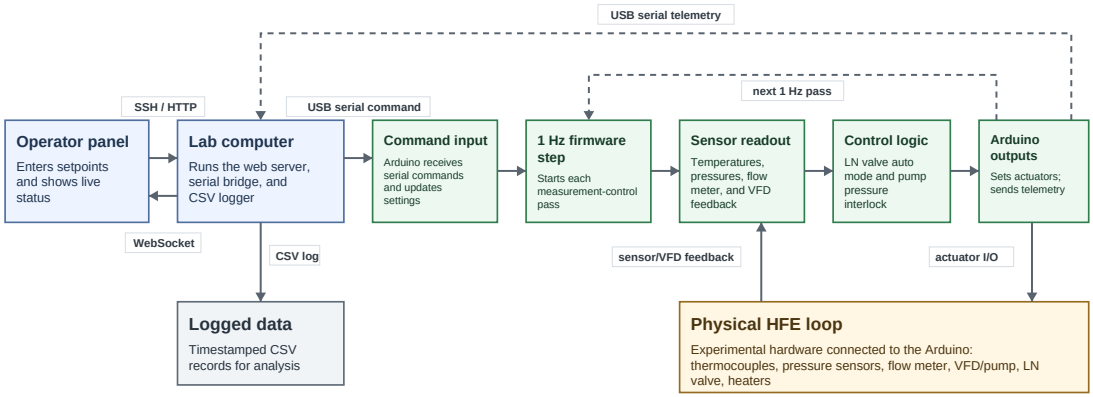


Figure 5.23: Control, telemetry, and logging architecture for the HFE recirculation system.

In Fig. 5.23, the box colors separate the four functional layers of the slow-control system: blue for the operator interface and laboratory-computer processes, green for the Arduino firmware, yellow for the physical HFE hardware, and gray for the logged CSV data products. Solid arrows indicate command, control, and hardware I/O paths, while dashed arrows indicate recurring telemetry and firmware-loop paths.

The Arduino Mega acts as the local controller for the apparatus. It reads the thermocouples, pressure transducers, flow meter, and VFD feedback; applies the $LN_2$ valve logic and pump differential-pressure interlock; updates the pump command and relay states; and sends the measured system state to the laboratory computer over a USB serial connection. Here, serial communication refers to digital messages exchanged between devices over a small number of wires, one bit at a time. The computer provides the operator interface, forwards user commands to the Arduino, displays the live telemetry, and records the data. In this configuration, safety-relevant actions remain local to the firmware, while the computer is used for supervision, visualization, and logging.

### 5.4.1 Electrical Architecture

The electrical system is housed in a grounded enclosure mounted on the rear side of the apparatus. The installed enclosure is shown in Fig. 5.24.

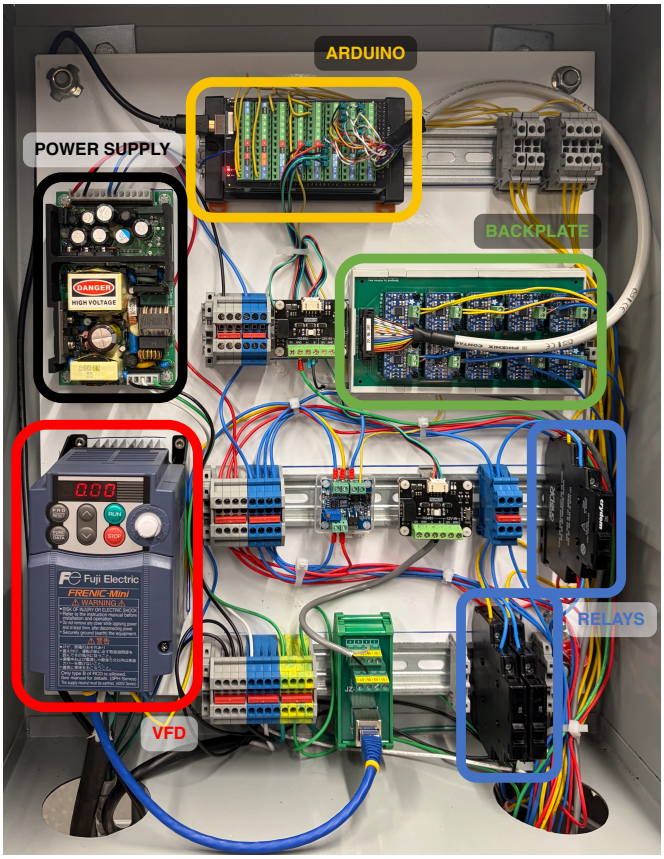


Figure 5.24: Electrical enclosure for the HFE slow-control system. The cabinet contains the Arduino, power supply, VFD, thermocouple backplate and relay modules.

The main components visible in Fig. 5.24 are:

1. the Arduino Mega at the top center;
2. the DC power supply at the top left;
3. the Fuji VFD at the lower left;
4. the thermocouple backplate at the middle right;
5. the relay modules at the lower right;
6. smaller signal-conversion boards used for the VFD command/readback and the flow-meter serial interface.

The wiring uses a simple color convention: black for 5 V DC or 120 V AC live, blue for COM, red for 24 V DC, green for ground, white for 120 V AC neutral, and yellow for data or signal lines.

The main power domains are:

1. 240 V AC for the pump motor through the Fuji VFD;
2. 120 V AC for the auxiliary heaters and AC-fed power supplies;
3. 24 V DC for the $LN_2$ valve, pressure transducers, flow meter, and signal converters;
4. 5 V DC for the Arduino-side electronics and thermocouple readout boards.

Figure 5.25 summarizes the main power domains, signal paths, and interface electronics connecting the laboratory computer, Arduino, sensors, actuators, and pump drive.

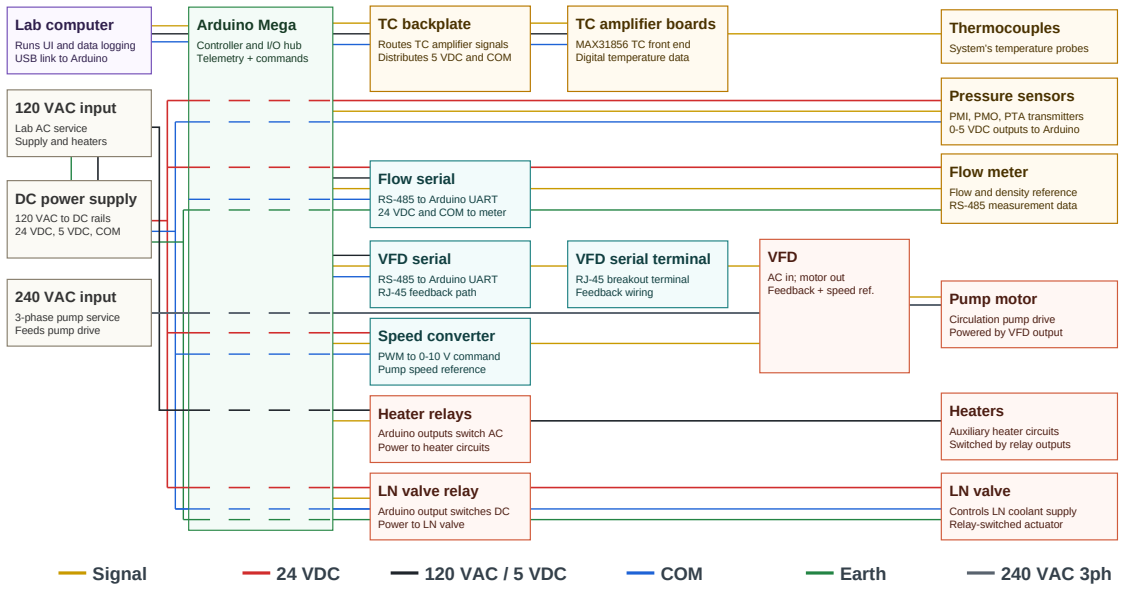


Figure 5.25: Simplified electrical wiring overview of the HFE slow-control system. The Arduino Mega is the central controller. It communicates with the laboratory computer over USB, reads the thermocouple backplate, pressure sensors, flow meter, and VFD monitor lines, and drives the pump-speed command, $LN_2$ valve relay, and heater relays.

The diagram is organized from left to right, from laboratory-side power and computer interfaces to devices on the apparatus. The box colors group components

by role: computer/supervisor, power supply, controller, instrumentation, signal-conversion electronics, and actuation or powered loads. The cable colors follow the legend and indicate the electrical function of each connection.

The Arduino acts as the central I/O controller. It receives thermocouple, pressure, flow-meter, and VFD feedback, and sends the pump-speed command, heater-relay commands, and $LN_2$ valve command. The higher-power circuits remain separated from the low-voltage instrumentation: 120 V AC is used for the heaters and power-supply input, 240 V three-phase AC is used only for the VFD and pump motor path, and 24 V DC is distributed to the external sensors, converters, relays, and $LN_2$ valve.

The thermocouple path runs from the system thermocouples to the amplifier boards, through the thermocouple backplate, and then to the Arduino. The pressure sensors are powered by 24 V DC and return analog voltage signals to the Arduino. The Coriolis flow meter and VFD are read through serial converters. The VFD also receives a 0 V to 10 V speed reference generated from the Arduino PWM command.

**Variable-frequency drive** The pump motor is driven by a Fuji Electric variable-frequency drive (VFD). The speed command is generated by an Arduino PWM output and converted to a 0 V to 10 V analog reference for the VFD. In the firmware, the pump command is expressed as a percentage of full scale, with 100 % corresponding to an output frequency of 71.7 Hz. For the four-pole motor, this corresponds to an estimated speed of about 2150 rpm, matching the maximum pump speed specified by the vendor for our applications.

The 0 V to 10 V signal from the Arduino sets the requested pump speed. This command path is separate from the VFD monitoring path. The VFD is read through a serial link, which records the drive frequency sent to the motor, the motor current and voltage, the electrical power drawn by the drive, and the motor speed inferred from the drive frequency. These quantities are logged with the slow-control telemetry and used later in the pump-performance analysis.

### Thermocouple Backplate

Thermocouple readout is performed with thermocouple-to-digital converter boards mounted on a custom backplate. The backplate logic is shown in Fig. 5.26.

The backplate distributes the shared digital communication and power lines to the readout boards, while keeping one chip-select line per channel. This reduces the number of point-to-point connections between the Arduino and the individual boards.

The shared lines are $V_{\mathrm{in}}$, GND, SDI, SDO, and SCK. $V_{\mathrm{in}}$ and GND provide power and the common electronics reference. SDI carries configuration and command data from the Arduino to the selected converter board, SDO returns measurement and status data from the selected board, and SCK provides the shared clock. The chip-select lines determine which board is active on the shared communication lines. The Arduino therefore reads the boards sequentially, one active channel at a time.

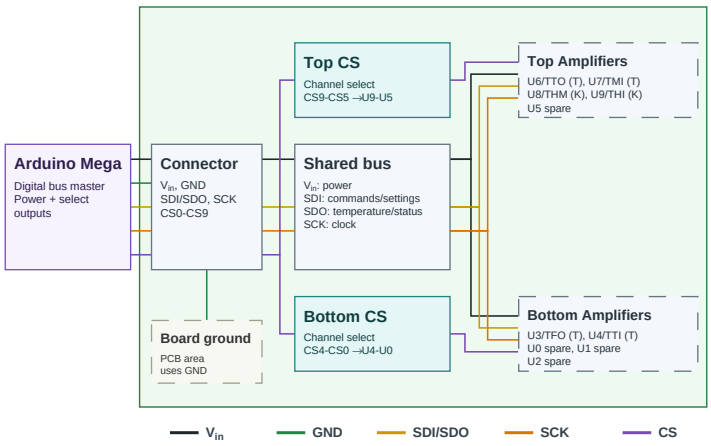


Figure 5.26: Logic diagram of the thermocouple backplate. The shared $V_{\mathrm{in}}$, GND, SDI, SDO, and SCK lines are distributed to the converter boards, while the chip-select lines select the active thermocouple channel.

The backplate is configured for ten possible thermocouple channels, of which six are used in the present system. The channel mapping is summarized in Table 5.11.

| Channel | Configured type | Assignment |
|---|---|---|
| U0 | K | Spare |
| U1 | K | Spare |
| U2 | T | Spare |
| U3 | T | TFO, flow-meter outlet |
| U4 | T | TTI, tank inlet |
| U5 | K | Spare |
| U6 | T | TTO, tank outlet |
| U7 | T | TMI, pump inlet |
| U8 | K | THM, heat-exchanger middle |
| U9 | K | THI, heat-exchanger inlet |

Table 5.11: Thermocouple channel mapping used by the HFE slow-control firmware. Spare channels correspond to installed or reserved backplate positions not assigned to active thermocouples in the present configuration.

In the present firmware, the converter boards are operated in blocking one-shot mode, with a measured readout time of about 0.21 s per channel. Reading the six active channels therefore takes about 1.25 s, comparable to the 1 Hz telemetry cadence. The same converter also supports continuous-conversion mode, with an update time of about 82 ms to 90 ms. This mode could be used in future firmware if sub-second thermocouple readout becomes necessary. One-shot mode was used for the data presented here because it provides a simple and robust readout sequence, and the resulting cadence is sufficient for the thermal time scales of the HFE system.

### 5.4.2 Control Logic

The firmware provides manual actuator control and basic automatic protection. From the operator interface, the pump speed can be set as a percentage command, the $LN_2$ valve can be opened or closed, and the heaters can be switched on or off. The firmware applies these commands after each sensor readout, so the commanded state is always evaluated together with the current temperature and pressure conditions.

**Pump control and interlock** The pump speed is controlled through the VFD reference described in Sec. 5.4.1. The operator sets a pump command in percent of the configured full-scale value, which is converted by the Arduino to the corresponding analog speed reference.

The pump has an independent protection condition based on the differential pressure across the pump,

$$\Delta P_{\mathrm{pump}} = P_{\mathrm{MO}} - P_{\mathrm{MI}}, \tag{5.43}$$

where $P_{\mathrm{MI}}$ and $P_{\mathrm{MO}}$ are the pressure readings before and after the pump. If $\Delta P_{\mathrm{pump}} > 8.0\,\mathrm{bar}$, the pump command is set to zero, the cooling is stopped and an emergency-stop latch is set. The latch blocks further positive pump commands until it is explicitly reset, and the reset is accepted only after the pressure condition has cleared. This software interlock complements the 10 bar mechanical relief valve described in Sec. 5.3.4.

**$LN_2$ valve control** The $LN_2$ valve can be forced closed, forced open, or operated in automatic mode. The automatic mode is an on–off control scheme with hysteresis, intended as an early cooldown controller rather than a full PID loop. Its firmware logic is summarized in Fig. 5.27.

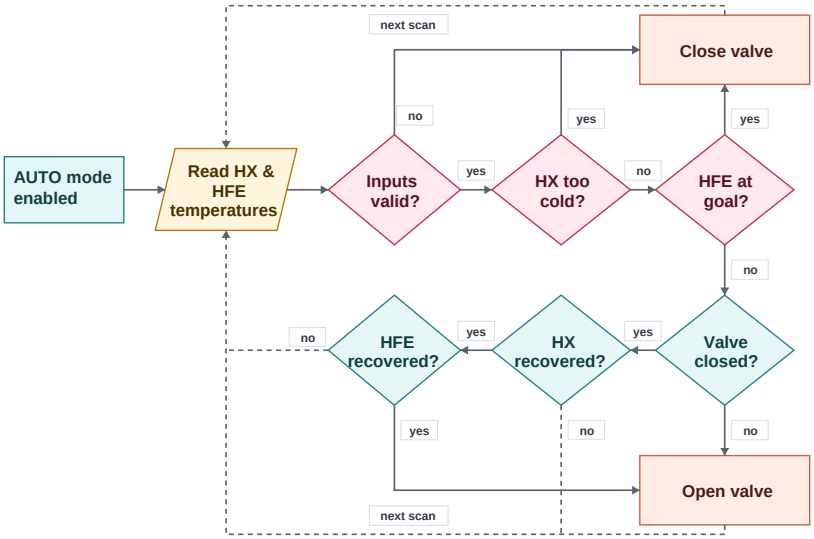


Figure 5.27: Automatic $LN_2$ valve logic implemented in the slow-control firmware.

At each control pass, the Arduino reads the HFE control temperature $T_{\mathrm{MI}}$ and the heat-exchanger guard temperature $T_{\mathrm{HI}}$. If either value is missing or invalid, the

valve is closed as a fail-safe. The valve is also closed if the heat exchanger becomes too cold,

$$T_{\mathrm{HI}} \leq T_{\mathrm{HX,limit}}, \tag{5.44}$$

or if the HFE reaches the selected cooling goal,

$$T_{\mathrm{MI}} \leq T_{\mathrm{HFE,goal}}. \tag{5.45}$$

After an automatic close command, the firmware latches the valve closed. Reopening requires both recovery criteria to be satisfied. The heat exchanger must warm to within the selected approach margin of the HFE temperature,

$$T_{\mathrm{HI}} \geq T_{\mathrm{MI}} - \Delta T_{\mathrm{HX,approach}}, \tag{5.46}$$

and the HFE must warm above the target by the configured hysteresis,

$$T_{\mathrm{MI}} \geq T_{\mathrm{HFE,goal}} + \Delta T_{\mathrm{hyst}}. \tag{5.47}$$

These conditions prevent the valve from reopening while the heat exchanger is still much colder than the circulating HFE, and avoid rapid valve cycling near the temperature set point.

**Heater control** The heaters are treated as auxiliary actuators. They can be switched manually from the operator interface. Future improvements can be made to automatically turn them on, to warm HFE above a specified temperature.

### 5.4.3 Data Acquisition and Logging

The slow-control firmware records telemetry at a 1 Hz cadence (with occasional longer intervals from sequential thermocouple readout). Each telemetry record contains thermocouple readings, pressure readings, flow-meter quantities, VFD monitor values, actuator states, interlock states, as well as $LN_2$ and HFE-reservoir information. The instrument resolutions are summarized in Table 5.12.

The CSV files store the raw thermocouple readings returned by the slow-control system. The thermocouple calibration constants are applied during analysis to convert these raw readings into calibrated channel temperatures using Eq. (5.57). For operator monitoring, the user interface displays the calibrated values online, but the saved data preserve the raw thermocouple readings.

The $LN_2$ dewar scale is read directly by the laboratory computer through a separate USB connection and included in the telemetry. The HFE reservoir scale was not yet connected to the slow-control system during the measurements described here; its value was recorded manually from the scale display. Direct electronic readout of the reservoir scale is under implementation.

The operator interface provides remote live monitoring through a web interface accessed over SSH, together with command entry, set-point adjustment, and data-logging controls. Separate tabs are used for the pump, heat exchanger, and fluid/system properties.

| Quantity | Source | Specification or resolution |
|---|---|---|
| Type-T temperatures | Loop TCs | $\begin{cases}\max(1.0\,^\circ\mathrm{C}, 0.0075\lvert T\rvert), & \geq 0\,^\circ\mathrm{C}\\ \max(1.0\,^\circ\mathrm{C}, 0.015\lvert T\rvert), & < 0\,^\circ\mathrm{C}\end{cases}$ |
| Type-K temperatures | HX TCs | $\begin{cases}\max(2.2\,^\circ\mathrm{C}, 0.0075\lvert T\rvert), & \geq 0\,^\circ\mathrm{C}\\ \max(2.2\,^\circ\mathrm{C}, 0.020\lvert T\rvert), & < 0\,^\circ\mathrm{C}\end{cases}$ |
| Pressures | Pressure sensors | $\pm 0.03$ bar |
| Mass flow | Flow meter | $\pm 0.1\%$ |
| Density | Flow meter | $\pm 1\,\mathrm{kg\,m^{-3}}$ |
| Flow-meter temperature | Flow meter | $\pm 0.5\,^\circ\mathrm{C} \pm 0.5\%$ |
| Volume flow | Flow meter | Reported from $\dot{V} = \dot{m}/\rho$ |
| Pump-drive frequency | VFD readback | 0.01 Hz |
| Pump-drive voltage | VFD readback | 0.01 V |
| Pump-drive current | VFD readback | 0.01 A |
| Pump-drive input power | VFD readback | 0.01 kW |
| $LN_2$ dewar mass | Dewar scale | 0.2 kg |
| HFE reservoir mass | Reservoir scale | 0.1 kg; recorded manually |
| Actuator/control state | Firmware | Digital state |

Table 5.12: Main slow-control measurements used for HFE operation and later analysis.

## 5.5 Commissioning and Performance Tests

During and after assembly, the HFE recirculation system was commissioned through a sequence of room-temperature tests. These tests verified basic fluid handling, pump operation, temperature-sensor calibration, leak tightness, sensor readout, and data logging. A separate heat-exchanger performance test was also performed in an antifreeze bath before the exchanger was installed in the system.

Filling and emptying procedures were then tested together with progressive cooldown runs. The system was operated step by step, from room temperature to 0 °C, then to −50 °C, and finally toward −100 °C, as discussed in the next section.

### 5.5.1 Room-Temperature Pump Commissioning

Before installing the pump on the system, the pump response was checked at room temperature using water. This test verified the VFD command chain, pump rotation, and basic flow response in a simple open-outlet configuration. Since the outlet was open to atmosphere, the comparison is made at approximately zero differential pressure.

The measured water data were compared with the vendor water performance curve for the same pump head. The vendor curve, shown in Fig. 5.28, gives volume flow as a function of differential pressure for several pump speeds. Since the commissioning test was performed with the outlet open to atmosphere, only the

approximately zero-pressure points are used in the comparison.

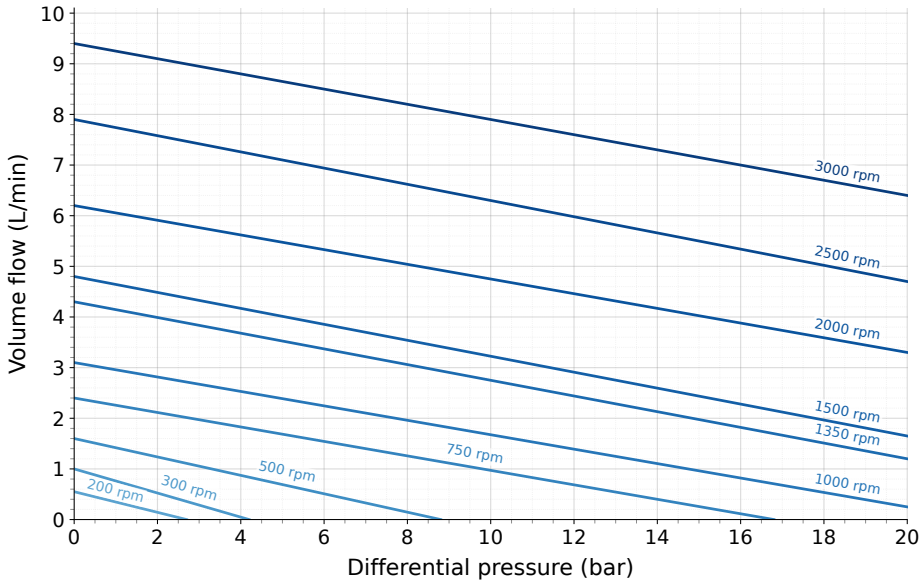


Figure 5.28: Digitized vendor water performance curve for the selected gear-pump head. The curves correspond to water at 20 °C. The zero-pressure intercepts are used as the vendor water reference for the room-temperature pump commissioning test.

For the four-pole motor, the pump speed was estimated from the induction-motor synchronous-speed relation [104],

$$n_{\mathrm{pump}} \simeq n_s = \frac{120 f_{\mathrm{VFD}}}{p} = 30 f_{\mathrm{VFD}}, \tag{5.48}$$

where $n_{\mathrm{pump}}$ is in $\mathrm{min}^{-1}$, $f_{\mathrm{VFD}}$ is in Hz, and $p = 4$ is the number of motor poles.

The pump was operated at $f_{\mathrm{VFD}} = 10\,\mathrm{Hz},\ 20\,\mathrm{Hz},\ 30\,\mathrm{Hz}$ and 40 Hz, corresponding to motor speeds of $n_{\mathrm{pump}} = 300\,\mathrm{min}^{-1},\ 600\,\mathrm{min}^{-1},\ 900\,\mathrm{min}^{-1}$ and $1200\,\mathrm{min}^{-1}$. The scan was stopped at 40 Hz because this point already corresponds to a flow of about $4\,\mathrm{L\,min}^{-1}$, which is the maximum flow rate specified by the vendor for our intended HFE application.

For each point, the flow was measured by timing the filling of a 500 mL container:

$$\dot{V}_i = \frac{60 V_{\mathrm{fill}}}{t_i}, \qquad \sigma_{\dot{V}_i} = \dot{V}_i \sqrt{\left(\frac{\sigma_V}{V_{\mathrm{fill}}}\right)^2 + \left(\frac{\sigma_t}{t_i}\right)^2}, \tag{5.49}$$

with $\dot{V}_i$ in $\mathrm{L\,min}^{-1}$. The factor 60 converts from seconds to minutes. The fill-volume uncertainty was taken as 5%, and the timing uncertainty as $\sigma_t = 0.5\,\mathrm{s}$. The measured points are summarized in Table 5.13.

The measured water data and the zero-pressure vendor points were each fitted with an origin-constrained linear model,

$$\dot{V}(f_{\mathrm{VFD}}) = S_V f_{\mathrm{VFD}}, \tag{5.50}$$

| $f_{\mathrm{VFD}}$ [Hz] | $n_{\mathrm{pump}}$ [min$^{-1}$] | Fill time [s] | $\dot{V}$ [L min$^{-1}$] |
|---|---|---|---|
| 10 | 300 | 28.82 | $1.041 \pm 0.055$ |
| 20 | 600 | 14.52 | $2.066 \pm 0.125$ |
| 30 | 900 | 9.77 | $3.071 \pm 0.220$ |
| 40 | 1200 | 7.37 | $4.071 \pm 0.343$ |

Table 5.13: Room-temperature water pump-speed measurements obtained by timing the filling of a 500 mL container.

where $S_V$ is the flow-per-frequency slope. The slope uncertainty, $\sigma_{S_V}$, was taken from the covariance matrix of the weighted least-squares fit. The fit was constrained to pass through the origin, since the flow should vanish at zero pump speed. As a check, free linear fits gave intercepts compatible with zero:

$$b_{\mathrm{meas}} = (0.0266 \pm 0.1084)\,\mathrm{L\,min^{-1}}, \qquad b_{\mathrm{vendor}} = (0.0147 \pm 0.0838)\,\mathrm{L\,min^{-1}}. \quad (5.51)$$

Figure 5.29 shows the measured points, the vendor zero-pressure reference points, and the corresponding linear fits.

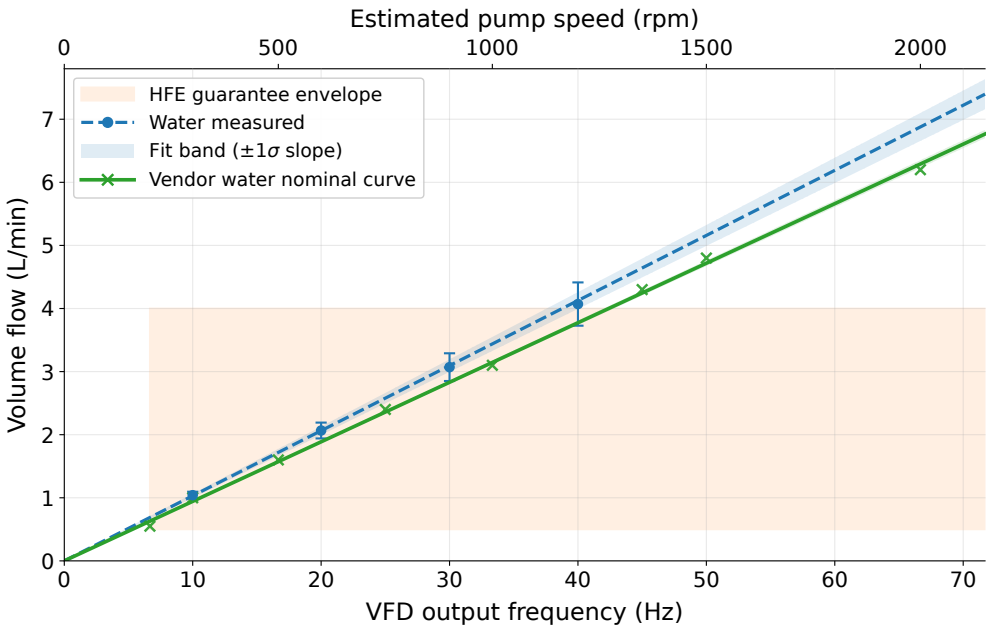


Figure 5.29: Room-temperature water pump-speed test compared with the zero-pressure points from the vendor water performance curve.

The fitted slope can also be converted to a volume displaced per pump revolution using Eq. (5.48). Since $n_{\mathrm{pump}} \simeq 30 f_{\mathrm{VFD}}$,

$$D_{\mathrm{eff}} = \frac{\dot{V}}{n_{\mathrm{pump}}} = \frac{S_V f_{\mathrm{VFD}}}{30 f_{\mathrm{VFD}}} = \frac{S_V}{30}, \quad (5.52)$$

with $S_V$ in mL min$^{-1}$ Hz$^{-1}$ and $D_{\mathrm{eff}}$ in mL rev$^{-1}$.

| Data set | $S_V$ [mL min$^{-1}$ Hz$^{-1}$] | $\chi^2$/ndf | $D_{\text{eff}}$ [mL rev$^{-1}$] |
|---|---|---|---|
| Measured water | $103.17 \pm 3.32$ | 0.07/3 | $3.439 \pm 0.111$ |
| Vendor water | $94.36 \pm 0.90$ | 1.53/9 | $3.145 \pm 0.030$ |

Table 5.14: Origin-constrained linear fit results for the measured water data and digitized vendor water reference. The slope $S_V$ is expressed per VFD output frequency. The displacement $D_{\text{eff}}$ is the corresponding volume displaced per pump revolution.

The origin-constrained fit results are summarized in Table 5.14.

The measured volume displaced per revolution is higher than the vendor value by

$$\Delta D = (0.294 \pm 0.115)\,\text{mL rev}^{-1}, \tag{5.53}$$

or about 9.3%. Because the vendor water chart gives no stated uncertainty, this difference is not treated as a strict disagreement. The pump response is linear in VFD frequency and agrees with the expected water performance.

**Expected HFE slip correction** For HFE operation, the volume flow is expected to follow the same first-order scaling with pump speed, with a correction for pump slip:

$$\dot{V} \simeq D_{\text{eff}} n_{\text{pump}} - \dot{V}_{\text{slip}}. \tag{5.54}$$

In a gear pump, slip is the internal leakage from the high-pressure outlet side back toward the low-pressure inlet side through the small clearances between the gears, housing, and side plates. For a fixed clearance geometry, this can be written as

$$\dot{V} \simeq D_{\text{eff}} n_{\text{pump}} - C_{\text{slip}} \frac{\Delta P}{\rho \nu}, \tag{5.55}$$

where $C_{\text{slip}}$ absorbs the clearance geometry, $\Delta P$ is the pump differential pressure, $\rho$ is the fluid density, and $\nu$ is the kinematic viscosity.

This dependence follows from an external-gear-pump leakage model in which the internal leakage paths are approximated as laminar flow through narrow clearances [105],

$$\dot{V}_{\text{slip}} = \frac{\Delta P\, b\, h^3}{12\, \rho \nu\, l}, \tag{5.56}$$

where $b$, $h$, and $l$ are the width, height, and length of the leakage path. For the cold HFE regime, this laminar approximation is a reasonable first-order model because the leakage paths are small and the HFE viscosity increases strongly at low temperature.

As the HFE is cooled, its viscosity increases, which increases the pressure drop across the loop and therefore the differential pressure across the pump. The slip model gives the expected trends: a larger differential pressure reduces the delivered flow, while a larger viscosity suppresses internal leakage. Since these two effects act in opposite directions, the net slip correction is expected to remain at the level of a few percent over the operating range considered here.

| Channel | Type | $g_j$ | $o_j$ [°C] |
|---|---|---|---|
| TTEST | T | 1.016382 | -0.385273 |
| TFO | T | 1.001612 | -0.625867 |
| TTI | T | 0.997152 | -0.891752 |
| TTO | T | 1.006183 | -0.187982 |
| TMI | T | 1.003589 | -0.195442 |
| THM | K | 0.990067 | -0.434418 |
| THI | K | 1.067338 | -0.738115 |

Table 5.15: Thermocouple calibration constants used in Eq. (5.57).

### 5.5.2 Thermocouple Calibration

The measured HFE loop temperatures, read out with Type-T thermocouples, and the heat-exchanger temperatures, read out with Type-K thermocouples, were calibrated using a two-point linear calibration,

$$T_{\mathrm{cal},j} = g_j T_{\mathrm{raw},j} + o_j, \tag{5.57}$$

where $T_{\mathrm{raw},j}$ is the raw thermocouple reading, and $g_j$ and $o_j$ are the fitted gain and offset for channel $j$. The calibration constants used in the analysis are listed in Table 5.15. The Type-T loop thermocouples were calibrated using the room-temperature and liquid-nitrogen anchors. The Type-K heat-exchanger thermocouples were calibrated using the room-temperature anchor and an in-system HFE recirculation point near $-35$°C.

TTEST was a temporary thermocouple used for the DSC test, and is not part of the six installed slow-control channels.

#### Calibration uncertainty

All thermocouple uncertainties quoted in this subsection are $1\sigma$ uncertainties. This uncertainty model includes only the uncertainty associated with the calibration anchors. Electronic and digitization noise are evaluated separately in each data-log analysis window. It does not include possible systematic effects such as imperfect thermal contact, local temperature gradients, or thermocouple placement error.

The thermocouple calibration deviation can be written as a sum of measured calibration-point deviations multiplied by interpolation functions [106],

$$\Delta V(t) = \sum_{i=1}^{N} \Delta V_i F_i(t), \tag{5.58}$$

where $t$ denotes temperature, $\Delta V_i$ is the voltage deviation at calibration point $i$, and the functions $F_i(t)$ are Lagrange polynomials. For $N$ calibration points,

$$F_i(t) = \prod_{\substack{j=1 \\ j \neq i}}^{N} \frac{t - t_j}{t_i - t_j}. \tag{5.59}$$

In this work, the amplifier converts the measured voltage $V$ to a raw temperature using its conversion function $f$. For uncertainty arising from voltage alone, first-order propagation gives

$$T_{\mathrm{raw}} = f(V), \qquad u(T_{\mathrm{raw}}) \simeq |f'(V)|\, u(V), \tag{5.60}$$

where $u(V)$ is the voltage standard uncertainty and $u(T_{\mathrm{raw}})$ is its contribution to the temperature uncertainty, in degrees Celsius.

The subsequent calibration in Eq. (5.57) is performed on these temperature readings. It uses two reference temperatures $T_1, T_2$ and the corresponding amplifier readings $T_{\mathrm{raw},1}, T_{\mathrm{raw},2}$. The calibrated temperature is

$$T_{\mathrm{cal}} = (1-w)T_1 + wT_2, \qquad w = \frac{T_{\mathrm{raw}} - T_{\mathrm{raw},1}}{T_{\mathrm{raw},2} - T_{\mathrm{raw},1}}. \tag{5.61}$$

The quantity $w$ indicates the position of the measured raw temperature relative to the two calibration readings: $w = 0$ at the first anchor and $w = 1$ at the second. The coefficients $1 - w$ and $w$ are the interpolation weights.

Writing $T$ for the calibrated reading obtained with the assigned reference values, the preceding equation gives $T - T_1 = w(T_2 - T_1)$. The weights can therefore also be written as

$$F_1(T) = 1 - w = \frac{T_2 - T}{T_2 - T_1}, \qquad F_2(T) = w = \frac{T - T_1}{T_2 - T_1}. \tag{5.62}$$

To evaluate the uncertainty from the calibration references, we calculate how the result would change if the assigned reference temperatures were slightly different, while using the same recorded amplifier readings. Since $w$ depends only on those readings, it remains unchanged. Reference-temperature errors $\delta T_1$ and $\delta T_2$ therefore produce

$$\delta T_{\mathrm{cal}} = F_1(T)\, \delta T_1 + F_2(T)\, \delta T_2. \tag{5.63}$$

The standard uncertainties of these reference temperatures are denoted $u_1$ and $u_2$, already expressed in degrees Celsius. Taking the variance and neglecting anchor covariance (conservative below the Type-K transfer point, where errors from a shared reference partly cancel) gives [107]

$$u_{\mathrm{cal}}^2(T) = F_1^2(T) u_1^2 + F_2^2(T) u_2^2, \tag{5.64}$$

where $u_{\mathrm{cal}}(T)$ is the resulting calibration contribution to the uncertainty of the temperature reading. Thus, $T$ determines the interpolation weights, while $u_1$ and $u_2$ quantify the uncertain reference values. The same expression can be used outside the calibration interval; in that case, one weight has magnitude greater than unity, so the uncertainty increases with extrapolation.

The room-temperature calibration point was 68.5°F, corresponding to

$$T_{\mathrm{room}} = 20.2778^{\circ}\mathrm{C}. \tag{5.65}$$

The room reference is expected to lie within ±0.1°C. Since this is a bounded accuracy statement rather than a measured standard deviation, it is treated as a rectangular distribution,

$$u_{\mathrm{room}} = \frac{0.1^{\circ}\mathrm{C}}{\sqrt{3}} = 0.058^{\circ}\mathrm{C}. \tag{5.66}$$

**Loop thermocouples.** The second calibration point used for the Type-T thermocouples was the liquid-nitrogen point, taken to be $T_{\mathrm{LN2}} = -195.8°\mathrm{C}$ at 1 atm. Near 1 atm, the nitrogen boiling temperature changes by approximately 8.38°C/bar [108]. Assuming the liquid-nitrogen bath pressure was within ±0.010 bar of 1 atm gives

$$u_{\mathrm{LN2}} = \frac{8.38°\mathrm{C/bar} \times 0.010\ \mathrm{bar}}{\sqrt{3}} = 0.049°\mathrm{C}. \tag{5.67}$$

The Type-T calibration anchors are therefore

$$T_1 = -195.8°\mathrm{C}, \qquad T_2 = 20.2778°\mathrm{C}, \tag{5.68}$$

with

$$u_1 = 0.049°\mathrm{C}, \qquad u_2 = 0.058°\mathrm{C}. \tag{5.69}$$

Substitution into Eq. (5.64) gives

$$u_{T,\mathrm{cal}}(T) = \sqrt{\left[\frac{20.2778 - T}{216.0778}(0.049)\right]^2 + \left[\frac{T + 195.8}{216.0778}(0.058)\right]^2}. \tag{5.70}$$

This is the calibration uncertainty only. It is 0.049°C at the liquid-nitrogen anchor, 0.058°C at the room-temperature anchor, and 0.037°C at −110°C.

**Heat-exchanger thermocouples.** The Type-K heat-exchanger thermocouples THM and THI were calibrated using the same room-temperature point. Because these thermocouples were already sealed in the tank before the first commissioning run, a well-mixed cooled HFE recirculation period was used as the low-temperature point instead of a liquid-nitrogen dip. A later commissioning phase is planned to apply the same liquid-nitrogen calibration procedure used for the Type-T loop thermocouples.

The lower Type-K calibration anchor, $T_{K,1}$, was defined as the Type-T reference temperature assigned to the selected recirculation window,

$$T_{K,1} = \langle T_{\mathrm{ref}} \rangle_{\mathcal{W}} = -35.04°\mathrm{C}. \tag{5.71}$$

Here $T_{\mathrm{ref}}$ is the calibrated Type-T estimate of the local HFE temperature at the THM/THI position, obtained from the nearby thermocouples during the selected window $\mathcal{W}$. The selected window contained $N = 78$ logged samples satisfying

$$-35.5°\mathrm{C} < T_{\mathrm{TTI}} < -34.5°\mathrm{C}.$$

Over this selected window, the median calibrated TTI and TTO temperatures were

$$\mathrm{median}_{\mathcal{W}}(T_{\mathrm{TTI}}) = -34.980°\mathrm{C}, \qquad \mathrm{median}_{\mathcal{W}}(T_{\mathrm{TTO}}) = -35.055°\mathrm{C}, \tag{5.72}$$

giving a local inlet–outlet difference of

$$\Delta_{\mathrm{TTI,TTO}} = |\mathrm{median}_{\mathcal{W}}(T_{\mathrm{TTI}}) - \mathrm{median}_{\mathcal{W}}(T_{\mathrm{TTO}})| = 0.075^{\circ}\mathrm{C}. \tag{5.73}$$

The uncertainty of the Type-K low-temperature anchor was computed from the Type-T calibration uncertainty at $T_{K,1}$, the statistical $1\sigma$ uncertainty of the selected-window reference $\langle T_{\mathrm{ref}}\rangle_{\mathcal{W}}$, and the finite TTI–TTO bracket:

$$u_{K,1} = \sqrt{u_{T,\mathrm{cal}}^2(T_{K,1}) + u_{\mathrm{sel}}^2 + u_{\mathrm{bracket}}^2}. \tag{5.74}$$

The selection term is the statistical $1\sigma$ uncertainty of $\langle T_{\mathrm{ref}}\rangle_{\mathcal{W}}$, the reference temperature assigned to the selected window.

$$u_{\mathrm{sel}} = \frac{s(T_{\mathrm{ref}})}{\sqrt{N}} = \frac{0.285^{\circ}\mathrm{C}}{\sqrt{78}} = 0.032^{\circ}\mathrm{C}. \tag{5.75}$$

The bracket term accounts for the unknown local temperature of THM/THI within the TTI–TTO interval. Treating this location as uniformly distributed within the half-width of the bracket gives

$$u_{\mathrm{bracket}} = \frac{\Delta_{\mathrm{TTI,TTO}}/2}{\sqrt{3}} = \frac{0.075^{\circ}\mathrm{C}/2}{\sqrt{3}} = 0.022^{\circ}\mathrm{C}. \tag{5.76}$$

At $T_{K,1}$, Eq. (5.70) gives $u_{T,\mathrm{cal}}(-35.04^{\circ}\mathrm{C}) = 0.045^{\circ}\mathrm{C}$. Thus,

$$u_{K,1} = \sqrt{(0.045)^2 + (0.032)^2 + (0.022)^2} = 0.060^{\circ}\mathrm{C}. \tag{5.77}$$

For the Type-K heat-exchanger thermocouples, the calibration anchors are therefore

$$T_1 = -35.04^{\circ}\mathrm{C}, \qquad T_2 = 20.2778^{\circ}\mathrm{C}, \tag{5.78}$$

with

$$u_1 = 0.060^{\circ}\mathrm{C}, \qquad u_2 = 0.058^{\circ}\mathrm{C}. \tag{5.79}$$

Substitution into Eq. (5.64) gives

$$u_{K,\mathrm{cal}}(T) = \sqrt{\left[\frac{20.2778 - T}{55.3178}(0.060)\right]^2 + \left[\frac{T + 35.04}{55.3178}(0.058)\right]^2}. \tag{5.80}$$

Between room temperature and the $-35.04^{\circ}\mathrm{C}$ transfer point, this gives calibration-anchor uncertainties of order 0.04–0.06°C:

$$u_{K,\mathrm{cal}}(20.2778^{\circ}\mathrm{C}) = 0.058^{\circ}\mathrm{C}, \qquad u_{K,\mathrm{cal}}(-35.04^{\circ}\mathrm{C}) = 0.060^{\circ}\mathrm{C}. \tag{5.81}$$

Below the transfer point, THM and THI are extrapolated. Equation (5.80) includes the extrapolation contribution from the stated calibration-anchor uncertainties through the Lagrange sensitivity coefficients. At the representative cryogenic temperature of $-110^{\circ}\mathrm{C}$, it gives $u_{K,\mathrm{cal}}(-110^{\circ}\mathrm{C}) = 0.16^{\circ}\mathrm{C}$.

| Configuration | $p_{LN2}$ [barg] | Bath | $LN_2$ inlet |
|---|---|---|---|
| MT-ST | 1.52 | still | middle tube |
| MT-MX | 1.52 | mixed | middle tube |
| CT-MX | 1.52 | mixed | coil top |
| CT-AU | 1.52 | mixed | coil top |
| CT-HP | 4.14 | mixed | coil top |

Table 5.16: Antifreeze-bath heat-exchanger test configurations. MT and CT denote $LN_2$ injection through the middle tube and coil top, respectively; ST and MX denote a still and mixed bath; AU denotes automatic $LN_2$ valve control; HP denotes higher dewar pressure. Pressures are dewar gauge pressures.

**Readout uncertainty treatment.** The amplifier readout uncertainty was not included in the calibration-anchor uncertainty above. The amplifier resolution is 0.0078125°C, which is negligible compared with the calibration-anchor uncertainties. Readout noise, digitization effects, and short-term electronic fluctuations are instead included in the observed scatter of the calibrated temperature samples in each analysis window. For an averaged temperature $\bar{T}$,

$$u_{\mathrm{stat}} = \frac{s_T}{\sqrt{N_{\mathrm{eff}}}}, \tag{5.82}$$

where $s_T$ is the standard deviation of the calibrated samples and $N_{\mathrm{eff}}$ is the number of independent samples. The total uncertainty is then

$$u_{\bar{T}} = \sqrt{u_{\mathrm{cal}}^2(\bar{T}) + u_{\mathrm{stat}}^2}, \tag{5.83}$$

with $u_{\mathrm{cal}}$ from Eq. (5.70) or Eq. (5.80).

### 5.5.3 Heat-Exchanger Performance

A stand-alone liquid-nitrogen heat-exchanger test was performed in an antifreeze bath before operation with HFE-7200. The goals were to measure the installed cooling power of the coil, compare $LN_2$ inlet configurations, and identify signatures of degraded thermal coupling from local freezing. Four thermocouples were logged during these tests: two in the antifreeze bath, located near the bottom and top of the bath, and two on the heat exchanger, located near the coil top and near the middle of the coil. The bath temperature $T_{\mathrm{AF}}$ is the bath thermocouple mean, and $T_{\mathrm{HX}}$ is the analysis mean of the two heat-exchanger thermocouples. A conservative $1\sigma$ uncertainty of $\pm 0.5$°C is used in the propagated errors and in the figure bands.

The tested configurations are summarized in Table 5.16. CT-AU uses the same mixed bath and coil-top $LN_2$ inlet as CT-MX, with additional automatic valve control. The valve was opened or closed depending on whether the top of the heat exchanger fell below −65°C, about 16°C below the antifreeze freezing point, to limit icing.

### Antifreeze-bath analysis

For a cooling interval with bulk bath temperature $T_{\mathrm{AF}}$, the heat-exchanger cooling power is estimated from the energy balance [98]

$$P_{\mathrm{HX}} = C_{\mathrm{bath}}\left(-\frac{dT_{\mathrm{AF}}}{dt}\right) + C_{\mathrm{HX,SS}}\left(-\frac{dT_{\mathrm{HX}}}{dt}\right) + P_{\mathrm{amb}}^{\mathrm{AF}}, \tag{5.84}$$

where $C_{\mathrm{bath}}$ is the antifreeze-bath heat capacity, $C_{\mathrm{HX,SS}}$ is the stainless-steel heat capacity of the heat-exchanger coil, and $P_{\mathrm{amb}}^{\mathrm{AF}}$ is the ambient heat leak obtained from a warm-up run with the $LN_2$ valve closed.

Using the heat-exchanger coil geometry and 304L density $\rho_{\mathrm{SS}} = 8000\ \mathrm{kg\,m^{-3}}$ gives

$$m_{\mathrm{HX,SS}} = 0.974\ \mathrm{kg}.$$

The cooling term is evaluated with the temperature-dependent stainless-steel heat capacity [109],

$$C_{\mathrm{HX,SS}}(T) = m_{\mathrm{HX,SS}}c_{p,304}(T), \tag{5.85}$$

giving $C_{\mathrm{HX,SS}} = 0.458\,\mathrm{kJ\,K^{-1}}$ at $25\,^{\circ}\mathrm{C}$ and $0.368\,\mathrm{kJ\,K^{-1}}$ at $-110\,^{\circ}\mathrm{C}$. The warm-up fit then gives $P_{\mathrm{amb}}^{\mathrm{AF}} = 15.20 \pm 0.02$ W.

The antifreeze used is an ethylene-glycol/water mixture with glycol mass fraction $x_{\mathrm{EG}} = 0.76 \pm 0.02$. The mixed-bath fill volume is $V_{\mathrm{AF}} = 5.65 \pm 0.05$ L giving a heat-capacity value of $C_{\mathrm{bath}} = 17.43 \pm 0.24\ \mathrm{kJ\,K^{-1}}$. The same ethylene-glycol concentration gives an antifreeze freezing temperature of approximately $-49^{\circ}\mathrm{C}$.

The coil-to-bath temperature difference is used as a diagnostic of local freezing,

$$\Delta T_{\mathrm{AF}} = T_{\mathrm{AF}} - T_{\mathrm{HX}}. \tag{5.86}$$

The corresponding apparent test conductance and resistance are

$$UA_{\mathrm{AF}} = \frac{P_{\mathrm{HX}}}{\Delta T_{\mathrm{AF}}}, \qquad R_{\mathrm{AF}} = \frac{\Delta T_{\mathrm{AF}}}{P_{\mathrm{HX}}}. \tag{5.87}$$

following the usual overall-heat-transfer form $P = UA\Delta T$ [98]. They include nitrogen-side heat transfer, tube-wall conduction, liquid-side coupling, and possible ice layers. The measured cooling performances are summarized in Table 5.17.

| Config. | $p_{\mathrm{LN2}}$ [barg] | $P_{\mathrm{HX}}$ [W] | $\Delta T_{\mathrm{AF}}$ [K] | $UA_{\mathrm{AF}}$ [W K$^{-1}$] | $R_{\mathrm{AF}}$ [mK W$^{-1}$] |
|---|---|---|---|---|---|
| MT-ST | $1.52 \pm 0.2$ | $269.5 \pm 5.4$ | $43.0 \pm 6.8$ | $6.26 \pm 1.00$ | $159.7 \pm 25.5$ |
| MT-MX | $1.52 \pm 0.2$ | $249.5 \pm 6.8$ | $1.37 \pm 0.12$ | $182.27 \pm 16.70$ | $5.5 \pm 0.5$ |
| CT-MX | $1.52 \pm 0.2$ | $307.3 \pm 7.2$ | $15.7 \pm 2.7$ | $19.57 \pm 3.36$ | $51.1 \pm 8.8$ |
| CT-AU | $1.52 \pm 0.2$ | $181.9 \pm 6.3$ | $29.8 \pm 0.6$ | $6.11 \pm 0.24$ | $163.6 \pm 6.4$ |
| CT-HP | $4.14 \pm 0.2$ | $843.1 \pm 20.7$ | $95 \pm 13$ | $8.85 \pm 1.25$ | $113.0 \pm 16.0$ |

Table 5.17: Measured antifreeze-bath cooling performance. The cooling power includes both antifreeze-bath cooling and cooling of the 304L heat-exchanger coil. $UA_{\mathrm{AF}}$ and $R_{\mathrm{AF}}$ are coil–bath quantities used to assess thermal coupling.

The mixed 1.52 barg top-inlet configuration gives the largest stable 1.52 barg cooling power, $P_{HX} = 307.3 \pm 7.2$ W. The high-pressure test reaches $843.1 \pm 20.7$ W, but with a much larger $\Delta T_{AF}$, indicating degraded local coupling from icing.

**Freezing detection** The first center-tube inlet tests cooled the bottom of the coil most aggressively and produced visible antifreeze icing at the lower coil, as shown in Fig. 5.30.

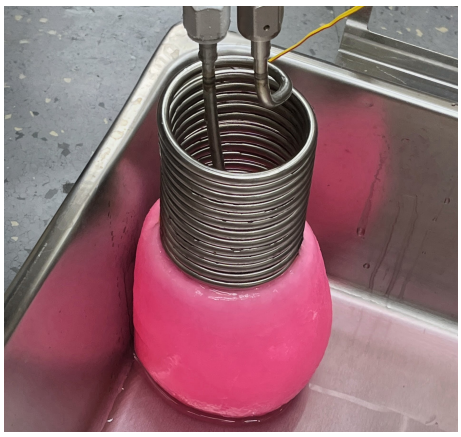

Figure 5.30: Antifreeze icing observed near the bottom of the coil during early center-inlet testing.

Since HFE flows top-to-bottom, this behavior motivated reversing the $LN_2$ flow to place the coldest part of the heat exchanger at the tank top. Incoming $LN_2$ then encounters warmer HFE first, while colder HFE below encounters nitrogen that has already absorbed heat along the coil.

Local freezing is detected by a growing $\Delta T_{AF}$ and a reduction in cooling power after the initial high-power phase. Once a local layer forms, heat must cross it mainly by conduction rather than by liquid convection, which increases the total resistance. This behavior is clearest in the high-pressure test, shown in Fig. 5.31.

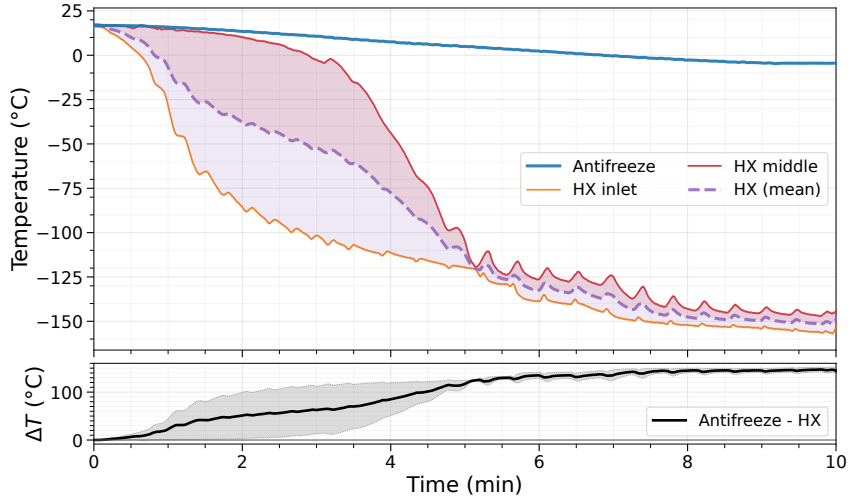


Figure 5.31: Temperature evolution during the 4.14 barg top-inlet antifreeze stress test. The growing $\Delta T_{AF}$ indicates degraded local coupling.

The heat-exchanger thermocouples cool rapidly far below the antifreeze bulk temperature, while $\Delta T_{\mathrm{AF}}$ grows during the run.

The same diagnostic applies to HFE operation, where a local HFE solidification layer would similarly increase the coil-to-bulk temperature difference.

The cooling-power comparison for all configurations is shown in Fig. 5.32.

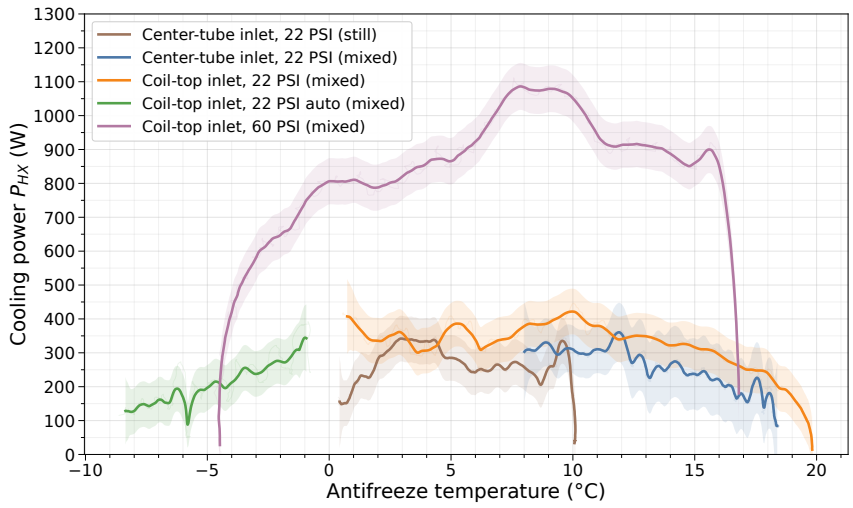


Figure 5.32: Cooling power versus antifreeze bulk temperature. Shaded bands are propagated $1\sigma$ uncertainties.

Most runs show reduced cooling power at the highest bath temperatures, corresponding to the initial cooling transient before stable $LN_2$ flow is established. The auto-mode test is an exception because it began after a previous cooldown, with the heat exchanger already partially primed. The 1.52 barg mixed tests give cooling powers of order 200–300 W, while the 4.14 barg test gives substantially higher power. The auto mode cooling shows a decrease in cooling power as temperature goes down due to increased freezing and a more restricting opening/close period.

For the two top-inlet mixed manual tests, the pressure-normalized powers are

$$\frac{P_{\mathrm{HX}}}{p_{\mathrm{LN2}}} = 202 \pm 27 \ \mathrm{W\,bar^{-1}} \quad \text{and} \quad 204 \pm 11 \ \mathrm{W\,bar^{-1}}, \tag{5.88}$$

for the 1.52 and 4.14 barg tests, respectively.

A two-point linear estimate gives

$$P_{\mathrm{HX}}^{\mathrm{top,mix}}(p_{\mathrm{LN2}}) = (-4 \pm 71) \ \mathrm{W} + (205 \pm 24) \ \mathrm{W\,bar^{-1}}\, p_{\mathrm{LN2}}, \tag{5.89}$$

with $p_{\mathrm{LN2}}$ in barg. The intercept is poorly constrained because it is obtained from only two pressure points and should not be interpreted physically. The positive pressure dependence indicates that the $LN_2$ flow and boiling side limits the cooling power. At the same dewar pressure and with a well-mixed bath, the installed cooling power should therefore be similar in antifreeze and HFE-7200.

### Equivalent HFE cooling power

For HFE-7200 operation, the antifreeze measurement is interpreted as an installed cooling-power measurement at a given $LN_2$ pressure. For the same $LN_2$ pressure

and a well-mixed liquid bath,

$$P_{\mathrm{HFE}}(p_{\mathrm{LN2}}) \simeq P_{\mathrm{HX}}(p_{\mathrm{LN2}}). \tag{5.90}$$

An equivalent HFE conductance is defined as the conductance required to deliver the measured power while keeping the heat-exchanger wall above the HFE freezing limit:

$$UA_{\mathrm{HFE,eq}} = \frac{P_{\mathrm{HX}}}{T_{\mathrm{HFE,bulk}} - T_{\mathrm{wall,lim}}}, \qquad T_{\mathrm{HFE,bulk}} = -110^{\circ}\mathrm{C}, \qquad T_{\mathrm{wall,lim}} = -121^{\circ}\mathrm{C}. \tag{5.91}$$

The uncertainty on $UA_{\mathrm{HFE,eq}}$ is obtained by propagating the cooling-power uncertainty through the fixed 11 K temperature difference $T_{\mathrm{HFE,bulk}} - T_{\mathrm{wall,lim}}$.

Since the cooling power was shown to scale approximately linearly with $LN_2$ pressure, Eq. (5.89) is also used to extrapolate to 10 barg, the maximum allowable operating pressure set by the $LN_2$ valve. The resulting values are summarized in Table 5.18.

| $p_{\mathrm{LN2}}$ [barg] | $UA_{\mathrm{HFE,eq}}$ [W K$^{-1}$] | $P_{\mathrm{HFE}}(-110^{\circ}\mathrm{C})$ [W] |
|---|---|---|
| 1.52 | $27.93 \pm 0.65$ | $307.3 \pm 7.2$ |
| 4.14 | $76.64 \pm 1.88$ | $843.1 \pm 20.7$ |
| 10.0 | $186 \pm 16$ | $2040 \pm 180$ |

Table 5.18: HFE cooling-power expectations from the antifreeze measurements. The 10 barg value is extrapolated using Eq. (5.89).

The measured 1.52 barg top-inlet configuration already exceeds the estimated parasitic heat load at $-110^{\circ}$C from Sec. 5.2.4, leaving about 120 W of net cooling power. The 4.14 barg test provides a much larger margin, while the 10 barg extrapolation represents the best-case cooling scale allowed by the $LN_2$ valve rating.

### 5.5.4 Leak-Tightness Tests

Leak tightness was tested by pressurizing the system with dry nitrogen and monitoring the pressure decay. These tests were performed before operation to identify dominant leak locations, verify repairs and later modifications, and estimate the HFE-equivalent loss expected during operation. The absolute pressure was fitted with the same pressure-relaxation model introduced in Sec. 5.3.1, and the HFE-equivalent loss was computed with the same vapor-throughput conversion. The relevant test volume is the gas volume connected to the pressure measurement during the nitrogen pressure-decay test. From the volumes listed in Sec. 5.3.4, the cold loop, gas trap, and return line give

$$V_{\mathrm{test}} = V_{\mathrm{cold}} + V_{\mathrm{GT}} + V_{\mathrm{LRT}} = 2.81\,\mathrm{L} + 3.0\,\mathrm{L} + 0.071\,\mathrm{L} = 5.88\,\mathrm{L}. \tag{5.92}$$

The obtained results are shown in Fig. 5.33. The left panel shows the initial large-leak checks and the effect of resealing the gas-trap NPT connection. The right

panel shows later commissioning leak checks after the main repair. Dashed curves are exponential fits. The colored bands around the pressure traces show the $\pm 1\sigma$ spread of the pressure samples in each 1 min time bin. The isolated top-of-system, bottom-of-system, and no-gas-trap points use the corresponding gauge-reading uncertainties as vertical error bars.

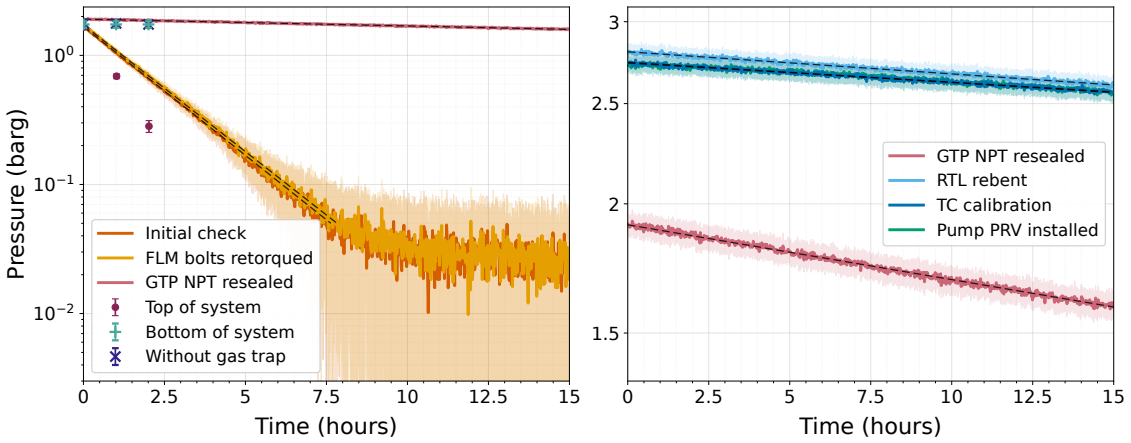


Figure 5.33: Nitrogen pressure-decay leak checks of the HFE system. The left panel shows the initial large-leak checks and the effect of resealing the gas-trap NPT connection. The right panel shows later commissioning leak checks after the main repair.

For ease of comparison, the fitted exponential was also expressed as an initial pressure-decay rate,

$$-\left.\frac{dP}{dt}\right|_{t=0} = -kA. \tag{5.93}$$

This quantity is not assumed to remain constant during the test; it is only a convenient way to compare the initial leak severity between measurements.

For the two largest leak checks, the late-time pressure excess becomes poorly resolved once it falls below about 50 mbar. In this region, $P_{\mathrm{abs}} - P_{\mathrm{atm}}$ is typically comparable to the one-minute binned pressure scatter, so the logarithmic fit variable $\ln(P_{\mathrm{abs}} - P_{\mathrm{atm}})$ becomes sensitive to small fluctuations near the fixed atmospheric asymptote. These two fits were therefore restricted to

$$P_{\mathrm{abs}}(t) - P_{\mathrm{atm}} \geq 50\,\mathrm{mbar}, \tag{5.94}$$

while keeping $P_{\mathrm{atm}}$ as the physical asymptote.

The results are summarized in Table 5.19. The fit quality was checked for each pressure-decay trace. The fitted curves are visibly consistent with the binned pressure-decay data in Fig. 5.33.

The initial system check corresponded to an HFE-7200 liquid-equivalent loss of about $24\,\mathrm{L\,yr^{-1}}$, which was manageable for short commissioning tests given the $\sim 4.8\,\mathrm{L}$ of spare HFE stored in the DRM drum, but not acceptable for long-term operation. Retorquing the flow-meter flange bolts did not improve the leak rate. The dominant improvement came from resealing the gas-trap NPT connection, after

| System update | Fit parameters | | Initial decay | HFE loss |
|---|---|---|---|---|
| | $P_0$ [bar abs] | $k$ [$10^{-3}\,\mathrm{h}^{-1}$] | [mbar $\mathrm{h}^{-1}$] | [L $\mathrm{yr}^{-1}$] |
| Initial check | $2.68 \pm 0.05$ | $-460 \pm 3$ | $768 \pm 8$ | $23.9 \pm 0.2$ |
| FLM bolts retorqued | $2.74 \pm 0.05$ | $-452 \pm 3$ | $779 \pm 8$ | $23.5 \pm 0.2$ |
| GTP NPT resealed | $2.92 \pm 0.05$ | $-12.20 \pm 0.12$ | $23.3 \pm 0.3$ | $0.635 \pm 0.006$ |
| RTL rebent | $3.82 \pm 0.05$ | $-4.92 \pm 0.10$ | $13.8 \pm 0.3$ | $0.253 \pm 0.005$ |
| TC calibration | $3.75 \pm 0.05$ | $-4.28 \pm 0.08$ | $11.7 \pm 0.2$ | $0.218 \pm 0.004$ |
| Pump PRV installed | $3.75 \pm 0.05$ | $-4.48 \pm 0.12$ | $12.3 \pm 0.3$ | $0.231 \pm 0.006$ |

Table 5.19: Summary of the nitrogen pressure-decay leak checks of the HFE system.

which the HFE-equivalent loss fell below $1\,\mathrm{L\,yr^{-1}}$. Subsequent commissioning checks remained at the lower leak level, with final HFE-equivalent losses of order $0.25\,\mathrm{L\,yr^{-1}}$. The final leak level was more than two orders of magnitude below the initial condition and was acceptable for the cryogenic recirculation tests.

**HFE vapor pressure** After the system had been nitrogen filled and evacuated, a residual pressure was measured on the gas-trap compound gauge. This check was used to determine whether the remaining pressure was consistent with HFE-7200 vapor from residual HFE left after the first system fill, and to check whether an additional water-vapor contribution from moisture in the HFE or system was visible. The measurement was performed at room temperature.

The HFE-7200 vapor pressure was calculated using 3M data giving,

$$P_{\mathrm{vap,HFE}} = 137.2\,\mathrm{mbar}. \tag{5.95}$$

For comparison, the saturated water vapor pressure was evaluated with the Antoine equation [110],

$$\log_{10}(P_{\mathrm{bar}}) = 5.40221 - \frac{1838.675}{T_K - 31.737}, \tag{5.96}$$

Here $P_{\mathrm{bar}}$ is in bar and $T_K$ is in K. At 21 °C, this gives

$$P_{\mathrm{vap,H_2O}} = 24.9\,\mathrm{mbar}. \tag{5.97}$$

The sum $P_{\mathrm{vap,HFE}} + P_{\mathrm{vap,H_2O}} = 162.1\,\mathrm{mbar}$ is treated only as an upper-bound case in which both condensed HFE and enough water are present to saturate the gas volume.

The gas-trap pressure gauge read $-26.0\,\mathrm{inHg}$, corresponding to

$$P_{\mathrm{meas}} = P_{\mathrm{atm}} - 26.0 \times 33.864\,\mathrm{mbar} = 132.8\,\mathrm{mbar}. \tag{5.98}$$

The total $1\sigma$ uncertainty was obtained by combining the Grade-A gauge accuracy and the $\pm 1\,\mathrm{inHg}$ readout resolution. The $-26\,\mathrm{inHg}$ reading lies in the end quarter of the gauge scale, so the accuracy term was taken as 2% of the full span,

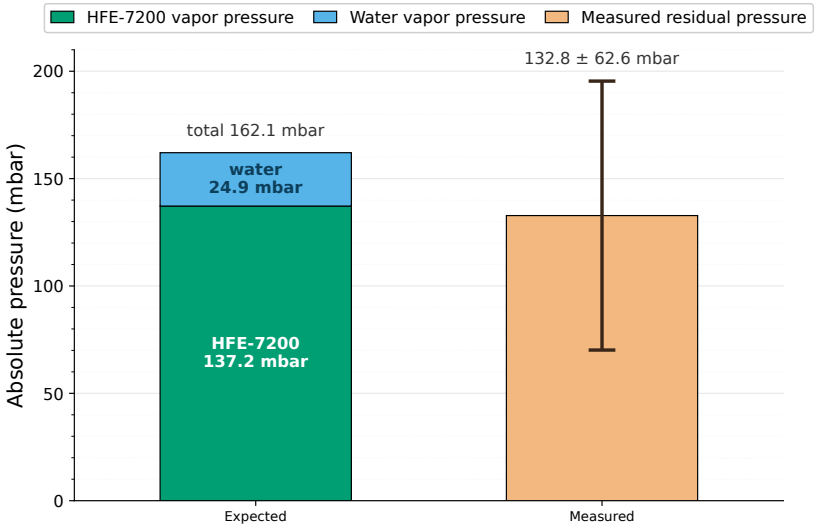


Figure 5.34: Residual pressure measured after evacuating the HFE system at approximately 21 °C. The measured value is shown with its $1\sigma$ uncertainty.

or $\pm 103.1$ mbar. Treating both contributions as uniformly distributed within their quoted bounds gives

$$\sigma_P = \sqrt{\left(\frac{103.1\,\text{mbar}}{\sqrt{3}}\right)^2 + \left(\frac{33.9\,\text{mbar}}{\sqrt{3}}\right)^2} = 62.6\,\text{mbar}. \tag{5.99}$$

The measured residual pressure is therefore

$$P_{\text{meas}} = 132.8 \pm 62.6\,\text{mbar} \quad (1\sigma). \tag{5.100}$$

The measured residual pressure differs from the HFE-7200 vapor-pressure expectation by only 4.4 mbar, or $0.07\sigma$. The HFE-plus-water upper-bound case differs by 29.2 mbar, or $0.47\sigma$. The measurement is therefore consistent with residual HFE-7200 vapor without moisture, but the gauge precision is not sufficient to clearly distinguish HFE-only vapor from an HFE-plus-water case.

### 5.5.5 Initial System Fill

A first room-temperature filling and emptying test was performed to verify that HFE-7200 could be transferred from the reservoir into the cold loop, circulated, and recovered into the reservoir. The HFE inventory was monitored from the reservoir mass. The RSV scale has a 0.1 kg readout increment, so a single reading was assigned an uncertainty of 0.1 kg, and the uncertainty on a mass difference was taken as

$$\sigma_{\Delta m} = \sqrt{2}\,0.1\,\text{kg} = 0.14\,\text{kg}. \tag{5.101}$$

The volumes were obtained using $\rho_{7200} = 1.43\,\text{kg}\,\text{L}^{-1}$ at 25 °C.

Before the first system fill, the RSV mass was 20.4 kg. After the first emptying and recovery procedure, the RSV mass was 19.8 kg. The unrecovered HFE inventory was therefore

$$m_{\text{res}} = (20.4 - 19.8)\,\text{kg} = 0.60 \pm 0.14\,\text{kg}, \tag{5.102}$$

corresponding to

$$V_{\mathrm{res}} = \frac{m_{\mathrm{res}}}{\rho_{7200}} = 0.42 \pm 0.10\,\mathrm{L}. \tag{5.103}$$

This residual corresponds to liquid remaining in the system after recovery, likely in low points of the feed line, pump head, feedthroughs, horizontal sections of the cold loop, and the bottom of the heat-exchanger tank.

Subsequent room-temperature fill and recovery cycles transferred approximately 4.0 kg between the RSV and the system (with an empty gas trap). Combining this repeated transferred mass with the residual inferred from the first recovery gives the total filled inventory, excluding the gas trap,

$$m_{\mathrm{meas,no\,GT}} = 4.0\,\mathrm{kg} + 0.60\,\mathrm{kg} = 4.60 \pm 0.20\,\mathrm{kg}, \tag{5.104}$$

or

$$V_{\mathrm{meas,no\,GT}} = \frac{m_{\mathrm{meas,no\,GT}}}{\rho_{7200}} = 3.22 \pm 0.14\,\mathrm{L}. \tag{5.105}$$

For the thermal analysis, the relevant inventory is the HFE volume that is cooled during operation. This excludes the gas trap and the feed and return lines. Since some HFE is expected to remain in the feed line after recovery, a residual feed-line fraction

$$f_{\mathrm{LFD}} = 0.65 \pm 0.15 \tag{5.106}$$

was assigned. The transfer-line volume excluded from the cooled inventory is therefore

$$V_{\mathrm{excl}} = V_{\mathrm{LRT}} + f_{\mathrm{LFD}} V_{\mathrm{LFD}} = 0.071\,\mathrm{L} + 0.65 \times 0.099\,\mathrm{L} = 0.135 \pm 0.020\,\mathrm{L}. \tag{5.107}$$

Subtracting this contribution from Eq. (5.105) gives the cooled HFE volume,

$$V_{\mathrm{cooled,meas}} = V_{\mathrm{meas,no\,GT}} - V_{\mathrm{excl}} = 3.08 \pm 0.15\,\mathrm{L}. \tag{5.108}$$

As a cross-check, the geometric estimate obtained from the corrected tank volume, after subtracting the immersed $LN_2$ heat-exchanger displacement and adding the cold-loop tubing, pump, flow meter, and feedthrough tubing volumes, gives

$$V_{\mathrm{cooled,geom}} \simeq 2.81\,\mathrm{L}. \tag{5.109}$$

The difference between Eqs. (5.108) and (5.109) is compatible with the scale precision and with the uncertainty on small internal volumes in the pump, flow meter, fittings, feedthroughs, and low points of the loop. The cooled HFE inventory used in the cryogenic analysis is therefore taken to be

$$\boxed{V_{\mathrm{cooled}} = 3.0 \pm 0.2\,\mathrm{L}}. \tag{5.110}$$

This corresponds to a room-temperature-equivalent HFE mass of

$$m_{\mathrm{cooled}}(25\,^{\circ}\mathrm{C}) = \rho_{7200}(25\,^{\circ}\mathrm{C}) V_{\mathrm{cooled}} = 4.3 \pm 0.3\,\mathrm{kg}. \tag{5.111}$$

At cryogenic temperature, the mass contained in the same fixed cold-loop volume is larger because the density increases. In the thermal analysis below, the HFE heat capacity is therefore evaluated as $V_{\mathrm{cooled}} \rho_{7200}(T) c_p(T)$, rather than by using a fixed room-temperature mass.

## 5.6 Analysis of Cryogenic Runs

The final commissioning runs tested the HFE-7200 loop under progressively colder recirculation conditions. Three data sets are analyzed here: the April 17, 2026 run, the first −50 °C run, with the HFE bypass open; the April 22, 2026 run, the second −50 °C run, with the bypass closed; and the April 24, 2026 run, which reached −100 °C with the bypass also closed.

Figure 5.35 shows the April 24, 2026 data log as a representative cryogenic recirculation run. The figure includes the pump command and measured flow, the temperature channels, the density, and the pressure sensors over the full cooldown and warm-up sequence.

The run began near room temperature and cooled rapidly once $LN_2$ cooling was enabled, reaching a minimum loop temperature near −100 °C. The heat-exchanger thermocouples stayed colder than the loop thermocouples throughout the cooldown, as expected from their location near the $LN_2$ coil. The density measured by the Coriolis meter increased from about 1430 kg m$^{-3}$ at room temperature to about 1700 kg m$^{-3}$ near the coldest point.

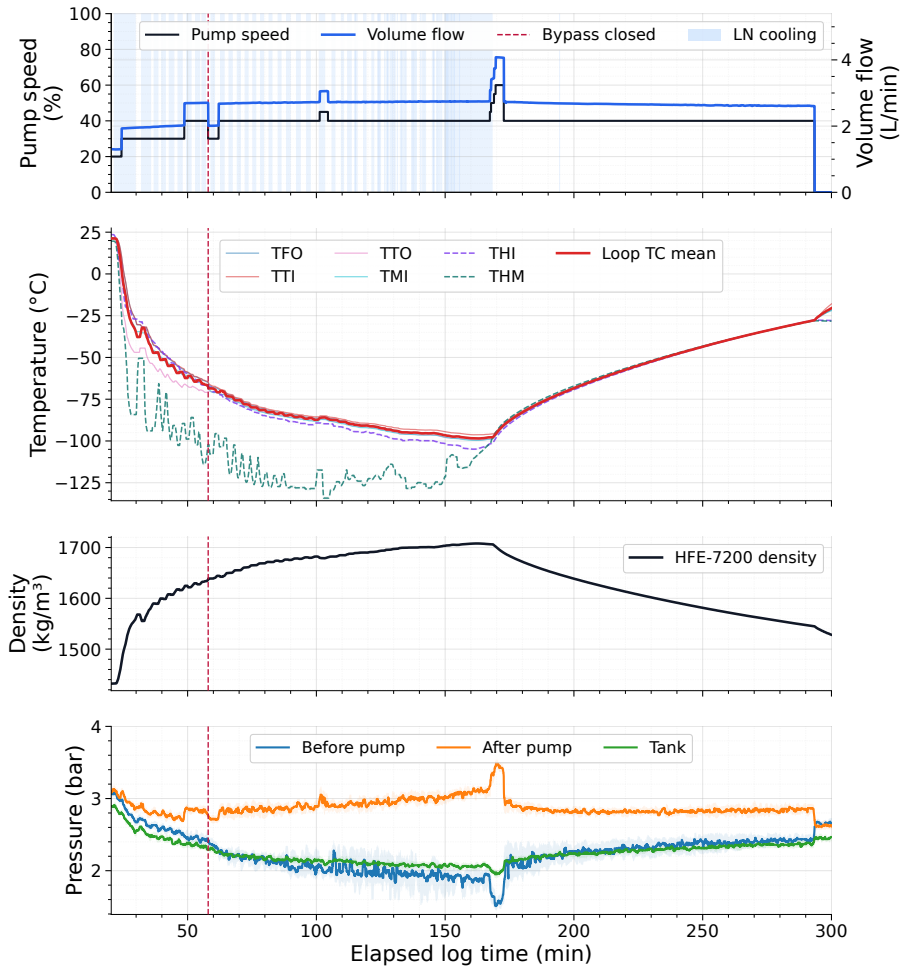


Figure 5.35: Overview of the April 24, 2026 HFE-7200 recirculation run.

At fixed pump command, the delivered volume flow remained stable. The pump

outlet pressure stayed above the inlet pressure throughout recirculation, with the largest separation at low temperature, consistent with the increased hydraulic resistance of the cold loop.

### 5.6.1 System Performance

The measured temperature evolution can be used to estimate the cooling performance of the system and the parasitic heat leak into the cold loop. The pressure evolution is determined by the system geometry and by the increase in HFE density and viscosity as the fluid cools. The thermal-capacity inputs used in the model are listed in Table 5.20.

| Component | Quantity | Basis |
|---|---|---|
| HFE-7200 cooled volume | $V_{\mathrm{cooled}} = 3.0 \pm 0.2\,\mathrm{L}$ | Fill/recovery estimate |
| HFE-7200 mass at 25 °C | $m_{25} = 4.3 \pm 0.3\,\mathrm{kg}$ | $\rho_{7200}(25\,^{\circ}\mathrm{C})V_{\mathrm{cooled}}$ |
| HFE-7200 mass at −110 °C | $m_{-110} \simeq 5.2 \pm 0.3\,\mathrm{kg}$ | $\rho_{7200}(-110\,^{\circ}\mathrm{C})V_{\mathrm{cooled}}$ |
| Cold-loop tubing | $1.061 \pm 0.053$ kg | 316 SS tube geometry |
| $LN_2$ heat-exchanger coil | $0.974 \pm 0.049$ kg | 304L SS coil geometry |
| Tank shell | $17.80 \pm 0.20$ kg | Measured |
| Pump head | $2.95 \pm 0.42$ kg | Cylinder estimate |
| Total cold stainless steel | $22.79 \pm 0.47$ kg | Hardware sum |

Table 5.20: Measured and estimated quantities included in the system thermal model.

The HFE volume is taken from the room-temperature fill and recovery estimate, while the stainless-steel hardware masses are either measured directly or estimated from the installed geometry. The flow-meter mass is not included because its body is thermally separated from the inner tubing by a dry-nitrogen volume. The stainless-steel heat capacity is evaluated using temperature-dependent specific heats for 304 and 316 stainless steel, weighted by the mass of each component.

#### Cooling Power and Heat Losses

The passive warm-up periods were used to estimate the heat leak into the insulated cold loop. Each selected period was fitted with an ambient-return model, assuming that the system can be described by a single mean temperature and that internal temperature gradients are negligible over the fitted interval,

$$T(t) = T_{\infty} + (T_0 - T_{\infty})\, e^{-t/\tau}, \tag{5.112}$$

and converted to an equivalent heat leak using

$$\dot{Q}_{\mathrm{leak}}(T) = U A\,(T_{\infty} - T)\,. \tag{5.113}$$

Here, $T_\infty$ is the ambient temperature of the surroundings and $T_0$ is the pump-inlet temperature at the start of the fitted warm-up interval.

The first 5 min of each selected warm-up period was excluded from the fit to reduce the effect of residual cooldown transients. Figure 5.36 shows the selected warm-up periods and the corresponding fits.

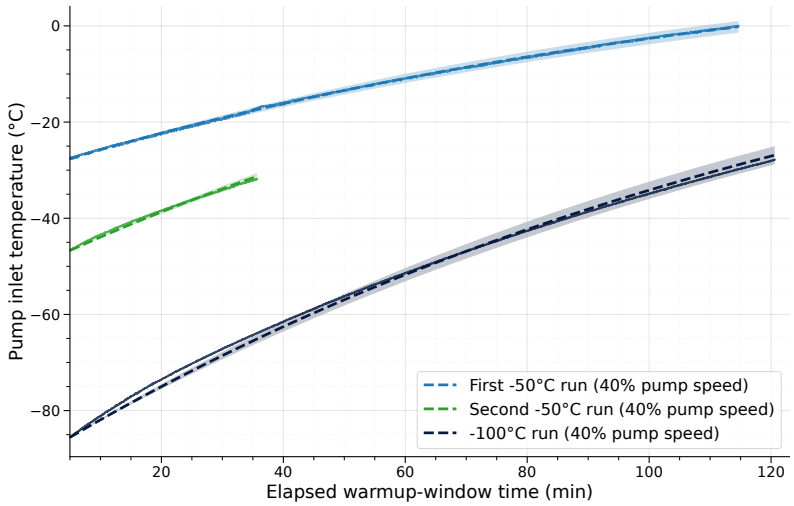


Figure 5.36: Warm-up periods used to estimate the parasitic heat leak into the HFE loop. The shaded bands show the propagated $1\sigma$ fit uncertainty.

These warm-ups were measured at a 40% pump-speed command, as defined in Sec. 5.4.1. The pump heat input was not subtracted from the warm-up fits because the hydraulic power delivered to the HFE was only a few watts, compared with an environmental heat leak of order 200 W, and was approximately constant over the selected periods.

The extracted heat-leak fit parameters are summarized in Table 5.21. The quoted uncertainties include the fit, mass, stainless-steel property, and ambient-temperature contributions. The inferred values are of the same order, with small run-to-run variations likely due to systematic effects such as temperature non-uniformity, room-temperature changes, or minor updates to the insulation. The heat leaks inferred at $-110\,^\circ\mathrm{C}$ are somewhat larger than the $\sim 189$ W component-level insulation estimate from Sec. 5.2.4, but they are still on the same scale. The insulation calculation is an order-of-magnitude design estimate based on the insulated piping, tank, flow-meter, and pump areas. In contrast, the warm-up fits measure the assembled system in operation, including pump operation and the thermal mass assigned to the cold hardware.

Cooldown powers were extracted with the same energy-balance approach used for the stand-alone heat-exchanger tests in Sec. 5.5.3. In the installed system, the antifreeze bath term is replaced by the heat capacity of the cooled HFE inventory and cold stainless-steel hardware listed in Table 5.20. Thus,

$$\dot{Q}_{\mathrm{HX}}(T) = -C_{\mathrm{eff}}(T)\frac{dT_{\mathrm{MI}}}{dt} + \dot{Q}_{\mathrm{leak}}(T), \tag{5.114}$$

| Run | $UA$ [W K$^{-1}$] | $\tau$ [min] | $\dot{Q}_{\mathrm{leak}}(-110\,^{\circ}\mathrm{C})$ [W] |
|---|---|---|---|
| First $-50\,^{\circ}$C run | $2.047 \pm 0.145$ | $127.0 \pm 9.0$ | $265.9 \pm 18.9$ |
| Second $-50\,^{\circ}$C run | $2.155 \pm 0.117$ | $116.6 \pm 6.3$ | $279.8 \pm 15.2$ |
| $-100\,^{\circ}$C run | $1.727 \pm 0.086$ | $142.1 \pm 7.1$ | $224.2 \pm 11.2$ |

Table 5.21: Heat-leak fit parameters extracted from the selected warm-up periods.

where $T_{\mathrm{MI}}$ is the pump-inlet temperature. The HFE contribution to $C_{\mathrm{eff}}$ is evaluated as $V_{\mathrm{cooled}}\rho_{7200}(T)c_p(T)$, while the stainless-steel contribution uses temperature-dependent specific heats for 304 and 316 stainless steel, weighted by the mass of each component. The heat leak $\dot{Q}_{\mathrm{leak}}(T)$ is taken from the warm-up fits in Table 5.21. As in Sec. 5.5.3, a heat-exchanger conductance is defined relative to the HFE wall-temperature limit,

$$UA_{\mathrm{HX}} = \frac{\dot{Q}_{\mathrm{HX}}}{\overline{T}_{\mathrm{MI}} - T_{\mathrm{wall,lim}}}, \qquad T_{\mathrm{wall,lim}} = -121\,^{\circ}\mathrm{C}. \tag{5.115}$$

This window-averaged quantity is used to compare cooldown periods and estimate the overall cooling power of the system under different operating conditions. Figure 5.37 shows the selected cooldown windows.

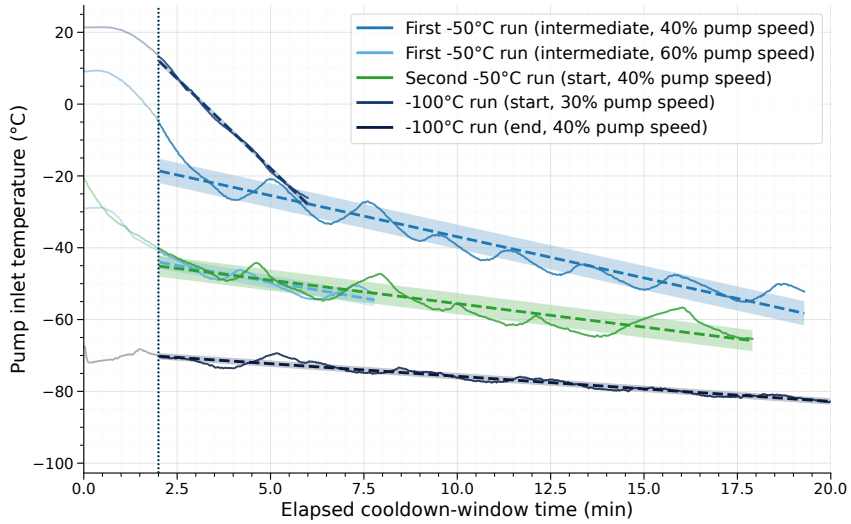


Figure 5.37: Pump-inlet temperature during selected cooldown windows. Linear fits start after the initial transient and are used to estimate the local cooling power.

The extracted cooldown parameters are summarized in Table 5.22. The quoted $\dot{Q}_{\mathrm{HX}}$ values are evaluated at $-110\,^{\circ}$C using Eq. (5.114).

The measured cooling power decreases as the system approaches lower temperature. The largest value, $\dot{Q}_{\mathrm{HX}} = 2385 \pm 94$ W, occurs at the start of the $-100\,^{\circ}$C run, when the HFE and stainless-steel inventory are cooling rapidly and the $LN_2$ valve remains open. Later in the cooldown, the $LN_2$ valve enters an increasingly frequent open–close cycle to avoid freezing the HFE, reducing the cooling power to $375 \pm 13$ W.

| Run | Pump speed | $dT_{\mathrm{MI}}/dt$ [°C min$^{-1}$] | $UA_{\mathrm{HX}}$ [W K$^{-1}$] | $\dot{Q}_{\mathrm{HX}}(-110\,^{\circ}\mathrm{C})$ [W] |
|---|---|---|---|---|
| 1st −50 °C run mid-cooldown | 40% | $-2.30 \pm 0.03$ | $8.4 \pm 0.3$ | $761 \pm 29$ |
| 1st −50 °C run mid-cooldown | 60% | $-1.82 \pm 0.08$ | $8.2 \pm 0.4$ | $659 \pm 30$ |
| 2nd −50 °C run start cooldown | 40% | $-1.31 \pm 0.03$ | $7.4 \pm 0.3$ | $562 \pm 20$ |
| −100 °C run start cooldown | 30% | $-10.02 \pm 0.06$ | $23.5 \pm 1.0$ | $2385 \pm 94$ |
| −100 °C run end cooldown | 40% | $-0.70 \pm 0.01$ | $7.4 \pm 0.2$ | $375 \pm 13$ |

Table 5.22: Cooling-performance parameters extracted from the selected cooldown windows.

The initial value is larger than, but still comparable in scale to, the 10 barg extrapolation from the antifreeze heat-exchanger test, $P_{\mathrm{HFE}} = 2040 \pm 180$ W.

**Temperature homogeneity** The loop temperature uniformity was checked using the four loop thermocouples: TTO, TMI, TFO, and TTI. The heat-exchanger thermocouples THM and THI are excluded because they probe the local $LN_2$ coil region.

The median loop temperature span is about 1.1 °C, with 95% of the selected samples below 3.6 °C. Below −50 °C, the median span increases to about 2.6 °C, with a maximum selected value of 4.6 °C. The pump inlet or tank outlet is usually the coldest point, while the tank inlet is warmer, consistent with gradual heat pickup around the loop.

The flow-meter temperature is higher than the calibrated loop thermocouples by about 2 °C, increasing to about 4 °C below −50 °C. This difference may come from a calibration offset or from the different probe location inside the flow meter. The flow-meter temperature is therefore not used for the loop-uniformity check, although it is still used for flow-meter quantities such as density and mass flow.

### Hydraulic Response

The combined pressure response is shown first in Fig. 5.38, using bypass-closed data from the two latest recirculation runs.

The pump pressure rise increases both as the HFE temperature decreases and as the pump-speed command increases. This is expected: colder HFE is more viscous, and higher pump speed drives a larger flow through the same hydraulic impedance. The temperature and pump-speed dependences are separated in Fig. 5.39.

The left panel shows the 40% pump-speed samples as a function of temperature. At fixed pump speed, the pressure rise increases during cooldown. The −100 °C

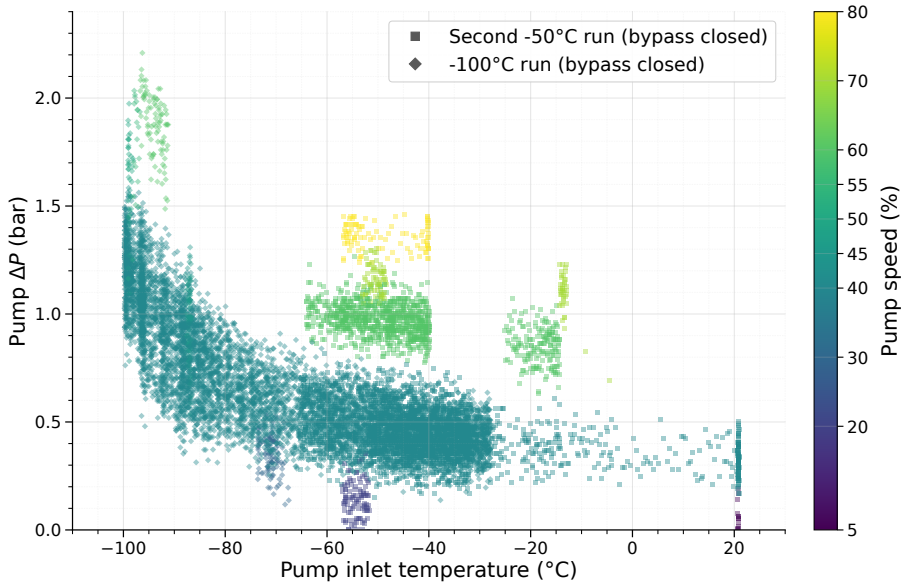


Figure 5.38: Pump differential pressure as a function of pump-inlet temperature and pump-speed command for bypass-closed data from the two latest recirculation runs.

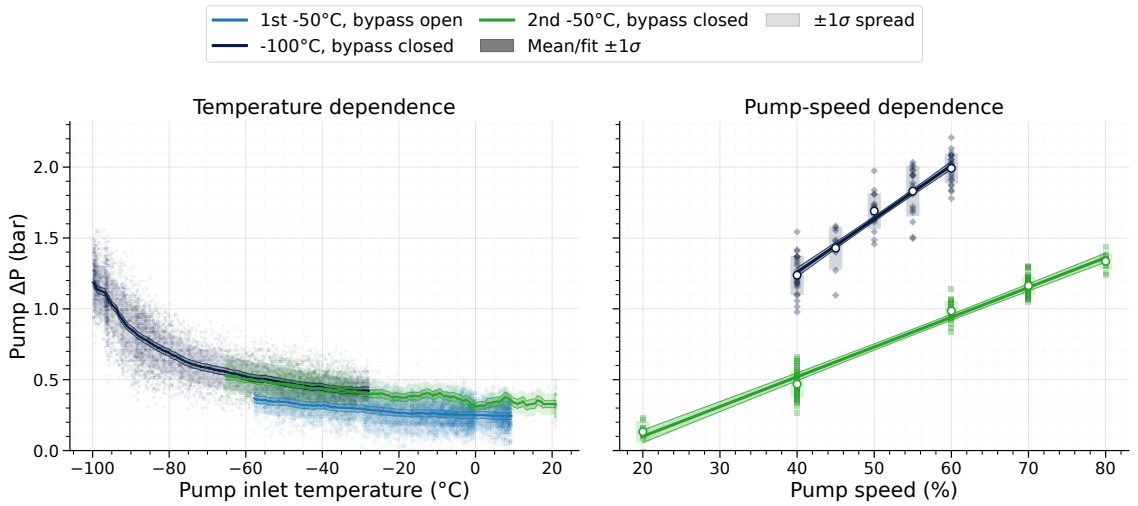


Figure 5.39: Pump differential pressure shown separately as a function of pump-inlet temperature at 40% pump speed, and as a function of pump-speed command at fixed temperature.

run reaches about 1.2 bar, compared with roughly 0.25 bar to 0.5 bar over much of the −50 °C data. This is consistent with the increase in HFE viscosity at low temperature, which becomes especially important below about −70 °C. Comparing the two −50 °C runs also shows the effect of the bypass state. With the bypass open, the loop has lower hydraulic resistance; over the overlapping temperature range of the two runs, the rolling-mean pressure rise is lower by about 0.12 bar.

The right panel shows the pump-speed dependence at nearly fixed temperature. The pressure rise is approximately linear in pump-speed command over the tested range, with a larger slope at lower temperature. Near −50 °C, it increases from about 0.47 bar at 40% to 1.34 bar at 80%. Near −100 °C, it increases from about 1.24 bar at 40% to about 1.99 bar at 60%. The fitted relations are

$$\Delta P_{\mathrm{pump}}^{-50\,^\circ\mathrm{C}} = (0.52 \pm 0.03)\,\mathrm{bar} + (0.210 \pm 0.011)\,\mathrm{bar}\left(\frac{s - 40\%}{10\%}\right), \tag{5.116}$$

and

$$\Delta P_{\mathrm{pump}}^{-100\,^\circ\mathrm{C}} = (1.26 \pm 0.03)\,\mathrm{bar} + (0.377 \pm 0.023)\,\mathrm{bar}\left(\frac{s - 40\%}{10\%}\right), \tag{5.117}$$

where $s$ is the pump-speed command. The larger slope at lower temperature again reflects the higher HFE viscosity, which makes each increase in pump speed produce a larger pressure drop through the loop.

**Pump-inlet and tank pressures** The pump-inlet and tank pressure channels are shown in Fig. 5.40. These pressures reflect the different overhead-pressure settings used during filling: about 0.8 barg for the −50 °C runs and about 2 barg for the −100 °C run.

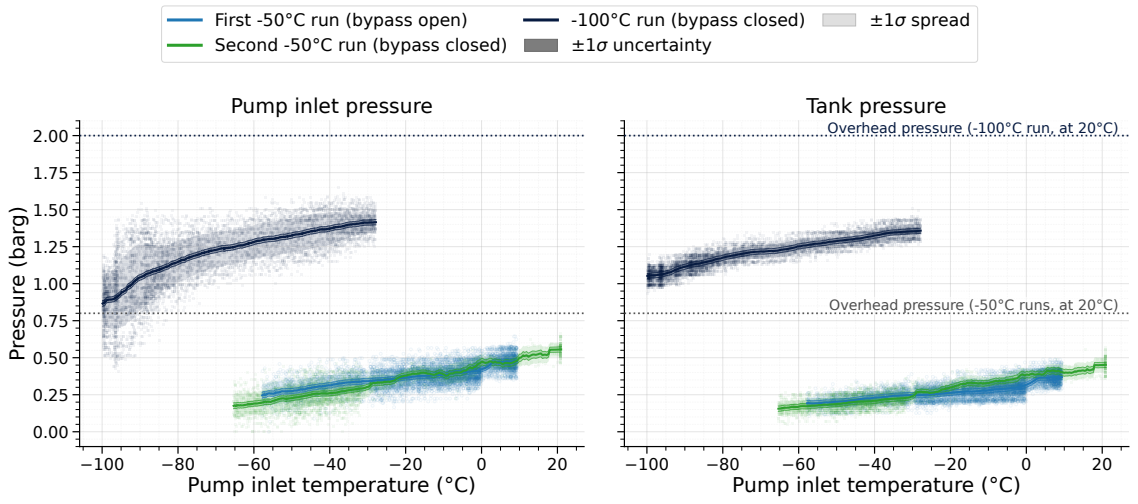


Figure 5.40: Pump-inlet and tank pressures as functions of pump-inlet temperature at 40% pump speed.

The tank pressure sensor is located near the top of the tank, about 1 m above the pump-inlet pressure sensor. A purely hydrostatic HFE column over this height

would give

$$P_{\text{tank}} - P_{\text{MI}} \simeq -\rho g \Delta z \simeq -\,0.15 \text{ bar to } -\,0.17 \text{ bar},$$

over the temperature range of these runs. The measured mean offsets at 40% pump speed are about $-0.10\,\text{bar}$, $-0.05\,\text{bar}$, and $+0.03\,\text{bar}$ for the first $-50\,^{\circ}\text{C}$, second $-50\,^{\circ}\text{C}$, and $-100\,^{\circ}\text{C}$ runs, respectively. The first value is close to the hydrostatic scale, while the colder runs are progressively shifted upward by the viscous pressure drop between the tank outlet and the pump inlet. This behavior is consistent with the increasing HFE viscosity making the outlet tubing a stronger hydraulic restriction at lower temperature.

As the HFE cools, its density increases and liquid is drawn from the gas-trap margin into the cold loop. This reduces the gas-trap overhead pressure relative to the value set during room-temperature filling. The $-50\,^{\circ}\text{C}$ runs showed that the pump inlet could approach atmospheric pressure, especially at higher pump speed. For this reason, the overhead pressure was increased for the $-100\,^{\circ}\text{C}$ run to preserve margin against cavitation. The larger pump-inlet pressure spread at low temperature is also consistent with the increased HFE viscosity and the stronger hydraulic restriction at the tank outlet.

### 5.6.2 Pump Performance

The cryogenic pump performance was evaluated from the same recirculation data used in Sec. 5.6.1. The relevant measured quantities are the volume flow, the pump inlet and outlet pressures, the reported pump speed, and the pump input power.

#### Volume and Mass Flow Rates

Figure 5.41 shows the measured HFE-7200 volume flow as a function of pump-speed command and pump differential pressure. The dashed curves are the vendor water reference curves from the room-temperature pump data discussed in Sec. 5.5.1. They are included only as a reference because the recirculation data were taken with HFE-7200 over a changing temperature and viscosity range, rather than with water at fixed temperature.

The flow rate is approximately proportional to pump-speed command, as expected for a positive-displacement gear pump. A 40% command gives around $2.6\,\text{L}\,\text{min}^{-1}$, while a 60% command gives about $4\,\text{L}\,\text{min}^{-1}$, close to the design maximum flow in Table 5.3. The highest tested speed settings reached about $5.2\,\text{L}\,\text{min}^{-1}$.

At fixed pump speed, the delivered volume flow changes only weakly with temperature, pressure rise, and bypass state. For the 40% command data, it increases from about $2.60\,\text{L}\,\text{min}^{-1}$ near room temperature to about $2.7\,\text{L}\,\text{min}^{-1}$ below $-80\,^{\circ}\text{C}$. Over the overlapping temperature range of the $-50\,^{\circ}\text{C}$ runs, opening the bypass lowers $\Delta P_{\text{pump}}$, but the measured volume flow remains close to the bypass-closed value. The bypass changes the hydraulic load seen by the pump more than it changes the commanded displacement rate.

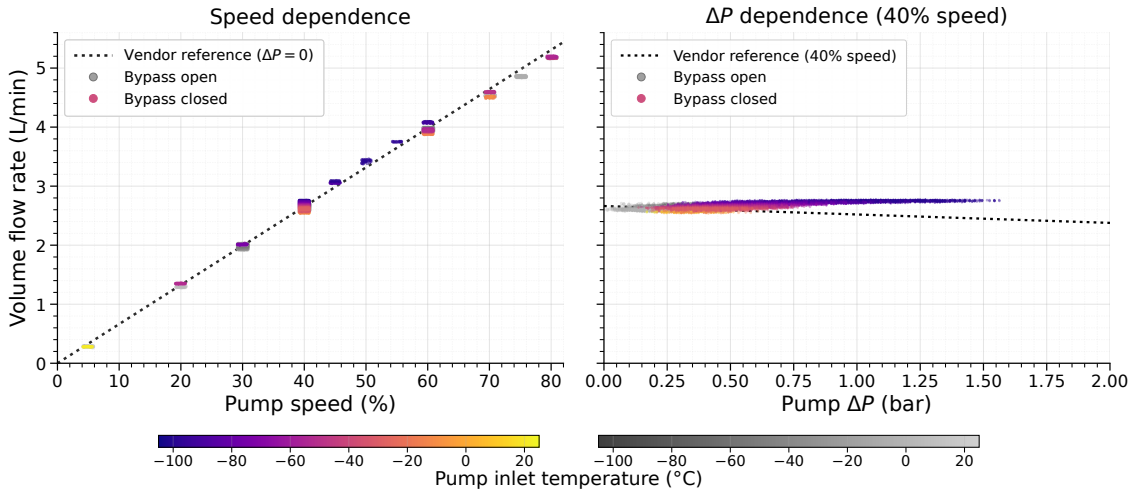


Figure 5.41: HFE-7200 volume flow during recirculation as a function of pump-speed command and pump differential pressure. The dashed curves show the corresponding vendor water reference behavior.

This behavior differs from the room-temperature water vendor curve, where a larger pressure rise reduces the delivered flow through pump slip. In the HFE data, increasing pressure rise is correlated with decreasing temperature. Cooling the HFE increases the loop pressure drop through the viscosity increase, but the higher viscosity also suppresses internal leakage through the pump clearances. These two effects partly compensate, so the delivered volume flow remains nearly constant over the measured pressure range.

The mass flow follows the same pump-speed dependence, with an additional contribution from the temperature-dependent HFE density. At 40% pump speed, the mass flow increases from about $3.8\,\mathrm{kg\,min^{-1}}$ near room temperature to about $4.5\,\mathrm{kg\,min^{-1}}$ in the coldest data. This follows from the higher HFE density at low temperature.

**Delivered volume per revolution** The delivered volume per pump revolution is used as a direct diagnostic of whether the pump displacement changes during cold operation. It is computed from

$$D_{\mathrm{del}} = \frac{\dot{V}_{\mathrm{HFE}}}{n_{\mathrm{pump}}}, \tag{5.118}$$

where $n_{\mathrm{pump}}$ is obtained from the VFD frequency using Eq. (5.48). In the numerical evaluation, $\dot{V}_{\mathrm{HFE}}$ is converted from $\mathrm{L\,min^{-1}}$ to $\mathrm{mL\,min^{-1}}$, so that $D_{\mathrm{del}}$ is reported in $\mathrm{mL\,rev^{-1}}$.

An apparent slip relative to the vendor zero-pressure water displacement is then defined as

$$s_{\mathrm{app}} = 100\left(1 - \frac{D_{\mathrm{del}}}{D_0}\right), \qquad D_0 = 3.145\ \mathrm{mL\,rev^{-1}}. \tag{5.119}$$

The reference displacement $D_0$ is taken from the vendor water curve in Table 5.14. Since the recirculation data use HFE-7200 over a changing temperature and viscosity

range, $s_{\mathrm{app}}$ is not treated as an absolute leakage measurement. It is instead used as a relative measure of the delivered displacement during cryogenic operation.

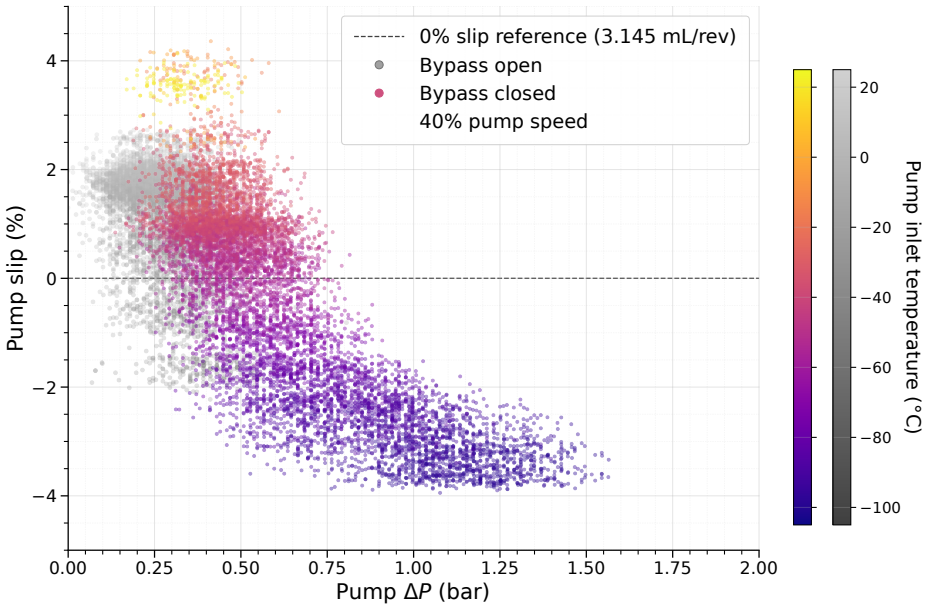


Figure 5.42: Apparent pump slip during HFE-7200 recirculation at 40% pump-speed command, evaluated relative to the vendor zero-pressure water displacement.

The apparent slip remains within a few percent over the measured range. Near room temperature it is slightly positive, while the coldest data are slightly negative, corresponding to a delivered displacement slightly larger than the vendor zero-pressure reference. The bypass-open data occupy the lower-$\Delta P_{\mathrm{pump}}$ part of the distribution, while the bypass-closed data extend to larger pressure rise, but both follow the same small-slip trend. This is consistent with the expectation from Eq. (5.55): the lower-temperature data have larger $\Delta P_{\mathrm{pump}}$, but also much larger $\rho\nu$, so the net change in delivered displacement remains small.

This supports the viscosity estimate in Sec. 5.6.3, because it supports treating the measured pressure rise primarily as a loop-viscosity effect rather than as a large change in pump displacement.

### Drawn Power

The electrical load of the pump was evaluated using the VFD-reported input power, which corresponds to the power drawn by the drive and motor system.

The measured input power, shown in Fig. 5.43, increases mainly with pump-speed command. It is about 40 W at the lowest tested speed and reaches 100 W to 120 W at the largest speed settings. At fixed 40% command, however, the input power remains mostly between 63 W and 75 W over the measured pressure range. The bypass-closed and colder data tend to lie at higher $\Delta P_{\mathrm{pump}}$, but they do not show a sharp increase in input power. This indicates that the electrical load is dominated by baseline drive, motor, coupling, and mechanical losses, with only a

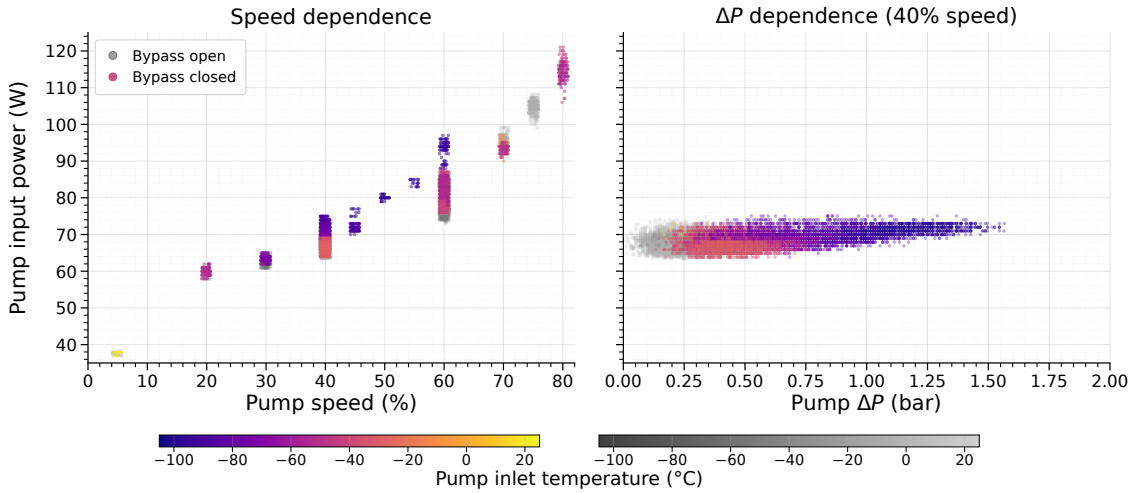


Figure 5.43: VFD-reported pump input power as a function of pump-speed command and pump differential pressure during HFE-7200 recirculation.

modest additional contribution from the hydraulic load. No power signature of pump overload or mechanical restriction was observed during the coldest operation.

The hydraulic pressure-flow work can then be estimated from the measured flow and pump pressure rise,

$$P_{\mathrm{hyd}} = \Delta P_{\mathrm{pump}} \dot{V}_{\mathrm{HFE}}, \tag{5.120}$$

using the standard pressure-flow work relation [98]. In the units used for the logged data,

$$P_{\mathrm{hyd}}[\mathrm{W}] = 1.667\, \Delta P_{\mathrm{pump}}[\mathrm{bar}] \dot{V}_{\mathrm{HFE}}[\mathrm{L\,min^{-1}}]. \tag{5.121}$$

This is the pressure-flow work delivered to the HFE by the pump. In the recirculation loop, it is dissipated through the total hydraulic resistance of the system. It is distinct from the full VFD input power, which also includes VFD, motor, magnetic-coupling, and pump mechanical losses.

The hydraulic-to-input power fraction is defined as

$$\eta_{\mathrm{hyd/in}} = \frac{P_{\mathrm{hyd}}}{P_{\mathrm{in}}}, \tag{5.122}$$

where $P_{\mathrm{in}}$ is the VFD-reported input power. This quantity is not the pump shaft efficiency because it is not corrected for VFD or motor losses. It is only the fraction of the logged electrical input that appears as hydraulic pressure-flow work in the HFE.

Figure 5.44 shows that $\eta_{\mathrm{hyd/in}}$ increases with pump speed and pressure rise, but remains small. Across the plotted data, it stays below about 17%. At fixed 40% pump speed, the volume flow and input power vary slowly, so the increase in $\eta_{\mathrm{hyd/in}}$ is driven mainly by $\Delta P_{\mathrm{pump}}$. It rises from near zero at low pressure to about 10% at the largest measured pressure rise. The bypass-open data occupy the lower-pressure, lower-fraction region, while the colder bypass-closed data extend to higher $\Delta P_{\mathrm{pump}}$.

The corresponding hydraulic power is at most about 15 W in the plotted data, and is typically only a few watts at 40% pump speed. The pump therefore pro-

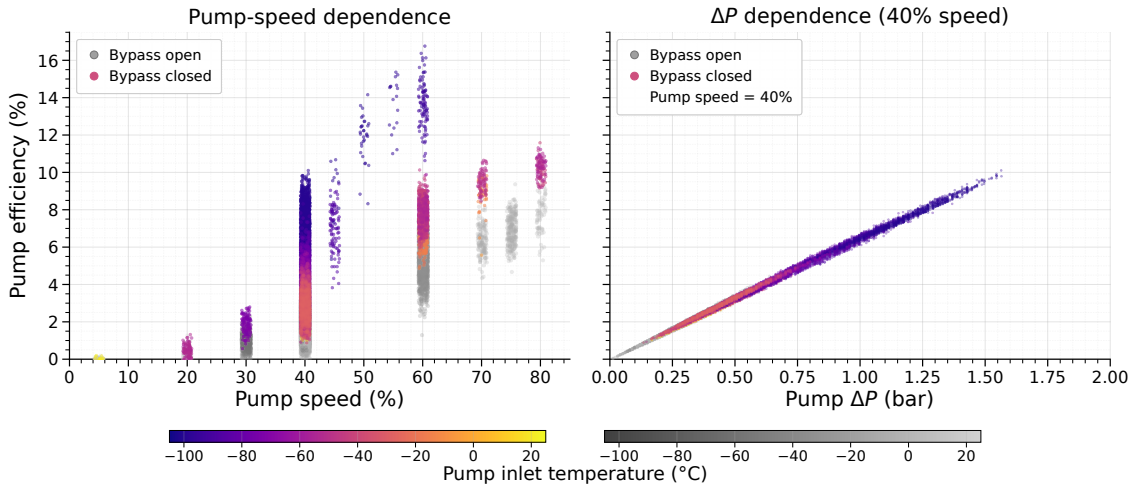


Figure 5.44: Hydraulic-to-input power fraction during HFE-7200 recirculation, computed from $P_{\mathrm{hyd}} = \Delta P_{\mathrm{pump}} \dot{V}_{\mathrm{HFE}}$ and the VFD-reported pump input power.

vides the required $2.5\,\mathrm{L\,min^{-1}}$ to $4\,\mathrm{L\,min^{-1}}$ operating flow range with only a modest hydraulic load and with enough pressure margin below the relief-valve limits.

### 5.6.3 Cryogenic HFE Behavior

The cryogenic runs also provide direct information on the HFE-7200 state during recirculation. The Coriolis flow meter measures the density and mass flow, while the pressure and flow data give an operating estimate of the changing hydraulic resistance. The heat-exchanger thermocouples also provide local information on the transition region, where partial freezing can reduce heat exchange before the bulk loop temperature reaches the same value.

#### Density

Figure 5.45 shows the HFE-7200 density measured by the Coriolis flow meter as a function of the flow-meter temperature.

The measured density increases approximately linearly as the HFE is cooled. A linear fit to the raw density samples gives

$$\rho_{\mathrm{meas}}(T) \simeq 1440\,\mathrm{kg\,m^{-3}} + 2.04\,\mathrm{kg\,m^{-3}\,K^{-1}}\,(20^{\circ}\mathrm{C} - T)\,. \tag{5.123}$$

The shaded band in Fig. 5.45 shows the combined $1\sigma$ uncertainty around the fit, including the raw residual spread, the flow-meter density uncertainty, and the temperature uncertainty propagated through the fitted slope. Its half-width is about $2\,\mathrm{kg\,m^{-3}}$ over the measured temperature range.

At the coldest measured temperatures, the measured density is lower than the vendor reference by roughly $30\,\mathrm{kg\,m^{-3}}$, or about 2%. This offset is much larger than the point-to-point scatter of the measured data, but the vendor curve is used here only as a reference because no uncertainty is quoted for that density.

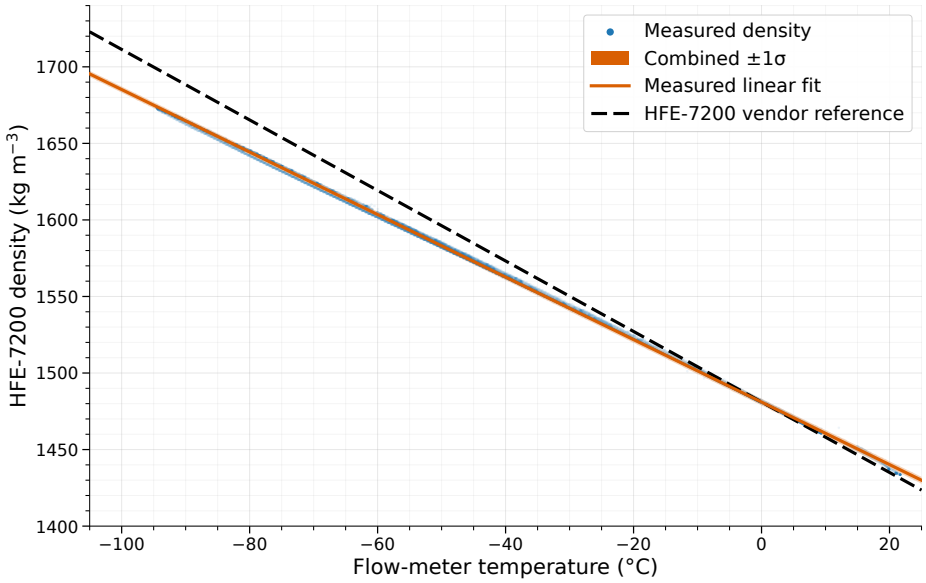


Figure 5.45: HFE-7200 density measured by the Coriolis flow meter during cryogenic recirculation, compared with the HFE-7200 vendor reference.

### Viscosity Estimates

The viscosity was not measured directly with a viscometer. Instead, an apparent viscosity index was built from the pump pressure rise and the measured HFE flow. The total hydraulic resistance of the loop is

$$R_{\mathrm{tot}} = \frac{\Delta P_{\mathrm{pump}}}{\dot{V}_{\mathrm{HFE}}}. \tag{5.124}$$

For a fixed geometry, the pressure loss has a viscous part and a flow-dependent inertial part [98]. Once divided by volume flow, the inertial term scales approximately as $\rho\dot{V}_{\mathrm{HFE}}$. The viscosity-sensitive proxy was therefore taken as

$$R_{\mathrm{visc},s} = R_{\mathrm{tot}} - C_s \rho_{\mathrm{HFE}} \dot{V}_{\mathrm{HFE}}, \tag{5.125}$$

where $s$ denotes the bypass state. The coefficients $C_s$ were obtained from short pump-speed sweeps at nearly steady HFE temperature and fixed bypass state, in units of $\mathrm{bar\,m^3\,kg^{-1}\,(L\,min^{-1})^{-2}}$:

$$C_{\mathrm{closed}} = (2.4 \pm 0.3) \times 10^{-5}, \quad C_{\mathrm{open}} = (1.9 \pm 0.1) \times 10^{-5}. \tag{5.126}$$

The higher bypass-closed value is expected, since closing the bypass sends more flow through the heat-exchanger path and increases the flow-dependent pressure drop.

The corrected resistance proxy was converted to a kinematic-viscosity index by anchoring it to the HFE-7200 reference value at 0 °C,

$$\nu_{\mathrm{est}}(T) = \nu_0 \frac{\rho_0}{\rho_{\mathrm{HFE}}(T)} \frac{R_{\mathrm{visc},s}(T)}{R_{\mathrm{visc},s}(T_0)}, \qquad \nu_0 = 0.67\,\mathrm{cSt}, \qquad T_0 = 0\,^{\circ}\mathrm{C}. \tag{5.127}$$

Here $\rho_0$ is the manufacturer density at $T_0$; the density factor reflects the assumed scaling $R_{\mathrm{visc},s} \propto \rho_{\mathrm{HFE}}\nu$ for a fixed geometry. The anchor resistance $R_{\mathrm{visc},s}(T_0)$ is the

median corrected resistance in the 0 °C anchor band. Each point is plotted against the mean of the four calibrated loop thermocouples TFO, TTI, TTO, and TMI.

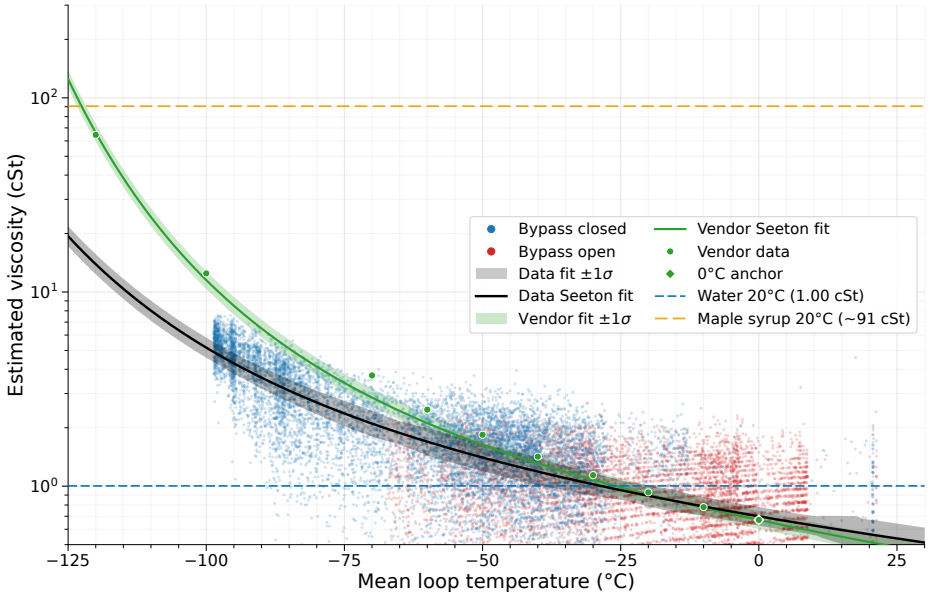


Figure 5.46: Apparent HFE-7200 kinematic-viscosity index from loop pressure, flow, and density data, compared with the HFE-7200 vendor reference. Bands show $1\sigma$ fit spreads.

The apparent viscosity rises strongly during cooldown, increasing from water-like values toward more syrup-like viscosities, as expected for HFE-7200. It is anchored near 0 °C and reaches about 5.3 cSt at the coldest loop temperatures, near −100 °C. After the bypass-state correction in Eq. (5.125), the bypass-open and bypass-closed samples follow the same main trend, so the correction removes most of the bypass-dependent hydraulic load. The red streaks are bypass-open samples taken at repeated pump speeds and flow rates; pressure-readback resolution maps these repeated operating points into visible narrow bands in the viscosity proxy, due to the low pressure rise in the bypass-open configuration.

At the coldest temperatures, the estimated viscosity falls below the vendor HFE-7200 curve. This offset can arise from several effects, including flow-dependent losses and temperature gradients in the loop. Since the vendor data have no stated uncertainty, the green band only shows the residual spread of the Seeton fit. The main result is the trend: the pressure-flow response follows the expected viscosity increase during cooldown.

A more quantitative viscosity estimate would require dedicated pump-speed sweeps at several stable temperatures, preferably with the bypass closed, together with more data around and above the warm anchor point near 0 °C. Longer steady plateaus would reduce temperature-gradient effects, and colder stable points would extend the comparison below the present −100 °C limit.

### Local Freezing Signature

The −100 °C run also shows freezing signatures near the heat exchanger when the $LN_2$ valve cycles at low temperature. Figure 5.47 shows one selected cycle of the middle heat-exchanger thermocouple, THM, after the local temperature drops below −95 °C. Other nearby cycles were inspected, but most were not suitable for this estimate because cooling restarted too early or residual cooling from the previous $LN_2$ opening distorted the warm-up branch.

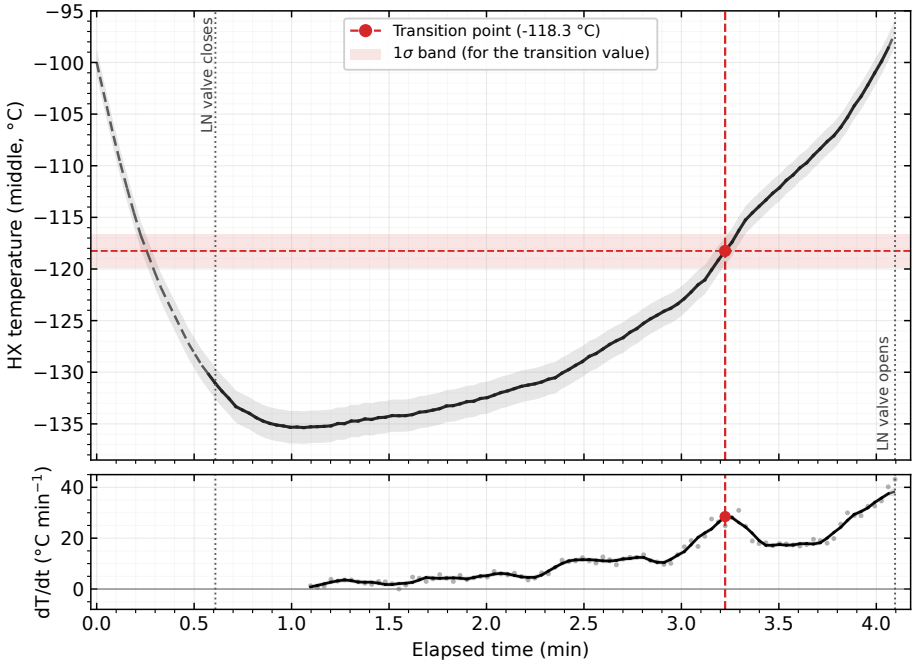


Figure 5.47: Heat-exchanger middle thermocouple during one low-temperature $LN_2$ cycle. The red marker identifies the local freezing signature, and the shaded bands show the corresponding $1\sigma$ uncertainties.

The transition point is taken as the local maximum of the smoothed $dT/dt$ trace, giving

$$T_{\mathrm{tr,local}} = -118.3 \pm 1.6\,^{\circ}\mathrm{C}. \tag{5.128}$$

The uncertainty combines the spread from the derivative/smoothing choices with the complete THM reading uncertainty.

This temperature is in the same range as the HFE-7200 transition features discussed in Sec. 5.1.2. It is close to the 3M cold-crystallization feature near −120 °C, and higher than the cold-dip cold-crystallization peak at $-131 \pm 1$ °C. This supports interpreting the feature as a local freezing signature near the heat exchanger.

This value remains only an estimate. It comes from one usable cycle and can be affected by $LN_2$ cooling history, recirculating-flow conditions, and the THM position, which is close to the heat exchanger but not directly on the coil. Future runs should repeat these scans with lower temperatures and longer warm-up branches.

## 5.7 Future Developments

Near-term work on the system should focus on improving control and monitoring during cryogenic operation. The longer-term goal is to test HFE-7072 mixtures, defined here as HFE-7000/HFE-7200 blends, that could reduce both the low-temperature viscosity and the risk of freezing near LXe temperature.

### 5.7.1 Controls and Monitoring

The first goal is to reach and hold $-110\,^{\circ}\mathrm{C}$ with stable HFE recirculation. The April 24 run reached $\sim -100\,^{\circ}\mathrm{C}$, but the final approach to LXe temperature requires better control of the $LN_2$ cooling power near the HFE transition region. Local overcooling at the heat exchanger can freeze HFE before the bulk temperature reaches the target, reducing the cooling power. This can be addressed by implementing PID control of the $LN_2$ cooling system, using the heat-exchanger and HFE temperatures as feedback variables. An $LN_2$ pressure regulator could also be added if needed, providing an additional control handle on the cooling power. This is motivated by the heat-exchanger tests, which showed an approximately linear dependence of cooling power on $LN_2$ supply pressure over the tested range.

Other monitoring and control improvements are under development:

1. add a nitrogen connection to the gas-trap headspace, so that the overhead pressure can be adjusted during cooldown rather than only during filling;
2. study whether variations in overhead pressure only affect the HFE density through thermal contraction, or whether nitrogen solubility and trapped gas also contribute;
3. design an ultrasound-based non-invasive HFE level sensor around the gas trap and return line, to determine whether liquid HFE is present during filling and full-system operation;
4. estimate the pump speed from the frequency spectrum of the pump vibration or acoustic signal, providing an independent check of the VFD readback;
5. perform a proper DSC measurement of the HFE samples using DSC equipment available at UMass.

These changes would make the next $-110\,^{\circ}\mathrm{C}$ run more controlled and easier to interpret.

### 5.7.2 HFE Mixtures

HFE mixtures are the main longer-term development for the system. The goal is to lower the viscosity while keeping freezing or crystallization away from LXe temperature. HFE-7000 is less viscous near LXe temperature, while HFE-7200 has a lower freezing point and is easier to handle at room temperature. A mixture could therefore combine the main advantages of both fluids.

Internal 3M data include viscosity measurements for HFE-7000, HFE-7100, HFE-7200, and several HFE-7000/HFE-7200 blends. The blend labels 70/30, 75/25, and 80/20 denote nominal HFE-7000/HFE-7200 fractions, with HFE-7000 listed first.

In Fig. 5.48, the pure fluids are fit with the Seeton model, while the mixture curves are two-point interpolations.

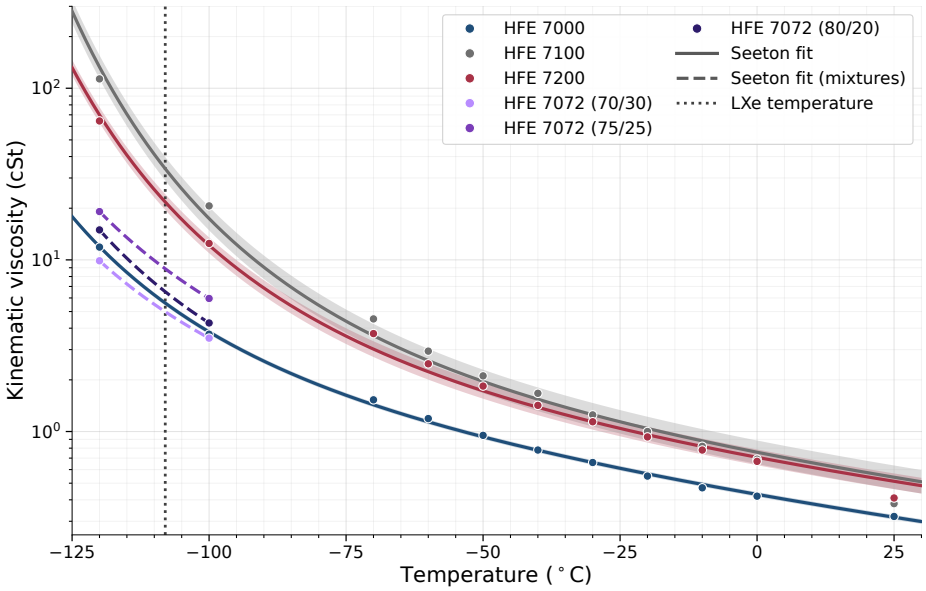


Figure 5.48: Kinematic viscosity of HFE-7000, HFE-7100, HFE-7200, and HFE-7000/HFE-7200 mixtures (7072) from internal 3M data. The shaded bands show the $1\sigma$ log-residual spread of the fits.

The mixture data show a clear viscosity reduction relative to pure HFE-7200. At $-100\,^{\circ}\mathrm{C}$, HFE-7200 has $\nu \simeq 12.5\,\mathrm{cSt}$, while the HFE-7072 mixtures are in the range $\sim 3.5\,\mathrm{cSt}$ to $6.0\,\mathrm{cSt}$. At $-120\,^{\circ}\mathrm{C}$, HFE-7200 reaches $\nu \simeq 64\,\mathrm{cSt}$, compared with $\sim 10\,\mathrm{cSt}$ to $19\,\mathrm{cSt}$ for the mixtures.

The freezing behavior should also be measured directly. In the internal DSC measurements, pure HFE-7000 shows the clearest freezing and melting features, while blends show much weaker transitions. This suggests that mixtures may move or suppress freezing near the operating range, but the existing data are not sufficient to assign a reliable freezing temperature.

These improvements would make the next cryogenic runs more controlled and directly comparable. The key tests are stable recirculation at $-110\,^{\circ}\mathrm{C}$, operation with controlled overhead pressure, and side-by-side runs with pure HFE-7200 and selected HFE-7000/HFE-7200 mixtures.

# Conclusion

This dissertation studied impurity control and radioactive-background mitigation for a cryogenic liquid-xenon rare-event detector, with emphasis on the requirements of a tonne-scale $^{136}$Xe neutrinoless double beta decay search. The central motivation is the search for $0\nu\beta\beta$, whose observation would establish lepton-number violation and demonstrate that neutrinos are Majorana particles. Reaching the required half-life sensitivity demands more than a large isotope mass: it requires stable charge transport over metre-scale drift lengths, extremely low radiogenic backgrounds near the $Q_{\beta\beta}$ region, and reliable operation of a large cryogenic shielding and cooling system.

Some of the main quantitative results are summarized in Table 5.23.

| **Theme** | **Quantity** | **Result** |
|---|---|---|
| LXe purity | $O_2$-eq. conc. limit | 0.085 ppb for $\tau_e = 5$ ms |
| LXe purity | $O_2$-eq. source rate limit | $3 \times 10^{-7}$ mbar L s$^{-1}$ (350 SLPM) |
| Rad. background | Reduced-HFE design | $R_{\mathrm{IV}} = 1308$ mm, $m_{\mathrm{HFE}} \simeq 13$ t |
| Rad. background | Smaller OV option | no OV/water background penalty |
| Rad. background | Cylindrical cryostat | 14% less HFE, 17% smaller IV |
| Cryogenic HFE | Cooling power | up to several kW |
| Cryogenic HFE | Pump flow rate | stable flow up to 4 L min$^{-1}$ |
| Cryogenic HFE | HFE-7200 viscosity | 0.43 cSt→28.35 cSt near $-110$ °C |

Table 5.23: Key results and design scales from this dissertation.

The first part of this work showed that electronegative impurities can be modeled and budgeted in a way analogous to radiogenic backgrounds. For the nEXO-scale drift length, the purity requirement corresponds to sub-0.1 ppb $O_2$-equivalent contamination. The purification model provides a direct connection between electron lifetime and the allowed impurity load, while diffusion and desorption models allow outgassing measurements on material samples to be extrapolated to detector components and to liquid-xenon temperatures.

The second part showed that ultra-pure nickel can reduce backgrounds and extend the science reach of large LXe TPCs. Replacing the earlier carbon-fiber-composite cryostat concept with all-nickel vessels reduces the vessel-related intrinsic background by roughly a factor of 380. The cryostat vessels therefore become subdominant, which opens the possibility of reducing the HFE inventory by about 60%

while keeping the background contribution from HFE-external components acceptable. This also leaves room for alternative shielding and cryostat choices, including additional water shielding or cylindrical cryostat vessels, which could simplify the detector design.

The third part of this work developed and tested a cryogenic HFE recirculation system at UMass Amherst. The system demonstrated controlled cooldown with $LN_2$ cooling powers up to the kW scale, and operation of a magnetically coupled gear pump within the target flow and pressure envelope. The tests also confirmed the main operational challenge: HFE-7200 remains liquid near LXe temperature, but its viscosity increases by more than an order of magnitude when cooled from room temperature to the $-100\,^{\circ}\mathrm{C}$ to $-110\,^{\circ}\mathrm{C}$ range. Cryogenic HFE operation therefore requires careful control of temperature gradients, especially around the heat exchanger.

Several directions remain for future work. The impurity budget should be completed using the final xenon-contact inventory and updated material measurements. The radiogenic-background model should be updated with final assays, optimized MLI, and dedicated simulations of reduced-HFE and modified-cryostat geometries. The HFE recirculation system will be used for longer cold runs, improved automatic control, more sensitive freezing diagnostics, and studies of HFE mixtures.

# Résumé en français

## Sommaire


1 Double désintégration bêta sans neutrinos . . . . . 207

2 Détecteur au xénon liquide pour la recherche de $0\nu\beta\beta$ . 208

3 Transport de charge et pureté du xénon liquide . . . . . 210

4 Réduction du bruit de fond par le cryostat et le blindage HFE . . . . . 212

5 Refroidissement et recirculation du HFE . . . . . 214

Cette thèse étudie plusieurs conditions expérimentales nécessaires à la recherche de la double désintégration bêta sans émission de neutrinos du $^{136}$Xe, notée $0\nu\beta\beta$, dans un détecteur cryogénique contenant plusieurs tonnes de xénon liquide. L'observation de ce processus établirait une violation du nombre leptonique et démontrerait que les neutrinos possèdent une composante de masse de Majorana, ce qui signifie qu'ils seraient leurs propres antiparticules. Une telle découverte aurait des implications profondes pour la physique des neutrinos, constituerait une preuve de physique au-delà du Modèle standard et pourrait contribuer à la compréhension de l'asymétrie entre matière et antimatière dans l'Univers.

Le signal recherché est extrêmement rare : les expériences de nouvelle génération visent des demi-vies proches de $10^{28}$ ans. Atteindre une telle sensibilité exige non seulement une grande quantité de $^{136}$Xe, mais aussi une mesure précise de l'énergie et de la position de chaque interaction, afin de distinguer de manière fiable le signal recherché des événements parasites qui constituent le bruit de fond. Ces événements peuvent notamment provenir de la radioactivité résiduelle des matériaux utilisés dans le détecteur et de son environnement.

Le travail présenté ici a été réalisé d'abord à SUBATECH, à Nantes, d'octobre 2023 à avril 2025, puis à l'Université du Massachusetts à Amherst, d'avril 2025 à août 2026.

# 1 Double désintégration bêta sans neutrinos

Les oscillations de neutrinos ont établi que les neutrinos ont des masses non nulles, ce qui n'est pas expliqué par le Modèle standard. Elles laissent toutefois plusieurs questions ouvertes :

- quelle est l'échelle absolue des masses des neutrinos ?
- les neutrinos sont-ils des particules de Dirac, distinctes de leurs antiparticules, ou des particules de Majorana, identiques à celles-ci ?
- le nombre leptonique est-il une symétrie exacte de la nature ?

La double désintégration bêta sans émission de neutrinos répond directement à ces questions. Dans ce processus hypothétique, deux électrons sont émis sans les deux antineutrinos présents dans le mode autorisé à deux neutrinos. Les diagrammes des deux modes sont comparés à la figure 1.6. Leurs signatures principales sont résumées dans le tableau 1.

| **Mode** | **État final** | **Énergie totale des $e^-$** | $\boldsymbol{\Delta L}$ |
|---|---|---|---|
| $2\nu\beta\beta$ | $2e^- + 2\bar{\nu}_e$ | Spectre continu jusqu'à $Q_{\beta\beta}$. | 0 |
| $0\nu\beta\beta$ | $2e^-$ | Pic à $Q_{\beta\beta}$. | 2 |

Table 1 : Comparaison des modes $2\nu\beta\beta$ et $0\nu\beta\beta$.

Pour le $^{136}$Xe, l'énergie de transition est $Q_{\beta\beta} \simeq 2458\,\text{keV}$. La figure 1.8 montre le spectre continu attendu pour $2\nu\beta\beta$ et le pic recherché pour $0\nu\beta\beta$. Si ce processus est observé, il impliquerait l'existence d'un terme de masse de Majorana pour les neutrinos, indépendamment du mécanisme microscopique dominant, selon l'argument de la boîte noire présenté à la figure 1.9.

Dans l'hypothèse où le processus est dominé par l'échange d'un neutrino léger de Majorana, la demi-vie est reliée à la masse effective de Majorana $m_{\beta\beta}$ par

$$\left(T_{1/2}^{0\nu}\right)^{-1} = G^{0\nu} g_A^4 \left|M^{0\nu}\right|^2 \left|\frac{m_{\beta\beta}}{m_e}\right|^2, \tag{1}$$

où $G^{0\nu}$ est le facteur d'espace de phase, $M^{0\nu}$ l'élément de matrice nucléaire, $g_A$ le couplage axial et $m_e$ la masse de l'électron. La masse effective de Majorana

$$m_{\beta\beta} = \left|\sum_{i=1}^{3} U_{ei}^2 m_i\right| \tag{2}$$

dépend des masses des neutrinos, de leurs angles de mélange et de phases de Majorana encore inconnues. Les régions permises sont présentées à la figure 1.10. Comme la conversion de $T_{1/2}^{0\nu}$ en $m_{\beta\beta}$ dépend des éléments de matrice nucléaire, encore incertains, la performance expérimentale est d'abord exprimée en termes de sensibilité à la demi-vie, directement reliée au nombre d'événements observés.

# 2 Détecteur au xénon liquide pour la recherche de $0\nu\beta\beta$

Le $^{136}$Xe est particulièrement adapté à la recherche de $0\nu\beta\beta$, puisque cet isotope peut se désintégrer par double bêta tout en constituant un milieu de détection produisant des signaux mesurables. Lorsqu'une particule dépose de l'énergie dans le xénon liquide, elle produit simultanément de la lumière de scintillation et des électrons d'ionisation, dont la mesure permet de reconstruire l'énergie et la position de l'interaction. Le xénon naturel peut également être enrichi à grande échelle en $^{136}$Xe et maintenu sous forme liquide, ce qui permet de réunir plusieurs tonnes de cet isotope dans une cible dense et homogène et d'augmenter ainsi la probabilité d'observer une désintégration $0\nu\beta\beta$. Cette forte densité assure également un autoblindage efficace contre les rayonnements parasites provenant de l'extérieur. Enfin, le xénon peut être continuellement recirculé et purifié afin d'éliminer les impuretés susceptibles de dégrader la collecte des charges d'ionisation. La faisabilité de cette approche a été démontrée par EXO-200, prédécesseur de nEXO utilisant environ 200 kg de xénon liquide enrichi.

nEXO reprend cette approche avec environ cinq tonnes de xénon enrichi à 90 % en $^{136}$Xe. La lumière de scintillation, détectée par des capteurs disposés autour de la TPC, permet de déterminer le temps initial de l'événement. Les électrons dérivent quant à eux sous l'effet d'un champ électrique jusqu'à une anode segmentée, qui collecte leur charge et mesure sa répartition afin de reconstruire les deux coordonnées

transverses. La coordonnée longitudinale est déterminée à partir du temps de dérive des électrons. Les signaux de scintillation et d'ionisation étant anticorrélés, leur combinaison améliore la résolution en énergie. Cette performance repose toutefois sur la collecte des électrons après une dérive pouvant atteindre environ 120 cm sous un champ de 400 V/cm. Le xénon liquide doit donc rester suffisamment pur pour limiter leur capture par des impuretés électronégatives.

La géométrie générale du détecteur est présentée à la figure 2.6. La TPC est entourée d'un bain d'hydrofluoroéther (HFE) contenu dans la cuve interne sphérique du cryostat. Le HFE stabilise la température de la TPC et atténue les rayonnements provenant des composants situés à l'extérieur de celle-ci. Une seconde cuve sphérique forme la paroi externe du cryostat ; l'espace entre les deux cuves est maintenu sous vide afin d'assurer l'isolation thermique. L'ensemble est placé dans une cuve d'eau, qui complète le blindage contre les rayonnements provenant de l'environnement du détecteur.

Malgré ces protections, certains événements produits par la radioactivité résiduelle des matériaux ou de l'environnement peuvent présenter des caractéristiques proches de celles d'une désintégration $0\nu\beta\beta$. L'ensemble de ces événements constitue le bruit de fond. La séparation entre signal et bruit de fond repose principalement sur trois observables, illustrées à la figure 2.14 :

**Énergie** le signal est reconstruit autour de $Q_{\beta\beta}$ ;

**Topologie** un événement $0\nu\beta\beta$ est compact, tandis qu'un rayonnement $\gamma$ peut produire plusieurs dépôts spatialement séparés ;

**Position** le signal est distribué uniformément dans le xénon, alors que les bruits de fond externes sont plus nombreux près des surfaces.

Ces distributions sont combinées dans une analyse multiparamétrique afin d'optimiser le rapport signal sur bruit de fond. Après dix ans de données, la sensibilité médiane d'exclusion projetée à 90 % de niveau de confiance est

$$T_{1/2}^{0\nu} \simeq 1{,}35 \times 10^{28} \text{ ans.} \tag{3}$$

La demi-vie correspondant à une découverte médiane à $3\sigma$ est de $0{,}74 \times 10^{28}$ ans.

Les travaux présentés dans cette thèse portent sur trois conditions expérimentales nécessaires pour préserver la sensibilité de nEXO. Les chapitres suivants sont organisés de la manière suivante :

1. le chapitre 3 étudie l'effet des impuretés électronégatives sur la collecte de charge et relie l'exigence de pureté du xénon liquide au dégazage des matériaux ;
2. le chapitre 4 étudie la réduction du bruit de fond par la radiopureté des matériaux du cryostat et par l'épaisseur du blindage cryogénique en HFE ;
3. le chapitre 5 présente le système développé à UMass pour refroidir et faire circuler le HFE à la température du xénon liquide.

# 3 Transport de charge et pureté du xénon liquide

Les impuretés électronégatives présentes dans le xénon peuvent capturer les électrons d'ionisation pendant leur dérive et atténuer le signal de charge. Cette atténuation est décrite par

$$N_e(t_{\text{drift}}) = N_e(0)\exp\left(-\frac{t_{\text{drift}}}{\tau_e}\right), \qquad \frac{1}{\tau_e} = \sum_S k_S c_S, \tag{4}$$

où $\tau_e$ est la durée de vie électronique, $k_S$ la constante d'attachement de l'espèce $S$ et $c_S$ sa concentration molaire. La durée de vie électronique mesure ainsi le taux total d'attachement du mélange d'impuretés.

Pour une hauteur de dérive d'environ 120 cm et une vitesse de dérive de l'ordre de 1.7 mm µs$^{-1}$ à 400 V/cm, le temps de dérive maximal est d'environ 0.69 ms. La durée de vie des électrons doit être suffisamment supérieure à ce temps afin de limiter la perte des charges d'ionisation au cours de leur dérive et son impact sur la reconstruction en énergie. nEXO impose donc une durée de vie électronique d'au moins 5 ms, valeur retenue pour établir le budget d'impuretés, et une valeur idéale de l'ordre de 10 ms.

Les constantes d'attachement variant fortement selon les impuretés, comme l'oxygène ou l'eau, le mélange est exprimé par sa fraction molaire $O_2$-équivalente, définie comme la concentration d'oxygène qui produirait le même taux total d'attachement. Néanmoins, cette convention ne suppose pas que l'oxygène soit l'impureté dominante. Le tableau 2 relie les durées de vie considérées à la charge collectée sur la dérive maximale, à la fraction $O_2$-équivalente et au débit source maximal admissible, exprimé en équivalent $O_2$, provenant du dégazage des composants en contact avec le xénon.

| $\tau_e$ | Charge collectée | Fraction $O_2$-eq. | $Q_{\max}$ [mbar L s$^{-1}$] |
|---|---|---|---|
| 5 ms | 87,1 % | 0,085 ppb | $3{,}0 \times 10^{-7}$ |
| 10 ms | 93,3 % | 0,042 ppb | $1{,}5 \times 10^{-7}$ |

TABLE 2 : Charge collectée sur la dérive maximale, fraction molaire $O_2$-équivalente et débit source maximal admissible pour les deux durées de vie considérées. Les débits de dégazage sont exprimés en équivalent $O_2$ et supposent une recirculation de 350 SLPM ainsi qu'une efficacité idéale du purificateur.

Le débit de dégazage maximal doit être réparti entre les composants en contact avec le xénon. Pour chacun d'eux, la contribution dépend du matériau, de la surface exposée, de l'épaisseur, de la température et de l'historique de nettoyage, de stockage et d'exposition à l'air. Dans le cadre des détecteurs au xénon liquide, le débit de dégazage est décrit comme la somme de deux contributions :

$$Q_{\text{dég}}(t,T) = Q_{\text{diff}}(t,T) + Q_{\text{dés}}(t,T). \tag{5}$$

La désorption correspond à la libération des molécules adsorbées à la surface du matériau, tandis que la diffusion correspond au transport vers la surface des mo-

lécules absorbées dans son volume. Pour les métaux, le dégazage moléculaire est généralement dominé par la désorption de surface. Dans les polymères et les époxys, les impuretés peuvent être stockées dans l'ensemble du matériau et leur diffusion vers la surface peut rester dominante pendant une longue durée. Une contribution de désorption peut néanmoins être présente au début du pompage. La perméation, la vaporisation et les fuites sont traitées séparément lorsqu'elles sont pertinentes. Ces mécanismes sont illustrés à la figure 3.5.

Une contribution de cette thèse porte sur l'analyse des mesures de dégazage sous vide réalisées à Yale avec des échantillons de PTFE, de VESPEL et d'époxy. Les modèles de diffusion et de désorption développés dans ce chapitre ont été utilisés pour ajuster les pressions partielles de $H_2O$ et de $O_2$ mesurées au cours de différentes évolutions de température. Les données sont d'abord ajustées avec le modèle de diffusion, puis une contribution de désorption est ajoutée lorsque la diffusion seule ne reproduit pas l'évolution de la pression.

La diffusion seule décrit les traces $O_2$ et $H_2O$ du VESPEL et de l'époxy, ainsi que la trace $O_2$ du PTFE. Pour l'eau issue du PTFE, une composante supplémentaire de désorption est nécessaire pour décrire correctement le début du dégazage mesuré, avant que la diffusion ne devienne dominante. Les paramètres de diffusion extraits sont regroupés dans le tableau 3.

| Matériau | Gaz | $D_{298}$ [$\mathrm{cm^2\,s^{-1}}$] | $E_D$ [eV] | $c_0$ [$\mathrm{mbar\,L\,cm^{-3}}$] |
|---|---|---|---|---|
| PTFE | $H_2O$ | $\left(5.92^{+0.51}_{-0.27}\right) \times 10^{-6}$ | $0.175^{+0.021}_{-0.044}$ | $\left(5.65^{+0.36}_{-0.18}\right) \times 10^{-4}$ |
| | $O_2$ | $\left(1.13^{+0.10}_{-0.12}\right) \times 10^{-6}$ | $0.238^{+0.013}_{-0.015}$ | $\left(3.33^{+0.22}_{-0.14}\right) \times 10^{-4}$ |
| VESPEL | $H_2O$ | $1.54 \times 10^{-8} \pm 7.78 \times 10^{-4}$ † | $0.374^{+0.011}_{-0.014}$ | $0.532 \pm 1.34 \times 10^{4}$ † |
| | $O_2$ | $6.15 \times 10^{-9} \pm 5.99 \times 10^{-4}$ † | $0.421^{+0.013}_{-0.019}$ | $1.46 \times 10^{-3} \pm 71.3$ † |
| Époxy | $H_2O$ | $6.98 \times 10^{-10} \pm 3.99 \times 10^{-5}$ † | $0.736^{+0.006}_{-0.006}$ | $0.633 \pm 1.81 \times 10^{4}$ † |
| | $O_2$ | $1.67 \times 10^{-9} \pm 3.03 \times 10^{-4}$ † | $0.441^{+0.010}_{-0.010}$ | $1.29 \times 10^{-3} \pm 117$ † |

TABLE 3 : Résultats finaux de l'analyse des mesures de dégazage réalisées à Yale. Les dagues signalent les ajustements pour lesquels $c_0$ et $D_{298}$ sont fortement corrélés. Les incertitudes combinent les estimations locales de l'ajustement et des thermocouples.

Le coefficient $D_{298}$ décrit la vitesse de diffusion à température ambiante, $E_D$ son évolution avec la température et $c_0$ la concentration initiale d'impuretés dans le volume du matériau, exprimée ici dans les unités équivalentes de pression utilisées pour analyser les mesures sous vide. La dépendance thermique du coefficient de diffusion est donnée par

$$D(T) = D_{298} \exp\left[-\frac{E_D}{k_B}\left(\frac{1}{T} - \frac{1}{298.15\,\mathrm{K}}\right)\right]. \tag{6}$$

Les très grandes incertitudes associées à $D_{298}$ et à $c_0$ pour les ajustements marqués d'une dague traduisent la forte corrélation entre ces paramètres en régime initial de diffusion, où les données contraignent surtout $c_0\sqrt{D_{298}}$. Les faibles signaux

$O_2$ du VESPEL et de l'époxy limitent également la précision des ajustements. Les valeurs de $E_D$ restent mieux déterminées, car la variation relative de la pression lors des changements de température demeure visible dans les données. Avec un conditionnement contrôlé et un historique de pompage connu, la séparation de $c_0$ et de $D_{298}$ pourrait être améliorée par des échantillons plus minces ou des mesures plus longues permettant d'observer la transition vers la déplétion, ou par une mesure indépendante de l'inventaire en impuretés.

La relation d'Arrhenius permet d'extrapoler les coefficients déterminés près de la température ambiante vers la température du xénon liquide. Combinés à la concentration initiale, à la surface exposée et à l'épaisseur du composant, les paramètres extraits permettent d'estimer son débit de dégazage pendant le refroidissement et le fonctionnement du détecteur. Cette extrapolation est particulièrement utile pour les polymères et les époxys, dont le dégazage dépend à la fois de leur géométrie et du ralentissement de la diffusion à basse température.

Ces mesures sous vide sont complétées par des mesures de durée de vie des électrons réalisées dans des volumes de xénon liquide au sein de la collaboration. Les premières isolent les matériaux et contraignent les mécanismes de dégazage, tandis que les secondes vérifient directement leur effet global sur la survie des électrons.

Ce chapitre établit ainsi une méthode pour traduire l'exigence sur $\tau_e$ en un débit maximal d'impuretés, puis répartir ce budget entre les composants. Les modèles développés permettent d'identifier les mécanismes dominants, d'extrapoler le dégazage à la température du xénon liquide et d'orienter le choix, la géométrie et la préparation des matériaux.

# 4 Réduction du bruit de fond par le cryostat et le blindage HFE

Le HFE entourant la TPC remplit plusieurs fonctions. Ce liquide très radiopur atténue les rayonnements $\gamma$ provenant du cryostat et de structures externes moins radiopures, permet de refroidir et de stabiliser thermiquement le xénon liquide, et contrebalance la pression exercée par le xénon sur la cuve de la TPC. Dans la géométrie de référence, environ 32 t de HFE forment une épaisseur minimale de 76 cm autour de la TPC, ce qui limite à 0,5 % la transmission de rayonnements $\gamma$ d'une énergie proche de 2.5 MeV, comparable à $Q_{\beta\beta}$.

Le concept initial du cryostat reposait sur des coques sphériques en fibres de carbone associées à des revêtements internes en titane. Leur remplacement par des cuves en nickel ultra-radiopur réduit la contribution du cryostat au bruit de fond d'environ un facteur 380 : elle passe de 69 % de son allocation initiale à moins de 0,2 %. Ce changement simplifie également la fabrication, puisque les cuves métalliques peuvent être réalisées à partir de panneaux formés en surface, plutôt qu'assemblées sous terre dans le laboratoire à partir de plusieurs couches de matériaux composites. Les cuves ne constituent alors plus une contribution dominante au budget total de bruit de fond de l'expérience, ce qui permet de réexaminer la quantité de HFE nécessaire.

Les simulations Monte Carlo réalisées étudient l'évolution du bruit de fond dans le détecteur lorsque la masse de HFE et le rayon de la cuve interne sont réduits. La diminution du blindage en HFE augmente la transmission des rayonnements provenant de l'ensemble des composants du détecteur, notamment des plateformes de manutention, du béton et du volume d'eau, mais réduit simultanément la masse de HFE et les dimensions du cryostat. Les principaux résultats sont résumés dans le tableau 4.

| **Configuration** | **HFE** | $\Delta m_{\mathrm{HFE}}$ | $\Delta R_{\mathrm{IV}}$ | $\Delta B_{\mathrm{tot}}$ | $\Delta T_{1/2}^{0\nu}$ |
|---|---|---|---|---|---|
| Référence | 31.8 t | — | — | — | — |
| Recommandée | 13 t | −59 % | −23 % | +6,3 % | −1,7 % |
| Agressive | 7 t | −78 % | −34 % | +51 % | −10,8 % |

TABLE 4 : Évolution de la masse de HFE, du rayon de la cuve interne, du bruit de fond total et de la sensibilité par rapport à la configuration de référence.

La configuration recommandée contient 13 t de HFE. Elle réduit son inventaire d'environ 60% et le rayon de la cuve interne de près d'un quart, tandis que le bruit de fond total n'augmente que d'environ 6%. L'effet estimé sur la sensibilité reste inférieur à 2%. Une réduction supplémentaire jusqu'à 7 t augmente en revanche le bruit de fond d'environ 50% et dégrade la sensibilité de près de 11%. La configuration à 13 t constitue le meilleur compromis identifié entre compacité, quantité de HFE et bruit de fond.

La diminution de la masse de HFE réduit la capacité du système à ralentir le réchauffement du xénon en cas d'arrêt inopiné du refroidissement. Une augmentation de 1 K de la température du LXe prendrait environ 16 h dans la configuration de référence, 7 h avec 13 t de HFE et 4 h avec 7 t. La configuration recommandée conserve donc une masse de HFE correspondant, dans ce modèle approximatif, à un délai estimé d'environ sept heures avant une augmentation de 1 K de la température du xénon liquide, ce qui pourrait permettre d'activer les systèmes d'urgence en cas de défaillance du refroidissement.

D'autres possibilités d'optimisation ont été étudiées, notamment :

- dans le cas d'une réduction de la coque sphérique interne du cryostat, le rayon de la coque sphérique externe pourrait également être diminué. Pour la configuration contenant 13 t de HFE, cela ajouterait près de 50 cm d'eau entre le cryostat et la paroi du détecteur externe. La contribution propre de l'eau resterait pratiquement inchangée, tandis que les rayonnements provenant de sources situées au-delà de cette couche seraient atténués d'environ un facteur 8 ;
- un cryostat cylindrique suivrait plus étroitement la forme de la TPC, simplifierait sa fabrication et réduirait d'environ 14 % l'inventaire de HFE pour une même épaisseur minimale de blindage de 76 cm. Dans cette configuration de référence, les parois en nickel devraient néanmoins être plus épaisses pour l'option cylindrique, ce qui augmenterait la contribution des coques au bruit de fond

d'un facteur d'environ 3 pour la cuve interne et 2 pour la cuve externe. Pour un inventaire d'environ 13 t de HFE, les contributions des géométries sphérique et cylindrique deviennent cependant comparables, ce qui fait du concept cylindrique une alternative crédible, sous réserve d'une validation mécanique des épaisseurs retenues.

Ces études montrent que le passage au nickel ne réduit pas seulement le bruit de fond du détecteur, mais permet également d'optimiser sa conception globale.

# 5 Refroidissement et recirculation du HFE

Le chapitre 5 étudie la possibilité de refroidir et de recirculer le HFE jusqu'à la température du xénon liquide. Les travaux présentés se concentrent dans un premier temps sur le HFE-7200, actuellement considéré comme le principal candidat pour nEXO en raison de ses caractéristiques de solidification et de l'évolution de sa viscosité à basse température. Le banc développé reproduit à échelle réduite les principales fonctions envisagées pour le système de HFE de nEXO :

- refroidir le HFE jusqu'à la température du xénon liquide à l'aide d'un échangeur de chaleur alimenté en azote liquide ;
- maintenir sa recirculation avec une pompe à engrenages malgré l'augmentation de la viscosité à basse température ;
- contrôler la pression exercée sur le HFE afin d'éviter la cavitation au niveau de la pompe ;
- garantir l'étanchéité du système afin de limiter l'évaporation et l'introduction d'humidité.

Le HFE-7200 a été retenu pour ces essais également car sa pression de vapeur saturante à température ambiante est environ quatre fois plus faible que celle du HFE-7000, ce qui facilite sa manipulation et réduit le risque de cavitation. Sa viscosité augmente toutefois de plus d'un facteur 60 entre la température ambiante et $-110\,°C$, passant d'environ 0.43 cSt à 28.35 cSt. Cette augmentation accroît fortement la résistance hydraulique de la boucle et, par conséquent, la pression différentielle imposée à la pompe, ce qui peut entraîner une surcharge et l'endommager.

Des essais par immersion dans l'azote liquide ont d'abord été réalisés afin de caractériser les transitions du HFE-7200 à basse température. Les températures extraites sont comparées aux mesures du fabricant dans le tableau 5.

Les écarts observés montrent que ces températures dépendent de l'échantillon, notamment de sa pureté, les impuretés pouvant abaisser les températures de transition de phase. Leur proximité avec la température du xénon liquide impose néanmoins de contrôler les gradients thermiques autour de l'échangeur afin d'éviter une solidification locale du HFE.

À la suite de l'endommagement par cavitation d'une pompe centrifuge lors d'essais antérieurs de la collaboration, le banc développé utilise une pompe volumétrique

| **Transition** | **Référence DSC 3M** [°C] | **Par immersion** [°C] |
|---|---|---|
| Transition vitreuse, $T_g$ | $-167$ | $-163 \pm 6$ |
| Cristallisation froide, $T_{cc}$ | $-120$ | $-131 \pm 1$ |
| Fusion, $T_m$ | $-100$ | $-120 \pm 2$ |

TABLE 5 : Transitions du HFE-7200 obtenues à partir de la référence DSC de 3M et des mesures par immersion dans l'azote liquide.

à engrenages à accouplement magnétique, moins sensible à ce mode de défaillance. Conçu pour reproduire au plus près le système prévu pour nEXO, il est équipé d'un débitmètre Coriolis, de capteurs de pression et de température, ainsi que d'un système de contrôle assurant l'acquisition des données et la protection contre les surpressions. Le schéma de tuyauterie et d'instrumentation est présenté à la figure 5.8.

Chaque élément du système a été vérifié avant les essais cryogéniques, notamment pour :

- valider l'étanchéité de la boucle par des essais sous vide et sous pression ;
- étalonner les capteurs et vérifier le fonctionnement de l'électronique, du contrôle et des protections ;
- confirmer que l'échangeur de chaleur fabriqué fournit une puissance de refroidissement suffisante.

Un bain d'antigel a été utilisé pour caractériser l'échangeur de chaleur avant son intégration à la boucle. Ces essais montrent que sa puissance de refroidissement augmente linéairement avec la pression d'alimentation en azote liquide et qu'elle est suffisante pour compenser les fuites thermiques du système et atteindre la plage de température requise.

Les principaux résultats des premiers essais sont résumés dans le tableau 6.

| **Grandeur** | **Valeur mesurée** | **Conclusion** |
|---|---|---|
| Température | $-100\,°\mathrm{C}$ | Recirculation stable |
| Débit | Jusqu'à $5.2\,\mathrm{L\,min^{-1}}$ | Objectif dépassé |
| Pression différentielle | $\approx 2\,\mathrm{bar}$ à $4\,\mathrm{L\,min^{-1}}$ | Facteur 5 sous la limite |

TABLE 6 : Principaux résultats obtenus lors des premiers essais cryogéniques du système de recirculation du HFE-7200.

Le débit reste stable pendant le refroidissement malgré l'augmentation de la viscosité, et la pression différentielle demeure largement inférieure à la limite de la pompe. Le contrôle de la pression du HFE à partir du piège à gaz rempli d'azote, situé au dessus du système, permet également de conserver une marge suffisante contre la cavitation.

La température minimale atteinte, −100 °C, a été limitée par l'épuisement de la réserve d'azote liquide, et non par un manque de puissance de refroidissement. À mesure que la température diminuait, la vanne d'azote liquide devait toutefois être actionnée de plus en plus fréquemment afin d'éviter une solidification locale du HFE autour de l'échangeur. Une régulation PID est donc en cours de développement pour atteindre et maintenir plus facilement et en toute sécurité −110 °C, puis explorer des températures plus basses.

Ce chapitre montre ainsi que le HFE peut être refroidi par un échangeur à azote liquide et recirculé de manière stable, à une température proche de celle du xénon liquide, au moyen d'une pompe à engrenages. Des mélanges de HFE seront également testés dans ce système afin d'évaluer leur effet sur la viscosité à basse température. Ces résultats confirment la faisabilité de l'utilisation du HFE comme blindage cryogénique dans les détecteurs au xénon liquide de nouvelle génération.

# Appendix A

# Additional Details on Background-Rate Propagation

## A.1 Monte Carlo Uncertainty on Hit Efficiencies

The parent-normalized hit efficiency $\varepsilon_{ij}$ is derived from simulations that generate decays of the relevant daughter isotope. If $N_{ij}^{\mathrm{gen}}$ such decays are generated and $N_{ij}^{\mathrm{ROI}}$ survive all selections, the simulated-isotope efficiency is

$$\varepsilon_{ij}^{\mathrm{sim}} = \frac{N_{ij}^{\mathrm{ROI}}}{N_{ij}^{\mathrm{gen}}}. \tag{A.1}$$

Because each simulated decay either contributes to the fiducial ROI or does not, the counting follows binomial statistics. The variance of $\varepsilon_{ij}^{\mathrm{sim}}$ is therefore

$$\mathrm{Var}\left(\varepsilon_{ij}^{\mathrm{sim}}\right) = \frac{\varepsilon_{ij}^{\mathrm{sim}}\left(1-\varepsilon_{ij}^{\mathrm{sim}}\right)}{N_{ij}^{\mathrm{gen}}}, \tag{A.2}$$

so that

$$\sigma_{\varepsilon_{ij}^{\mathrm{sim}}} = \sqrt{\frac{\varepsilon_{ij}^{\mathrm{sim}}\left(1-\varepsilon_{ij}^{\mathrm{sim}}\right)}{N_{ij}^{\mathrm{gen}}}}. \tag{A.3}$$

If $b_{ij}$ denotes the branching fraction connecting the parent isotope used in the activity budget to the simulated daughter, the parent-normalized efficiency is

$$\varepsilon_{ij} = b_{ij}\,\varepsilon_{ij}^{\mathrm{sim}}. \tag{A.4}$$

Propagating the variance then gives

$$\mathrm{Var}(\varepsilon_{ij}) = b_{ij}^2\,\mathrm{Var}\left(\varepsilon_{ij}^{\mathrm{sim}}\right) = \frac{\varepsilon_{ij} b_{ij}}{N_{ij}^{\mathrm{gen}}}\left(1-\frac{\varepsilon_{ij}}{b_{ij}}\right), \tag{A.5}$$

and therefore

$$\sigma_{\varepsilon_{ij}} = \sqrt{\frac{\varepsilon_{ij} b_{ij}}{N_{ij}^{\mathrm{gen}}}\left(1-\frac{\varepsilon_{ij}}{b_{ij}}\right)}. \tag{A.6}$$

In the small-efficiency limit relevant to rare-event background studies, $\varepsilon_{ij} \ll b_{ij}$, this reduces to

$$\sigma_{\varepsilon_{ij}} \simeq \sqrt{\frac{\varepsilon_{ij} b_{ij}}{N_{ij}^{\mathrm{gen}}}}. \tag{A.7}$$

If no event survives the full selection, the estimated efficiency is zero, but its one-sided 68% confidence upper limit is, in the Poisson approximation,

$$\varepsilon_{ij}^{\mathrm{UL},68} \simeq \frac{-\ln(1-0.68)\, b_{ij}}{N_{ij}^{\mathrm{gen}}} \simeq \frac{1.14\, b_{ij}}{N_{ij}^{\mathrm{gen}}}. \tag{A.8}$$

For uncertainty propagation, this limit is used as $\sigma_{\varepsilon_{ij}}$. This is an approximate prescription, not a measured $1\sigma$ uncertainty.

## A.2 Standard-Normal Functions and Mills Ratio

The TG-spread method is formulated in terms of the standard normal probability density and cumulative distribution functions,

$$\phi(z) = \frac{1}{\sqrt{2\pi}} e^{-z^2/2}, \qquad \Phi(z) = \int_{-\infty}^{z} \phi(u)\, du, \tag{A.9}$$

together with the Mills ratio

$$\lambda(z) = \frac{\phi(z)}{\Phi(z)}, \tag{A.10}$$

appropriate for a lower truncation at zero. These functions are shown in Figs. A.1 and A.2.

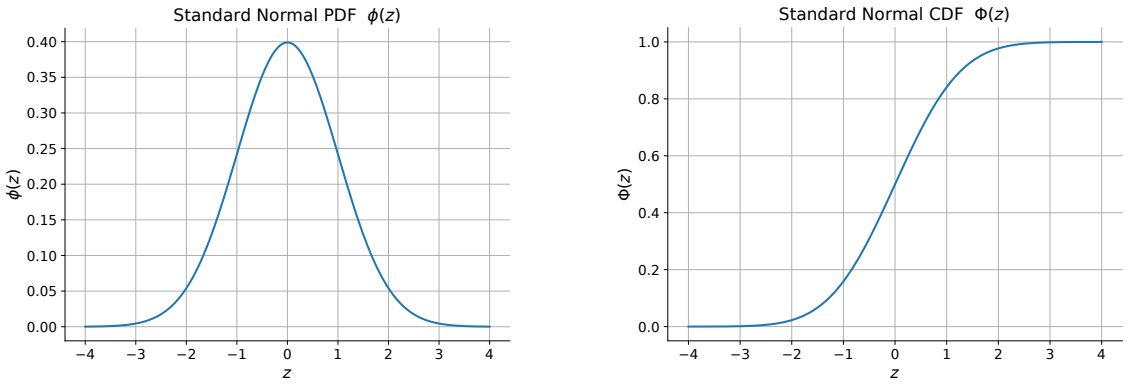


(a) Standard-normal PDF $\phi(z)$ (b) Standard-normal CDF $\Phi(z)$

Figure A.1: Standard-normal probability density and cumulative distribution functions used in the truncated-Gaussian propagation.

## A.3 Moments of the One-Sided Truncated Gaussian

Consider a Gaussian random variable

$$X \sim \mathcal{N}(\mu, \sigma^2), \tag{A.11}$$

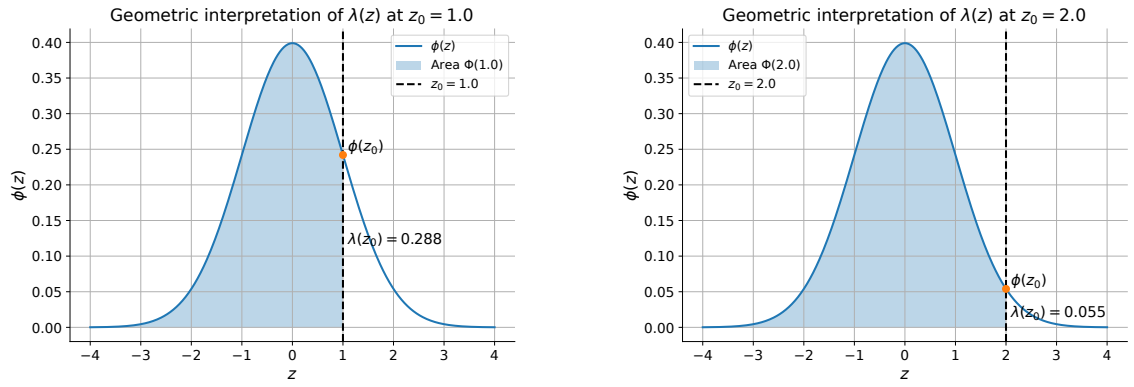


(a) $z = 1$ $(\lambda \approx 0.29)$ (b) $z = 2$ $(\lambda \approx 0.055)$

Figure A.2: Illustration of the Mills ratio $\lambda(z) = \phi(z)/\Phi(z)$ for a lower truncation at zero. As $z$ increases, the truncation removes a smaller fraction of the Gaussian support, so the correction to the mean and variance decreases.

truncated at zero so that only $X \geq 0$ is retained. Writing

$$z = \frac{\mu}{\sigma}, \qquad \alpha = \frac{0-\mu}{\sigma} = -z, \tag{A.12}$$

the normalization factor of the truncated distribution is

$$Z = 1 - \Phi(\alpha) = \Phi(z). \tag{A.13}$$

The corresponding probability density is

$$f_+(x) = \frac{f(x)}{\Phi(z)}, \qquad x \geq 0. \tag{A.14}$$

Using the Mills ratio,

$$\lambda(z) = \frac{\phi(z)}{\Phi(z)}, \tag{A.15}$$

the first moment is

$$\mathbb{E}[X \mid X \geq 0] = \mu + \sigma\lambda(z), \tag{A.16}$$

and the variance is

$$\mathrm{Var}(X \mid X \geq 0) = \sigma^2 \left[1 - z\lambda(z) - \lambda^2(z)\right]. \tag{A.17}$$

The TG-spread used in the main text is therefore

$$u^{\mathrm{TG}} = \sigma\sqrt{1 - z\lambda(z) - \lambda^2(z)}. \tag{A.18}$$

These expressions reduce to the usual Gaussian mean and standard deviation when $z \gg 1$, since the probability removed below zero becomes negligible. At $z = 0$, they recover the half-normal limits,

$$\mathbb{E}[X \mid X \geq 0] = \sigma\sqrt{\frac{2}{\pi}}, \qquad \mathrm{Var}(X \mid X \geq 0) = \sigma^2\left(1 - \frac{2}{\pi}\right). \tag{A.19}$$

A concise derivation can be written from the lower-truncation formula

$$\mathrm{Var}[X \mid X > a] = \sigma^2 \left[1 - \delta(\alpha)\right], \qquad \delta(\alpha) = \lambda(\alpha)\left[\lambda(\alpha) - \alpha\right], \tag{A.20}$$

with $\lambda(\alpha) = \phi(\alpha)/\left[1 - \Phi(\alpha)\right]$. Setting $a = 0$ and $\alpha = -z$, and using the symmetries $\phi(-z) = \phi(z)$ and $\Phi(-z) = 1 - \Phi(z)$, gives directly

$$\mathrm{Var}(X \mid X \geq 0) = \sigma^2 \left[1 - z\lambda(z) - \lambda^2(z)\right]. \tag{A.21}$$

A standard reference for this result is Greene, *Econometric Analysis*, 5th ed., Theorem 22.2.

## A.4 Equivalent Form in Terms of exp and erf

Using

$$\phi(z) = \frac{e^{-z^2/2}}{\sqrt{2\pi}}, \qquad \Phi(z) = \frac{1}{2}\left[1 + \mathrm{erf}\left(\frac{z}{\sqrt{2}}\right)\right], \tag{A.22}$$

the Mills ratio becomes

$$\lambda(z) = \sqrt{\frac{2}{\pi}}\,\frac{e^{-z^2/2}}{1 + \mathrm{erf}(z/\sqrt{2})}. \tag{A.23}$$

Substituting into the TG variance gives

$$\frac{\mathrm{Var}(X \mid X \geq 0)}{\sigma^2} = 1 - z\sqrt{\frac{2}{\pi}}\,\frac{e^{-z^2/2}}{1 + \mathrm{erf}(z/\sqrt{2})} - \frac{2}{\pi}\left(\frac{e^{-z^2/2}}{1 + \mathrm{erf}(z/\sqrt{2})}\right)^2, \tag{A.24}$$

and therefore

$$u^{\mathrm{TG}} = \sigma\sqrt{1 - z\sqrt{\frac{2}{\pi}}\,\frac{e^{-z^2/2}}{1 + \mathrm{erf}(z/\sqrt{2})} - \frac{2}{\pi}\left(\frac{e^{-z^2/2}}{1 + \mathrm{erf}(z/\sqrt{2})}\right)^2}. \tag{A.25}$$

Defining the shorthand

$$R(\mu, \sigma) \equiv \frac{\exp[-\mu^2/(2\sigma^2)]}{1 + \mathrm{erf}\Big(\mu/(\sqrt{2}\sigma)\Big)}, \tag{A.26}$$

one may equivalently write

$$\lambda(z) = \sqrt{\frac{2}{\pi}}\,R(\mu, \sigma), \tag{A.27}$$

so that

$$\frac{\mathrm{Var}(X \mid X \geq 0)}{\sigma^2} = 1 - z\sqrt{\frac{2}{\pi}}\,R(\mu, \sigma) - \frac{2}{\pi}R^2(\mu, \sigma). \tag{A.28}$$

# Appendix B

# Mean HFE and Attenuation-Equivalent Thicknesses

This appendix summarizes the geometric estimate of the HFE-7200 thickness distribution between the cylindrical TPC and the spherical inner cryostat vessel. Its purpose is to quantify the mean thickness and the attenuation-equivalent thickness relevant to external $\gamma$-ray attenuation.

## B.1 Geometry and Definitions

The TPC is modeled as a cylinder of radius $a_{\mathrm{TPC}}$ and full height $H_{\mathrm{TPC}}$, centered inside a spherical inner cryostat vessel of radius $R_{\mathrm{IC}}$, with HFE-7200 filling the intervening volume. Using spherical coordinates $(r, \theta, \phi)$, the radial distance from the origin to the TPC boundary is

$$r(\theta) = \min\left(\frac{a_{\mathrm{TPC}}}{\sin\theta}, \frac{H_{\mathrm{TPC}}/2}{|\cos\theta|}\right). \tag{B.1}$$

The corresponding HFE thickness along direction $\theta$ is

$$\Delta r(\theta) = R_{\mathrm{IC}} - r(\theta). \tag{B.2}$$

The transition angle between the cylindrical side and the end caps is obtained from

$$\tan\theta_c = \frac{2a_{\mathrm{TPC}}}{H_{\mathrm{TPC}}}. \tag{B.3}$$

For the nominal baseline dimensions used in this estimate,

$$R_{\mathrm{IC}} = 1691\,\mathrm{mm}, \qquad a_{\mathrm{TPC}} = 638.5\,\mathrm{mm}, \qquad H_{\mathrm{TPC}} = 1277\,\mathrm{mm}, \tag{B.4}$$

this defines the full angular thickness profile $\Delta r(\theta)$.

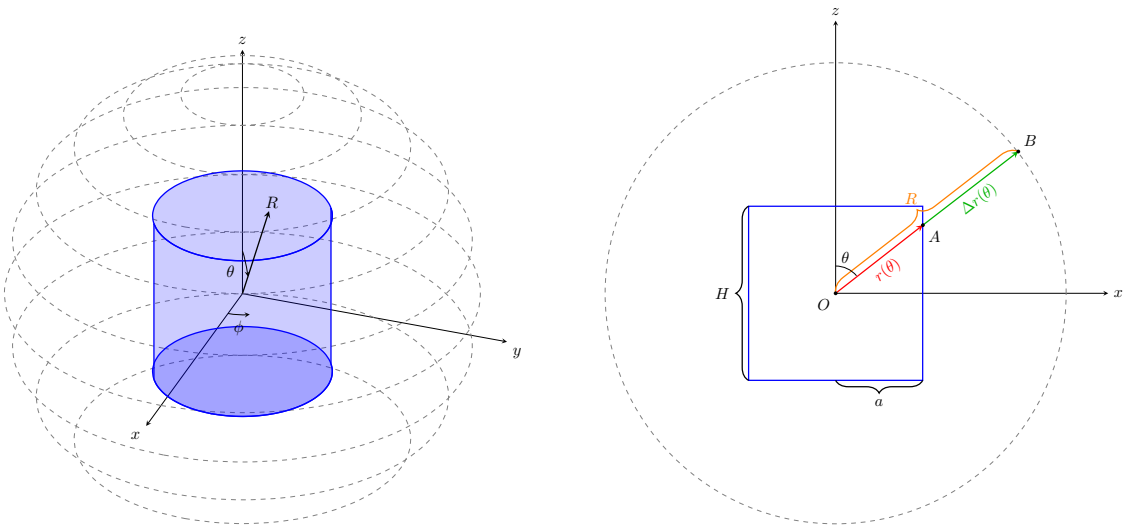


(a) 3D schematic of the cryostat geometry (b) 2D cross-sectional view

Figure B.1: Geometry used for the mean HFE-thickness calculation. A cylindrical TPC is enclosed within a spherical inner cryostat vessel, producing a direction-dependent HFE shell.

The radial distance $r(\theta)$ can be written piecewise as

$$r(\theta) = \begin{cases} \dfrac{H_{\mathrm{TPC}}/2}{|\cos\theta|}, & 0 \le \theta < \theta_c \text{ or } \pi - \theta_c < \theta \le \pi, \\ \dfrac{a_{\mathrm{TPC}}}{\sin\theta}, & \theta_c \le \theta \le \pi - \theta_c. \end{cases} \tag{B.5}$$

Figure B.2 shows the resulting intersection distance and HFE thickness as functions of polar angle.

## B.2 Minimum Thickness

The minimum HFE thickness occurs at the TPC corner, where the radial distance from the origin is maximal:

$$r_{\max} = \sqrt{a_{\mathrm{TPC}}^2 + \left(\frac{H_{\mathrm{TPC}}}{2}\right)^2}. \tag{B.6}$$

The corresponding minimum thickness is

$$\Delta r_{\min} = R_{\mathrm{IC}} - r_{\max}. \tag{B.7}$$

Using the nominal dimensions above gives

$$r_{\max} \simeq 903.0\,\mathrm{mm}, \qquad \Delta r_{\min} \simeq 788.02\,\mathrm{mm}. \tag{B.8}$$

This value is close to, though slightly larger than, the $\sim$ 760 mm minimum thickness requirement used in the baseline design. The difference is attributable to structural details and support elements not included in the simplified geometric model.

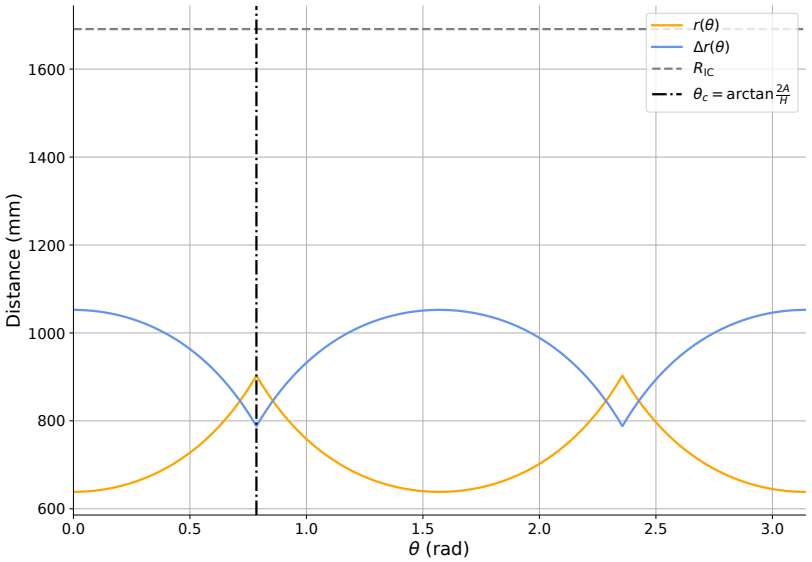


Figure B.2: Intersection distance $r(\theta)$ and HFE thickness $\Delta r(\theta)$ as functions of polar angle.

## B.3 Angular Mean Thickness and Transmission

For attenuation at $\sim 2.5\,\mathrm{MeV}$, the transmission along direction $\theta$ is

$$T(\theta) = e^{-\mu_{\mathrm{HFE}}\Delta r(\theta)}, \tag{B.9}$$

where $\mu_{\mathrm{HFE}}$ is the linear attenuation coefficient of HFE-7200 at that energy. The angular mean transmission is

$$\langle T\rangle = \frac{1}{4\pi}\int_0^{2\pi}\int_0^{\pi} e^{-\mu_{\mathrm{HFE}}\Delta r(\theta)}\sin\theta\,d\theta\,d\phi = \frac{1}{2}\int_0^{\pi} e^{-\mu_{\mathrm{HFE}}\Delta r(\theta)}\sin\theta\,d\theta. \tag{B.10}$$

The corresponding angular mean thickness is

$$\langle \Delta r\rangle = \frac{1}{2}\int_0^{\pi}\Delta r(\theta)\sin\theta\,d\theta. \tag{B.11}$$

It is also useful to define the attenuation-equivalent thickness through

$$\delta_{\mathrm{att}} = -\frac{\ln\langle T\rangle}{\mu_{\mathrm{HFE}}}, \tag{B.12}$$

so that a uniform shell of thickness $\delta_{\mathrm{att}}$ would give the same mean transmission as the full angular distribution.

Figure B.3 shows the integrand used to calculate the angular mean transmission.

Numerical evaluation gives

$$\langle T\rangle = 1.687\times10^{-3}, \qquad \langle \Delta r\rangle = 968.24\,\mathrm{mm}, \qquad \delta_{\mathrm{att}} = 946.72\,\mathrm{mm}. \tag{B.13}$$

The full thickness range is

$$\Delta r_{\min} \simeq 788.02\,\mathrm{mm}, \qquad \Delta r_{\max} \simeq 1052.5\,\mathrm{mm}. \tag{B.14}$$

These values correspond to an average attenuation of about

$$\langle A\rangle = 1 - \langle T\rangle \simeq 0.998313, \tag{B.15}$$

or equivalently a mean transmission of about $0.17\,\%$ for $\sim 2.5\,\mathrm{MeV}$ $\gamma$-rays.

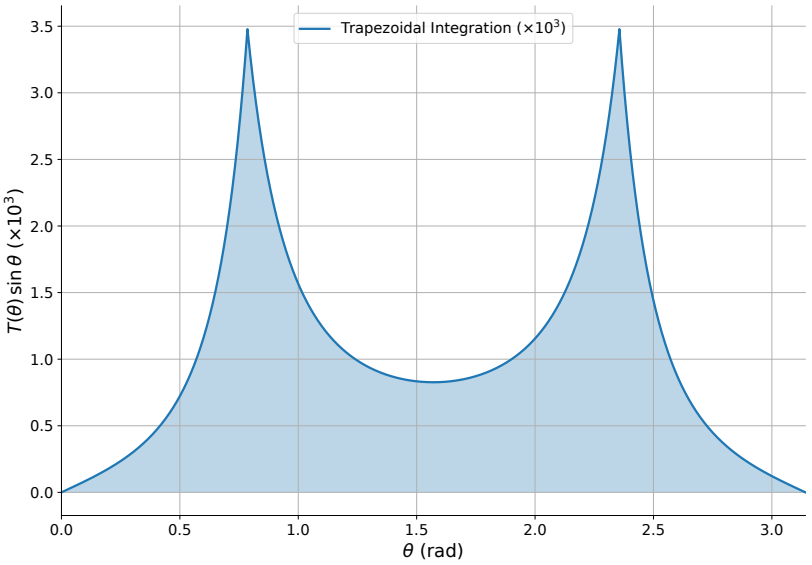


Figure B.3: Integrand $T(\theta)\sin\theta$ used to calculate the angular mean transmission for $\sim 2.5\,\mathrm{MeV}$ $\gamma$-rays in HFE-7200.

## B.4 Interpretation

The main result is that the baseline HFE shell is substantially thicker on average than the minimum design requirement. While the minimum thickness is close to 0.8 m, the angular mean thickness is close to 1.0 m, and the corresponding attenuation-equivalent thickness is about 0.95 m. The resulting mean transmission, $\sim 0.17\,\%$, is comfortably below the baseline design requirement of $\lesssim 0.5\,\%$ transmission for a $\sim 2.5\,\mathrm{MeV}$ $\gamma$-ray.

# Appendix C

# Component Hit-Efficiency and Water Radioassay Tables

This appendix lists numerical inputs used in Chapter 4: the parent-normalized hit efficiencies used in the HFE and cryostat-vessel scans and the water-radioactivity assay values used for the water-shield study.

## C.1 Parent-normalized hit-efficiency tables

The quoted efficiencies include the parent normalization of Sec. 4.1.2, with $b_{\mathrm{Th}} = 0.3594$ and $b_{\mathrm{U}} \simeq 1$. The quoted uncertainties are propagated binomial uncertainties.

### C.1.1 HFE hit efficiencies

| Part | Isotope | $R_{\mathrm{IV}}$ [mm] | $m_{\mathrm{HFE}}$ [t] | Hit efficiency | |
|---|---|---|---|---|---|
| | | | | $\varepsilon$ [counts/ROI/2t/decay] | Error |
| HFE | $^{232}$Th ($^{208}$Tl) | 1000 | 4.16 | $1.03 \times 10^{-6}$ | $6.08 \times 10^{-8}$ |
| | | 1026 | 4.73 | $8.58 \times 10^{-7}$ | $1.76 \times 10^{-8}$ |
| | | 1100 | 6.52 | $7.03 \times 10^{-7}$ | $1.59 \times 10^{-8}$ |
| | | 1300 | 12.7 | $3.81 \times 10^{-7}$ | $1.17 \times 10^{-8}$ |
| | | 1691 | 31.6 | $1.67 \times 10^{-7}$ | $7.75 \times 10^{-9}$ |
| | $^{238}$U ($^{214}$Bi) | 1000 | 4.16 | $1.12 \times 10^{-6}$ | $1.06 \times 10^{-7}$ |
| | | 1026 | 4.73 | $1.05 \times 10^{-6}$ | $3.24 \times 10^{-8}$ |
| | | 1100 | 6.52 | $7.60 \times 10^{-7}$ | $2.76 \times 10^{-8}$ |
| | | 1300 | 12.7 | $4.38 \times 10^{-7}$ | $2.09 \times 10^{-8}$ |
| | | 1691 | 31.6 | $1.77 \times 10^{-7}$ | $1.33 \times 10^{-8}$ |

Table C.1: Parent-normalized HFE hit efficiencies. The $R_{\mathrm{IV}} = 1000\,\mathrm{mm}$ point used $10^8$ simulated decays, while the other points used $10^9$ simulated decays.

### C.1.2 Cryostat-vessel hit efficiencies

| Part | Isotope | $R_{\mathrm{IV}}$ [mm] | $m_{\mathrm{HFE}}$ [t] | Hit efficiency | |
|---|---|---|---|---|---|
| | | | | $\varepsilon$ [counts/ROI/2t/decay] | Error |
| IV | $^{232}$Th ($^{208}$Tl) | 1026 | 4.73 | $2.63 \times 10^{-7}$ | $3.07 \times 10^{-9}$ |
| | | 1226 | 10.25 | $6.59 \times 10^{-8}$ | $1.54 \times 10^{-9}$ |
| | | 1510 | 21.8 | $8.95 \times 10^{-9}$ | $5.67 \times 10^{-10}$ |
| | | 1691 | 31.8 | $2.19 \times 10^{-9}$ | $2.81 \times 10^{-10}$ |
| | $^{238}$U ($^{214}$Bi) | 1026 | 4.73 | $1.65 \times 10^{-7}$ | $4.06 \times 10^{-9}$ |
| | | 1226 | 10.25 | $2.87 \times 10^{-8}$ | $1.69 \times 10^{-9}$ |
| | | 1510 | 21.8 | $3.10 \times 10^{-9}$ | $5.57 \times 10^{-10}$ |
| | | 1691 | 31.8 | $8.00 \times 10^{-10}$ | $2.83 \times 10^{-10}$ |
| OV | $^{232}$Th ($^{208}$Tl) | 1026 | 4.73 | $4.46 \times 10^{-8}$ | $1.27 \times 10^{-9}$ |
| | | 1226 | 10.25 | $1.73 \times 10^{-8}$ | $7.89 \times 10^{-10}$ |
| | | 1510 | 21.8 | $3.23 \times 10^{-9}$ | $3.41 \times 10^{-10}$ |
| | | 1691 | 31.8 | $1.26 \times 10^{-9}$ | $2.13 \times 10^{-10}$ |
| | $^{238}$U ($^{214}$Bi) | 1026 | 4.73 | $2.50 \times 10^{-8}$ | $1.58 \times 10^{-9}$ |
| | | 1226 | 10.25 | $7.10 \times 10^{-9}$ | $8.43 \times 10^{-10}$ |
| | | 1510 | 21.8 | $1.20 \times 10^{-9}$ | $3.46 \times 10^{-10}$ |
| | | 1691 | 31.8 | $2.00 \times 10^{-10}$ | $1.41 \times 10^{-10}$ |

Table C.2: Parent-normalized hit efficiencies for the inner and outer cryostat vessels at the scanned inner-vessel radii. All points use $10^{10}$ simulated decays.

### C.1.3 Direct HFE-shielding comparison for the inner vessel

To isolate the direct shielding effect of the baseline HFE volume, the inner-vessel hit efficiency was also evaluated in the nominal geometry and in the same geometry with the HFE replaced by vacuum.

The resulting parent-normalized hit efficiencies are summarized in Table C.3. For the baseline geometry with HFE, the efficiencies were obtained from $10^{10}$ generated decays. For the no-HFE geometry, they were obtained from $10^{7}$ generated decays. The quoted uncertainties are propagated binomial uncertainties, using the same prescription as in Sec. 4.1.2.

The equivalent HFE thickness $\delta_{\mathrm{eq}}$ is defined from

$$\varepsilon_{\mathrm{HFE}} = \varepsilon_{\mathrm{vac}}\, e^{-\mu_{\mathrm{HFE}}\delta_{\mathrm{eq}}}, \tag{C.1}$$

so that

$$\delta_{\mathrm{eq}} = \frac{1}{\mu_{\mathrm{HFE}}} \ln\!\left(\frac{\varepsilon_{\mathrm{vac}}}{\varepsilon_{\mathrm{HFE}}}\right), \tag{C.2}$$

with

$$\mu_{\mathrm{HFE}} = 6.744 \times 10^{-3}\ \mathrm{mm}^{-1}. \tag{C.3}$$

| Isotope | With HFE [cts/(FWHM · 2 t)] | Without HFE [cts/(FWHM · 2 t)] | Ratio $\varepsilon_{\mathrm{vac}}/\varepsilon_{\mathrm{HFE}}$ | Eq. HFE thickness [mm] |
|---|---|---|---|---|
| $^{232}$Th | $(2.19 \pm 0.28) \times 10^{-9}$ | $(3.59 \pm 1.14) \times 10^{-7}$ | $164 \pm 56$ | $756 \pm 51$ |
| $^{238}$U | $(8.00 \pm 2.83) \times 10^{-10}$ | $(6.00 \pm 2.45) \times 10^{-7}$ | $750 \pm 405$ | $982 \pm 80$ |

Table C.3: Parent-normalized inner-vessel hit efficiencies obtained in the baseline geometry with HFE-7200 and in the same geometry with the HFE volume replaced by vacuum.

These values can be compared with the geometric and shielding quantities derived in Appendix B and summarized in Table 4.4. In the baseline spherical geometry, the minimum HFE thickness is about 760 mm, the geometric mean thickness is about 968 mm, and the attenuation-equivalent thickness corresponding to the mean $\sim 2.5$ MeV transmission is about 946 mm. The direct comparison shows that:

1. for the $^{238}$U chain, the inferred attenuation thickness, $(982 \pm 80)$ mm, is compatible with the attenuation-equivalent thickness of the baseline HFE layer;
2. for the $^{232}$Th chain, the inferred attenuation thickness, $(756 \pm 51)$ mm, is smaller and lies instead close to the minimum HFE thickness.

This difference reflects the different physical origin of the ROI events in the two chains. For the $^{238}$U chain, the relevant $\gamma$-ray energies extend up to 2448 keV, just below $Q_{\beta\beta}$. The ROI-producing population is therefore dominated by photons whose transmission is strongly controlled by the total HFE path length, and the corresponding attenuation thickness stays close to the attenuation-equivalent thickness of the full HFE layer.

For the $^{232}$Th chain, by contrast, the ROI is fed mainly by the $^{208}$Tl 2615 keV line through Compton scattering and partial energy deposition. In this case, the HFE does not simply remove photons from the ROI-producing population. A fraction of the $\gamma$ rays that scatter in the HFE can still reach the xenon with reduced energy and continue to contribute to the broad Compton continuum below the full-energy peak. The inferred attenuation thickness is therefore smaller than the attenuation-equivalent thickness of the full baseline HFE volume.

This does not contradict the HFE-thickness scans discussed in Chap. 4. The direct comparison with and without HFE probes the total suppression produced by the full baseline HFE volume, including the effect of its non-uniform thickness. By contrast, the scan slope is extracted by comparing nearby detector configurations in which the HFE layer is only increased or reduced incrementally. That differential evolution is therefore governed mainly by how the surviving high-energy $^{208}$Tl $\gamma$-ray population is attenuated by the added or removed HFE. As a result, the fitted slope can still remain close to the characteristic attenuation coefficient of a $\sim 2.5$ MeV $\gamma$ ray in HFE, even for the $^{232}$Th chain.

## C.2 Water-radioactivity assay values

Table C.4 summarizes the water-radioactivity assay values collected for comparison in the water-shield study.

| Source | Part | Isotope | Activity [Bq/kg] | Error [Bq/kg] |
|---|---|---|---|---|
| SNO [111] | AV $D_2O$ | $^{232}$Th | $3.13 \times 10^{-9}$ | $8.53 \times 10^{-10}$ |
| | | $^{238}$U | $7.58 \times 10^{-8}$ | $1.25 \times 10^{-8}$ |
| | | $^{222}$Rn | N/A | N/A |
| SNO [111] | $H_2O$ water shield | $^{232}$Th | $1.22 \times 10^{-7}$ | $5.81 \times 10^{-8}$ |
| | | $^{238}$U | $4.32 \times 10^{-6}$ | $9.45 \times 10^{-7}$ |
| | | $^{222}$Rn | N/A | N/A |
| SNO+ [90] | AV water | $^{232}$Th | $9.36 \times 10^{-8}$ | $3.85 \times 10^{-8}$ |
| | | $^{238}$U | $4.00 \times 10^{-6}$ | $1.16 \times 10^{-6}$ |
| | | $^{222}$Rn | N/A | N/A |
| SNO+ [90] | $H_2O$ water shield | $^{232}$Th | $3.93 \times 10^{-7}$ | $1.38 \times 10^{-8}$ |
| | | $^{238}$U | $1.98 \times 10^{-6}$ | $3.93 \times 10^{-7}$ |
| | | $^{222}$Rn | N/A | N/A |
| SNO+ [112] | AV water | $^{232}$Th | 0.00 | $1.19 \times 10^{-9}$ |
| | | $^{238}$U | $7.14 \times 10^{-8}$ | $1.93 \times 10^{-8}$ |
| | | $^{222}$Rn | 0.00 | 0.00 |
| JUNO [113] | $H_2O$ water shield | $^{232}$Th | N/A | N/A |
| | | $^{238}$U | N/A | N/A |
| | | $^{222}$Rn | $6.10 \times 10^{-7}$ | $5.00 \times 10^{-7}$ |

Table C.4: Collected water-radioactivity assay values relevant to the water-shield study

For SNO and SNO+, the reported $^{238}$U-chain values generally trace $^{214}$Bi and therefore include contributions supported by dissolved $^{222}$Rn. The later SNO+ AV-water values are also shown, illustrating the order-of-magnitude improved purity reached after water-system commissioning and purification.

# Appendix D

# Pressure-Drop in the HFE Recirculation Loop

This appendix summarizes the pressure-drop calculation used to size the HFE tubing in Sec. 5.2.1. The original pressure-drop study for the UMass recirculation system was carried out by Graeme Sullivan as part of the mechanical design of the apparatus. The presentation here records the model, assumptions, and numerical inputs in the notation used in this dissertation.

The model is a steady, single-phase, incompressible estimate for the nominal tank path. It assumes one active flow path and does not include simultaneous tank–bypass flow sharing, pump internal losses, cavitation, freezing, or two-phase flow. For a closed recirculation loop evaluated between the pump outlet and pump inlet, the inlet and outlet velocities are equal and the static-head term cancels. The pump differential pressure is therefore modeled as the sum of straight-pipe and minor losses,

$$\Delta P_{\mathrm{loop}} = \left( f_D \frac{L}{D} + K_{\mathrm{minor}} \right) \frac{\rho \bar{u}^2}{2}, \tag{D.1}$$

where $f_D$ is the Darcy friction factor, $L$ is the tubing length, $D$ is the tubing inner diameter, and $K_{\mathrm{minor}}$ is the aggregate minor-loss coefficient for bends, valves, contractions, and expansions [114]. The mean velocity and Reynolds number are

$$\bar{u} = \frac{4\dot{V}_{\mathrm{HFE}}}{\pi D^2}, \qquad Re = \frac{\bar{u} D}{\nu}. \tag{D.2}$$

Here $\nu$ is the kinematic viscosity, expressed in $\mathrm{m^2\,s^{-1}}$ in the flow equations.

The Darcy friction factor is not a constant. It depends on the flow regime and, for turbulent flow, on the pipe roughness. At the cold design point considered here, Eq. (D.2) gives $Re \simeq 386$, so the flow is laminar and the Darcy friction factor is

$$f_D = \frac{64}{Re}. \tag{D.3}$$

In this limit, the straight-pipe term in Eq. (D.1) is equivalent to the Hagen–Poiseuille pressure drop,

$$\Delta P_{\mathrm{pipe}} = \frac{128 \rho \nu L \dot{V}_{\mathrm{HFE}}}{\pi D^4}, \tag{D.4}$$

which gives the $D^{-4}$ dependence used to interpret Fig. 5.9.

The tubing inner diameter is computed from the outer diameter and wall thickness,

$$D = D_{\mathrm{OD}} - 2t. \tag{D.5}$$

For the installed 3/8-in.-OD stainless-steel tubing, using $t = 0.035\,\mathrm{in}$ gives

$$D = (0.375 - 2 \times 0.035)\,\mathrm{in} = 7.747\,\mathrm{mm}. \tag{D.6}$$

The minor-loss coefficient was evaluated from

$$K_{\mathrm{minor}} = 6K_{90} + K_{\mathrm{valve}} + K_c + K_e. \tag{D.7}$$

The values used in the calculation are summarized in Table D.1. They are approximate tabulated engineering coefficients and are included only to account for local losses at the level required for tubing-size selection [115]. The contraction and expansion terms are treated conservatively as abrupt area changes between the tubing and a much larger volume, with $\beta_c$ and $\beta_e$ denoting the corresponding small-to-large area ratios.

| Element | Count | Coefficient | Contribution |
|---|---|---|---|
| 90° bend | 6 | $K_{90} = 0.65$ | 3.90 |
| Full-bore ball valve, open | 1 | $K_{\mathrm{valve}} = 0.04$ | 0.04 |
| Abrupt contraction | 1 | $K_c = 0.45(1 - \beta_c)$, $\beta_c = 0.001$ | 0.45 |
| Abrupt expansion | 1 | $K_e = (1 - \beta_e)^2$, $\beta_e = 0.001$ | 1.00 |
| Total | | | $K_{\mathrm{minor}} = 5.39$ |

Table D.1: Minor-loss coefficients used in the HFE pressure-drop calculation. The coefficients are approximate tabulated engineering values; their contribution is small compared with the straight-pipe loss at the cold design point.

The numerical inputs are summarized in Table D.2.

| Quantity | Value | Basis |
|---|---|---|
| Volume flow | $\dot{V}_{\mathrm{HFE}} = 4\,\mathrm{L\,min^{-1}}$ | Design flow |
| HFE temperature | $T = -110\,^{\circ}\mathrm{C}$ | Cold design point |
| Tubing inner diameter | $D = 7.747\,\mathrm{mm}$ | Installed geometry |
| Nominal tank-path length | $L = 3.75\,\mathrm{m}$ | Installed geometry |
| HFE-7200 density | $\rho = 1734\,\mathrm{kg\,m^{-3}}$ | Property at $-110\,^{\circ}\mathrm{C}$ |
| HFE-7200 kinematic viscosity | $\nu = 28.35\,\mathrm{cSt}$ | Property at $-110\,^{\circ}\mathrm{C}$ |
| Minor-loss coefficient | $K_{\mathrm{minor}} = 5.39$ | Table D.1 |

Table D.2: Inputs for the HFE-7200 pressure-drop calculation at the cold design point.

The HFE density is evaluated at $-110\,^{\circ}\mathrm{C}$ using the manufacturer correlation, while the kinematic viscosity is obtained by log-linear interpolation of the manufacturer data described in Sec. 5.1.1. The geometric inputs are independent of temperature, and the minor-loss coefficients are treated as temperature-independent in this sizing model.

For the design flow,

$$\dot{V}_{\mathrm{HFE}} = 4\,\mathrm{L\,min^{-1}} = 6.667 \times 10^{-5}\,\mathrm{m^3\,s^{-1}}, \tag{D.8}$$

Eq. (D.2) gives

$$\bar{u} = 1.414\,\mathrm{m\,s^{-1}}, \qquad Re = 386, \qquad f_D = 0.166. \tag{D.9}$$

The corresponding straight-pipe and total loss coefficients are

$$f_D \frac{L}{D} = 80.2, \qquad K_{\mathrm{tot}} = f_D \frac{L}{D} + K_{\mathrm{minor}} = 85.6. \tag{D.10}$$

The velocity head at the design point is

$$\frac{\rho \bar{u}^2}{2} = 1.735 \times 10^3\,\mathrm{Pa}. \tag{D.11}$$

The straight-pipe and minor-loss contributions are

$$\Delta P_{\mathrm{pipe}} = 1.39\,\mathrm{bar}, \qquad \Delta P_{\mathrm{minor}} = 0.093\,\mathrm{bar}. \tag{D.12}$$

Substitution in Eq. (D.1) gives

$$\Delta P_{\mathrm{loop}} = 85.6 \frac{(1734\,\mathrm{kg\,m^{-3}})\,(1.414\,\mathrm{m\,s^{-1}})^2}{2} = 1.484\,\mathrm{bar} = 21.5\,\mathrm{psi}. \tag{D.13}$$

The straight-pipe term dominates the loss. Scaling $K_{\mathrm{minor}}$ by $\pm 30\%$ changes the result only to 1.46 bar to 1.51 bar, so the tubing inner diameter is the dominant parameter in the sizing calculation.

# Appendix E

# Preliminary Sizing of the $LN_2$ Heat Exchanger

This appendix gives the simplified model used to size the $LN_2$ heat-exchanger coil introduced in Sec. 5.2.5. The purpose of the calculation is to estimate the HFE-side tube length needed to remove the expected parasitic heat load while keeping the tube-wall temperature above a conservative freezing limit. The model is limited to the HFE side of the exchanger. It does not explicitly describe two-phase $LN_2$ flow, axial temperature gradients along the coil, changes in nitrogen-flow conditions, or local freezing and melting of HFE on the tube surface.

The design inputs are summarized in Table E.1. The heat leak is a rounded value based on the insulation estimate in Sec. 5.2.4. The wall temperature should be interpreted as the uniform HFE-side surface temperature assumed in the model, rather than the local $LN_2$ temperature.

| Quantity | Value |
|---|---|
| Target HFE bulk temperature | $T_{\mathrm{target}} = -110\,^{\circ}\mathrm{C}$ |
| Minimum wall temperature | $T_{\mathrm{freeze}} = -121\,^{\circ}\mathrm{C}$ |
| Ambient temperature | $T_{\mathrm{amb}} = 25\,^{\circ}\mathrm{C}$ |
| Design heat leak | $\dot{Q}_{\mathrm{leak}} = 200\,\mathrm{W}$ |
| Tube outside diameter | $d_o = 6.35\,\mathrm{mm}$ |
| HFE-side heat-transfer coefficient | $h_{\mathrm{HFE}} = 250\,\mathrm{W\,m^{-2}\,K^{-1}}$ |

Table E.1: Inputs used for the preliminary $LN_2$ heat-exchanger sizing model.

For a tube of outside diameter $d_o$ and length $L$, the outside heat-transfer area is

$$A_o = \pi d_o L. \tag{E.1}$$

The heat-removal rate from the HFE bulk liquid to the tube wall is estimated using the Newton-law form for convective heat transfer [98],

$$\dot{Q}_{\mathrm{HX}} = h_{\mathrm{HFE}} A_o \left(T_{\mathrm{bulk}} - T_{\mathrm{wall}}\right) = h_{\mathrm{HFE}} \pi d_o L \left(T_{\mathrm{bulk}} - T_{\mathrm{wall}}\right), \tag{E.2}$$

where $h_{\mathrm{HFE}}$ is an effective HFE-side heat-transfer coefficient. At the limiting design point, $T_{\mathrm{bulk}} = T_{\mathrm{target}}$ and $T_{\mathrm{wall}} = T_{\mathrm{freeze}}$. Requiring $\dot{Q}_{\mathrm{HX}} \geq \dot{Q}_{\mathrm{leak}}$ gives

$$L_{\mathrm{req}} = \frac{\dot{Q}_{\mathrm{leak}}}{\pi d_o h_{\mathrm{HFE}} \left(T_{\mathrm{target}} - T_{\mathrm{freeze}}\right)}. \tag{E.3}$$

The HFE-side coefficient was estimated with the Churchill–Bernstein correlation for cross-flow over a cylinder [98],

$$Nu_D = 0.3 + \frac{0.62 Re_D^{1/2} Pr^{1/3}}{\left[1 + (0.4/Pr)^{2/3}\right]^{1/4}} \left[1 + \left(\frac{Re_D}{282000}\right)^{5/8}\right]^{4/5}, \qquad h_{\mathrm{HFE}} = \frac{Nu_D k}{D}. \tag{E.4}$$

The low-temperature $Pr$ and $k$ inputs were taken from Graham Corporation helical heat-exchanger tests with HFE-7000 and $LN_2$ cooling, which report $Pr = 46$ and $k = 0.0974\,\mathrm{W\,m^{-1}\,K^{-1}}$ at $-90\,^{\circ}\mathrm{C}$ [102]. These values were used as representative HFE properties because direct HFE-7200 heat-transfer data near $-110\,^{\circ}\mathrm{C}$ were not available. The Reynolds number was set to $Re_D = 50$ as a conservative weak-mixing condition, rather than as a measured flow state. With $D = 6.35\,\mathrm{mm}$,

$$Nu_D = 15.9, \qquad h_{\mathrm{HFE}} = \frac{(15.9)(0.0974\,\mathrm{W\,m^{-1}\,K^{-1}})}{6.35 \times 10^{-3}\,\mathrm{m}} = 244\,\mathrm{W\,m^{-2}\,K^{-1}}. \tag{E.5}$$

The value used in the sizing calculation was rounded to

$$h_{\mathrm{HFE}} = 250\,\mathrm{W\,m^{-2}\,K^{-1}}. \tag{E.6}$$

Substituting the design values into Eq. (E.3) gives

$$L_{\mathrm{req}} = \frac{200\,\mathrm{W}}{\pi\,(6.35 \times 10^{-3}\,\mathrm{m})\,(250\,\mathrm{W\,m^{-2}\,K^{-1}})\,(11\,\mathrm{K})} = 3.65\,\mathrm{m}. \tag{E.7}$$

The dependence on the assumed HFE-side coefficient is shown in Fig. E.1. The inverse scaling follows directly from Eq. (E.3): weaker mixing or lower HFE-side heat transfer increases the required tube length.

The cooldown time was then estimated with a lumped-capacitance energy balance, in which the HFE inventory and cold stainless-steel hardware are described by a single bulk temperature $T(t)$ [98]:

$$C\frac{dT}{dt} = UA_{\mathrm{amb}}\left(T_{\mathrm{amb}} - T\right) - UA_{\mathrm{HX}}\left(T - T_{\mathrm{freeze}}\right). \tag{E.8}$$

The heat-transfer coefficients entering this estimate are

$$UA_{\mathrm{HX}} = h_{\mathrm{HFE}} \pi d_o L, \qquad UA_{\mathrm{amb}} = \frac{200\,\mathrm{W}}{T_{\mathrm{amb}} - T_{\mathrm{target}}}. \tag{E.9}$$

The HFE thermal capacitance was computed from the cooled HFE inventory estimated from the room-temperature filling and recovery measurements,

$$V_{\mathrm{HFE}} = V_{\mathrm{cooled}} = 3.0 \pm 0.2\,\mathrm{L}. \tag{E.10}$$

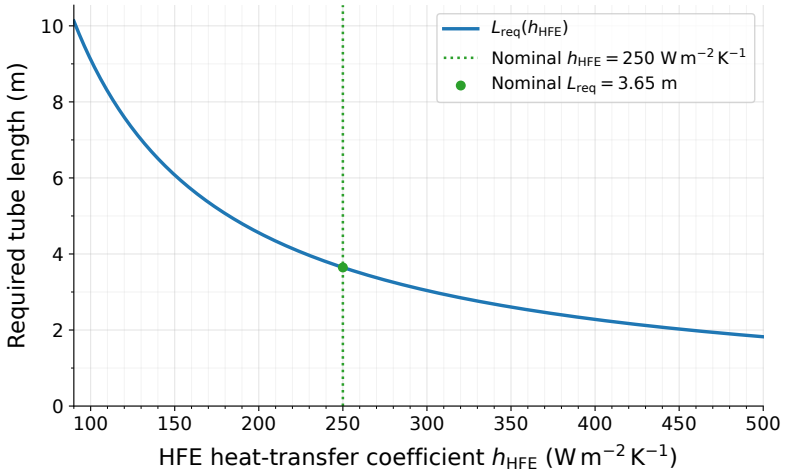


Figure E.1: Required heat-exchanger tube length as a function of the assumed HFE-side heat-transfer coefficient. The nominal design point is $h_{\mathrm{HFE}} = 250\,\mathrm{W\,m^{-2}\,K^{-1}}$, giving $L_{\mathrm{req}} = 3.65\,\mathrm{m}$.

This value excludes the gas trap and the transfer-line inventory not expected to be cooled during operation. For this fixed cooled volume, the HFE-7200 density law gives

$$m(25\,^{\circ}\mathrm{C}) = 4.3 \pm 0.3\,\mathrm{kg}, \qquad m(-110\,^{\circ}\mathrm{C}) = 5.2 \pm 0.3\,\mathrm{kg}. \tag{E.11}$$

The HFE contribution to the thermal capacitance in Eq. (E.8) is

$$C_{\mathrm{HFE}} = V_{\mathrm{HFE}}\overline{\rho c_p}, \tag{E.12}$$

with the average volumetric heat capacity defined as

$$\overline{\rho c_p} = \frac{1}{T_0 - T_{\mathrm{target}}} \int_{T_{\mathrm{target}}}^{T_0} \rho_{7200}(T) c_{p,7200}(T)\, dT. \tag{E.13}$$

The HFE-7200 heat capacity was anchored to $c_p(25\,^{\circ}\mathrm{C}) = 1220\,\mathrm{J\,kg^{-1}\,K^{-1}}$ and scaled using the HFE-7000 temperature dependence. Over the interval from $25\,^{\circ}\mathrm{C}$ to $-110\,^{\circ}\mathrm{C}$, this gives

$$\overline{c_p} = 1025\,\mathrm{J\,kg^{-1}\,K^{-1}}, \qquad \overline{\rho c_p} = 1.608\,\mathrm{MJ\,m^{-3}\,K^{-1}}. \tag{E.14}$$

Using $V_{\mathrm{HFE}} = 3.0 \pm 0.2\,\mathrm{L}$ gives

$$C_{\mathrm{HFE}} = 4.8 \pm 0.3\,\mathrm{kJ\,K^{-1}}. \tag{E.15}$$

The cold stainless-steel mass is $m_{\mathrm{SS}} = 22.79 \pm 0.47\,\mathrm{kg}$, as summarized in Table 5.20. Its heat capacity is temperature dependent over this cooldown [109, 116]. The interval-averaged value is

$$\overline{c_{p,\mathrm{SS}}} = \frac{1}{T_0 - T_{\mathrm{target}}} \int_{T_{\mathrm{target}}}^{T_0} c_{p,\mathrm{SS}}(T)\, dT \simeq 440\,\mathrm{J\,kg^{-1}\,K^{-1}}. \tag{E.16}$$

The 304 and 316 averages differ by less than 2% over this interval; $440\,\mathrm{J\,kg^{-1}\,K^{-1}}$ is used for the mixed stainless-steel hardware. Assigning a conservative 5% material-property uncertainty gives

$$C_{\mathrm{SS}} = m_{\mathrm{SS}}\overline{c_{p,\mathrm{SS}}} = 10.0 \pm 0.6\,\mathrm{kJ\,K^{-1}}. \tag{E.17}$$

The total interval-averaged thermal capacitance used in the analytic cooldown estimate is therefore

$$C = C_{\mathrm{HFE}} + C_{\mathrm{SS}} = 14.8 \pm 0.6\,\mathrm{kJ\,K^{-1}}. \tag{E.18}$$

At the target temperature, the cooldown estimate with $L = 6.0\,\mathrm{m}$ gives a heat-exchanger removal rate of about 329 W, compared with the 200 W design heat leak. The system therefore cools toward an equilibrium bulk temperature slightly below the target,

$$T_{\mathrm{eq}} \simeq -114.1\,^{\circ}\mathrm{C}. \tag{E.19}$$

The estimated cooldown time from $25\,^{\circ}\mathrm{C}$ to $-110\,^{\circ}\mathrm{C}$ is

$$t_{\mathrm{cool}} \simeq 27.6 \pm 1.2\,\mathrm{min}. \tag{E.20}$$

Using a latent-only $\mathrm{LN_2}$ enthalpy of $165\,\mathrm{kJ\,kg^{-1}}$, the corresponding nitrogen use is

$$m_{\mathrm{LN2}} \simeq 13.5 \pm 0.6\,\mathrm{kg}, \qquad \dot{V}_{\mathrm{LN2,hold}} \simeq 0.090\,\mathrm{L\,min^{-1}}, \tag{E.21}$$

to reach the target and to hold a 200 W heat load, respectively.

# Appendix F

# Purification Model Solution

This appendix gives the solution of the purification equation used in Sec. 3.1.3. The $O_2$-equivalent impurity concentration in the liquid xenon is denoted $c(t)$, the total $O_2$-equivalent molar source rate is $J(t)$, and the LXe-equivalent recirculation flow is $F_{\mathrm{LXe}}$. The liquid xenon volume is

$$V_{\mathrm{LXe}} = \frac{m_{\mathrm{Xe}}}{\rho_{\mathrm{LXe}}^{\mathrm{enr}}}. \tag{F.1}$$

The impurity balance is

$$V_{\mathrm{LXe}} \frac{dc(t)}{dt} = J(t) - \eta F_{\mathrm{LXe}} c(t) + F_{\mathrm{LXe}} c^{\mathrm{clean}}. \tag{F.2}$$

Here $\eta$ is the fraction of the incoming impurity concentration removed by the purifier in one pass, and $c^{\mathrm{clean}}$ is the $O_2$-equivalent concentration returned by the purified xenon stream.

For a constant source rate $J(t) = J$, Eq. (F.2) can be written as

$$\frac{dc(t)}{dt} + \frac{\eta F_{\mathrm{LXe}}}{V_{\mathrm{LXe}}} c(t) = \frac{J + F_{\mathrm{LXe}} c^{\mathrm{clean}}}{V_{\mathrm{LXe}}}. \tag{F.3}$$

The steady-state solution is obtained by setting $dc/dt = 0$:

$$c_\infty = \frac{J + F_{\mathrm{LXe}} c^{\mathrm{clean}}}{\eta F_{\mathrm{LXe}}}. \tag{F.4}$$

Subtracting $c_\infty$ from Eq. (F.3) gives the homogeneous equation for $c(t) - c_\infty$:

$$\frac{d}{dt}\left[c(t) - c_\infty\right] = -\frac{\eta F_{\mathrm{LXe}}}{V_{\mathrm{LXe}}}\left[c(t) - c_\infty\right]. \tag{F.5}$$

The solution is therefore

$$c(t) = c_\infty + \left[c(0) - c_\infty\right] \exp\left(-\frac{\eta F_{\mathrm{LXe}}}{V_{\mathrm{LXe}}} t\right). \tag{F.6}$$

Defining the purification time constant as

$$t_{\mathrm{pur}} = \frac{V_{\mathrm{LXe}}}{\eta F_{\mathrm{LXe}}}, \tag{F.7}$$

the solution becomes

$$c(t) = c_\infty + [c(0) - c_\infty] \exp\left(-\frac{t}{t_{\text{pur}}}\right). \tag{F.8}$$

For the baseline case used in Sec. 3.1.3, the source rate is set to the allowed value, with $c^{\text{clean}} \simeq 0$ and $\eta = 1$, so that $c_\infty = c_\infty^{\max} = c_{\text{O}_2,\text{eq}}^{\max}$. In that case $t_{\text{pur}} = t_{\text{rec}}$, and the normalized evolution is

$$\frac{c(t)}{c_\infty^{\max}} = 1 + \left[\frac{c(0)}{c_\infty^{\max}} - 1\right] \exp\left(-\frac{t}{t_{\text{rec}}}\right). \tag{F.9}$$

This expression is valid for any initial impurity concentration. If $c(0) > c_\infty^{\max}$, purification reduces the concentration toward the allowed steady-state value; if $c(0) < c_\infty^{\max}$, the concentration increases toward the same steady state because of the continuous source term.

The same solution gives the source-rate condition used in Sec. 3.1.3. Requiring $c_\infty \leq c_{\text{O}_2,\text{eq}}^{\max}$ gives

$$\frac{J + F_{\text{LXe}} c^{\text{clean}}}{\eta F_{\text{LXe}}} \leq c_{\text{O}_2,\text{eq}}^{\max}. \tag{F.10}$$

Solving for the allowed source rate gives

$$J^{\max} = F_{\text{LXe}} \left(\eta c_{\text{O}_2,\text{eq}}^{\max} - c^{\text{clean}}\right). \tag{F.11}$$

Using $c_{\text{O}_2,\text{eq}}^{\max} = 1/(k_{\text{O}_2}\tau_e)$, this can also be written as

$$J^{\max} = F_{\text{LXe}} \left(\frac{\eta}{k_{\text{O}_2}\tau_e} - c^{\text{clean}}\right). \tag{F.12}$$

In the limit $c^{\text{clean}} \simeq 0$, this reduces to

$$J^{\max} \simeq \frac{\eta F_{\text{LXe}}}{k_{\text{O}_2}\tau_e}. \tag{F.13}$$

# Appendix G

# Diffusion Model Details

## G.1 Initial Bulk Concentration

The initial bulk concentration $c_0$ of a dissolved gas can be estimated from the gas solubility and the partial pressure during exposure. Let $S$ be the solubility expressed as the volume of gas at STP dissolved per unit volume of solid for the pure gas at reference pressure $P_{\text{ref}}$. For a material exposed to air, the gas partial pressure is

$$p = \alpha P_{\text{atm}}, \tag{G.1}$$

where $\alpha$ is the gas abundance in air.

Assuming Henry-law scaling with partial pressure, the equivalent gas volume at STP dissolved in a material volume $V_{\text{mat}}$ is

$$V_{\text{gas}}^{\text{STP}} = V_{\text{mat}} S \frac{\alpha P_{\text{atm}}}{P_{\text{ref}}}. \tag{G.2}$$

The corresponding number of molecules is

$$N_0 = \frac{V_{\text{gas}}^{\text{STP}}}{V_{\text{mol}}^{\text{STP}}} N_A. \tag{G.3}$$

Dividing by the material volume gives the initial bulk concentration,

$$c_0 = \frac{N_0}{V_{\text{mat}}} = S \frac{\alpha P_{\text{atm}}}{P_{\text{ref}}} \frac{N_A}{V_{\text{mol}}^{\text{STP}}}. \tag{G.4}$$

If the solubility is quoted for the pure gas at 1 atm and the material was exposed to air at 1 atm, then $P_{\text{atm}} = P_{\text{ref}}$, and Eq. (G.4) reduces to

$$c_0 = S\alpha \frac{N_A}{V_{\text{mol}}^{\text{STP}}}. \tag{G.5}$$

Using $V_{\text{mol}}^{\text{STP}} = 2.2414 \times 10^{-2}\,\text{m}^3\,\text{mol}^{-1}$, Eq. (G.4) gives $c_0$ in $\text{m}^{-3}$. Equivalently, using $V_{\text{mol}}^{\text{STP}} = 2.2414 \times 10^{4}\,\text{cm}^3\,\text{mol}^{-1}$ gives $c_0$ in $\text{cm}^{-3}$. For oxygen in air, $\alpha \simeq 0.21$. If a tabulated solubility already corresponds to air rather than to the pure gas, the factor $\alpha P_{\text{atm}}/P_{\text{ref}}$ should not be applied again.

## G.2 Finite-Slab Diffusion Solution

Consider a slab of thickness $d$ with uniform initial bulk concentration $c_0$. The coordinate $x$ runs from one exposed surface to the other. The diffusion-limited boundary condition is that the concentration at both exposed surfaces is zero for $t > 0$, meaning that molecules reaching the surface are removed faster than they are supplied from the bulk. The initial and boundary conditions are

$$c(x, 0) = c_0, \qquad 0 \le x \le d, \tag{G.6}$$

$$c(0, t) = c(d, t) = 0, \qquad t > 0. \tag{G.7}$$

The initial concentration $c_0$ is obtained from the material exposure history and solubility, as described in App. G.1.

The concentration evolves according to Fick's second law,

$$\frac{\partial c}{\partial t} = D \frac{\partial^2 c}{\partial x^2}, \tag{G.8}$$

where $D$ is assumed constant at the material temperature considered. Separation of variables gives

$$c(x, t) = \sum_{m=1}^{\infty} B_m \sin\left(\frac{m\pi x}{d}\right) \exp\left[-\left(\frac{m\pi}{d}\right)^2 Dt\right]. \tag{G.9}$$

Expanding the uniform initial concentration $c_0$ as a sine series gives

$$B_m = \frac{2}{d} \int_0^d c_0 \sin\left(\frac{m\pi x}{d}\right) dx = \frac{2c_0}{m\pi} \left[1 - (-1)^m\right]. \tag{G.10}$$

Only odd terms contribute. Writing $m = 2n + 1$, the concentration profile becomes

$$c(x, t) = \frac{4c_0}{\pi} \sum_{n=0}^{\infty} \frac{1}{2n+1} \sin\left[\frac{\pi(2n+1)x}{d}\right] \exp\left[-\left(\frac{\pi(2n+1)}{d}\right)^2 Dt\right]. \tag{G.11}$$

Integrating Eq. (G.11) over the slab thickness gives the remaining areal inventory,

$$\Sigma_{\text{rem}}(t) = \int_0^d c(x, t)\, dx \tag{G.12}$$

$$= \frac{4c_0}{\pi} \sum_{n=0}^{\infty} \frac{1}{2n+1} \exp\left[-\left(\frac{\pi(2n+1)}{d}\right)^2 Dt\right] \int_0^d \sin\left[\frac{\pi(2n+1)x}{d}\right] dx \tag{G.13}$$

$$= \frac{8c_0 d}{\pi^2} \sum_{n=0}^{\infty} \frac{1}{(2n+1)^2} \exp\left[-\left(\frac{\pi(2n+1)}{d}\right)^2 Dt\right]. \tag{G.14}$$

For a slab face of area $A_{\text{face}}$, the total number of molecules remaining in the slab is

$$N_{\text{rem}}(t) = A_{\text{face}} \Sigma_{\text{rem}}(t). \tag{G.15}$$

At $t = 0$, this reduces to $N_{\text{rem}}(0) = A_{\text{face}} d c_0$, since $\sum_{n=0}^{\infty} (2n+1)^{-2} = \pi^2/8$.

The molecular flux from the slab is obtained from Fick's first law. First, differentiating Eq. (G.11) gives

$$\frac{\partial c}{\partial x} = \frac{4c_0}{d} \sum_{n=0}^{\infty} \cos\left[\frac{\pi(2n+1)x}{d}\right] \exp\left[-\left(\frac{\pi(2n+1)}{d}\right)^2 Dt\right]. \tag{G.16}$$

At $x = 0$, the outward direction is $-x$, so the outward flux magnitude from one surface is

$$\phi_{\mathrm{diff}}(t) = D \left.\frac{\partial c}{\partial x}\right|_{x=0} = \frac{4c_0 D}{d} \sum_{n=0}^{\infty} \exp\left[-\left(\frac{\pi(2n+1)}{d}\right)^2 Dt\right]. \tag{G.17}$$

The same flux magnitude is obtained at the opposite face. Equation (G.17) gives a molecular flux in $\mathrm{m^{-2}\,s^{-1}}$ when $c_0$ is in $\mathrm{m^{-3}}$, $D$ is in $\mathrm{m^2\,s^{-1}}$, and $d$ is in m.

The total molecular source rate is

$$\dot{N}_{\mathrm{diff}}(t) = A_{\mathrm{out}} \phi_{\mathrm{diff}}(t), \tag{G.18}$$

where $A_{\mathrm{out}}$ is the total emitting area represented by the model. For a slab emitting from both faces, $A_{\mathrm{out}} = 2A_{\mathrm{face}}$. For a one-sided geometry, a different boundary condition should be used.

The pressure–volume throughput follows from the ideal gas law,

$$PV = nRT = \frac{N}{N_A} RT. \tag{G.19}$$

Using the LXe-equivalent convention adopted in the impurity budget,

$$\mathcal{Q}^{\mathrm{LXe}}_{\mathrm{diff}}(t) = \frac{\dot{N}_{\mathrm{diff}}(t)}{N_A} R_{\mathrm{PV}} T_{\mathrm{LXe}}, \tag{G.20}$$

where $R_{\mathrm{PV}} = 83.14\,\mathrm{mbar\,L\,mol^{-1}\,K^{-1}}$. Combining Eqs. (G.17)–(G.20) gives

$$\mathcal{Q}^{\mathrm{LXe}}_{\mathrm{diff}}(t) = \frac{c_0 A_{\mathrm{out}}}{N_A} R_{\mathrm{PV}} T_{\mathrm{LXe}} F_D(t), \tag{G.21}$$

with

$$F_D(t) = \frac{4D}{d} \sum_{n=0}^{\infty} \exp\left[-\left(\frac{\pi(2n+1)}{d}\right)^2 Dt\right]. \tag{G.22}$$

This is the expression used in Eq. (3.57) of the main text.

The characteristic diffusion time is

$$\tau_D = \frac{d^2}{\pi^2 D}. \tag{G.23}$$

For $t \lesssim 0.5\tau_D$, only the near-surface region is depleted, and

$$F_D(t) \simeq \sqrt{\frac{D}{\pi t}}. \tag{G.24}$$

For $t \gtrsim 0.5\tau_D$, the finite slab thickness becomes important. At sufficiently long times, the release rate is well approximated by

$$F_D(t) \simeq \frac{4D}{d} \exp\left(-\frac{\pi^2 Dt}{d^2}\right). \tag{G.25}$$

Thus the diffusion-limited release initially follows an approximately $t^{-1/2}$ decrease and later approaches an exponential depletion regime.

# Bibliography


[1] S. Navas et al. "Review of particle physics". In: *Physical Review D* 110.3 (2024). ISSN: 24700029. DOI: 10.1103/PhysRevD.110.030001.

[2] Peter W. Higgs. "Broken symmetries and the masses of gauge bosons". In: *Physical Review Letters* 13.16 (1964). ISSN: 00319007. DOI: 10.1103/PhysRevLett.13.508.

[3] Steven Weinberg. "A model of leptons". In: *Physical Review Letters* 19.21 (1967). ISSN: 00319007. DOI: 10.1103/PhysRevLett.19.1264.

[4] R. P. Feynman and M. Gell-Mann. "Theory of the fermi interaction". In: *Physical Review* 109.1 (1958). ISSN: 0031899X. DOI: 10.1103/PhysRev.109.193.

[5] E. C.G. Sudarshan and R. E. Marshak. *Chirality invariance and the universal Fermi interaction*. 1958. DOI: 10.1103/PhysRev.109.1860.2.

[6] Michael Peskin and Dan Schroeder. *An Introduction To Quantum Field Theory (Frontiers in Physics)*. 1995.

[7] Nicola Cabibbo. "Unitary symmetry and leptonic decays". In: *Physical Review Letters* 10.12 (1963). ISSN: 00319007. DOI: 10.1103/PhysRevLett.10.531.

[8] Makoto Kobayashi and Toshihide Maskawa. "CP -Violation in the Renormalizable Theory of Weak Interaction ". In: *Progress of Theoretical Physics* 49.2 (1973). ISSN: 0033-068X. DOI: 10.1143/ptp.49.652.

[9] Emmy Noether. "Invariant Variation Problems". In: *Transport Theory and Statistical Physics* (1971). ISSN: 15322424. DOI: 10.1080/00411457108231446.

[10] J Schechter and J W F Valle. "Neutrinoless double-beta decay in SU(2)xU(1) theories". In: *Phys. Rev. D* 25.11 (1982).

[11] Wolfgang Pauli. "Dear radioactive ladies and gentlemen". In: *Physics Today* 31.9 (1978).

[12] J. S. Nico. "Neutron beta decay". In: *Journal of Physics G: Nuclear and Particle Physics* 36.10 (2009). ISSN: 09543899. DOI: 10.1088/0954-3899/36/10/104001.

[13] E. Fermi. "Versuch einer Theorie der $\beta$-Strahlen. I". In: *Zeitschrift für Physik* 88.3-4 (1934). ISSN: 14346001. DOI: 10.1007/BF01351864.

[14] H. Bethe and R. Peierls. *The neutrino*. 1934. DOI: 10.1038/133689b0.

[15] C. L. Cowan et al. "Detection of the free neutrino: A confirmation". In: *Science* 124.3212 (1956). ISSN: 00368075. DOI: 10.1126/science.124.3212.103.

[16] F. J. Hasert et al. "Observation of neutrino-like interactions without muon or electron in the gargamelle neutrino experiment". In: *Physics Letters B* 46.1 (1973). ISSN: 03702693. DOI: 10.1016/0370-2693(73)90499-1.

[17] C. S. Wu et al. *Experimental test of parity conservation in beta decay*. 1957. DOI: 10.1103/PhysRev.105.1413.

[18] M. Goldhaber, L. Grodzins, and A. W. Sunyar. *Helicity of neutrinos*. 1958. DOI: 10.1103/PhysRev.109.1015.

[19] Steven Weinberg. "Baryon- and lepton-nonconserving processes". In: *Physical Review Letters* 43.21 (1979). ISSN: 00319007. DOI: 10.1103/PhysRevLett.43.1566.

[20] Ziro Maki, Masami Nakagawa, and Shoichi Sakata. "Remarks on the Unified Model of Elementary Particles". In: *Progress of Theoretical Physics* 28.5 (1962). ISSN: 0033-068X. DOI: 10.1143/ptp.28.870.

[21] S. M. Bilenky and S. T. Petcov. "Massive neutrinos and neutrino oscillations". In: *Reviews of Modern Physics* 59.3 (1987). ISSN: 00346861. DOI: 10.1103/RevModPhys.59.671.

[22] Y. Fukuda et al. "Evidence for oscillation of atmospheric neutrinos". In: *Physical Review Letters* 81.8 (1998). ISSN: 10797114. DOI: 10.1103/PhysRevLett.81.1562.

[23] Q. R. Ahmad et al. "Direct Evidence for Neutrino Flavor Transformation from Neutral-Current Interactions in the Sudbury Neutrino Observatory". In: *Physical Review Letters* 89.1 (2002). ISSN: 10797114. DOI: 10.1103/PhysRevLett.89.011301.

[24] K. Eguchi et al. "First results from KamLAND: Evidence for reactor antineutrino disappearance". In: *Physical Review Letters* 90.2 (2003). ISSN: 00319007. DOI: 10.1103/physrevlett.90.021802.

[25] F. P. An et al. "Observation of electron-antineutrino disappearance at Daya Bay". In: *Physical Review Letters* 108.17 (2012). ISSN: 00319007. DOI: 10.1103/PhysRevLett.108.171803.

[26] Ivan Esteban et al. "NuFit-6.0: updated global analysis of three-flavor neutrino oscillations". In: *Journal of High Energy Physics* 2024.12 (2025). ISSN: 10298479. DOI: 10.1007/JHEP12(2024)216.

[27] S. P. Mikheyev and A. Yu Smirnov. "Resonant amplification of $\nu$ oscillations in matter and solar-neutrino spectroscopy". In: *Il Nuovo Cimento C* 9.1 (1986). ISSN: 03905551. DOI: 10.1007/BF02508049.

[28] Angel Abusleme et al. *JUNO physics and detector*. 2022. DOI: 10.1016/j.ppnp.2021.103927.

[29] N. Aghanim et al. "Planck 2018 results: VI. Cosmological parameters". In: *Astronomy and Astrophysics* 641 (2020). ISSN: 14320746. DOI: 10.1051/0004-6361/201833910.

[30] Max Aker et al. "Direct neutrino-mass measurement based on 259 days of KATRIN data". In: *Science* 388.6743 (2025). ISSN: 10959203. DOI: 10.1126/science.adq9592.

[31] Ettore Majorana. "Teoria simmetrica dell'elettrone e del positrone". In: *Il Nuovo Cimento* 14.4 (1937). ISSN: 00296341. DOI: 10.1007/BF02961314.

[32] Murray Gell-Mann, Pierre Ramond, and Richard Slansky. "Complex Spinors and Unified Theories". In: *Murray Gell-Mann: Selected Papers*. Ed. by Harald Fritzsch. Vol. 40. World Scientific Series in 20th Century Physics. World Scientific, 2010, pp. 266–272. ISBN: 9789812836847. URL: https://doi.org/10.1142/9789812836854_0018.

[33] M. Goeppert-Mayer. "Double beta-disintegration". In: *Physical Review* 48.6 (1935). ISSN: 0031899X. DOI: 10.1103/PhysRev.48.512.

[34] W. H. Furry. "On transition probabilities in double beta-disintegration". In: *Physical Review* 56.12 (1939). ISSN: 0031899X. DOI: 10.1103/PhysRev.56.1184.

[35] J. B. Albert et al. "Search for $2\nu\beta\beta$ decay of Xe 136 to the 01+ excited state of Ba 136 with the EXO-200 liquid xenon detector". In: *Physical Review C* 93.3 (2016). ISSN: 24699993. DOI: 10.1103/PhysRevC.93.035501.

[36] B. Pritychenko and V. I. Tretyak. "Comprehensive review of $2\beta$ decay half-lives". In: *Atomic Data and Nuclear Data Tables* 161 (2025). ISSN: 10902090. DOI: 10.1016/j.adt.2024.101694.

[37] Masaru Doi, Tsuneyuki Kotani, and Eiichi Takasugi. "Double Beta Decay and Majorana Neutrino". In: *Progress of Theoretical Physics Supplement* 83 (1985). ISSN: 0375-9687. DOI: 10.1143/ptps.83.1.

[38] J. Kotila and F. Iachello. "Phase-space factors for double-$\beta$ decay". In: *Physical Review C - Nuclear Physics* 85.3 (2012). ISSN: 1089490X. DOI: 10.1103/PhysRevC.85.034316.

[39] Jonathan Engel and Javier Menéndez. *Status and future of nuclear matrix elements for neutrinoless double-beta decay: A review*. 2017. DOI: 10.1088/1361-6633/aa5bc5.

[40] Michael Jewell. "Search for Neutrinoless Double-Beta Decay with the EXO-200 Detector". PhD thesis. Stanford University, June 2020.

[41] H. Acharya et al. "First Results on the Search for Lepton Number Violating Neutrinoless Double-$\beta$ Decay with the LEGEND-200 Experiment". In: *Physical Review Letters* 136.2 (2026). ISSN: 10797114. DOI: 10.1103/25tk-nctn.

[42] S. Abe et al. “Search for Majorana Neutrinos with the Complete KamLAND-Zen Dataset”. In: *Physical Review Letters* 135.26 (2025). ISSN: 10797114. DOI: 10.1103/jkf6-48j8.

[43] D. Q. Adams et al. “Constraints on lepton number violation with the 2 tonne · year CUORE dataset”. In: *Science* 390.6777 (2025). ISSN: 10959203. DOI: 10.1126/science.adp6474.

[44] G. Anton et al. “Search for Neutrinoless Double-$\beta$ Decay with the Complete EXO-200 Dataset”. In: *Physical Review Letters* 123.16 (2019). ISSN: 10797114. DOI: 10.1103/PhysRevLett.123.161802.

[45] A. Agrawal et al. “Improved Limit on Neutrinoless Double Beta Decay of Mo 100 from AMoRE-I”. In: *Physical Review Letters* 134.8 (2025). ISSN: 10797114. DOI: 10.1103/PhysRevLett.134.082501.

[46] nEXO Collaboration et al. “nEXO Pre-Conceptual Design Report”. In: (May 2018). URL: http://arxiv.org/abs/1805.11142.

[47] G Adhikari et al. “nEXO: Neutrinoless double beta decay search beyond 10 to the power of 28 year half-life sensitivity”. In: *Journal of Physics G: Nuclear and Particle Physics* 49.1 (Jan. 2022), p. 015104. ISSN: 1361-6471. DOI: 10.1088/1361-6471/ac3631. URL: https://arxiv.org/abs/2106.16243.

[48] E. Aprile and T. Doke. “Liquid xenon detectors for particle physics and astrophysics”. In: *Reviews of Modern Physics* 82.3 (2010). ISSN: 00346861. DOI: 10.1103/RevModPhys.82.2053.

[49] E. Aprile et al. “The XENON1T dark matter experiment”. In: *European Physical Journal C* 77.12 (2017). ISSN: 14346052. DOI: 10.1140/epjc/s10052-017-5326-3.

[50] M. Auger et al. “The EXO-200 detector, part I: Detector design and construction”. In: *Journal of Instrumentation* 7.5 (2012). ISSN: 17480221. DOI: 10.1088/1748-0221/7/05/P05010.

[51] J. B. Albert et al. “Improved measurement of the $2\nu\beta\beta$ half-life of 136 Xe with the EXO-200 detector”. In: *Physical Review C - Nuclear Physics* 89.1 (2014). ISSN: 1089490X. DOI: 10.1103/PhysRevC.89.015502.

[52] Lucia Votano. “Underground laboratories”. In: *Proceedings of the 6th Patras Workshop on Axions, WIMPs and WISPs, PATRAS 2010*. 2010. DOI: 10.21468/scipostphysproc.12.007.

[53] M. Jewell et al. “Characterization of an Ionization Readout Tile for nEXO”. In: *Journal of Instrumentation* 13.1 (2018). ISSN: 17480221. DOI: 10.1088/1748-0221/13/01/P01006.

[54] Z. Li et al. “Simulation of charge readout with segmented tiles in nEXO”. In: *Journal of Instrumentation* 14.9 (2019). ISSN: 17480221. DOI: 10.1088/1748-0221/14/09/P09020.

[55] A. Jamil et al. "VUV-Sensitive Silicon Photomultipliers for Xenon Scintillation Light Detection in nEXO". In: *IEEE Transactions on Nuclear Science* 65.11 (2018). ISSN: 00189499. DOI: 10.1109/TNS.2018.2875668.

[56] G. Gallina et al. "Performance of novel VUV-sensitive Silicon Photo-Multipliers for nEXO". In: *European Phys. Journal C* 82.12 (2022). ISSN: 14346052. DOI: 10.1140/epjc/s10052-022-11072-8.

[57] I. Ostrovskiy et al. "Characterization of Silicon Photomultipliers for nEXO". In: *IEEE Transactions on Nuclear Science* 62.4 (2015). ISSN: 00189499. DOI: 10.1109/TNS.2015.2453932.

[58] G. Anton et al. "Measurement of the scintillation and ionization response of liquid xenon at MeV energies in the EXO-200 experiment". In: *Physical Review C* 101.6 (2020). ISSN: 24699993. DOI: 10.1103/PhysRevC.101.065501.

[59] G. Gallina et al. "Characterization of the Hamamatsu VUV4 MPPCs for nEXO". In: *Nuclear Instruments and Methods in Physics Research, Section A: Accelerators, Spectrometers, Detectors and Associated Equipment* 940 (2019). ISSN: 01689002. DOI: 10.1016/j.nima.2019.05.096.

[60] S. Sangiorgio. *Multi-parametric Sensitivity Study and Sensitivity-derived Requirements (NEXO-12211)*. Tech. rep. nEXO Collaboration, Oct. 2022.

[61] A Belley et al. *Ab initio calculations of neutrinoless $\beta\beta$ decay refine neutrino mass limits*. 2023. DOI: 10.48550/arXiv.2307.15156. URL: https://arxiv.org/abs/2307.15156.

[62] Antoine Belley. "Probing beyond standard model physics through ab initio calculations of exotic weak processes in atomic nuclei". PhD thesis. University of British Columbia, 2024. DOI: 10.14288/1.0445137. URL: https://doi.org/10.14288/1.0445137.

[63] N. Abgrall et al. *The large enriched germanium experiment for neutrinoless $\beta\beta$ decay LEGEND-1000 preconceptual design report*. 2021.

[64] CUPID Interest Group. *CUPID pre-CDR*. 2019. DOI: 10.48550/arXiv.1907.09376. URL: https://arxiv.org/abs/1907.09376.

[65] SNO+ Collaboration. "The SNO+ Experiment". In: *Journal of Instrumentation* 16.08 (2021), P08059. DOI: 10.1088/1748-0221/16/08/P08059. URL: https://doi.org/10.1088/1748-0221/16/08/P08059.

[66] Nina Burlac. "Early results of the LEGEND-200 experiment". In: *Nuclear Instruments and Methods in Physics Research, Section A: Accelerators, Spectrometers, Detectors and Associated Equipment* 1080 (2025). ISSN: 01689002. DOI: 10.1016/j.nima.2025.170779.

[67] K. Alfonso et al. "Sensitivity of the CUPID experiment to $0\nu\beta\beta$ decay of 100Mo". In: (Feb. 2026). URL: http://arxiv.org/abs/2504.14369.

[68] K. Asakura et al. "Results from KamLAND-Zen". In: *AIP Conference Proceedings*. Vol. 1666. 2015. DOI: 10.1063/1.4915593.

[69] J. Martín-Albo et al. “Sensitivity of NEXT-100 to neutrinoless double beta decay”. In: *Journal of High Energy Physics* 2016.5 (2016). ISSN: 10298479. DOI: 10.1007/JHEP05(2016)159.

[70] George Bakale, Ulrich Sowada, and Werner F. Schmidt. “Effect of an electric field on electron attachment to sulfur hexafluoride, nitrous oxide, and molecular oxygen in liquid argon and xenon”. In: *The Journal of Physical Chemistry* 80.23 (1976). ISSN: 0022-3654. DOI: 10.1021/j100564a006.

[71] Y. Li et al. “Parameterization of electron attachment rate constants for impurities in LArTPC detectors”. In: *Journal of Instrumentation* 17.11 (2022). ISSN: 17480221. DOI: 10.1088/1748-0221/17/11/T11007.

[72] Ako Jamil. “Rare Event Searches in Liquid Xenon with EXO-200, nEXO and Beyond”. PhD thesis. Yale: Yale University, Dec. 2022.

[73] G. Plante et al. “Liquid-phase purification for multi-tonne xenon detectors”. In: *European Physical Journal C* 82.10 (2022). ISSN: 14346052. DOI: 10.1140/epjc/s10052-022-10832-w.

[74] E. Aprile et al. “The XENONnT dark matter experiment”. In: *The European Physical Journal C* 84.8 (Aug. 2024), p. 784. ISSN: 1434-6052. DOI: 10.1140/epjc/s10052-024-12982-5.

[75] Peter Rowson. *Simple Model of Xenon Purification in EXO-200*. Tech. rep. SLAC, Mar. 2022.

[76] John F. O’hanlon and Timothy A. Gessert. *A Users Guide to Vacuum Technology, Fourth Edition*. 2023. DOI: 10.1002/9781394174232.

[77] Sergio Giacomo Sammartano. *Outgassing Rates of PEEK, Kapton® and Vespel® Polymers*. 2020.

[78] P. Chiggiato. “Vacuum technology for ion sources”. In: *CAS-CERN Accelerator School: Ion Sources - Proceedings*. 2013. DOI: 10.5170/CERN-2013-007.463.

[79] N. T.S. Evans and T. H. Quinton. “Permeability and diffusion coefficient of oxygen in membranes for oxygen electrodes”. In: *Respiration Physiology* 35.1 (1978). ISSN: 00345687. DOI: 10.1016/0034-5687(78)90044-0.

[80] a Teverovsky. “A Rapid Technique for Moisture Diffusion Characterization of Molding Compounds in PEMs”. In: *EEE Links, NASA/GSFC* January, V.D (2003).

[81] D. W. Van Krevelen. *Properties of Polymers: Their Correlation with Chemical Structure; their Numerical Estimation and Prediction from Additive Group Contributions: Fourth Edition*. 2009.

[82] Evan Angelico et al. “A flexible test facility for liquid xenon detector development”. In: *Journal of Instrumentation* 20.11 (2025). ISSN: 17480221. DOI: 10.1088/1748-0221/20/11/p11005.

[83] Rebecca Grinham and Andrew Chew. "A Review of Outgassing and Methods for its Reduction". In: *Applied Science and Convergence Technology* 26.5 (2017). DOI: 10.5757/asct.2017.26.5.95.

[84] T. J. Roosendaal et al. "Ultra-pure nickel for structural components of low-radioactivity instruments". In: *Nuclear Instruments and Methods in Physics Research, Section A: Accelerators, Spectrometers, Detectors and Associated Equipment* 1087 (2026). ISSN: 01689002. DOI: 10.1016/j.nima.2026.171402.

[85] National Nuclear Data Center. *NuDat 2 Database*. 2025. URL: https://www.nndc.bnl.gov/nudat2/.

[86] R. H.M. Tsang et al. "An integrated online radioassay data storage and analytics tool for nEXO". In: *Nuclear Instruments and Methods in Physics Research, Section A: Accelerators, Spectrometers, Detectors and Associated Equipment* 1055 (2023). ISSN: 01689002. DOI: 10.1016/j.nima.2023.168477.

[87] William H Greene. *Econometric Analysis*. 5th ed. Upper Saddle River, NJ: Prentice Hall, 2003. ISBN: 9780130661890.

[88] R MacLellan et al. *The nEXO Radioassay Program*. 2026. DOI: 10.48550/arXiv.2604.15406. URL: https://arxiv.org/abs/2604.15406.

[89] M.J. Berger et al. *XCOM: Photon Cross Section Database*. 1999. URL: https://www.nist.gov/pml/xcom-photon-cross-sections-database.

[90] M. Anderson et al. "Search for invisible modes of nucleon decay in water with the SNO+ detector". In: *Physical Review D* 99.3 (2019). ISSN: 24700029. DOI: 10.1103/PhysRevD.99.032008.

[91] D. S. Akerib et al. "Identification of radiopure titanium for the LZ dark matter experiment and future rare event searches". In: *Astroparticle Physics* 96 (2017). ISSN: 09276505. DOI: 10.1016/j.astropartphys.2017.09.002.

[92] Richard Budynas and J. Keith Nisbett. *Shigley's Mechanical Engineering Design*. Vol. New York. 2015.

[93] M Chase. *NIST-JANAF Thermochemical Tables, 4th Edition*. 1998.

[94] 3M. *3M Novec 7000 Engineered Fluid*. Tech. rep. St. Paul, MN: 3M Electronics Materials Solutions Division, Sept. 2021.

[95] 3M. *3M Novec 7200 Engineered Fluid*. Tech. rep. St. Paul, MN: 3M Electronics Materials Solutions Division, Sept. 2009.

[96] Christopher J. Seeton. "Viscosity-temperature correlation for liquids". In: *Tribology Letters* 22.1 (2006). ISSN: 10238883. DOI: 10.1007/s11249-006-9071-2.

[97] G W H Höhne, W F Hemminger, and H.-J. Flammersheim. *Differential Scanning Calorimetry*. 2nd ed. Berlin, Heidelberg: Springer, 2003. ISBN: 9783540004677. DOI: 10.1007/978-3-662-06710-9.

[98] Theodore L Bergman et al. *Fundamentals of Heat and Mass Transfer*. 7th ed. Hoboken, NJ: John Wiley & Sons, 2011. ISBN: 9780470501979.

[99] Baggie W. Nyande et al. *Crystallization in the presence of impurities: mechanisms, models and controls*. 2025. DOI: 10.1016/j.cherd.2025.08.002.

[100] John Richards. *Centrifugal Pumps: An Essay on Their Construction and Operation, and Some Account of the Origin and Development in This and Other Countries*. New York: The Industrial Publishing Company, 1894.

[101] Rbalieiro. *Gear pump.svg*. 2025.

[102] Jim Lines. "How low can you go?" In: *Chemical Processing* 66.1 (2003). ISSN: 00092630.

[103] John F O'Hanlon. *A User's Guide to Vacuum Technology*. 3rd ed. Hoboken, NJ: John Wiley & Sons, 2003. ISBN: 9780471270522. DOI: 10.1002/0471467162.

[104] Stephen J. Chapman. *Electric Machinery Fundamentals*. 5th ed. New York: McGraw-Hill Education, 2012.

[105] HyunWoo Yang, Ho Sung Jang, and Sangwon Ji. "Volumetric Efficiency Prediction of External Gear Pumps Using a Leakage Model Based on Dynamic Clearances". In: *Actuators* 15.1 (2026). ISSN: 20760825. DOI: 10.3390/act15010056.

[106] F Edler et al. *Guide to Secondary Thermometry. Thermocouple Thermometry*. Tech. rep. 2021.

[107] Barry N Taylor and Chris E Kuyatt. "NIST Technical Note 1297 1994 Edition, Guidelines for Evaluating and Expressing the Uncertainty of NIST Measurement Results". In: *National Institute of Standards and Technology* (1994).

[108] NIST Standard Reference Data Program. *Thermophysical Properties of Fluid Systems - NIST Chemistry WebBook*. 2025.

[109] National Institute of Standards and Technology. *Material Properties: 304 Stainless (UNS S30400)*. URL: https://trc.nist.gov/cryogenics/materials/304Stainless/304Stainless_rev.htm.

[110] O. C. Bridgeman and E. W. Aldrich. "Vapor pressure tables for water". In: *Journal of Heat Transfer* 86.2 (1964). ISSN: 15288943. DOI: 10.1115/1.3687121.

[111] B. Aharmim et al. "Measurement of the $\nu$e and total 8B solar neutrino fluxes with the Sudbury Neutrino Observatory phase-III data set". In: *Phys. Rev. C - Nuclear Physics* 87.1 (2013). ISSN: 1089490X. DOI: 10.1103/PhysRevC.87.015502.

[112] A. Allega et al. "Improved search for invisible modes of nucleon decay in water with the SNO+ detector". In: *Physical Review D* 105.11 (2022). ISSN: 24700029. DOI: 10.1103/PhysRevD.105.112012.

[113] B. Wang et al. “Measurement of the radon concentration in the ultrapure water of the JUNO-LS UPW system”. In: *Journal of Instrumentation* 20.3 (2025). ISSN: 17480221. DOI: 10.1088/1748-0221/20/03/P03028.

[114] Frank M White. *Fluid Mechanics*. 6th ed. New York: McGraw-Hill, 2008. ISBN: 9780072938449.

[115] CraneCo. *Flow of fluids through valves, fittings and pipe. Technical Paper No. 410*. 1988.

[116] National Institute of Standards and Technology. *Material Properties: 316 Stainless*. URL: https://trc.nist.gov/cryogenics/materials/316Stainless/316Stainless_rev.htm.

COLLEGE DOCTORAL PAYS DE LA LOIRE
ED MATIERE, MOLECULES MATERIAUX ET GEOSCIENCES

IMT Atlantique
Bretagne-Pays de la Loire
École Mines-Télécom

Titre : **Contrôle des impuretés et des bruits de fond radioactifs dans un détecteur cryogénique $0\nu\beta\beta$ au xénon liquide**

Mots clés : **double désintégration bêta sans neutrinos ; xénon liquide ; chambre à projection temporelle ; nEXO ; dégazage ; radiopureté ; blindage ; HFE**

Résumé : La nature des neutrinos reste encore mal connue. Bien que les oscillations aient établi qu'ils sont massifs, leur masse absolue demeure indéterminée. La désintégration $0\nu\beta\beta$ constitue une sonde particulièrement prometteuse : son observation démontrerait une violation du nombre leptonique, établirait la nature de Majorana des neutrinos et pourrait aider à mieux comprendre l'asymétrie entre matière et antimatière dans l'Univers. Le $^{136}$Xe est particulièrement adapté à cette recherche, car il est à la fois un isotope émetteur double bêta et un milieu de détection efficace. Une chambre à projection temporelle remplie de xénon liquide produit un signal lumineux et un signal d'ionisation permettant d'identifier les interactions ayant lieu dans le détecteur. L'expérience nEXO repose sur ce principe et vise à améliorer de deux ordres de grandeur la sensibilité actuelle à la recherche de $0\nu\beta\beta$. Atteindre cet objectif nécessite une reconstruction précise de l'énergie et un environnement à très faible bruit de fond. La précision de cette mesure est affectée par la concentration en impuretés électronégatives dans le xénon, qui peuvent capturer les électrons pendant leur dérive ; un modèle a donc été développé pour quantifier leur effet et orienter la construction et le fonctionnement de l'instrument. L'environnement à très faible bruit de fond impose également une conception spécifique du détecteur. Cette thèse étudie l'utilisation de nickel et l'évolution de la géométrie du cryostat afin d'optimiser la conception de base du détecteur. Le fluide cryogénique entourant la TPC, le HFE, doit quant à lui assurer à la fois le blindage radiologique et la stabilité cryogénique. Particulièrement adapté puisqu'il reste liquide à température ambiante comme à celle du xénon liquide, le HFE a été étudié au moyen d'un banc d'essai de refroidissement et de recirculation afin de caractériser son comportement à basse température.

Title: **Impurities & Radioactive Background Control in a Cryogenic Liquid-Xenon $0\nu\beta\beta$ Rare-Event Detector**

Keywords: **neutrinoless double beta decay; liquid xenon; time projection chamber; nEXO; outgassing; radiopurity; shielding; HFE**

Abstract: The nature of neutrinos remains incompletely understood. Although neutrino oscillations have established that they are massive, their absolute mass scale remains undetermined. Neutrinoless double beta decay, denoted $0\nu\beta\beta$, is a particularly promising probe: its observation would demonstrate lepton-number violation, establish the Majorana nature of neutrinos, and could help improve our understanding of the matter–antimatter asymmetry in the Universe. The $^{136}$Xe isotope is particularly well suited to this search because it is both a double-beta emitter and a detection medium. A liquid-xenon time projection chamber produces scintillation and ionization signals that allow interactions within the detector to be identified. The nEXO experiment is based on this principle and aims to improve the current sensitivity of searches for $0\nu\beta\beta$ by two orders of magnitude. Achieving this goal requires precise energy reconstruction and a very low-background environment. The accuracy of this measurement is affected by the concentration of electronegative impurities in the xenon, which can capture electrons during their drift; a model was therefore developed to quantify their impact and guide the construction and operation of the detector. The very low-background environment also imposes specific requirements on the detector design. This thesis investigates the use of nickel and changes to the cryostat geometry in order to optimize the baseline design of the instrument. HFE, the cryogenic fluid surrounding the TPC, must provide both radiation shielding and cryogenic stability. Well suited because it remains liquid at both room temperature and the operating temperature of liquid xenon, HFE was studied using a cooling and recirculation test stand to characterize its low-temperature behavior.